HIGH-OUTPUT DIESEL ENGINE HEAT TRANSFER

by

Eric M. Gingrich

A dissertation submitted in partial fulfillment of

the requirements for the degree of

Doctor of Philosophy

(Mechanical Engineering)

at the

UNIVERSITY OF WISCONSIN–MADISON

2020

Date of final oral examination: 7/22/2020

The dissertation is approved by the following members of the Final Oral Committee:

Jaal B. Ghandhi, Professor, Mechanical Engineering

Gregory F. Nellis, Professor, Mechanical Engineering

David A. Rothamer, Associate Professor, Mechanical Engineering

Sage L. Kokjohn, Associate Professor, Mechanical Engineering

Riccardo Bonazza, Professor, Engineering Physics

Terry L. Hendricks, Chief Technical Officer, Exo-Atmospheric Technologies, LLC

Peter J. Schihl, ST Ground Vehicle Propulsion and Mobility, U.S. Army

© Copyright by Eric M. Gingrich 2020

All Rights Reserved

DISTRIBUTION A. Approved for public release; distribution unlimited. OPSEC # 4299

Abstract

High-output diesel engine heat transfer was investigated using a single-cylinder research engine. Engine operating conditions near 30 bar IMEPg and 250 bar in-cylinder pressure were tested. This study had three primary goals. The first was to compare local piston heat transfer, based on fast-response piston surface temperature data, to global engine heat transfer based on thermodynamic data. A wireless telemetry system was used to acquire fast-response piston surface temperature data, from which heat flux was calculated. The local measurements were then spatially averaged to find total heat transfer, which agreed relatively well with the global measurements.

In the second part of this research, thermal barrier coatings of various thickness and surface roughness were applied to the piston crown. Three coated pistons were tested. Coatings with higher roughness did not show any statistically significant improvement to engine performance when compared to the metal baseline piston, and produced higher filter smoke numbers. The lower roughness coated piston showed an increase of gross indicated thermal efficiency of up to 3.5 % (relative) compared to the metal baseline piston for some operating conditions. The increase in efficiency was found to correlate with additional late-cycle apparent heat release rate and a reduction in in-cylinder heat transfer.

In the third part of this research, a new instantaneous spatially averaged heat transfer correlation was developed using the local heat flux data. Previous correlations are based on the correlation of Nusselt and Reynolds numbers. The new correlation included an additional term, dimensionless chemical energy release rate. The new term was derived from dimensional analysis, which should enable similitude for diesel engines. A new interpretation of the characteristic velocity, as found in the Reynolds number, was developed and included the integrated fuel mass injection rate. The existing and new correlations were calibrated to the experimental data by minimizing the least squares error. On average, the new formulation was found to match the experimental data better than the existing models.

Acknowledgments

This work would not have been possible without the support of many individuals along the way. First, I want to acknowledge and thank my wife Amanda for her continuous support in this nearly decade-long process. She has tolerated the long days and extra hours that come with graduate research. She has managed the evolving burden that graduate school has on a family, from living in different states, supporting her own career and raising children; she always found a way to make it work. I would like to thank my parents for always encouraging to do my best and for providing me the means and direction to achieve my goals.

I am grateful for the support from many of my colleagues at U.S. Army Ground Vehicle Systems Center (GVSC). I want to thank Peter Schihl for his mentorship and his ability to continuously encourage research staff. In following with your many Star Wars jokes, thank you for using the *Force* to protect the internal research. Steven Stoll, thank you for being by my side for every data point in the lab and not letting me blow up the engine. Our daily discussions about home brewing and craft beer made the long hours of data collection much more enjoyable. Michael Tess, thank you for camaraderie and support through this process and helping solve the many technical issues that come with experimental work. I am appreciative that Steven Thrush made himself available for surface roughness characterization every time I called. Thank you to the many other individuals in the propulsion lab that have supported me in many ways.

The thermal barrier coating portion of this project would not exist without the many individuals at Stony Brook University's Center Thermal Spray Research (CTSR). Thank you Sanjay Sampath for your leadership of the research center and John Saputo and Gregory Smith for many hours put into the lab perfecting the coatings.

To all the student, faculty and staff at the Engine Research Center (ERC) thank you for your friendship, camaraderie and support. Although my time on campus was limited compared to most, the experiences will shape me for a lifetime. I would like to thank Rolf Reitz for advising through my Master's degree and ultimately putting me up to the challenge

of completing a PhD. Last, I want to thank my advisor Jaal Ghandhi for his support, guidance and mentorship. I am thankful you supported the non-traditional research path that I took. You have instilled in me the need to always critically think through my research and produce the highest quality work.

Dedication

To my sons Miles and Wesley.

Table of Contents

Abstract i

Acknowledgments ii

Dedication iv

Table of Contents v

List of Tables ix

List of Figures xi

Nomenclature xx

1 Introduction 1

1.1 Motivation 1

1.2 Objectives 3

1.3 Approach 3

2 Literature Review 5

2.1 Thermal Barrier Coatings in Engines 5

2.2 Experimental Methods in Heat Transfer 10

2.2.1 Global Measurements 10

2.2.2 Local Measurements 11

2.3 Heat Transfer Correlations in Engines 15

2.3.1 Time-Averaged Heat Transfer Correlations 16

2.3.2 Instantaneous Spatially Averaged Heat Transfer Correlations 18

2.3.3 Instantaneous Local Heat Transfer Correlations 25

3 Experimental Apparatus and Methodology 27

3.1 Single-cylinder Research Engine . . . 27
3.2 Instrumentation and Data Acquisition . . . 28
3.2.1 High Speed Data Acquisition . . . 28
3.2.2 Low Speed Data Acquisition . . . 29
3.2.3 Piston Wireless Telemetry System . . . 32
3.3 Engine Operating Conditions . . . 34
3.3.1 Load / Speed . . . 34
3.3.2 Fuel . . . 35
3.4 Data Analysis . . . 36
3.4.1 Global Heat Transfer . . . 36
3.4.2 Local Heat Transfer . . . 38
3.4.3 In-cylinder Pressure and Temperature . . . 40
3.4.4 Heat Release Rate . . . 42
3.4.5 Uncertainty Analysis . . . 42
3.5 Summary of Pistons Tested . . . 43

4 Metal Piston Heat Flux Measurements in a High-output Diesel Engine 45
4.1 Summary of Major Assumptions . . . 46
4.2 Data Mapping to Sector Mesh . . . 46
4.2.1 Injector Spray Pseudo Thermocouple Locations . . . 47
4.2.2 Radial Data Reduction . . . 49
4.2.3 Interpolation . . . 51
4.2.4 Pegging Area Averaged Heat Flux . . . 52
4.2.5 Data Validation and Availability . . . 54
4.3 Heat Flux Results . . . 55
4.3.1 Operating Condition 1 . . . 58
4.3.2 Operating Condition 2 . . . 64
4.3.3 Operating Condition 3 . . . 69

4.3.4 Operating Condition 4 75
4.3.5 Operating Condition 5 75
4.4 Comparison of Local and Global Heat Transfer 80
4.5 Summary and conclusion 85

5 Impact of Thermal Barrier Coating Roughness 88
5.1 Thermal Barrier Coating 88
5.1.1 Architecture 88
5.1.2 Surface Roughness 89
5.2 Results 91
5.2.1 Standard Output: Operating Conditions 1-3 91
5.2.2 Very High-Output: Operating Conditions 4 & 5 106
5.2.3 Rated Power Heat Transfer 111
5.3 Summary and conclusion 113

6 Engine Heat Transfer Correlation for High-output Operating Conditions 116
6.1 Motivation based on Experimental Data 116
6.2 Dimensional Analysis 120
6.3 Comparison of Existing Heat Transfer Correlations to Experiments 122
6.4 Investigation into a New Heat Transfer Correlation 128
6.4.1 Proposed Dimensionless Form 129
6.4.2 Proposed Dimensional Form 129
6.4.3 Optimization of Constants 133
6.4.4 Combustion Multiplier 135
6.4.5 Velocity Term 138
6.4.6 Comparison of Cases Tested 139
6.5 New Heat Transfer Correlation 142
6.5.1 Comparison of Dimensionless Values 151

6.6 Summary and conclusion 155

7 Summary and Recommendations 156

7.1 Summary 156

7.1.1 Metal Piston Heat Flux Measurements in a High-output Diesel Engine 156

7.1.2 Impact of Thermal Barrier Coating Roughness 158

7.1.3 Engine Heat Transfer Correlation for High-output Operating Conditions 159

7.2 Recommendations 160

7.2.1 Metal Piston Heat Flux Measurements in a High-output Diesel Engine 160

7.2.2 Impact of Thermal Barrier Coating Roughness 161

7.2.3 Engine Heat Transfer Correlation for High-output Operating Conditions 162

Bibliography 164

A Appendix 172

A.1 Lower Heating Value 172

A.2 Combustion Efficiency 172

A.3 Global Energy Balance 173

A.4 Heat Transfer from AHRR 174

A.5 Thermal Barrier Coating Processing and Properties 175

A.6 Piston Thermocouple Locations 177

A.7 Piston Thermocouple Drawing 179

A.8 Injector Spray Locations 182

A.9 Thermocouple Functionality 184

A.10 Pair-wire Thermocouple Results 186

A.11 Heat Flux Results- Operating Condition 4 189

A.12 Heat Flux Contours for all Conditions 193

A.13 Final Heat Transfer Correlation 2 217

A.14 MATLAB Functions 222

List of Tables

2.1 Instantaneous spatially averaged heat transfer correlations 24

3.1 Single-cylinder Research engine specifications with valving timing based on 1.27 mm of static lift 29
3.2 High-speed instruments 30
3.3 Emissions instruments 30
3.4 Temperature and flow instruments 31
3.5 Detailed operating conditions targets 35
3.6 Selected fuel properties for F-24 jet fuel 36
3.7 Summary of pistons tested 44

4.1 Operating condition 1 (1700 rpm, 12.3 bar IMEPg) available thermocouple measurements and substitutions 59
4.2 Operating condition 2 (1500 rpm, 23.8 bar IMEPg) available thermocouple measurements and substitutions 65
4.3 Operating condition 3 (2500 rpm, 20.3 bar IMEPg) available thermocouple measurements and substitutions 69
4.4 Operating condition 5 (2750 rpm, 29.7 bar IMEPg) available thermocouple measurements and substitutions 76

5.1 Piston Nomenclature 90

6.1 Summary of intermediate steps in heat transfer correlation development 141
6.2 Constants for final heat transfer correlations 143

A.1 Coating layer properties 177
A.2 Fuel injector specifications 182
A.3 Fuel injector nomenclature 182

A.4 Thermocouple functionality as a function of date for instrumented pistons . . . 185

A.5 Operating condition 4 (1700 rpm, 30.3 bar IMEPg) available thermocouple measurements and substitutions 190

List of Figures

2.1 Cummins / TACOM turbocompounded adiabatic engine reproduced from Kamo and Bryzik [46]. 6
2.2 Comparison of heat release rate for metal and insulated engine from Dickey et al. [24]. 7
2.3 Bendersky-type co-axial surface thermocouple, taken from [56] 12
2.4 Radiant heat flux and AHRR for 1500 RPM, 100 percent load with SOI –14.5 °ATDC. taken from [87] 15
2.5 Time-averaged heat transfer for multiple engines from Taylor [88] 17
2.6 Comparison of heat transfer coefficient as a function of crank angle for various correlations taken from Caton [16] 23

3.1 Piston bowl profile 27
3.2 Experimental engine laboratory setup 28
3.3 Wireless telemetry system schematic 33
3.4 Cross-section of piston showing 15 fast-response thermocouples 34
3.5 Comparison of operating conditions to typical truck engine and SCRE maximum 35
3.6 Example raw temperature data at thermocouple 3 as acquired from wireless telemetry system 39
3.7 Example processed temperature and heat flux data at thermocouple 3 41

4.1 Example heat flux contour map showing piston thermocouple locations (red dots) and bowl edges (gray lines) 45
4.2 Injector spray targeting relative to thermocouple plane for on-plume, split-plume and off-plume locations 48
4.3 Comparison of actual and area modified thermocouple radial locations on piston bowl 50

4.4 Operating condition 3 (2500 rpm, 20.3 bar IMEPg) SOI timing of -25 °ATDC comparison of left and right side thermocouple groups 50
4.5 Sector mesh used for temperature and heat flux interpolation with pseudo thermocouple locations marked in with red dots (solid markers for measured data, open markers for duplicate data) 51
4.6 Operating condition 3 (2500 rpm, 20.3 bar IMEPg) pegging sensitivity of local heat transfer ($\langle Q \rangle$) compared to global heat transfer ($\dot{Q}_{gas}$) 54
4.7 Comparison of piston temperature and heat flux area interpolated metrics for all operating conditions (open markers used for higher uncertainty data) 57
4.8 Operating condition 1 (1700 rpm, 12.3 bar IMEPg) SOI timing of -16 °ATDC area averaged and individual heat flux with line color indicating piston location 60
4.9 Operating condition 1 (1700 rpm, 12.3 bar IMEPg) high-speed crank angle measurements for all SOI (solid lines left axis, dotted lines right axis) 61
4.10 Operating condition 1 (1700 rpm, 12.3 bar IMEPg) contours of heat flux integrated w.r.t. time from -20 to 100 °ATDC (energy flux) for all SOI 62
4.11 Operating condition 1 (1700 rpm, 12.3 bar IMEPg) SOI timing of -16 °ATDC contours of heat flux at selected crank angles 63
4.12 Operating condition 2 (1500 rpm, 23.8 bar IMEPg) SOI timing of -17 °ATDC area averaged and individual heat flux with line color indicating piston location 65
4.13 Operating condition 2 (1500 rpm, 23.8 bar IMEPg) high-speed crank angle measurements for all SOI (solid lines left axis, dotted lines right axis) 66
4.14 Operating condition 2 (1500 rpm, 23.8 bar IMEPg) contours of heat flux integrated w.r.t. time from -20 to 100 °ATDC (energy flux) for all SOI 67
4.15 Operating condition 2 (1500 rpm, 23.8 bar IMEPg) SOI timing of -17 °ATDC contours of heat flux at selected crank angles 68
4.16 Operating condition 3 (2500 rpm, 20.3 bar IMEPg) SOI timing of -25 °ATDC area averaged and individual heat flux with line color indicating piston location 70

4.17 Operating condition 3 (2500 rpm, 20.3 bar IMEPg) high-speed crank angle measurements for all SOI (solid lines left axis, dotted lines right axis) 71
4.18 Operating condition 3 (2500 rpm, 20.3 bar IMEPg) high-speed measurements for intake manifold temperature sweep 72
4.19 Operating condition 3 (2500 rpm, 20.3 bar IMEPg) contours of heat flux integrated w.r.t. time from -20 to 100 °ATDC (energy flux) for all SOI 73
4.20 Operating condition 3 (2500 rpm, 20.3 bar IMEPg) SOI timing of -25 °ATDC contours of heat flux at selected crank angles 74
4.21 Operating condition 5 (2750 rpm, 29.7 bar IMEPg) SOI timing of -21 °ATDC area averaged and individual heat flux with line color indicating piston location 76
4.22 Operating condition 5 (2750 rpm, 29.7 bar IMEPg) high-speed crank angle measurements for all SOI (solid lines left axis, dotted lines right axis) 77
4.23 Operating condition 5 (2750 rpm, 29.7 bar IMEPg) contours of heat flux integrated w.r.t. time from -20 to 100 °ATDC (energy flux) for all SOI 78
4.24 Operating condition 5 (2750 rpm, 29.7 bar IMEPg) SOI timing of -21 °ATDC contours of heat flux at selected crank angles 79
4.25 Comparison of local ($\langle Q \rangle$) and global ($\dot{Q}_{gas}$) heat transfer metrics for all operating conditions. Arrows show direction of advancing SOI (open markers used for higher uncertainty data) 81
4.26 Comparison of location of maximum heat flux and maximum bulk gas temperature for all operating conditions (open markers used for higher uncertainty data) . . 82
4.27 Comparison of location of heat flux rise and start of combustion for all operating conditions (open markers used for higher uncertainty data) 83
4.28 Operating condition 1 (1700 rpm, 12.3 bar IMEPg) SOI timing of -5 °ATDC area averaged, individual heat flux (with line color indicating piston location) and AHRR 84

4.29 Comparison of heat flux delay in units of time (top) and crank angle (bottom) as function of start of combustion for all operating conditions (open markers used for higher uncertainty data) 85

5.1 Thermal barrier coating architecture 89
5.2 3D Contour of 1.16 by 0.87 mm portion of piston for an as sprayed TBC, polished TBC and stock metal piston 90
5.3 Histogram of height for an as sprayed TBC, polished TBC and stock metal piston 91
5.4 Initial experiments operating condition 3 (2500 rpm, 20.3 bar IMEPg) ITEg, $\dot{Q}_{gas}$ and FSN 93
5.5 Operating condition 1 (1700 rpm, 12.3 bar IMEPg) in-cylinder pressure and AHRR for SOI timing of -17 °ATDC 94
5.6 Operating condition 1 (1700 rpm, 12.3 bar IMEPg) ITEg, $\dot{Q}_{gas}$ and FSN 95
5.7 Operating condition 2 (1500 rpm, 23.8 bar IMEPg) in-cylinder pressure and AHRR for SOI timing of -16 °ATDC 96
5.8 Operating condition 2 (1500 rpm, 23.8 bar IMEPg) ITEg, $\dot{Q}_{gas}$ and FSN 98
5.9 Operating condition 3 (2500 rpm, 20.3 bar IMEPg) in-cylinder pressure and AHRR for SOI timing of -25 °ATDC 99
5.10 Operating condition 3 (2500 rpm, 20.3 bar IMEPg) in-cylinder pressure and AHRR for SOI timing of -10 °ATDC 99
5.11 Operating condition 3 (2500 rpm, 20.3 bar IMEPg) ITEg, $\dot{Q}_{gas}$ and FSN 100
5.12 Operating condition 3 (2500 rpm, 20.3 bar IMEPg) NO_x, CO and HC emission indexes 101
5.13 Operating conditions 1, 2 and 3 comparison of location of $\langle \dot{q}''_{max} \rangle$ to location of $\Delta AHHH_{max}$ 103
5.14 Operating conditions 1, 2 and 3 comparison of change in ITEg as function of $\langle \dot{q}''_{max} \rangle$ 104
5.15 Operating conditions 1, 2 and 3 contours of heat flux at crank angle with maximum $\langle \dot{q}'' \rangle$ 105

5.16 Operating condition 4 (1700 rpm, 30.3 bar IMEPg) in-cylinder pressure and AHRR for SOI timing of -12 °ATDC 106
5.17 Operating condition 4 (1700 rpm, 30.3 bar IMEPg) ITEg, $\dot{Q}_{gas}$ and FSN 108
5.18 Operating condition 5 (2750 rpm, 29.7 bar IMEPg) in-cylinder pressure and AHRR for SOI timing of -21 °ATDC 109
5.19 Operating condition 5 (2750 rpm, 29.7 bar IMEPg) ITEg, $\dot{Q}_{gas}$ and FSN 110
5.20 Operating condition 3 (2500 rpm, 20.3 bar IMEPg) normalized heat transfer . . 112
5.21 Operating condition 5 (2750 rpm, 29.7 bar IMEPg) normalized heat transfer . . 113

6.1 Operating conditions 1, 2, 3 and 5 $\langle Nu \rangle$ as a function of Re using mean piston speed as velocity (open circle markers show SOC and × markers show EOC). In general, the trajectory follows a counterclockwise path. 119
6.2 Operating condition 1 (1700 rpm, 12.3 bar IMEPg), SOI of -22 and -5 °ATDC, comparing experimental data $\langle h \rangle$, correlation 1 (Woschni), and correlation 2 (Woschni optimized) 124
6.3 Operating condition 2 (1500 rpm, 23.8 bar IMEPg), SOI of -19 and -7 °ATDC, comparing experimental data $\langle h \rangle$, correlation 1 (Woschni), and correlation 2 (Woschni optimized) 125
6.4 Operating condition 3 (2500 rpm, 20.3 bar IMEPg), SOI of -29 and -14 °ATDC, comparing experimental data $\langle h \rangle$, correlation 1 (Woschni), and correlation 2 (Woschni optimized) 126
6.5 Operating condition 5 (2750 rpm, 29.7 bar IMEPg), SOI of -21 and -9 °ATDC, comparing experimental data $\langle h \rangle$, correlation 1 (Woschni), and correlation 2 (Woschni optimized) 126
6.6 Operating conditions 1, 2, 3 and 5 $\langle Nu \rangle$ as a function of Re using velocity from correlation 1 (Woschni) (open circle markers show SOC and × markers show EOC) 127
6.7 Operating condition 1-5, typical values of $\tilde{q}_{ch}$, most advanced SOI shown for each operating condition 130

6.8 Operating condition 3 (2500 rpm, 20.3 bar IMEPg), SOI= -14 °ATDC comparing $\tilde{q}_{ch}$ to measured heat transfer coefficient, $\langle h \rangle$, and correlation 2 (Woschni optimized) 131

6.9 Conductivity, k, and viscosity, μ as a function of temperature using real air properties at 130 bar 133

6.10 Specific heat, c_p as a function of temperature using ideal gas properties of 21 percent O_2 and 79 percent N_2 134

6.11 Operating condition 1 (1700 rpm, 12.3 bar IMEPg), SOI of -22 °ATDC, comparing experimental data $\langle h \rangle$ and correlation 3 (combustion multiplier 1) 136

6.12 Examples of $f_2(\tilde{q}_{ch})$ 137

6.13 Operating condition 3 (2500 rpm, 20.3 bar IMEPg), SOI of -23 °ATDC, comparing experimental data $\langle h \rangle$, correlation 4 ($f_2(\tilde{q}_{ch})$) and correlation 5 (combustion multiplier off) 138

6.14 Operating condition 2 (1500 rpm, 23.8 bar IMEPg), SOI of -7 °ATDC, comparing experimental data $\langle h \rangle$, correlation 7 (velocity- no constant term) and correlation 8 (no $\bar{S}_p$) 139

6.15 Comparison of error for all correlations developed as part intermediate steps . . 140

6.16 Operating condition 3 (2500 rpm, 20.3 bar IMEPg), SOI of -25 °ATDC, comparing typical dependence of each component of final correlation 1 (shown as ratio of value at -40 °ATDC) 145

6.17 Comparison of Q_h and $\dot{Q}_{gas}$ for final correlation 1 146

6.18 Operating condition 1 (1700 rpm, 12.3 bar IMEPg), SOI sweep, comparing experimental data $\langle h \rangle$ (solid lines) and final correlation 1 (dashed lines) 147

6.19 Operating condition 2 (1500 rpm, 23.8 bar IMEPg), comparing experimental data $\langle h \rangle$ (solid lines) and final correlation 1 (dashed lines) 148

6.20 Operating condition 3 (2500 rpm, 20.3 bar IMEPg), comparing experimental data $\langle h \rangle$ (solid lines) and final correlation 1 (dashed lines) 148

6.21 Operating condition 3 IMT (2500 rpm, 20.3 bar IMEPg), comparing experimental data $\langle h \rangle$ (solid lines) and final correlation 1 (dashed lines) 149
6.22 Operating condition 4 (1700 rpm, 30.3 bar IMEPg), comparing experimental data $\langle h \rangle$ (solid lines) and final correlation 1 (dashed lines) 149
6.23 Operating condition 5 (2750 rpm, 29.7 bar IMEPg), comparing experimental data $\langle h \rangle$ (solid lines) and final correlation 1 (dashed lines) 150
6.24 Operating conditions 1, 2, 3 and 5 $\langle Nu \rangle$ as a function of Re using velocity from final correlation 2 (open circle markers show SOC and $\times$ markers show EOC) . 152
6.25 Operating conditions 1, 2, 3 and 5 $\langle Nu \rangle$ as a function of $Re \cdot f(\tilde{q}_{ch})$ using velocity from final correlation 1 (open circle markers show SOC and $\times$ markers show EOC) 153
6.26 Operating conditions 1, 2, 3 and 5 $\langle Nu \rangle$ as a function of $Re \cdot f(\tilde{q}_{ch})$ using velocity from final correlation 1 all on same axes 154

A.1 Comparison of different heat transfer metrics 175
A.2 Post testing TBC pistons from left to right: 0.185 mm as-sprayed, 0.325 mm as-sprayed, 0.325 mm polished 176
A.3 Piston thermocouple locations with oil cooling jet (underside), intake valves (cylinder head), and exhaust valves (cylinder head) superimposed 177
A.4 Single-cylinder engine intake port layout 178
A.5 Telemetry piston installed in engine 178
A.6 Soot witness marks on pistons run with $\epsilon = 22.5°$ injector where red lines represent injector spray targeting and blue represent soot witness mark estimated center of mass. The center of mass is approximately 2.0° off the piston thermocouple axis and 7.5° off each spray plume location. 183
A.7 Example of pair-wire type thermocouple taken from [43] 186
A.8 Operating condition 3 (2500 rpm, 20.3 bar IMEPg) SOI timing of -25 °ATDC comparison of heat flux from co-axial and pair-wire type thermocouples 187

A.9 Operating condition 3 (2500 rpm, 20.3 bar IMEPg) SOI timing of -25 °ATDC sub-surface temperature for Pair-wire TBC piston 188
A.10 Operating condition 3 (2500 rpm, 20.3 bar IMEPg) comparison of mean temperature at thermocouple 12 using Pair-wire Metal, Co-axial Metal 1 and Pair-wire TBC piston 189
A.11 Operating condition 4 (1700 rpm, 30.3 bar IMEPg) SOI timing of -12 °ATDC area averaged and individual heat flux with line color indicating piston location 190
A.12 Operating condition 4 (1700 rpm, 30.3 bar IMEPg) high-speed crank angle measurements for all SOI (solid lines left axis, dotted lines right axis) 191
A.13 Operating condition 4 (1700 rpm, 30.3 bar IMEPg) contours of heat flux integrated w.r.t. time from -20 to 100 °ATDC (energy flux) for all SOI 192
A.14 Operating condition 1 (1700 rpm, 12.3 bar IMEPg) SOI timing of -22 °ATDC . 194
A.15 Operating condition 1 (1700 rpm, 12.3 bar IMEPg) SOI timing of -18 °ATDC . 195
A.16 Operating condition 1 (1700 rpm, 12.3 bar IMEPg) SOI timing of -16 °ATDC . 196
A.17 Operating condition 1 (1700 rpm, 12.3 bar IMEPg) SOI timing of -13 °ATDC . 197
A.18 Operating condition 1 (1700 rpm, 12.3 bar IMEPg) SOI timing of -5 °ATDC . . 198
A.19 Operating condition 2 (1500 rpm, 23.8 bar IMEPg) SOI timing of -19 °ATDC . 199
A.20 Operating condition 2 (1500 rpm, 23.8 bar IMEPg) SOI timing of -17 °ATDC . 200
A.21 Operating condition 2 (1500 rpm, 23.8 bar IMEPg) SOI timing of -14 °ATDC . 201
A.22 Operating condition 2 (1500 rpm, 23.8 bar IMEPg) SOI timing of -9 °ATDC . . 202
A.23 Operating condition 2 (1500 rpm, 23.8 bar IMEPg) SOI timing of -7 °ATDC . . 203
A.24 Operating condition 3 (2500 rpm, 20.3 bar IMEPg) SOI timing of -29 °ATDC . 204
A.25 Operating condition 3 (2500 rpm, 20.3 bar IMEPg) SOI timing of -25 °ATDC . 205
A.26 Operating condition 3 (2500 rpm, 20.3 bar IMEPg) SOI timing of -23 °ATDC . 206
A.27 Operating condition 3 (2500 rpm, 20.3 bar IMEPg) SOI timing of -19 °ATDC . 207
A.28 Operating condition 3 (2500 rpm, 20.3 bar IMEPg) SOI timing of -14 °ATDC . 208
A.29 Operating condition 4 (1700 rpm, 30.3 bar IMEPg) SOI timing of -12 °ATDC . 209

A.30 Operating condition 4 (1700 rpm, 30.3 bar IMEPg) SOI timing of -10 °ATDC . 210
A.31 Operating condition 4 (1700 rpm, 30.3 bar IMEPg) SOI timing of -6 °ATDC . . 211
A.32 Operating condition 4 (1700 rpm, 30.3 bar IMEPg) SOI timing of 0 °ATDC . . 212
A.33 Operating condition 5 (2750 rpm, 29.7 bar IMEPg) SOI timing of -21 °ATDC . 213
A.34 Operating condition 5 (2750 rpm, 29.7 bar IMEPg) SOI timing of -17 °ATDC . 214
A.35 Operating condition 5 (2750 rpm, 29.7 bar IMEPg) SOI timing of -13 °ATDC . 215
A.36 Operating condition 5 (2750 rpm, 29.7 bar IMEPg) SOI timing of -9 °ATDC . . 216
A.37 Comparison of Q_h and Q_{gas} for final correlation 2 217
A.38 Operating condition 1 (1700 rpm, 12.3 bar IMEPg), SOI sweep, comparing experimental data $\langle h \rangle$ (solid lines) and final correlation 2 (dashed lines) 218
A.39 Operating condition 2 (1500 rpm, 23.8 bar IMEPg), comparing experimental data $\langle h \rangle$ (solid lines) and final correlation 2 (dashed lines) 218
A.40 Operating condition 3 (2500 rpm, 20.3 bar IMEPg), comparing experimental data $\langle h \rangle$ (solid lines) and final correlation 2 (dashed lines) 219
A.41 Operating condition 3 IMT (2500 rpm, 20.3 bar IMEPg), comparing experimental data $\langle h \rangle$ (solid lines) and final correlation 2 (dashed lines) 219
A.42 Operating condition 4 (1700 rpm, 30.3 bar IMEPg), comparing experimental data $\langle h \rangle$ (solid lines) and final correlation 2 (dashed lines) 220
A.43 Operating condition 5 (2750 rpm, 29.7 bar IMEPg), comparing experimental data $\langle h \rangle$ (solid lines) and final correlation 2 (dashed lines) 220
A.44 Operating conditions 1, 2, 3 and 5 $\langle Nu \rangle$ as a function of Re using velocity from final correlation 2 all on same axes 221

Nomenclature

Abbreviations

AC - alternating current
AFR - air-fuel ratio
APS - atmospheric plasma spray
ATDC - after top dead center
BDC - bottom dead center
BRC - blue ribbon committee
CAC - charge-air cooler
CAD - crank angle degrees
CFD - computational fluid dynamics
CO - carbon monoxide
CONUS - contiguous United States
COTS - commercial off-the-shelf
DAQ - data acquisition
DI - direct injection
EES - engineering equation solver
EGR - exhaust gas recirculation
EMF - electromotive force
EOC - end of combustion
EOI - end of injection
ESD - extreme studentized deviate
EVC - exhaust valve closure
EVO - exhaust valve opening
FEA - finite element analysis
FFT - fast fourier transform
FSN - filter smoke number
HC - hydrocarbon
HCCI - homogeneous charge compression ignition
IC - internal combustion
IDI - indirect injection diesel
IMEPg - gross indicated mean effective pressure
IMEPn - net indicated mean effective pressure
IMT - intake manifold temperature
ISFC - indicated specific fuel consumption
ITEg - gross indicated thermal efficiency
IVC - intake valve closure
IVO - intake valve opening
JP-8 - jet propellant 8
LHV - lower heating value
LTC - low temperature combustion

NiCrAl - nickel chromium aluminum
NO_x- nitrous oxides
OCONUS - outside the contiguous United States
PM - particulate matter
PSZ - partially stabilized zirconia
Ra - arithmetical mean deviation of the assessed profile (surface roughness)
ROI - rate of injection
RTD - resistance temperature detector
SCRE - single-cylinder research engine
SEM - scanning electron microscope
SI - spark-ignition
SiRPa - Silica-reinforced porous anodized aluminum
SOC - start of combustion
SOI - stat of injection
TACOM - U.S. Army tank-automotive and armaments command
TBC - thermal barrier coating
TDC - top dead center
YSZ - yttria stabilized zirconia

Notation

α	thermal diffusivity
Δh_f	heat of formation
δ	distance
ϵ	error, emissivity or injector angle
η_c	combustion efficiency
γ	ratio of specific heats
μ	dynamic viscosity
ν	kinematic viscosity
ω	angular velocity
ρ	density
θ	crank angle
A	Area
A_n	Fourier coefficient
a	constant for final correlations
$AHRR$	apparent heat release rate
B	bore
B_n	Fourier coefficient
C	constant
c	speed of sound
c_p	specific heat capacity
$\dot{E}$	energy rate
h	heat transfer coefficient or enthalpy
$\langle h \rangle$	instantaneous spatially averaged heat transfer coefficient
k	thermal conductivity
L	stroke
MW	molecular weight
m	mass or Reynolds number exponent
$\dot{m}$	mass flow rate
N	engine speed
n	harmonic number
Nu	Nusselt number
$\langle Nu \rangle$	Nusselt number based on instantaneous spatially averaged data
P	pressure
Pr	Prandtl number
Q	heat transfer, energy transfered by heat
$\dot{Q}$	heat transfer rate
$\langle Q \rangle$	spatially averaged heat transfer
$\dot{q}''$	heat flux, rate of heat transfer per unit area
$\langle \dot{q}'' \rangle$	spatially averaged heat flux per unit area
$\dot{q}_{ch}$	chemical energy release rate per unit volume
$\tilde{q}_{ch}$	dimensionless chemical energy release rate

Notation (Continued)

R	universal gas constant
$\bar{R}$	specific gas constant
Re	Reynolds number
$\bar{S}_p$	mean piston speed
T	temperature (any) or average in-cylinder gas temperature
$\langle T_{piston} \rangle$	spatially averaged piston temperature
t	time
V	volume
v	velocity
$\dot{W}$	power
y	mass fraction
z	axial cylinder length

Subscripts

air	intake air
b	brake
ch	chemical
$cool$	coolant
$cycle$	cycle
exh	exhaust
$fric$	friction
$fuel$	fuel
gas	gas
$global$	global
i, g	gross indicated
i, n	net indicated
in	inlet
int	interpolated
max	maximum
oil	oil
out	outlet
peg	pegged
r	reference
$rise$	rise
s	surface
$sector$	sector
$trap$	trapped
w	wall

1 Introduction

1.1 Motivation

The use of liquid fuels as the primary energy source for U.S. Army ground vehicles is likely to continue into the foreseeable future. Liquid fuels have high energy density and specific energy, which makes storage, distribution, and on-vehicle use possible. The United States Armed Forces attempts to design and operate as many fuel-consuming devices with kerosene-type fuels to reduced battlefield logistics [63]. The use of a single fuel reduces the logistics burden by allowing the maximum interoperability of fuel-consuming devices. For ground vehicle systems, this often means a diesel engine power plant is operated on jet fuel rather than diesel fuel, which it was designed for.

In addition to a somewhat unique fuel, Army ground vehicles are subject to a range of vehicle-level requirements that impact the design and selection of the power plant. The performance requirements for combat vehicle systems are significantly different than commercial propulsion systems. The Blue Ribbon Committee (BRC), which was formed to help U.S. Army Tank-automotive and Armaments Command (TACOM) identify research and development needed for future military combat propulsion systems, identified four major differences [84, 85]:

1. **Duty cycle-** The combat vehicle duty cycle is more heavily weighted toward low-load when compared to on-road commercial trucks.

2. **Extremes of operating conditions-** Combat vehicles are required to operate at extreme ambient temperatures from -60 to 120 °F while maintaining vehicle propulsion requirements, *e.g.*, top speed, gradeability and acceleration. Additionally, the terrain that these vehicles operate over are extreme and may include paved roads, snow, ice, sand or mud.

3. **Armor enclosure-** The entire propulsion system is enclosed in armor for combat vehicles. Ballistic grilles are used on air inlets and outlets which can drive up the cooling system fan power to as much as 10 to 15 percent of propulsion system power.

4. **Reliability versus durability-** The lifetime of a combat vehicle is significantly less than a commercial truck. In peacetime combat vehicles cover less than 1,000 miles per year whereas commercial trucks accumulate up to 250,000 miles annually. Additionally, the inability of a combat vehicle to operate in the critical moment may be fatal.

Vehicle-level design decisions many times result in a trade-off between vehicle mobility and survivability. To create a vehicle that can survive more enemy threats, additional vehicle armor is needed. Armor adds weight to a vehicle, which in turn degrades its mobility. Many times vehicles are fielded at a design weight but incur a significant weight growth due to new and evolving threats. Although the BRC primarily focused on combat vehicles, which have tactical offensive and defensive capabilities, their analysis is also applicable to non-combat vehicles such as tactical trucks. Many of the Army's trucks now include additional armor due to threats encountered in the Iraq and Afghanistan theaters.

The unique requirements of combat vehicles puts under-armor space at a premium, which motivates the need for a compact propulsion system. A compact propulsion system allows vehicle designers to include additional under-armor space for munitions, equipment or soldiers; giving battlefield commanders additional capabilities. Raffa *et al.* discussed the need to make combat vehicle engine selection based on installed (system level) power density rather than exclusively looking at engine size [75]. Installed power density is the ratio of sprocket power divided by the entire propulsion system volume where the propulsion system volume includes the engine, transmission, final drive(s), cooling system, air filter(s), intake, exhaust, fuel tank, plumbing, miscellaneous items, and unusable space. This analysis assumes a mission profile, *i.e.*, drive cycle, and system-level efficiency to estimate fuel tank size. This holistic vehicle-level metric of installed power density allows assessment of radically different propulsion systems such as diesel engines, turbines, fuel cells, or others. For example, at first

glance a turbine or marine diesel may seem like an obvious choice because of their small size but system-level analysis would show that the turbine requires a large air filter due to its high air consumption and the marine diesel has multiple stages of turbochargers and inter-cooling, which requires a large cooling system that does not package in the limited under-armor space.

An important attribute of a military specific diesel engine is a low brake-specific heat rejection, which is defined as the heat rejected to the cooling system per brake power. This metric captures the need for both a high-output engine while managing the vehicle cooling system size. This unique requirement and other military specific requirements have driven engine selection away from commercial products and more toward modified commercial engines and engines designed specifically for military application [79]. As such, research opportunities exist to further improve engine performance with vehicle integration considerations in mind. This work seeks to advance understanding of engine heat transfer with the hope further understanding will lead to higher-output engines with low brake-specific heat rejection.

1.2 Objectives

There are three primary objectives of this research all of which focus on high-output diesel engine operation:

1. Investigate spatial and temporal variation of piston heat flux (Chapter 4).
2. Explore the impact a piston thermal barrier coating has on engine heat transfer and performance (Chapter 5).
3. Develop a new instantaneous spatially averaged heat transfer correlation (Chapter 6).

1.3 Approach

In this study a high-output single-cylinder research engine (SCRE) was used to acquire data at selected operating conditions. The engine was configured with different pistons,

some that included thermal barrier coatings. The experimental setup included a range of sensors to measure speed, torque, temperature, pressure and flow that were used to calculate thermodynamic quantities, including *global* heat transfer. For some of the experiments, pistons instrumented with fast-response thermocouples were used to acquire instantaneous surface temperature, from which a temporally varying heat flux could be calculated. *Local* heat transfer, based on the piston surface temperature measurements, were compared to other measurements of heat transfer. Area-averaged heat flux was used to develop a new instantaneous spatially averaged heat transfer correlation.

2 Literature Review

2.1 Thermal Barrier Coatings in Engines

For nearly 40 years, research has been conducted on thermal barrier coatings (TBC) applied to internal combustion engines with the intention of increasing efficiency and decreasing heat rejection. A TBC consists of a low thermal conductivity material applied to base-metal engine parts including: pistons, valves, cylinder heads, cylinder liners, and exhaust ports. This review of the literature is not intended to be exhaustive but rather capture trends in the development history. Other authors have attempted to organize the literature through review papers [20, 44, 80] that offer additional details.

A large number of studies were conducted on TBCs in the 1980's and 1990's that brought to light durability issues with the coatings and mixed results in terms of engine performance and heat rejection. Much of the initial work was based on the adiabatic engine concept advanced by Cummins and TACOM [45], which explored possible diesel engine configurations (including the addition of turbocompounding and Rankine cycles) that benefited from near-adiabatic operation. Subsequent work from the same group focused extensively on the engine with turbocompounding [46]. Figure 2.1 shows the proposed turbocompounding configuration.

In the 1970's researchers conducted experiments using monolithic ceramics such as silicon-carbide (SiC) and silicon-nitride (Si_3N_4). Additionally, many studies have used partially stabilized zirconia (PSZ) as a TBC on a metal substrate. Havstad *et al.* reported a 5-9 percent lower indicated specific fuel consumption (ISFC) and a 30 percent reduction in heat rejection on a single-cylinder with a solid PSZ ceramic insert for the head, liner and piston top [36]. Kamo *et al.* used a six-cylinder turbocharged direct injection diesel engine with a 0.1 mm TBC on the piston and head and 0.5 mm TBC on the liner and reported a 5-6 percent improvement in fuel efficiency over a range of engine speeds and loads [47]. However, other researchers have presented performance results with insulated combustion chambers that were worse than the metal baseline [18, 60, 97]. Woschni *et al.* [97] postulated that the

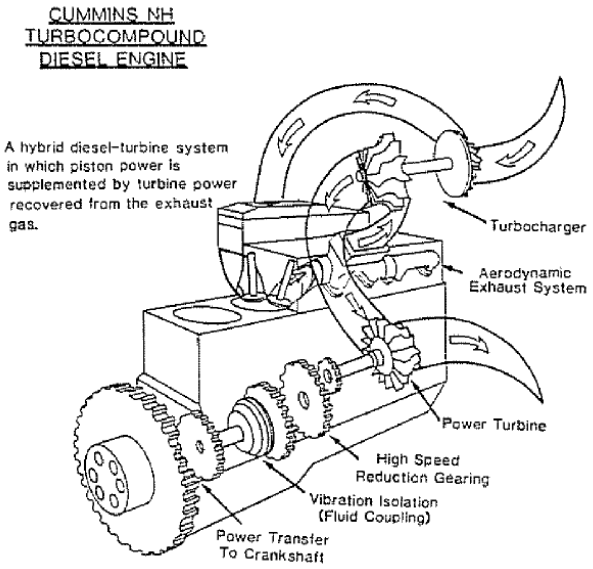


Figure 2.1: Cummins / TACOM turbocompounded adiabatic engine reproduced from Kamo and Bryzik [46].

increased surface temperature that resulted from the addition of TBCs actually resulted in increased heat transfer due to thinner boundary layers and increased temperature gradients. Consequently, the gas side heat transfer coefficients increased and overcame any reduction in heat transfer due to increased conduction resistance of the wall.

In many of these studies volumetric efficiency was negatively impacted, which for naturally aspirated engines meant air flow and performance were also reduced. It is believed that the increased surface temperature of TBCs causes heating of the intake air, subsequently reducing the density of the inducted air. Turbocharged and turbocompounded, engines could recover some of the additional energy in the exhaust stream to produce a net benefit in brake work. Simulation results from Assanis *et al.* show that some of the volumetric efficiency losses may be compensated by the increased exhaust temperature driving the turbocharger [8]. The performance penalty associated with the loss of volumetric efficiency on a multi-cylinder four-stroke engine suggests that there may be some optimum TBC thickness for a given set of TBC thermal properties.

Much of the subsequent work on TBCs focused on relatively thin coatings to reduce in-cylinder heat transfer rather than maximizing insulation for a near-zero heat transfer. Using a single-cylinder engine, Assanis *et al.* reported as much as a 10 percent increase in thermal efficiency for a piston coated with 0.5 mm TBC. The same study found a 1 mm thick TBC resulted in inferior performance compared to the metal baseline [10]. Researchers have reported a reduction in premixed burn fraction and consequently an increase in diffusion combustion for diesel engines with TBCs [24, 47]. Not surprisingly, the reduced premixed burn fraction resulted from the shorter ignition delays associated with the increased gas temperature caused by the TBC. Figure 2.2 shows the heat release rate for an engine with a TBC compared to the metal baseline. Increased diffusion combustion can result in non-optimal or deteriorated combustion. Alkidas attempted to optimize the combustion system after the addition of a TBC. The optimized combustion system had equal or superior performance when compared to the metal baseline. Alkidas refuted Woschni's hypothesis of increased heat transfer, suggesting changes in combustion can result in reduced performance of TBCs [1]. Work by Kamo *et al.* seemed to confirm Alkidas's results and also suggests that changes to the injector needle lift profile may change the injection rate and subsequently impact the combustion process [47].

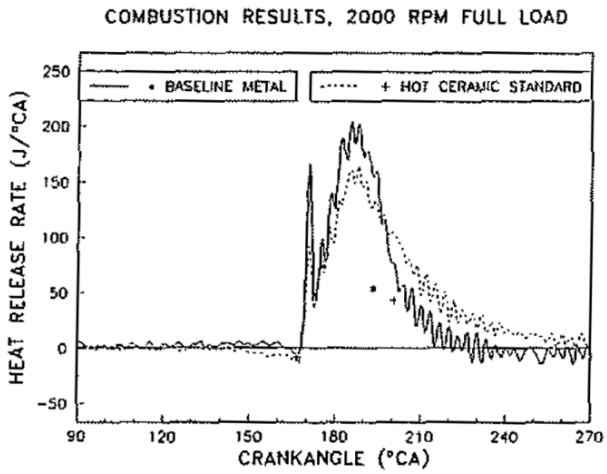


Figure 2.2: Comparison of heat release rate for metal and insulated engine from Dickey et al. [24].

Overall, the literature presents a somewhat mixed picture of the impact of TBCs on emissions. With higher gas temperatures one may expect increased levels of nitrous oxides (NO_x) due to the sensitivity of the production reactions to temperature. While many studies have observed increased NO_x [1, 59] some actually observed decreases [10, 24]. Conversely, more complete combustion may be expected with higher temperatures, reducing hydrocarbon (HC) and carbon monoxide (CO) emissions. Some studies have reported lower HC and CO [10] over a range of conditions while others seem to have less-clear trends showing increases at some operating conditions and decreases at others [1, 32, 59]. Similarly the impact of TBCs on smoke emissions is not clear. Much of the disagreement of the impact TBCs have on emissions may result from whether the combustion system was re-optimized after the addition of the TBC.

Recently, Toyota Motor Corporation has introduced a new composite material and the concept of "Temperature Swing Heat Insulation" through numerous publications and patents [31, 50, 51, 65, 92, 93]. This concept relies on a low thermal capacitance coating that allows the coated combustion chamber surface temperature to change rapidly with the in-cylinder gas temperature, which is similar to recommendations by Wong *et al.* [94]. The silica reinforced porous anodized aluminum (SiRPA) coating developed by Toyota consists of porous anodized aluminum that is coated with silica to stop in-cylinder gases from entering the porous structure. Work at General Motors and the University of Valencia attempted to extend the temperature swing idea for spark ignition (SI) engines through development of a material of hollow nickel alloy spheres sintered together to form an insulation layer with 95 % porosity [4, 25, 26]. This coating relies on the same basic idea that a TBC should closely follow the in-cylinder gas temperature. Initial testing using intake and exhaust valves experienced multiple failures of the sealing layer which the researchers believe was the cause of higher hydrocarbon emissions for the spark-ignition conditions tested. The high porosity that gives these coatings the low thermal capacitance can also introduce durability problems. Andrie *et al.* showed a 4.6 percent decrease in fuel consumption on a small SI engine by creating

a coating mixing binders, blends of aluminosilicate, metals, and oxide powders to decrease density, thermal conductivity, and specific heat capacity of the coating [3]. This study used gaseous fuels (Methane and Propane) which may have eliminated one of the challenges of unburned hydrocarbon getting trapped in the coating but still demonstrated the benefits of a coating with low thermal capacitance.

The effect of TBCs on homogeneous charge compression ignition (HCCI) engines has been investigated. Yttria stabilized zirconia (YSZ) coatings were tested and compared to Gadolinium Zirconate (GdZr), which was selected as a coating because it has a 30% lower conductivity than YSZ and a dense low-porosity structure [61, 69, 70, 73, 74]. The researchers suggested that focusing on reducing thermal conductivity and limiting coating thickness was a more practical approach to achieving a TBC that most closely follows the combustion gas temperature without introducing durability issues that can arise from high porosity and thick coatings. The results showed an improvement in ITEg in the range of 4 to 6 percent on a relative basis for matched combustion phasing. Yan *et al.* used a thick TBC for HCCI operation and found an improvement to thermal efficiency through reduced exhaust hydrocarbons and reduced heat transfer [98].

The atmospheric plasma spray (APS) process used to apply many TBCs results in surface roughness with Ra > 10 μm, which is about an order of magnitude greater than the surface finish on many production metal pistons. The APS process involves accelerating solid thermal spray powders (with grain size typically between 10-100 μm) through a high temperature environment where they melt and impinge on the target surface. The cooling and accumulation of particles results in a coating that has surface roughness inherently linked to particle size and spray process parameters. Many studies of engine TBCs have suspected that surface roughness plays a role on engine performance and heat transfer [50, 57, 73].

Kogo *et al.* [50] compared fully insulating a piston crown to only coating the most outer portion of the piston to limit the impact that increased surface roughness had on combustion motion. They found that the piston with only the outer region coated performed better than

the fully insulated version, attributing the differences to higher gas temperatures retained closer to the wall from reduced combustion gas motion. Powell attempted to isolate the effect of surface roughness from open porosity by applying aluminum coatings treated with surface finishes [73]. These HCCI experiments seemed to confirm that roughness did increase heat transfer but the impact of open porosity was not clear because of the accumulation of surface deposits over time.

2.2 Experimental Methods in Heat Transfer

Analysis to quantify engine heat transfer can be categorized into *global* and *local* methods. Global methods are based on thermodynamic measurements of fluid streams entering and exiting the engine. Local methods seek to quantify the temporal variation in heat transfer rate per unit area, *i.e.*, heat flux, for discreet locations in the combustion chamber.

2.2.1 Global Measurements

Global Measurements of heat transfer are based on drawing a thermodynamic control volume that surrounds the entire engine. Equation 2.1 gives a simplified breakdown of the energy distribution with each of the terms written such that positive values are expected. For a detailed discussion and definition of global heat transfer see Appendix A.3. When the First Law of Thermodynamics is enforced for the control volume, the largest contributor is fuel chemical enthalpy, $\dot{Q}_{fuel}$, which is based on a measured flow rate of fuel and knowing the chemical energy content of the fuel, *i.e.*, lower heating value (LHV). The brake power, $\dot{W}_b$, of the engine is quantified by measuring torque and speed. The enthalpy of the exhaust, $\dot{E}_{exh}$, is calculated from the flow rate and temperature of the exhaust. The energy removed by *intentional* cooling, $\dot{Q}_{cool}$, is, for many engines, dominated by the flow stream of coolant and is calculated by measuring a temperature increase across the engine and flow rate. Some engines have built in oil and fuel coolers that reject heat to the ambient air or coolant which

would also need to be included. Other flow streams, such as oil and fuel, also need to be account for. The miscellaneous heat losses, $\dot{Q}_{misc}$, represents all the other unaccounted for heat loss such as convection to the surroundings. Because all the terms except $\dot{Q}_{misc}$ can be quantified, many times $\dot{Q}_{misc}$ is calculated and used as a check on the energy balance. In practice, the temperature rise to calculate $\dot{Q}_{cool}$ is small compared to the uncertainty of the measurement, therefore a better approach is many times to combine $\dot{Q}_{cool}$ and $\dot{Q}_{misc}$ and calculate a total global heat transfer based on the remaining terms.

$$\dot{Q}_{fuel} = \dot{W}_b + \dot{E}_{exh} + \dot{Q}_{cool} + \dot{Q}_{misc} \tag{2.1}$$

2.2.2 Local Measurements

To quantify the temporal and spatial variation of combustion chamber heat flux, measurements of transient surface temperatures are needed. A common approach is to flush-mount fast-response thermocouples on surface of the combustion chamber. If a one-dimensional assumption is made the time-varying temperature can be used to calculate heat flux, which will be discussed in the next section. The measured change in temperature is from both forced convection and radiation so the measured local heat flux is representative of the total combined heat transfer, although convection is considered the dominant effect.

Acquiring fast-response temperature data on the surface of an engine combustion chamber is challenging for a variety of reasons. Surface thermocouple mounting is typically limited to the cylinder head, liner, and piston. It is difficult to mount thermocouples in the cylinder head due to valves and coolant passages can interfere with signal-wire routing. Liner mounting is difficult because the coolant jacket surrounds the liner and the fact that the piston rings may pass over the thermocouple mounted in the liner. Thermocouple mounting in the piston is possible, but a telemetry system is required to extract data from the moving piston. Wired mechanical linkages systems have been use by researchers [9, 17, 40] for piston measurements, but suffer from durability problems due to the flexing of wires as the engine rotates. Wireless

telemetry systems eliminate many of the durability problems of wired systems but have the added complexity and cost of an additional data acquisition system. Many of the wireless systems are limited in acquisition frequency and suffer degraded signal quality, but many researchers have overcome the challenges of these systems [34, 39, 58].

Fast-response thermocouples have been used in a variety of temperature measurement applications. One of the most common types is the Bendersky-type co-axial surface thermocouple [13]. This probe can come in a number of configurations but is typically around 1 mm in diameter and is surface mounted though a press fit or threads located on the backside of the probe. The probe is constructed using two standard thermocouple metals. The center element is coated on its circumference with a dielectric insulation that electrically insulates it from a coaxial outer element. The thermocouple junction can be formed by plating or cold-weld slivers [56]. For plated junctions, advertised products claim a 1 microsecond response time [56]. An example of this co-axial configuration is shown in figure 2.3.

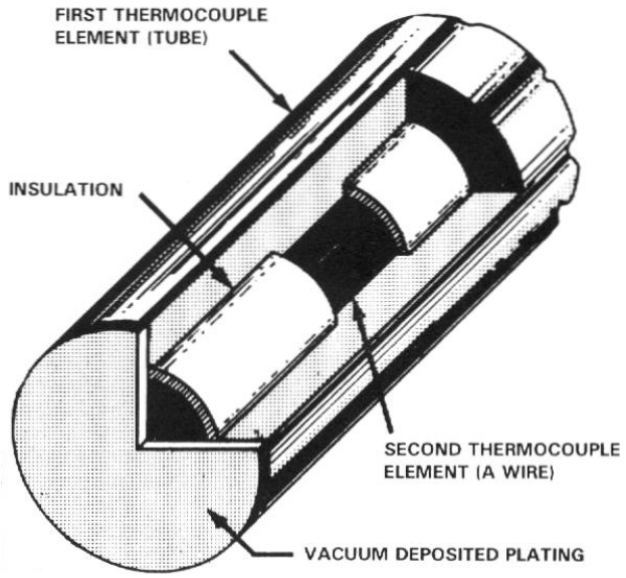


Figure 2.3: Bendersky-type co-axial surface thermocouple, taken from [56]

2.2.2.1 Heat Flux from Surface Temperature

In order to generate crank-angle resolved heat flux from surface temperature data, a one-dimensional assumption is made. The surface heat flux in an internal combustion engine can be represented by two components: the steady-state and the transient response. The steady-state component is calculated from a time-averaged surface temperature measurement and a back-side thermocouple at a known depth beneath the surface. The transient component is calculated using the time-varying surface temperature measurement.

For semi-infinite problems with periodic boundary conditions, Fourier analysis can be utilized to decompose the temperature data into frequency components, see equation 2.2, where the Fourier coefficients A_n and B_n are found using a Fast Fourier Transform (FFT), T_w is the surface temperature, n is harmonic number and ω is the angular velocity of the engine. The FFT method, as it is commonly known, has been widely used by other researchers to calculate surface heat flux in internal combustion (IC) engines [17, 37, 72].

$$T_w(t) = \bar{T}_w + \sum_{n=1}^{N} \Big[A_n cos(n\omega t) + B_n sin(n\omega t) \Big] \tag{2.2}$$

In equation 2.3, $\dot{q}''(t)$ is the instantaneous surface heat flux as a function of time. The material properties k, thermal conductivity, ρ, density, c_p, specific heat and, $\alpha = \frac{k}{\rho c_p}$ the thermal diffusivity are known. The solution can be broken down into two parts; the first part of the equation is the steady-state heat flux, which requires a second temperature measurement, T_δ, at known distance, δ below the surface. The second part of the solution is known as the transient portion of the solution and only requires the surface fast-response temperature information along with the thermal properties.

$$\dot{q}''(t) = \overbrace{\frac{k}{\delta}(\bar{T}_w - T_\delta)}^{\text{Steady State}} + \overbrace{k \sum_{n=1}^{N} \sqrt{\frac{n\omega}{2\alpha}} \Big[A_n(cos(n\omega t) - sin(n\omega t)) + B_n(sin(n\omega t) + cos(n\omega t)) \Big]}^{\text{Transient}} \tag{2.3}$$

The FFT method is instructive because it highlights how the complete solution for the instantaneous heat flux is a combination of both the steady-state and transient heat flux. The FFT method is limited to surface problems with constant thermal properties (properties cannot be a function of temperature). Other analytical methods such as an inverse heat conduction solver [11] are able to handle both surface and sub-surface problems (with temperature-dependent properties) and have been used by engine researchers for processing of noisy temperature data [37] and sub-surface problems [68].

2.2.2.2 Radiation

Radiation heat transfer in engines is primarily from two sources: blackbody emission from particulate mater and spectral emission from gases. Many heat transfer correlations in engines are formulated with the assumption that forced convection is the dominant heat transfer mechanism so it is helpful to understand the limit of this assumption. The spectral emission for gases is relativity small; CO_2 and H_2O are the dominant products of combustion and their spectral emission is limited to relatively narrow bands. Particulate matter emits radiation over a larger spectral range at higher intensity and is considered a significant source of heat transfer. Spark-ignition and low temperature combustion regimes don't produce soot particles in high enough quantity to need to consider radiation. Conversely, diesel engines operate with a mixing-controlled combustion event from which the fuel-rich regions of the combustion produce relatively large amounts of soot.

Studies of diesel engine radiation in the 1960's and 1970's estimated that 20-40 percent of the in-cylinder heat transfer was from radiation [27, 30, 71]. More recent studies have significantly lowered the estimate to 1-10 percent [12, 62, 83, 87]. Improvements to measurement techniques (primarily from better optical access to the combustion chamber) and changes to engine fuel systems may have been the primary differences. Modern high-pressure common rail injection system are known to reduce soot formation and residence time which would result in a lower total radiation contribution.

Although a significant discrepancy in the literature exists for the total contribution of radiation to in-cylinder heat transfer, nearly all studies show that the total contribution of radiation, as a percent of in-cylinder heat transfer, increases with engine load and fueling. Additionally, studies that compared the heat release rate to the temporal variations in radiation showed that radiation rises sharply after the pre-mixed burn and peaks later during the diffusion burn. Figure 2.4 compares the temporal variation of radiation and apparent heat release rate for a high-load diesel operating condition.

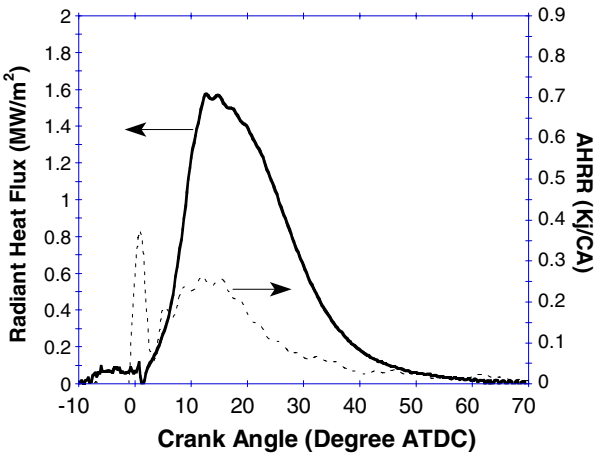


Figure 2.4: Radiant heat flux and AHRR for 1500 RPM, 100 percent load with SOI –14.5 °ATDC. taken from [87]

2.3 Heat Transfer Correlations in Engines

A significant amount of literature exists on the topic of engine heat transfer. A detailed review of engine heat transfer up until the late 1980's is given by Borman and Nishiwaki [14] and Heywood [41]. More recent reviews are given by Finol and Robinson [29] and Caton [16]. These reviews include discussion of experimental methods, radiant heat transfer, heat transfer models and other related topics. Much of the work was on indirect- and direct-injection diesel engines that were limited in in-cylinder pressure and many times had mechanical injections systems. More recent work on heat transfer correlations focus on future low

temperature combustion (LTC) engines that rely on dilute, kinetically controlled combustion regimes. Heat transfer correlations for diesel engines were developed using, by modern standards, antiquated hardware, that leads to questions about their validity. Advances in commercial and military diesel engine technology since the the 1980's have included the addition of high pressure common rail injection systems (with higher injection pressures) and increases in allowable maximum in-cylinder pressure. The following discussion of heat transfer correlations is broken down into three sections. The first section includes time-averaged heat transfer correlations based on global engine measurements. The second section focuses on instantaneous, spatially averaged heat transfer correlations that are typically based on in-cylinder pressure and temperature. The third and final section discusses instantaneous local heat transfer correlations with application to current engine computational fluid dynamic (CFD) simulations.

2.3.1 Time-Averaged Heat Transfer Correlations

Taylor and Toong [88, 89] proposed a time-averaged heat transfer correlation based on the non-dimensional Reynolds analogy of boundary layer theory in the form:

$$Nu = CRe^m \tag{2.4}$$

where Nu is Nusselt number, Re is Reynolds number, and C and m are constants. The Nusselt number is a dimensionless number representing the ratio of convective to conductive heat transfer in the form $Nu = hL/k$, where h is the heat transfer coefficient, L is a characteristic length scale, and k is the thermal conductivity of the fluid. The Reynolds number is a dimensionless number that represents the ratio of inertial forces to viscous forces in a fluid given by $Re = \frac{\rho v L}{\mu}$, where ρ is the density of the fluid, v is velocity, L is a characteristic length scale, and μ is the dynamic viscosity of the fluid.

For the Taylor and Toong correlation Nu and Re are defined as:

$$Nu = \frac{\dot{Q}_{cool} B}{k A_{piston} (\bar{T} - T_{cool})} \tag{2.5}$$

$$Re = \frac{\dot{m}_{air} B}{\mu A_{piston}} \tag{2.6}$$

where $\dot{Q}_{cool}$ is the heat transfer to the coolant, B is bore, A_{piston} is the piston area, $\dot{m}_{air}$ is the charge mass flow rate, $\bar{T}$ is the mean gas temperature for the engine cycle, T_{cool} is the mean coolant temperature, k is the gas conductivity (measured at $\bar{T}$) and μ is gas viscosity (measured at $\bar{T}$).

The authors found that the constant values of equation 2.4 to fit the data were $m = 0.75$ and C between 7.7 to 15.5, depending on engine type. Figure 2.5 shows the data for 19 different engines operating at various conditions with a line plotted for a $n = 0.75$ and $C = 10.4$.

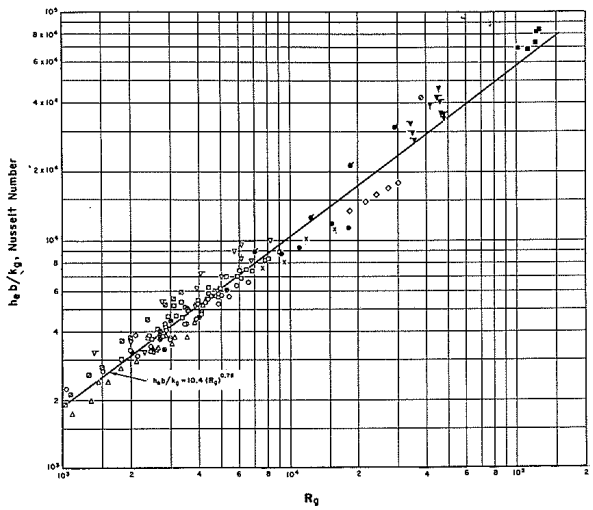


Figure 2.5: Time-averaged heat transfer for multiple engines from Taylor [88]

2.3.2 Instantaneous Spatially Averaged Heat Transfer Correlations

A number of instantaneous spatially averaged engine heat transfer correlations have been proposed in an attempt to predict an overall empirical heat transfer coefficient, h. Most correlations make a quasi-steady assumption in the form of:

$$\dot{q}'' = h(T - T_w) \tag{2.7}$$

where $\dot{q}''$ is heat flux, T is temperature based on a calculated bulk-mean gas temperature (obtained from an equation of state with in-cylinder pressure and density), and T_w is the wall surface temperature. The definition of h becomes problematic for researchers that attempt to solve for $h = \dot{q}''/(T - T_w)$, because during portions of the engine cycle $T = T_w$ which causes h to trend toward infinity. This challenge has been noted by others [14, 72] and is many times handled by limiting the calculation of h to portions of the cycle where $T - T_w$ is sufficiently large.

In some applications T_w is unknown and assumed as a constant because under most operating conditions the variation within one cycle is less than 20 °C. Some correlations include a T^4 dependence to account for radiation effects. In practice accounting for radiation can be difficult because small errors in temperature amount to large changes in heat flux.

Some of the first correlations were completely empirical in nature. Nusselt took measurements on a spherical combustion vessel and referenced engine data for a correlation [67]. The heat transfer coefficient was presented as a sum of convective, h_c and radiant components, h_r.

$$h = h_c + h_r \tag{2.8}$$

$$h_c = C_1(1 + C_2\bar{S}_p)(P^2T)^{1/3} \tag{2.9}$$

$$h_r = \frac{C_3}{1/\epsilon_g + 1/\epsilon_w - 1} \frac{(T/100)^4 - (T_w/100)^4}{T - T_w} \tag{2.10}$$

where $\bar{S_p}$ is the mean piston speed , P is pressure , and ϵ_g and ϵ_w are the emissivities of the gas and wall, respectively. Nusselt's correlation was originally intended for steady state heat flux but has often been used for instantaneous heat flux.

Eichelberg made some of the first transient heat flux measurements and proposed another empirical model based on experimental data [28]. Data were taken on multiple low speed engines including: a two-stroke marine engine with 600 mm bore and 1060 mm stroke running at 100 rpm and 7.09 bar net indicated mean effective pressure (IMEPn), a two-stroke with 380 mm bore and 460 mm stroke operating at 412 rpm and 7.86 bar IMEPn, and a four-stroke running with 280 mm bore and 420 mm stroke operating at 211 rpm and 6.89 bar. The equation he came up with was:

$$h = C_1 \bar{S_p}^{1/3} (PT)^{1/2} \tag{2.11}$$

Seeking a more fundamental approach, more recent-work is based on the non-dimensional Reynolds analogy of boundary layer theory. The work is similar to that of Taylor and Toong [89] but Nu and Re are now defined to accommodate time-varying heat transfer. The selection of the characteristic length scale and velocity term varies for different engine heat transfer correlations. For a detailed discussion of dimensional analysis, see Section 6.2.

The first widely used correlation based on the Reynolds analogy was proposed by Annand [7]. Annand reviewed existing correlations and data and proposed a new correlation:

$$\dot{q}'' = C_1 \frac{k}{B} Re^{0.7} (T - T_w) + C_2 (T^4 - T_w^4) \tag{2.12}$$

where C_1 is a constant ranging from 0.35 to 0.8 depending on charge motion, C_2 is a constant for the radiation term, which was different for diesel engines and SI engines. Mean piston speed was used as the characteristic velocity and bore, B, was used as the characteristic length

scale in the Reynolds number. Gas properties were taken at the bulk-mean temperature. The equation was written in terms of $\dot{q}''$ to allow inclusion of the radiation term.

In later work Annand modified his formula based on data from a direct injection (DI) diesel engine with swirl [6].

$$\dot{q}'' = \frac{k}{D} Re^{0.7} \left\{ C_1(T - T_w) + \frac{C_3}{\omega} \frac{dT}{dt} \right\} + C_2 \sigma (T^4 - T_w^4) \tag{2.13}$$

The updated formula included ω, the angular velocity term and a time derivative of the bulk mean temperature. The constants C_1, C_2, and C_3 were generated for different engine operating conditions and had significant variations, which led to questions about the correlations validity. The reference velocity for the updated equation used energy mean velocity proposed by Knight [49]. The mean energy was calculated by subtracting the kinetic energy of the inflowing gas from the outflowing gas.

Woschni also assumed a correlation based on the Reynolds analogy in the form [96]: $Nu = CRe^m$. The bore was taken as the characteristic length and assuming $k \propto T^{0.75}$, $\mu \propto T^{0.62}$, and $P = \rho \bar{R} T$ leads to:

$$h = C_3 B^{m-1} P^m T^{0.75-1.62m} v^m \tag{2.14}$$

With velocity defined by:

$$v = C_1 \bar{S}_p + C_2 \frac{V_d T_r}{P_r V_r} (P - P_m) \tag{2.15}$$

where V_d is displacement volume, and the sub-script r is for a known reference point in cycle, such at IVC. $P - P_m$ is the difference between the in-cylinder pressure during combustion and motoring.

In subsequent work [81, 95] Woschni added a swirl term to equation 2.15 modifying the C_1 term to be: $C_1 = 6.18 + (0.417 \cdot \text{swirl})$ for the gas exchange process and $C_1 = 2.28 + (0.308 \cdot \text{swirl})$ for remainder of the cycle.

Hohenberg [42] made modification to each of the components of Woschni's [95] equation. Hohenberg thought it was more appropriate to use the characteristic length as the diameter of a sphere whose volume corresponded to the instantaneous cylinder volume, V. The gas temperature exponent was also adjusted based on systematic experiments and an assumed relationships with the velocity term. The modified correlation is:

$$h = C_1 V^{-0.06} P^{0.8} T^{-0.4} (\bar{S}_p + C_2)^{0.8} \tag{2.16}$$

Experiments were conducted for a range of DI diesel engines with varying bore and stroke.

Sitkei [82] examined available data and concluded that the exponent m should be 0.7 and proposed the following correlation:

$$h = C(1+b) P^{0.7} \bar{S}_p^{\ 0.7} T^{-0.2} d_e^{-0.3} \tag{2.17}$$

where b is for consideration of additional turbulent velocity, d_e is an equivalent diameter given by $d_e = 4V_{dis}/A$ where A is heat-absorbing area.

The final instantaneous spatially averaged heat transfer correlation presented is by Chang et al. [17]. The model was developed based on experimental results from a homogeneous charge compression ignition (HCCI) engine and is based on a modified form of Sihling and Woschni [81]. The new correlation took the characteristic length to be the instantaneous chamber height constrained to less than cylinder radius. Equations 2.18 and 2.19 reflect the changes made to the original correlation including modifying the temperature exponent to be -0.73 and reducing the C_2 constant by a factor of 6.

$$h = \alpha_{scaling} B^{-0.2} P^{0.8} v^{0.8} T^{-0.73} \tag{2.18}$$

The velocity, v is given by:

$$v = C_1 \bar{S}_p + \frac{C_2}{6} \frac{V_d T_r}{P_r V_r} (P - P_m) \tag{2.19}$$

Table 2.1 shows a summary of the instantaneous spatially averaged heat transfer correlations discussed in chronological order. Figure 2.6 shows a comparison of many of the correlations (from Caton [16]). A few general comments based on the table and figure can be made:

1. Correlations since Annand [7] are based on dimensional analysis and the resulting non-dimensional form: $Nu = CRe^m$. Some correlations make modifications to the resulting dimensional equation based on experimental data, *e.g.*, change exponent of variables or add new multiplicative terms. Such changes are not consistent with the dimensional analysis and could impact the correlations' ability to be predictive over a larger range of conditions.

2. Correlations in the form: $Nu = CRe^m$ all have the exponent, m, in the range of 0.7 to 0.8.

3. The choice of velocity definition is many times mean piston speed, $\bar{S}_p$, or includes an additional additive term to $\bar{S}_p$ that accounts for changes in velocity from the combustion process (expansion).

4. Recent investigation of in-cylinder heat transfer from radiation (see discussion Section 2.2.2.2) shows that that convection is about and order magnitude larger than radiation and the addition of radiation terms in correlations may not be necessary.

5. The phasing and shape of h calculated in figure 2.6 is similar for all the correlations, which is not surprising because all correlations have in-cylinder pressure as part of the formulation. For the correlations based on $Nu = CRe^m$ the pressure dependence is included in the density portion of Re.

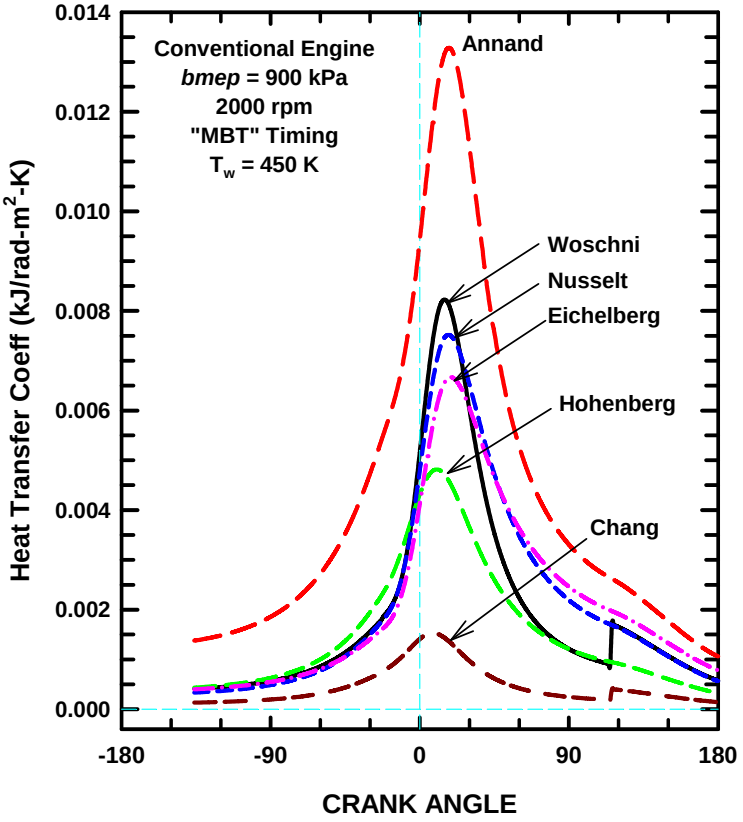


Figure 2.6: Comparison of heat transfer coefficient as a function of crank angle for various correlations taken from Caton [16]

Table 2.1: Instantaneous spatially averaged heat transfer correlations

First Author	**Year**	**Correlation**	**Engine Type**	**Bore × stroke (mm)**	**rpm**	**Location**	**IMEPn (bar)**
Nusselt [67]	1923	$h = CP^{2/3}T^{1/3}(1 + 1.24\bar{S_p}) + rad$	Spherical bomb	N/A	N/A	N/A	N/A
Elichelberg [28]	1939	$h = CP^{0.5}T^{0.5}\bar{S_p}^{1/3}$	DI, DI	380 × 460, 280 × 420, 600 × 1060	100-412	P	6.89-7.86
Annand [7]	1963	$Nu = CRe^{0.7} + rad$	IDI, SI	mult	mult	mult	mult
Woschni [81, 95, 96]	1967	$Nu = CRe^{0.8}$, $h = CL^{-0.2}P^{0.8}v^{0.8}T^{-0.53}$	DI, SI	mult	mult	mult	mult
Annand [6]	1970	$Nu = CRe^{0.7}f(\frac{dT}{dt}) + rad$	DI	80 × 110	1200-1800	H	
Sitkei [82]	1972	$Nu = CRe^{0.7}$, $h = C(1 + b)P^{0.7}\bar{S_p}^{0.7}T^{-0.2}L^{-0.3}$	DI, IDI	mult	mult	mult	mult
Hohenberg [42]	1979	$Nu = CRe^{0.8}$, $h = C_1V^{-0.06}P^{0.8}T^{-0.4}(\bar{S_p}+C_2)^{0.8}$	DI	128×142		H	
Chang [17]	2004	$Nu = CRe^{0.8}$, $h = CL^{-0.2}P^{0.8}v^{0.8}T^{-0.73}$	HCCI	86 × 94.6	1600, 2000, 2400	H, P	2.86-4.60

Note: Correlations are presented in compressed form with limited information on radiation component (if applicable). The symbols in the correlations are defined as: h is the convective heat transfer coefficient, P is cylinder pressure, T is cylinder gas temperature, $\bar{S_p}$ is mean piston speed, v is a specially defined velocity, L is the characteristic length. The abbreviation for engine type are: indirect injection diesel (IDI), direct inject diesel (DI), spark-ignition (SI), homogeneous charge compression ignition (HCCI). When information was not provided in the citation that item was left blank from the table. When multiple items types are discussed the abbreviation mult is used.

2.3.3 Instantaneous Local Heat Transfer Correlations

Correlations that vary both spatially and temporally are discussed next. LeFeuvre et al. [53] proposed an instantaneous local heat transfer correlation based on changes of heat flux across the radius of the combustion chamber. The correlation was formed based on motored engine data and extended to fired data with limited success. The correlation in equation 2.20 is based on the Nu-Re correlation and also includes a Prandtl number, Pr, term.

$$\dot{q} = C\frac{k_g}{r}Re^{0.8}Pr^{0.33}(T - T_w) \tag{2.20}$$

$$Re = \frac{r^2\omega_g}{\nu} \tag{2.21}$$

The Re is defined in equation 2.21 and includes the characteristic length scale as r, the radial position, ω is the angular velocity of the cylinder gases, ν is the kinematic viscosity based on the averaged boundary layer temperature, and C is constant.

Dent and Suliaman [23] proposed a form similar to that of LeFeuvre *et al.* but assumed a constant Pr. The gas properties were evaluated at the instantaneous gas temperature. The correlation was based on experiments from an air-cooled DI diesel engine with higher swirl ratios than LeFeuvre et al. The correlation is:

$$\dot{q} = 0.023\frac{k_g}{r}Re^{0.8}(T - T_w) \tag{2.22}$$

Commonly used engine CFD simulation codes use the energy law-of-the-wall heat transfer model [2, 5, 35, 52]. Many times, computational limits do not allow sufficient grid resolution for direct modeling of the boundary layer. The law-of-the-wall allows a prediction of local instantaneous heat transfer based on a logarithmic velocity profile. One interpretation found in KIVA-3V is [2]:

$$\dot{q} = \frac{\rho \nu_l C_p}{Pr_l} \frac{F}{y}(T - T_w) \tag{2.23}$$

$$F = \begin{cases} \frac{R' Pr_l \cdot RPR}{1/\kappa ln R' + B + 11.05(PR_l \cdot RPR - 1)} & R' > 11.05 \\ 1.0 & R' < 11.05 \end{cases} \tag{2.24}$$

$$R' = \frac{C_\mu K^{1/2} y}{\nu_l} \tag{2.25}$$

where ν_l is the laminar kinematic viscosity of air, Pr_l is the laminar Prandtl number, κ is Karman's constant, RPR is the reciprocal of the turbulent Prandtl number, T_w is the wall temperature, T is the gas temperature, K is turbulent kinetic energy, and y is distance from the wall.

3 Experimental Apparatus and Methodology

3.1 Single-cylinder Research Engine

Experiments were performed on an AVL 530 single-cylinder research engine that has a custom head designed for high output diesel engine operation. The engine is rated for 107 kW at 2750 rpm; full engine specifications are given in table 3.1. The piston bowl profile is shown in figure 3.1. An AVL 576 oil and coolant cart was used to control oil and coolant temperature. The oil and coolant lines were instrumented with Coriolis flow meters to measure mass flow rates. The engine has a high pressure common rail fuel system with capability to command multiple injections in an engine cycle, and provide fuel pressures up to 2000 bar. An 8×168 μm injector with 147 ° included angle was used. See Appendix A.8 for additional injector details. The engine fuel system was fed by an AVL P404 fuel cart that includes a Coriolis flow meter for fuel mass flow rate measurement.

A diagram of the experimental setup is shown in figure 3.2. Air was provided by an external compressed air system that dries the air to a dew point less than -40 °C. The intake manifold was temperature- and flow-controlled to simulate a turbocharger for steady-state measurement points. Exhaust back pressure was controlled via a butterfly valve in the exhaust system. Air was delivered using a control valve, with feedback control from a Coriolis flow meter plumbed in series. There are two swirl-control vanes in the intake manifold that provide an adjustable swirl ratio between 0 and 3.5. Exhaust gas was sampled and analyzed using a Horiba MEXA-7100 emissions bench. Particulate measurements were made using an AVL 415S smoke meter.

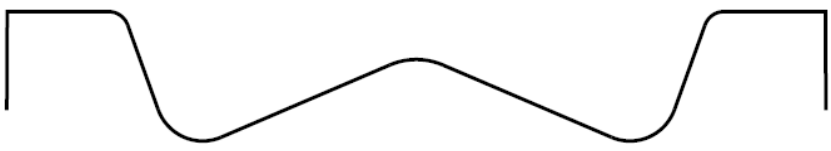


Figure 3.1: Piston bowl profile

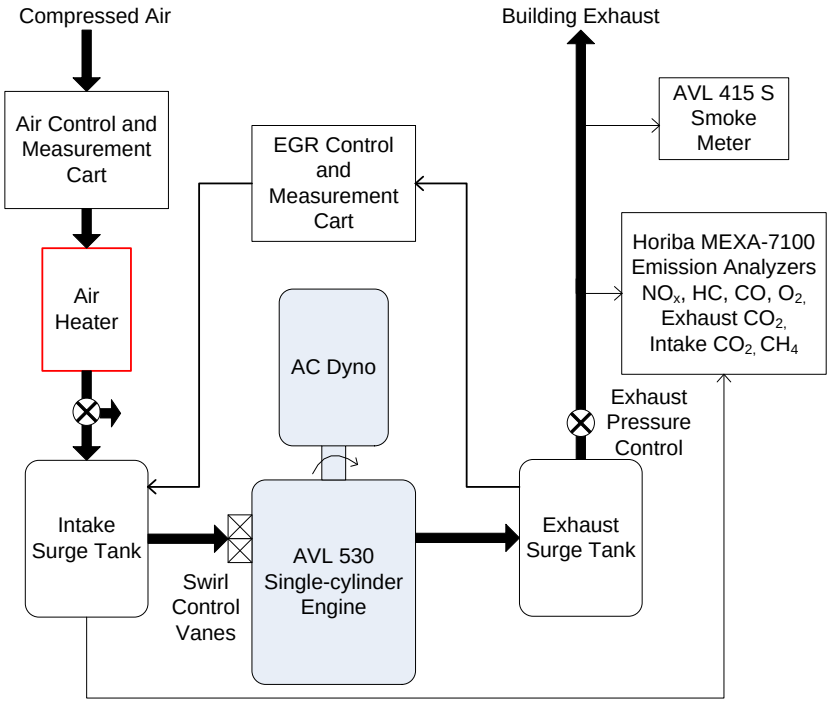


Figure 3.2: Experimental engine laboratory setup

3.2 Instrumentation and Data Acquisition

Data were acquired using three data acquisition (DAQ) systems: High speed data sampled at 0.1 ° of crank-shaft rotation, low speed data sampled at 10 Hz and a piston telemetry system used for instrumented piston experiments at 1.0 ° of crank-shaft rotation.

3.2.1 High Speed Data Acquisition

High speed engine data were acquired using an AVL Indiset 642 system in conjunction with IndiCom 2.3 software. Most signals were acquired at 0.1 ° of crank-shaft rotation (or equivalent maximum response of sensor). An AVL 365C angle encoder measured crank position at 360 pulse/rev, which was subsequently up-sampled to 3600 pulse/rev by an AVL 365Z04M pulse amplifier. Table 3.2 lists the high speed sensors and amplifiers with range and resolution.

Table 3.1: Single-cylinder Research engine specifications with valving timing based on 1.27 mm of static lift

Displacement [L]	1.49
Bore [mm]	122
Stroke [mm]	128
Connecting Rod Length [mm]	239
Number of Valves	4
IVO [°ATDC]	-354
IVC [°ATDC]	-158
EVO [°ATDC]	148
EVC [°ATDC]	346
Swirl Ratio	1.3
Peak Firing Pressure [bar]	250

IVO: intake valve opening; ATDC: after top dead center;
IVC: intake valve closing; EVO: exhaust valve opening;
EVC: exhaust valve closing.

3.2.2 Low Speed Data Acquisition

Low speed data were acquired though the test cell automation system, AVL PUMA 1.4.1. The system functions as both dynamometer controller and data acquisition system. The system is configurable with various modules for a range of inputs and outputs used for either data acquisition or control of test cell accessory equipment. When the engine reaches steady state, the operator triggers a measurement request. 120 s of low speed data are saved and the high speed DAQ is simultaneously triggered to record data. Low- and high-speed data sets are timestamped and have cross-referenced names allowing for data to be easily organized and analyzed.

A Horiba MEXA-7100DEGR with attached heated oven unit (OVN-720A) was used to measure gaseous emissions and housed all Horiba analyzers. Emissions instrument, manufacturer, model and measurement method are listed in table 3.3. HC, NO_x and CH_4 were all measured on a wet basis using a heated sampling system. CO, CO_2, O_2 and intake CO_2 were all measured on a dry basis by flowing through a condenser before entering the

Table 3.2: High-speed instruments

Measurement	Model	Range / Resolution
In-cylinder pressure	AVL GU22C	0 to 250 bar
Intake/Exhaust pressure	AVL GU21C	0 to 250 bar
Charge amplifier (In-cylinder, intake & exhaust)	AVL Microifem Piezo Module	8 to 800 pC/V
Intake/Exhaust pressure Absolute	Omega PX429-100A10-XL	0 to 6.895 bar_a
Common rail fuel pressure	AVL SL31D-3000	0 to 3000 bar
Amplifier (fuel pressure)	AVL Microifem Combi Module	0.1 to 5000 V/V
Injector Needle Lift	Micro-epsilon ES04	0 to 0.4 mm
Amplifier (needle lift)	Micro-epsilon eddyNCDT 3301	0 to 100 kHz
Injector current probe	LEM PR40/SP6	0 to 40 A
Crankshaft encoder	AVL 365C	360 pulses/rev
Multiplier Supply (encoder)	AVL 365Z04M	3600 pulses/rev

instruments. An AVL 415S Smoke Meter was used to to make measurements of filter smoke number (FSN).

Table 3.3: Emissions instruments

Species / Instrument	Manufacturer	Model	Measurement Method
Exhaust NO/NO_2 (NO_x)	Horiba	CLA-720MA	heated chemiluminescence detector
Exhaust CO and CO_2	Horiba	AIA-722	non-dispersive infrared detector
Exhaust HC	Horiba	FIA-725A	heated flame ionization detector
Exhaust CH_4	Horiba	FIA-721HA	heated flame ionization detector
Exhaust O_2	Horiba	MPA-720	magnetopneumatic detector
Intake CO_2	Horiba	AIA-722	non-dispersive infrared detector
Particulate Matter	AVL	415s Smoke Meter	filter paper reflectivity

Temperature and flow instruments are listed in table 3.4. Temperature measurements for the oil, coolant, fuel and intake air were measured using a resistance temperature detector (RTD). Because measured engine heat rejection to each fluid stream is a function of temperature difference across the engine, a special RTD calibration procedure was used. An insulated, temperature-controlled and well-stirred oil bath was used to simultaneously calibrate all RTDs while connected to the normal laboratory DAQ. Each sensor was removed from its location in the fluid stream and placed in the oil bath. Temperature of the oil bath was allowed to stabilize for each of the calibration points. This procedure ensured that all RTDs were calibrated to the same reference temperature and allowed for any variance between inputs on the DAQ to be accounted for.

Coriolis flow meters were used for fuel, oil coolant and air flow rate. The fuel flow meter was packaged as part of the AVL P404 fuel measurement cart which, allowed for a return fuel flow from the engine along with other fuel temperature and pressure controls. An in-house air measurement and control cart was designed to have a high- and low-range flow meter, each paired with an appropriately sized regulator and control valve. Oil and coolant supply lines had Coriolis flow meters installed in-line.

Table 3.4: Temperature and flow instruments

Measurement	Model	Range
Temperature (Oil, Coolant, Fuel, Intake Air)	RTD PT100	0 to 120 °C
Temperature (Exhaust)	K-type thermocouple	-270 to 1260 °C
Dew Point	Vaisala DMT348	-56 to -10 °C
Fuel flow rate	Coriolis Micromotion CMF010	0 to 34.0 kg/h
Oil flow rate	Coriolis Endress+Hauser Promass 83 F 1.0 in	0 to 1587.6 kg/h
Coolant flow rate	Coriolis Endress+Hauser Promass 83 F 1.5 in	0 to 5443.1 kg/h
Air flow rate (high range)	Coriolis Endress+Hauser Promass 83 F 1.0 in	0 to 907.2 kg/h
Air flow rate (low range)	Coriolis Endress+Hauser Promass 83 F 3/8 in	0 to 272.2 kg/h

3.2.3 Piston Wireless Telemetry System

For experiments that included a thermocouple-instrumented piston a wireless telemetry system was used to record high speed piston temperatures. Temperature data were transferred from the piston through an IR Telemetrics model 3051 microwave transmitter system. The electromotive force (EMF) generated at each thermocouple was converted to a frequency-modulated square wave over the range of 10 to 50 kHz. A voltage-controlled oscillator then converts the square wave into a microwave signal. The microwave signal is broadcast into the crankcase where four receiving antennas are mounted. The signal is amplified, converted back to a modulated square wave, downconverted, then the original EMF is recorded. The signal conversion process induces a degree of filtering but the advertised bandwidth of the system is 10 kHz.

The microwave transmitter only broadcasts data from one channel at a time; it cycles though the 15 different channels (+1 marker channel). The transmitter was configured to broadcast each channel for 0.5 seconds independent of engine speed. At higher engine speed more engines cycles will be transmitted than at slower engine speeds. For each operating condition data streaming off the engine was collected for three minutes and saved to a local computer. Data were collected in the time domain and mapped to the corresponding crank angle (at one degree resolution) through use of firing TDC *sync* pulse which was provided by the test cell high-speed DAQ and recorded in the telemetry system.

The electronics associated with the wireless telemetry system were powered by an inductive power supply. An exciter coil, mounted on the underside of the piston liner, is powered by an alternating current (AC) inductive power supply. When the piston is near bottom dead center (BDC) a secondary coil that is mounted on the piston skirt interfaces with the exciter coil allowing power to transfer inductively. Capacitors and other electronics store enough energy to power the piston though the entire engine cycle. Figure 3.3 shows a schematic of the wireless telemetry system.

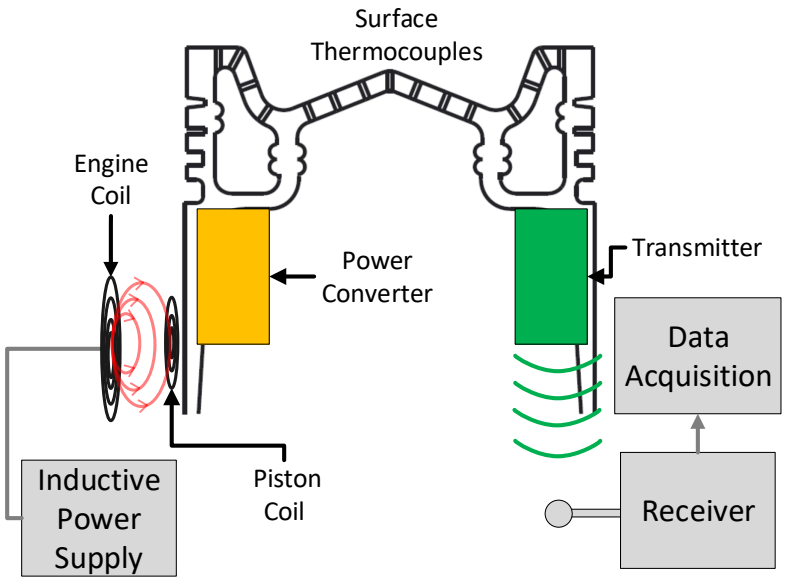


Figure 3.3: Wireless telemetry system schematic

Fifteen fast-response coaxial J-type thermocouples were installed in the piston crown to measure dynamic surface temperature. Coaxial type thermocouples have been used in a variety of applications and can survive the harsh environment including the high temperatures, pressures, and accelerations typically encountered in an engine. Section 2.2.2 gives additional details on the the thermocouple design. All of the thermocouples were flush mounted with the surface of the piston and installed in a plane perpendicular to the wrist pin. Figure 3.4 shows and isometric view of the piston cross-section that contains the thermocouples. The installation locations were chosen to have roughly equal spacing between each thermocouple and to be symmetric across the center of the piston. For details of thermocouple location see Appendices A.6 and A.7.

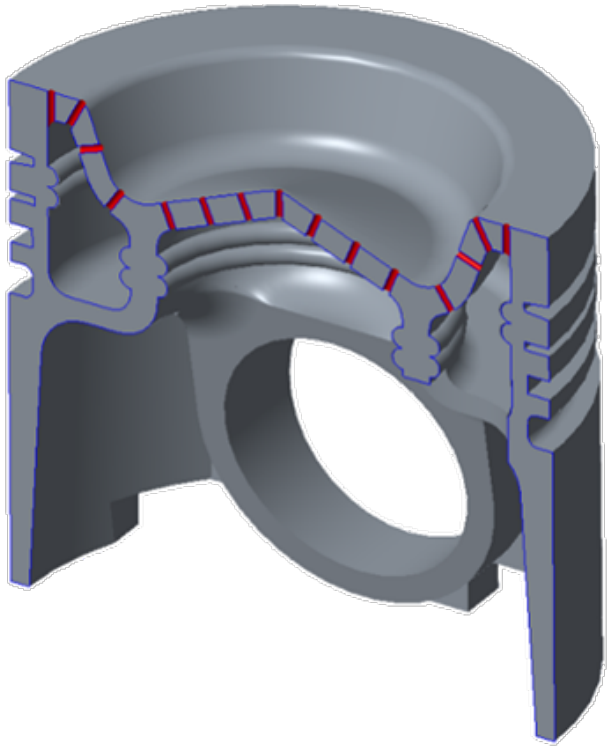


Figure 3.4: Cross-section of piston showing 15 fast-response thermocouples

3.3 Engine Operating Conditions

3.3.1 Load / Speed

The engine was operated with a fixed speed and injection duration for each of the operating conditions shown in figure 3.5 and table 3.5. Load / speed selection was weighted toward high load operation with two operating conditions near 30 bar gross indicated mean effective pressure (IMEPg). Part-load, peak torque and rated power conditions typical of a production diesel engine were selected (conditions 1-3). Additionally, two very high output cases were included (conditions 4 and 5). Data were collected after all measured quantities were allowed to stabilized. When possible, data collection was randomized to reduced progressively increasing errors. A start of injection (SOI) sweep was conducted for each of the operating conditions. The injection duration was held constant, which meant load varied slightly with changes to SOI. For most cases the earliest injection timing was limited by excessive peak in-cylinder

pressure (250 bar maximum) and the latest injection timing was limited by either excessive exhaust temperature (800 °C) or exhaust smoke (FSN > 2). The exhaust pressure target was set to a value slightly above or below the intake pressure (ΔExhaust Pressure= $P_{exh} - P_{air}$) depending on condition, see table 3.5.

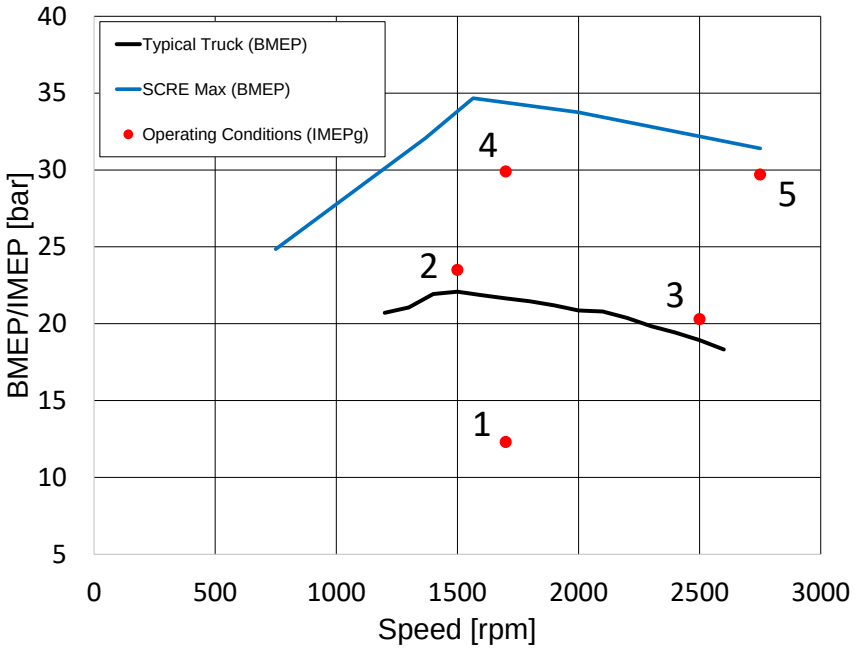


Figure 3.5: Comparison of operating conditions to typical truck engine and SCRE maximum

Table 3.5: Detailed operating conditions targets

Condition	Speed [rpm]	IMEPg [bar]	AFR [-]	Intake Air Flow [kg/h]	Intake Temperature [°C]	ΔExhaust Pressure [kPa$_a$]	Fuel Pressure [bar]	Injection duration [CA°]
1	1700	12.3	29	133.8	48.9	-46	1200	10.7
2	1500	23.8	24.5	195.0	48.9	-40	1700	18.6
3	2500	20.3	26.8	297.1	48.9	33	2000	21.6
4	1700	30.3	24.5	283.5	48.9	-28	2000	25.0
5	2750	29.7	25.5	487.6	48.9	35	2000	40.5

3.3.2 Fuel

All experiments were run using F-24 which is a kerosene-based jet fuel. The U.S. Army attempts to design and operate as many fuel-consuming devices with kerosene-type fuels to

reduced battlefield logistics [63]. For ground systems, this often means that engines designed to run on diesel fuel are operated using jet fuel. For operation in the contiguous United States (CONUS) F-24 is used (Jet-A plus military additives). For operations outside the contiguous United States (OCONUS) JP-8 (Jet-A-1 plus military additives) is used. Overall, for JP-8 and F-24 that meet the military fuel specifications [64, 90], the ignition and combustion process is similar for diesel and jet fuels. Table 3.6 shows select fuel properties and the associated test method.

Table 3.6: Selected fuel properties for F-24 jet fuel

Property	Value	ASTM Test Method
Percent Carbon [% mass]	86.12	D5291
Percent Hydrogen [% mass]	13.87	D5291
Net Heating Value [MJ/kg]	43.045	D4809
Aromatics [% vol]	14.7	D1319
Olenfins [% vol]	2.4	D1319
Saturates [% vol]	82.9	D1319
Sulfur, Total [% mass]	0.0257	D2622
Initial Boiling Point [°C]	165.5	D86
10% Recovered Distillation [°C]	189.3	D86
50% Recovered Distillation [°C	213.9	D86
90% Recovered Distillation [°C]	245.2	D86
Final Boiling Point [°C]	263.7	D86
Density at 15 °C [kg/L]	0.8161	D4052
Viscosity at 40 °C [mm^2/s]	1.475	D445
Cetane Number	47.2	D613
Derived Cetane Number	41.8	D6890

3.4 Data Analysis

3.4.1 Global Heat Transfer

Different measurements were used to quantify *global* heat transfer in this study. All methods to calculate heat transfer are grounded in the First Law of Thermodynamics, but the required assumptions combined with measurement uncertainty practically limit each method. A

comparison of the different methods along with a detailed First Law analysis (including expansion into measured variables) for a control volume that surrounds the entire engine is given in Appendix A.3. A short-form of the resulting equation is:

$$\dot{Q}_{global} = \dot{E}_{fuel} - \dot{W}_b - \dot{E}_{exh} \tag{3.1}$$

where $\dot{Q}_{global}$ is heat transfer, $\dot{E}_{fuel}$ is power delivered to the system through fuel, $\dot{W}_b$ is brake power, and $\dot{E}_{exh}$ is sensible enthalpy flow of the exhaust minus that of the intake.

A portion of $\dot{Q}_{global}$ includes heat transfer from the engine to the surroundings, $\dot{Q}_s$, which can not be directly quantified. The heat transfer to the oil and coolant, $\dot{Q}_{oil}$ and $\dot{Q}_{cool}$ are also part of the total heat transfer and can be calculated by measuring the temperature rise and flow rate of each fluid. The uncertainty of these values, however, is constrained because the temperature difference of each fluid across the engine is only on the order 1-5 °C, depending on operating condition. Rather than using $\dot{Q}_{oil}$ and $\dot{Q}_{cool}$ as a representation of engine heat transfer, for this work $\dot{Q}_{global}$ is found through enforcing an energy balance of $\dot{E}_{fuel}$, $\dot{W}_b$ and $\dot{E}_{exh}$.

Because the majority of engine friction ends up as thermal energy in the oil and coolant, and friction on a single-cylinder engine is larger on a percentage basis than for a corresponding multi-cylinder engine, a metric that eliminated friction bias was used. In addition to reporting $\dot{Q}_{global}$ an additional heat transfer metric, $\dot{Q}_{gas}$, is defined in equation 3.2.

$$\dot{Q}_{gas} = \dot{Q}_{global} - \dot{W}_{fric} = \dot{E}_{fuel} - \dot{W}_{i,n} - \dot{E}_{exh} \tag{3.2}$$

Friction power, $\dot{W}_{fric}$ is subtracted from $\dot{Q}_{global}$ to find $\dot{Q}_{gas}$, where $\dot{W}_{fric} = \dot{W}_{i,n} - \dot{W}_b$. The the subscripts b and i, n represents brake and net indicated work. $\dot{Q}_{gas}$ eliminates the use of $\dot{W}_b$ in calculating heat transfer, which is advantageous because the uncertainty of indicated power is typically less than brake power for a single-cylinder engine. For this work,

both heat transfer metrics are also normalized by the delivered fuel power, $\dot{m}_{fuel}LHV$, and given as a percentage.

Both $\dot{Q}_{global}$ and $\dot{Q}_{gas}$ are imperfect metrics for heat transfer when attempting to analyze results with a multi-cylinder application in mind. Multi-cylinder applications will include an air handling system with turbo- and or super-chargers to boost intake manifold pressure. Subsequently, the compressed air temperature will rise and need to be cooled through a charge-air-cooler (CAC) which will also contribute to system-level heat transfer. Analyzing intake manifold cooling is dependent on system design and beyond the scope of this work.

3.4.2 Local Heat Transfer

To better understand *local* in-cylinder heat transfer, measurements of piston surface temperatures were made and used to compute heat flux, $\dot{q}''$. This section describes the data processing methods to estimate $\dot{q}''$ at each temperature measurement location. Chapter 4 will later describe how $\dot{q}''$ at each location is combined into a single metric that represents the spatially averaged heat flux for the entire combustion chamber.

3.4.2.1 Fast-response Thermocouple Data and Outlier Rejection

The temperature data recorded by the wireless telemetry system included spurious spikes that needed to be removed before the heat flux could be calculated. The spikes in the data were caused by the wireless telemetry process. When the piston-mounted transmitter has direct line of sight with one of the receiving antennas, the transfer of data from the piston to the antennas is nearly 100 %. During times of the engine cycle when the transmitter does not have good visibility with the antennas, the transmission efficiency is degraded. Figure 3.6 shows an example raw temperature data as recorded by the vendor software at thermocouple 3.

Spurious raw data were eliminated by applying the generalized extreme Studentized deviate (ESD) test at each crank angle. The ESD test is used to detect one or more outliers

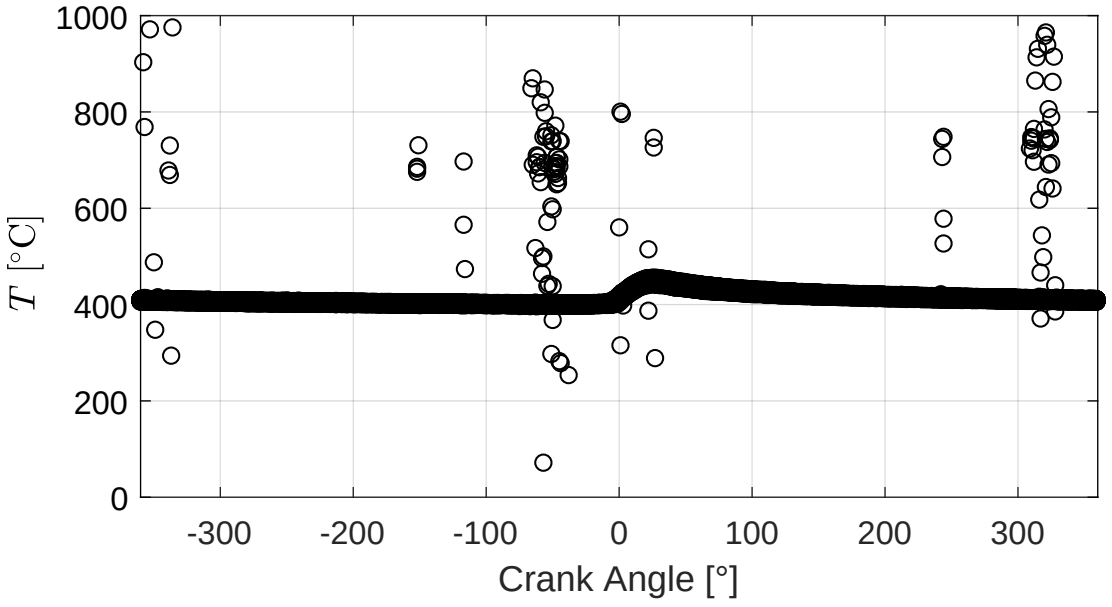


Figure 3.6: Example raw temperature data at thermocouple 3 as acquired from wireless telemetry system

in a data set that approximately follows a normal distribution [76]. This statistical tool is preferred over other tests because it does not require that the number of outliers be predefined before the test is run [66]. Typically less than 2 % of all data were removed by this procedure. In the region between -20 and 20 °ATDC, data quality was very good and less than 1 % of the data were removed.

3.4.2.2 Heat Flux Estimation- Fourier Method

The Fourier transform method described in Section 2.2.2.1 was used to calculate heat flux at each of the 15 thermocouple locations. A second backside temperature at each location was not available so the steady state portion of equation 2.3 was dropped, which becomes:

$$\dot{q}''(t) = k \sum_{n=1}^{N} \sqrt{\frac{n\omega}{2\alpha}} \Big[A_n(cos(n\omega t) - sin(n\omega t)) + B_n(sin(n\omega t) + cos(n\omega t)) \Big] \tag{3.3}$$

Section 4.2.4 will later provide details on an *ad hoc* method developed to recover the steady-state heat portion of heat transfer using an area average heat flux and temperature.

To calculate heat flux in equation 3.3 material thermal properties k and α must be known. The J-type thermocouples used have Constantan as the inner wire and Iron as the outer tube. The piston is constructed from a steel alloy. But, the simplified one-dimensional analysis only allows for a single set of properties to be used. Two-dimensional finite element analysis (FEA) has shown that the heat flux measurement most closely matches the input value when the material properties for the thermocouple inner wire are used [38]. The thermal properties for Constantan were used in equation 3.3 to calculate the heat flux. For each case the time-average surface temperature was used to calculate the conductivity and thermal diffusivity based on measurements made by Sasaki *et al.* [78]. The thermal properties are allowed to vary slightly to account for changes in operating conditions from run to run, but were held constant as temperature varies throughout the engine cycle.

Figure 3.7 shows the full-cycle temperature and heat flux. The raw temperature data from figure 3.6 were averaged at each crank angle, filtered using a low pass filter with 2000 Hz cut off frequency and then used in equation 3.3. The heat flux is relatively constant at a negative value through the intake and exhaust part of the cycle. This negative value is a result of only solving for the dynamic part of the heat flux solution, which will later be corrected (*i.e.*, pegged) using the in-cylinder thermodynamic state (see Section 4.2.4). During the compression and expansion part of the cycle, the heat flux increases due to the increased gas temperature first due to compression, and then from the high-temperature combustion products.

3.4.3 In-cylinder Pressure and Temperature

Three hundred cycles of engine data were acquired for each operating point, then ensemble averaged and filtered using a bandpass type filter with transmission frequencies between 500

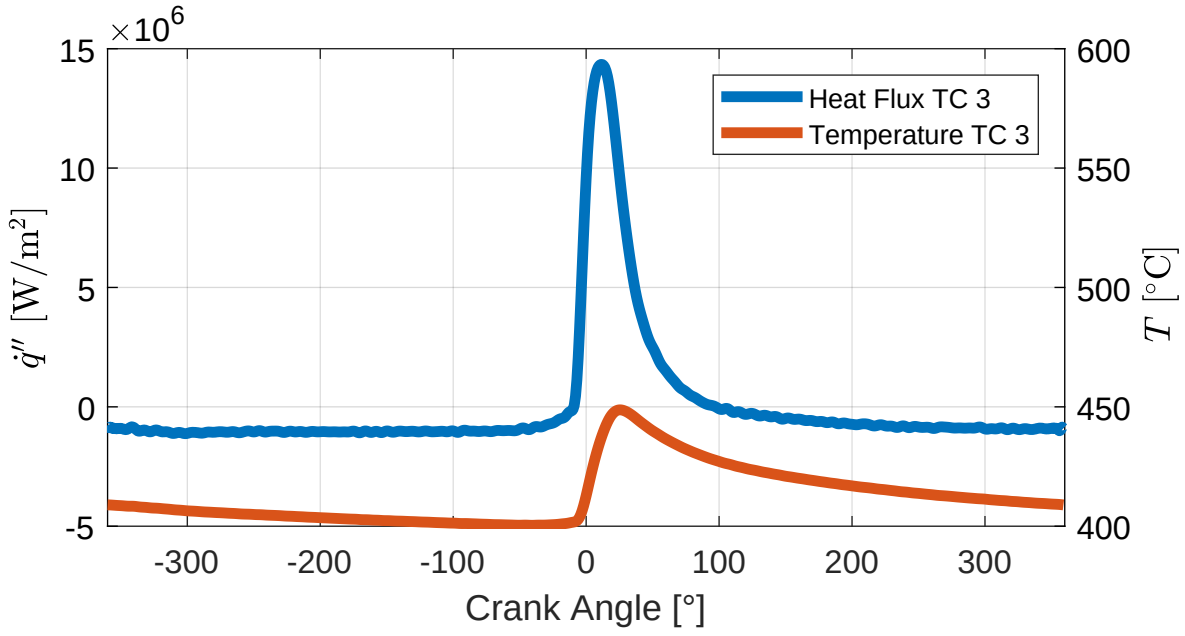


Figure 3.7: Example processed temperature and heat flux data at thermocouple 3

and 3500 Hz to calculate in-cylinder pressure, P. The average in-cylinder temperature, T can be found for the closed portion of the cycle using the Ideal Gas Law:

$$T = R\frac{PVm}{MW} \tag{3.4}$$

where R is the universal gas constant, V is the combustion chamber volume, m is mass and MW is molecular weight. m is found by:

$$m = m_{trap} + \int_{\theta_{SOI}}^{\theta_{EOI}} \frac{dm_{fuel}}{d\theta} d\theta \tag{3.5}$$

where m_{trap} is the trapped mass found using measured air flow and the Yun and Mirsky correlation [99], and $\frac{dm_{fuel}}{d\theta}$ is fuel mass addition rate, which was assumed to be constant from the start of injection command (SOI) and end of injection command (EOI). MW was found

by calculating mole fractions assuming an instantaneous and ideal conversion of reactants to products such that:

$$\mathrm{CH}_y\mathrm{O}_z + a(\mathrm{O}_2 + 3.76\,\mathrm{N}_2) \longrightarrow b\mathrm{CO}_2 + c\mathrm{H}_2\mathrm{O} + d\mathrm{N}_2 + e\mathrm{O}_2 \tag{3.6}$$

where y and z are known fuel properties and the constants a, b, c, d and e are calculated for each crank angle, θ.

3.4.4 Heat Release Rate

The apparent heat release rate (AHRR) was calculated with a single-zone analysis using equation 3.7. The ratio of specific heats, γ, was allowed to vary as a function of crank-angle and was based on the instantaneous bulk thermodynamic state. Specific heat was calculated based on varying mole fractions (from equation 3.6) and bulk temperature (from equation 3.4) using NASA ideal gas properties [55]. The AHRR calculated is a representation of chemical energy, $\dot{Q}_{ch}$, added to the system minus losses, that are primarily dominated by wall heat transfer, $\dot{Q}_w$. Appendix A.4 compares $\dot{Q}_w$ to other heat transfer metrics. Appendix A.14 has the MATLAB function that was used to calculate the AHRR and average in-cylinder temperature.

$$AHRR = \frac{\gamma}{\gamma - 1} P \frac{\mathrm{d}V}{\mathrm{d}\theta} + \frac{1}{\gamma - 1} V \frac{\mathrm{d}P}{\mathrm{d}\theta} = \dot{Q}_{ch} - \dot{Q}_w \tag{3.7}$$

3.4.5 Uncertainty Analysis

Error bar that are presented on the data represent the 95 % confidence interval by combining accuracy and precision in quadrature. Each scalar value recorded by the data acquisition system represents a mean of 120 s of N data points that has a corresponding reported standard deviation, σ, which was used in: $t_{95:N-1}\sigma/\sqrt{N}$ to find the measurement precision, where $t_{95:N-1}$ is from the Student's t-distribution. The sensors' manufacturer specifications

as a percent of reading, was used as the accuracy value in the combined total error. For fuel flow measurements, data from a system calibration (fuel cart including accessories) was used as a function of flow rate, which should represent a worse-case accuracy estimation for this device.

3.5 Summary of Pistons Tested

Table 3.7 gives a summary of the eight pistons tested as part of this work and provides the nomenclature, thermocouple type (if any), thermal barrier coating thickness (if any) and the chapters where the data will be discussed. Co-axial Metal 1 and Co-axial Metal 2 pistons were the same design (duplicate hardware) and used MEDTHERM co-axial thermocouples with a wireless telemetry system. These two pistons provided high quality heat flux data that are discussed in all three results chapters 4, 5 and 6. The next four pistons in table 3.7: Metal, 0.185mm TBC, 0.325mm TBC and 0.325mm TBC Polished were part of a sub-study on the impact of TBC roughness on engine performance in Chapter 5. These pistons did not include thermocouples but the *global* heat transfer results were supplemented with *local* heat flux data from Co-axial Metal 1 and Co-axial Metal 2. The final two pistons: Pair-wire Metal and Pair-wire TBC used a pair-wire type fast-response thermocouple. The original goal of these two pistons were to reconstruct surface heat flux on a piston with a TBC and compare to a metal piston. Results from these pistons were limited by excessive thermocouple failures and poor transient temperature response, and therefore, are only included in Appendix A.10.

Table 3.7: Summary of pistons tested

Nomenclature	Thermocouple Type	TBC Thickness [mm]	Chapter
Co-axial Metal 1	Co-axial	none	Chapters 4, 5, 6
Co-axial Metal 2	Co-axial	none	Chapters 4, 5, 6
Metal	none	none	Chapter 5
0.185mm TBC	none	0.185	Chapter 5
0.325mm TBC	none	0.325	Chapter 5
0.325mm TBC Polished	none	0.325	Chapter 5
Pair-wire Metal	Pair-wire	none	Appendix A.10
Pair-wire TBC	Pair-wire	0.325	Appendix A.10

4 Metal Piston Heat Flux Measurements in a High-output Diesel Engine

Two pistons were instrumented with fast-response surface thermocouples (Co-axial Metal 1 and Co-axial Metal 2, nomenclature from table 3.7) and run to quantify the spatial and temporal variation of piston heat flux. Both the pistons used were stock metal pistons, *i.e.*, no applied coating, and instrumented with MEDTHERM type co-axial type thermocouples [56]. For each operating condition three fuel injectors with varying spray location relative to a thermocouple axis were used to investigate variation of heat flux on and off the spray's axis.

This chapter describes the method and assumptions used to combine individual heat flux measurements into a map of spatially and temporally varying heat flux, which was then area averaged to determine the global time-varying heat transfer for the entire combustion chamber. Figure 4.1 shows an example contour of piston heat flux on a 1/8 sector mesh. These data will be used in Chapter 5 to help understand heat transfer on a piston coated with a TBC and in Chapter 6 for heat transfer correlation development.

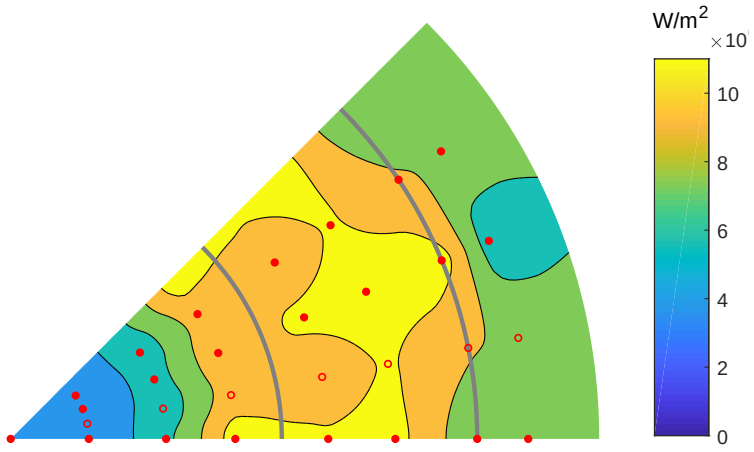


Figure 4.1: Example heat flux contour map showing piston thermocouple locations (red dots) and bowl edges (gray lines)

4.1 Summary of Major Assumptions

To calculate a time-varying heat transfer that is representative on the entire combustion chamber a number of assumptions were made:

1. The co-axial thermocouples accurately captured the time-varying piston surface temperature. The instantaneous local heat flux was calculated, which further assumes one-dimensional heat transfer and proper selection of thermal properties. See Section 3.4.2.2 for details on this assumption.

2. The selected thermocouple locations combined with an interpolation method accurately reflect the overall piston heat transfer.

3. Piston heat transfer was used to represent heat transfer to entire area combustion chamber.

These assumptions are explored and discussed at various levels throughout this chapter. Ultimately, some of the assumptions are difficult to justify with sufficient detail so the local piston heat flux measurements are compared to engine-out thermodynamic measurements of heat transfer and calculated quantities based on in-cylinder pressure to provide confidence in the data.

4.2 Data Mapping to Sector Mesh

A data reduction method was developed to take individual point data (temperature and calculated heat flux) and combine to a sector mesh that represents 1/8 (45 °) of the piston. The method utilized piston thermocouple symmetry (relative to the injector spray plumes), which enabled robust data reduction even with thermocouple failures.

4.2.1 Injector Spray Pseudo Thermocouple Locations

For most operating conditions, data were collected using three injectors with spray plumes rotated relative the thermocouple axis, *i.e.*, the spray pattern was clocked. Notionally these injectors were configured to target the thermocouple axis for the *on-plume* configuration, between the adjacent spray-plume for *off-plume* configuration and halfway between in the *split-plume* configuration. Figure 4.2 shows the three injector spray patterns relative to the installed thermocouple locations, which are located on a diameter perpendicular to the piston wrist pin. For each spray pattern the angle between the closest spray plume and thermocouple axis was include in the figure with the thermocouple axis: 5.5 ° down-stream of the spray for on-plume, 5.75 ° up-stream of the spray for split-plume, and 17.0 ° up-stream of the spray for off-plume, where up- and down-stream is in reference to the bulk swirl motion. Details of the exact thermocouple positions can be found in Appendix A.6 and A.7. Additional information on the injector geometry can be found in Appendix A.8.

The three injector spray locations were used to develop a *pseudo* thermocouple locations on a sector mesh. The relative angle between the injectors was used to fix the azimuthal angle between the interpolated points. Using spray location to capture azimuthal variation in data makes an assumption that any gradients in the data are dominated by the spray and other geometric effects, other than radial, are minimal, *e.g.*, flow and temperature differences from valves layout.

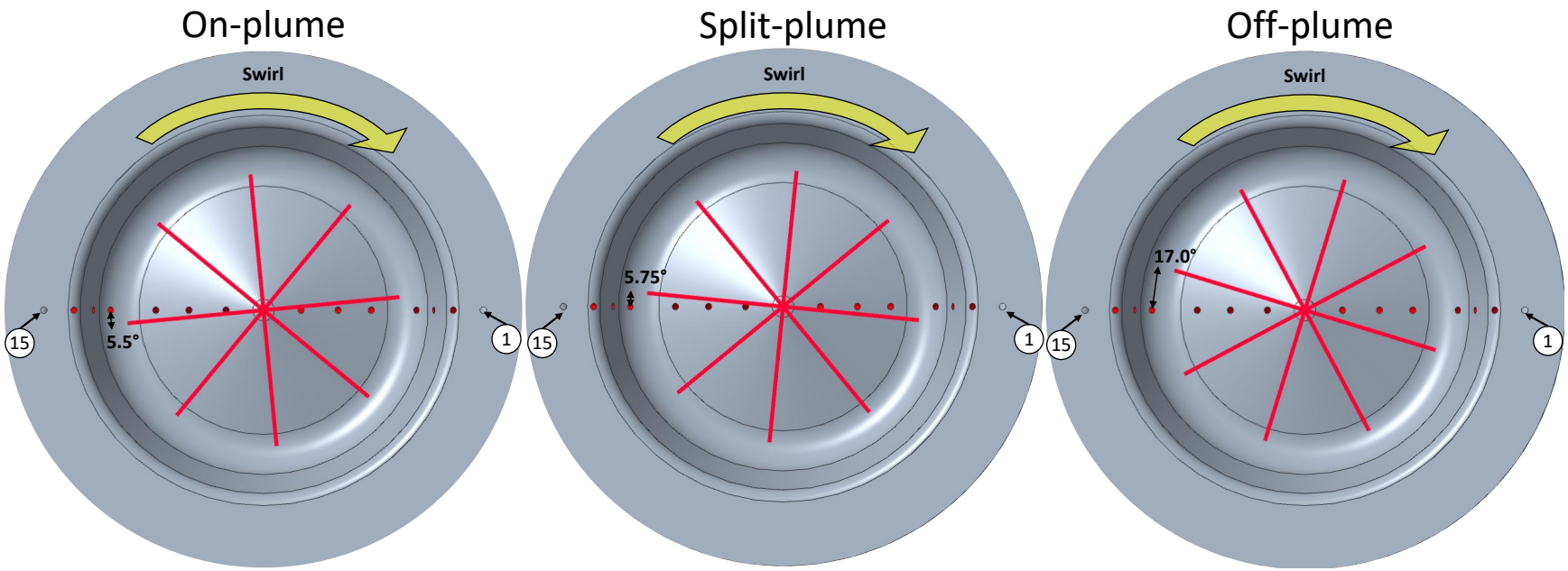


Figure 4.2: Injector spray targeting relative to thermocouple plane for on-plume, split-plume and off-plume locations

4.2.2 Radial Data Reduction

The 15 thermocouples installation locations were designed with radial symmetry (left-to-right in figure 4.2). All thermocouples, other than the center (thermocouple 8), had a matching thermocouple at the same radius that was installed on the other side of the piston (in the same diameter) and was used to reduced the data to a sector mesh. Measurements with the same radial location were combined to a single data interpolation group. When data (temperature and heat flux) from both locations were available the data were averaged. In all cases heat flux was calculated for the individual location before averaging.

The actual geometry of the piston is three-dimensional so additional assumptions were needed to reduce the data to a two-dimensional sector mesh. The overall approach was to use the three-dimensional area of the piston in the two-dimensional mesh. The radial location of each thermocouple in the mesh was adjusted to achieve the same radial area (from the center outward) as the actual three-dimensional geometry. Figure 4.3 shows actual and area adjusted radial location of each thermocouples with a cross-section image of the piston locating each thermocouple. The biggest difference between actual and adjusted radial location were in the piston bowl.

Operating condition 3 was the only condition for which there was enough data to separately generate spatially averaged heat flux using only data from left side (thermocouples 8-15) and right side (thermocouples 1-8) of the piston individually. Details of how the spatially averaged heat flux was calculated are provided in the following section. Figure 4.4 shows a comparison between left and right side data for operating condition 3 with a SOI of -25 °ATDC. Overall the agreement between the left and right side data was good and confirmed that grouping thermocouples radially was reasonable.

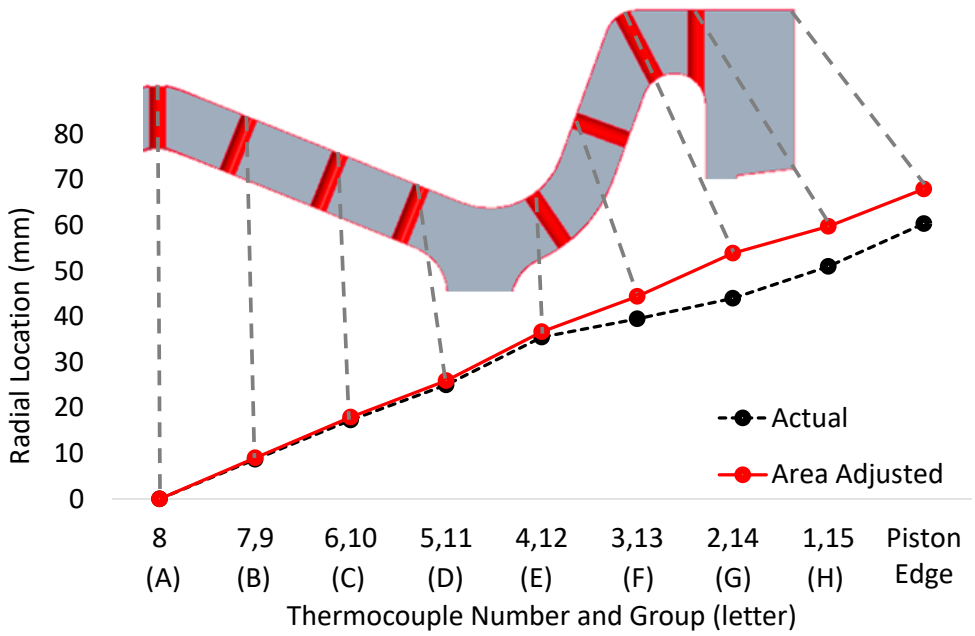


Figure 4.3: Comparison of actual and area modified thermocouple radial locations on piston bowl

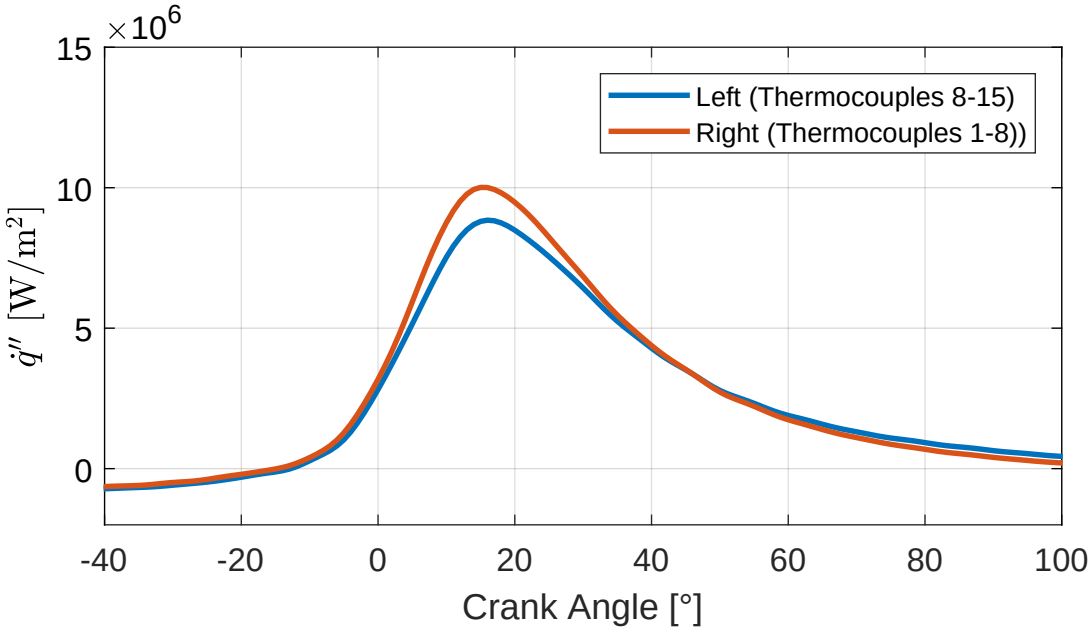


Figure 4.4: Operating condition 3 (2500 rpm, 20.3 bar IMEPg) SOI timing of -25 °ATDC comparison of left and right side thermocouple groups

4.2.3 Interpolation

Figure 4.5 shows the 45 ° sector mesh that was used to interpolate measured temperature and heat flux data. The mesh consists of 100 nodes in the radial direction and 100 in the azimuthal direction. The total area of the sector, A_{sector}, was equal to 1/8 the actual piston area. The red dots represent thermocouple locations at the new area-adjusted radius, *i.e.*, pseudo locations. The azimuthal angle between the rows is 11.25 ° which is 1/4 the sector size and equal to the injector spray clocking angle. The split-plume data were included twice to achieve equal azimuthal grid spacing and to be consistent with the data collected. Including this data twice assumes that the data on both sides of the on-plume measurement were the same, which will be verified in Section 4.3 therefore any data duplication should have minor impact to the spatially averaged heat flux. The duplicate split-plume set of data is marked with red open markers in figure 4.5 and all following contour plots to remind the reader of this assumption.

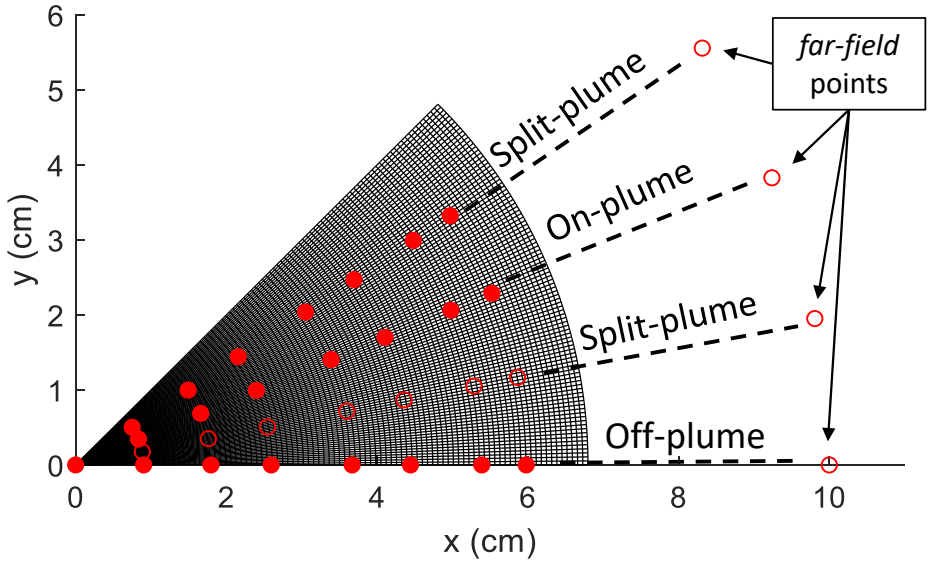


Figure 4.5: Sector mesh used for temperature and heat flux interpolation with pseudo thermocouple locations marked in with red dots (solid markers for measured data, open markers for duplicate data)

The data were interpolated on the two-dimensional sector mesh using The MATLAB function *TriScatteredInterp* utilizing *natural neighbor interpolation* that was based on Delaunay

triangulation. Further inspection of figure 4.5 shows no measured data at the edge of the piston (maximum radial location). The interpolation method requires data to bound the interpolated area, *i.e.*, extrapolation is not allowed. Four *far-field* points were added to each row of data. The data at the corresponding furthest radial point on the grid (group h) was duplicated, which had the effect eliminating azimuthal gradients near the edge of mesh (squish region of piston).

The interpolation method results in a grid of interpolated data, either interpolated temperature, $T_{int}(\theta)$, or interpolated heat flux, $\dot{q}''_{int}(\theta)$. The interpolated data were average for each θ in a time-invariant fashion. Equation 4.1 shows spatially averaged (denoted with triangular braces, $\langle\ \rangle$) piston temperature, $\langle T_{piston}(\theta)\rangle$. Equation 4.2 shows spatially averaged heat flux, $\langle \dot{q}''(\theta)\rangle$, which is calculated similar to $\langle T_{piston}(\theta)\rangle$ but also included a constant term $\dot{q}''_{peg}$ that was needed to recover the steady-state portion of heat flux, which is discussed next.

$$\langle T_{piston}(\theta)\rangle = \frac{1}{A_{sector}} \int T_{int}(\theta) dA \tag{4.1}$$

$$\langle \dot{q}''(\theta)\rangle = \frac{1}{A_{sector}} \int \dot{q}''_{int}(\theta) dA + \dot{q}''_{peg} \tag{4.2}$$

4.2.4 Pegging Area Averaged Heat Flux

An *ad hoc* method was developed to recover the steady-state portion of heat transfer that was eliminated in equation 3.3 when calculating heat flux. The method was similar to correction methods used for in-cylinder pressure data where the sensor is only able to capture the dynamic portion of the signal and a second, time-invariant measurement is used to adjust (peg) the dynamic measurement. The basis of the method is that $\langle \dot{q}''\rangle = 0$ when the mean gas temperature, T, is equal to area-averaged piston temperature, $\langle T_{piston}\rangle$. Because the overall functional form for heat transfer is assumed to be: $\langle \dot{q}''\rangle = h(T - \langle T_{piston}\rangle)$ the value of the

heat transfer coefficient, h, is irrelevant when $T - \langle T_{piston} \rangle = 0$. The pegging crank angle, θ_{peg}, is defined as the crank angle where $\langle T_{piston} \rangle = T$:

$$\theta_{peg} \equiv \theta_{\langle T_{piston} \rangle = T} \tag{4.3}$$

An arithmetic mean in a crank angle range ± 5 around θ_{peg} was taken and used as the pegging heat flux:

$$\dot{q}''_{peg} = -\frac{1}{n+1} \sum_{n=\theta_{peg}-5}^{\theta_{peg}+5} \dot{q}''_{int}(\theta_n) \tag{4.4}$$

which includes a negative sign because the pegged value should be opposite of the measured value.

To compare the pegged $\langle \dot{q}'' \rangle$ to other independent global heat transfer metrics it was integrated over the full engine cycle to find spatially averaged heat transfer:

$$\langle Q \rangle = \int_{t=0}^{t=t_{cycle}} \left\langle \dot{q}'' \right\rangle A_\theta dt \tag{4.5}$$

The limits of integration in equation 4.5 are shown as $t = 0$, which corresponds to -360 °ATDC, and $t = t_{cycle}$ which corresponds to 360 °ATDC. Combustion chamber area, A_θ, is shown with the subscript θ to emphasize that it is a function of crank angle. A_θ is defined as the piston area (constant), head area (constant, $\pi B^2/4$) and cylindrical liner area (variable). Because $\langle \dot{q}'' \rangle$ is only calculated using measurements on the piston and total area of combustion chamber is used to calculate $\langle Q \rangle$ there is an assumption that the piston heat transfer is representative of the entire combustion chamber.

Figure 4.6 shows a 1:1 plot comparing $\langle Q \rangle$ to $\dot{Q}_{gas}$, as given in equation 3.2, which is effectively the heat transfer to the combustion chamber plus heat transfer to the exhaust ports. Ideally $\langle Q \rangle$ would fall slightly below the 1:1 line because $\langle Q \rangle$ does not include heat transfer to the exhaust ports. Given the number of assumptions made to produce $\langle \dot{q}'' \rangle$ this agreement is considered to be very good.

To understand the sensitivity of the selected pegging method θ_{peg} was perturbed ±10 °ATDC. There was some sensitivity to the choice of θ_{peg} but $\langle \dot{q}'' \rangle$ was of correct magnitude, captured other heat transfer trends associated with an SOI sweep and overall suggested that the selected pegging method is reasonable. Additional comparisons and discussion for all operating conditions are given in Section 4.4.

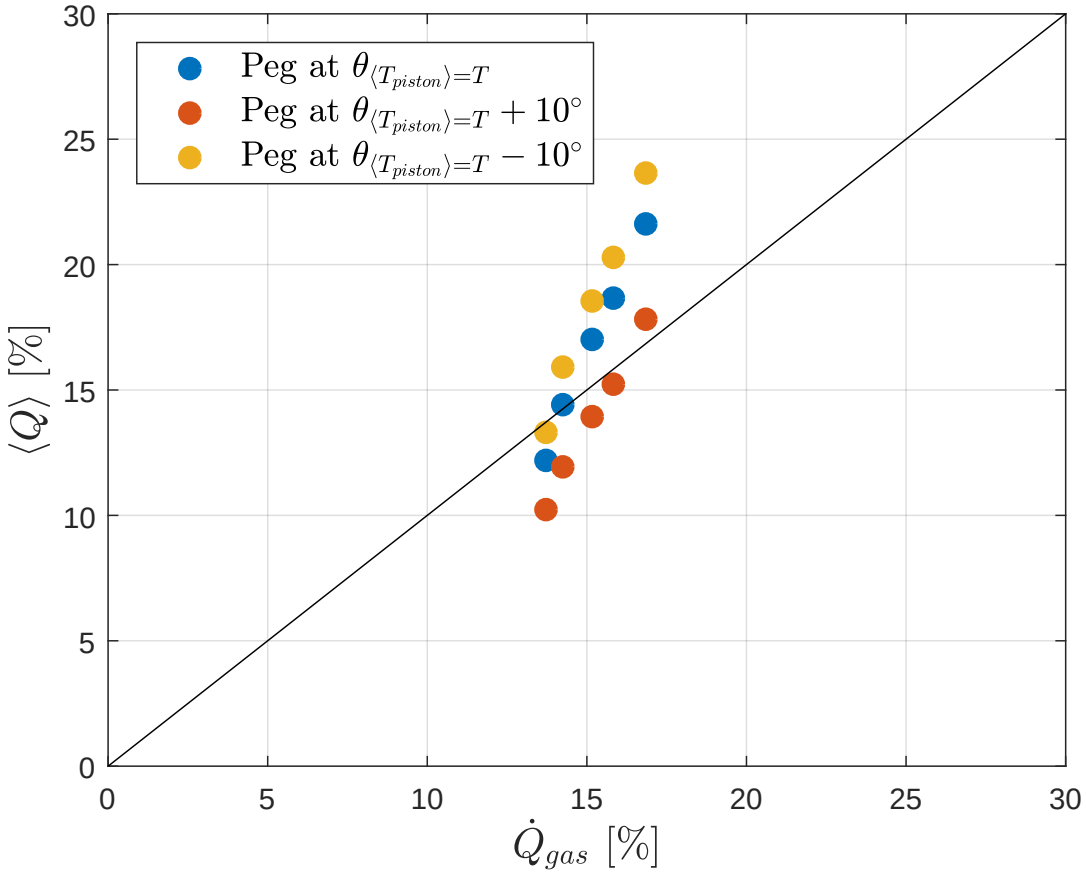


Figure 4.6: Operating condition 3 (2500 rpm, 20.3 bar IMEPg) pegging sensitivity of local heat transfer ($\langle Q \rangle$) compared to global heat transfer ($\dot{Q}_{gas}$)

4.2.5 Data Validation and Availability

Data were collected using two thermocouple-instrumented pistons (Co-axial Metal 1 and Co-axial Metal 2, see table 3.7) with each unique case (operating condition, spray location, SOI) sometimes run multiple times. Data validation was first performed in the crank angle

domain by comparing temperature at each crank angle across multiple engine cycles using a statistical outlier rejection method (see Section 3.4.2.1). The fast-response thermocouples that were used have a limited useful life at the extreme in-cylinder pressures and temperatures. As such, the specific thermocouples that were operational for any given case were a function of when the data were acquired and on which piston.

The validity of each thermocouple was assessed by comparing data at two standard operating points (motored and part-load at 1700 rpm) that were run at the start and end of each day. For each thermocouple location repeatability was checked for both temperature and heat flux. When the data were found to not be repeatable that thermocouple location was eliminated for that day and every subsequent day. Appendix A.9 gives additional details on thermocouple functionality.

For each thermocouple group between zero and six sets of data were considered valid and were included in the operating condition results. For cases with zero data sets available, substitution from another group was made and noted. When greater than one data set was available the mean was taken to produce a single temporally varying data set (heat flux and temperature). Heat flux was calculated before averaging to prevent any artificial biasing of the data.

4.3 Heat Flux Results

For each of the five operating conditions a standard set of data were calculated, and these data are shown in the subsequent sections separated by operating condition. Operating condition 4 is only available in the appendix because of the limited availability of data. For each condition a table showing the number of validated data sets at each thermocouple and corresponding group is given. Thermocouple groups substitutions are noted in the table and all the subsequent contour plots that include the substitution are shown with an open red marker. The first figure that follows the table (figures 4.8, 4.12, 4.16, 4.21) shows all the

individual heat flux data before averaging overlaid with the area-averaged result, which helps understand the spatial variability in heat flux that makes up the average.

The second plot (figures 4.9, 4.13, 4.17, 4.22) includes crank angle resolved data from both the high speed data acquisition (see Section 3.2.1) and the piston wireless telemetry system (see Section 3.2.3) plotted on the same x-axis. The data presented in these plots will be used in a subsequent chapter for the development of a heat transfer correlation.

The next plot (figures 4.10, 4.14, 4.19, 4.23) shows contours of time-integrated heat flux, which represents the location of energy deposition on the surface of the piston. The following plot (figures 4.11, 4.15, 4.19, 4.24) shows contours of instantaneous heat flux for selected crank-angles at a single SOI. Additional contours of instantaneous heat flux for all operating conditions and SOI can be found in Appendix A.12.

Before going into the detailed results of each operating condition, trends that were observed in $\langle \dot{q}'' \rangle$ and $\langle T_{piston} \rangle$ for all operating conditions are discussed. Figure 4.7 shows the maximum spatially averaged heat flux, $\langle \dot{q}''_{max} \rangle$, the difference in minimum and maximum $\langle T_{piston} \rangle$ and cycle-averaged piston temperature, $\left\langle \bar{T}_{piston} \right\rangle$, for all operating conditions as a function of SOI. Large changes to $\langle \dot{q}''_{max} \rangle$ were observed for each SOI sweep; accordingly SOI was chosen as the independent variable. For the operating conditions studied, $\langle \dot{q}''_{max} \rangle$ changes by a factor of $3\times$ from operating condition 1 (1700 rpm, 12.3 bar IMEPg) to the high power of operating condition 2 (1500 rpm, 23.8 bar IMEPg). For figure 4.7 and other figures later in this chapter, operating condition 4 and operating condition 3 IMT are shown with open markers to remind the reader that these have relatively higher uncertainty data because of the large number of measurement substitutions.

The middle plot of figure 4.7, which shows the difference in minimum and maximum $\langle T_{piston} \rangle$, looks similar to the top plot of maximum $\langle \dot{q}'' \rangle$ because ultimately the swing in piston surface temperature is driving the heat flux calculation. The bottom plot in 4.7 shows cycle-averaged piston temperature, which changes by up to 75 °C within an SOI sweep and is also dependent on engine load and speed.

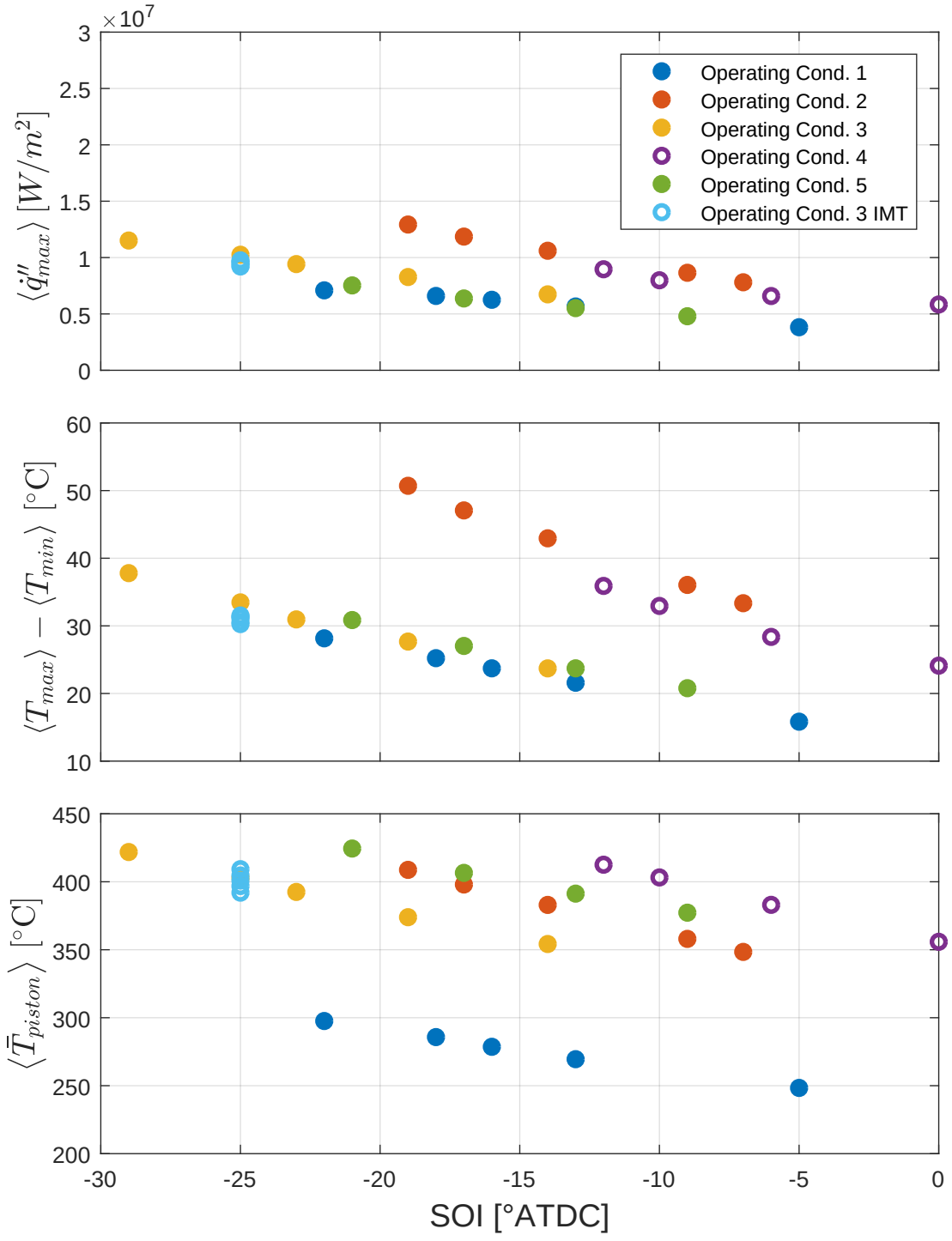


Figure 4.7: Comparison of piston temperature and heat flux area interpolated metrics for all operating conditions (open markers used for higher uncertainty data)

4.3.1 Operating Condition 1

A detailed discussion of all the trends and figures is given for operating condition 1. Many of the trends observed in this operating condition were also prevalent in the others, so subsequent discussions are more limited with a focus on operating-condition specific observations.

Table 4.1 shows that data were available at nearly all thermocouple groups and spray locations with only one substitution needed at off-plume group b. This substitution is very minor because heat flux gradients near the center of the piston are small and the total area near the center of the piston is small. Figure 4.8 shows all 41 individual heat flux measurements that were tabulated along with the area-average heat flux (no pegging correction). The average is shown with a thick black line, center measurements (thermocouples 6-10) with thin magenta lines, bowl measurements (thermocouples 3-5, 11-13) with thin green lines and squish measurements with thin blue lines (thermocouples 1-2, 14-15). These three radial groups of thermocouples were found to have unique trends. The center region typically has a lower maximum heat flux and is somewhat delayed relative to the other groups. The bowl region was the first to show a rise and had the highest maximum heat flux. The squish region typically fell between the other two groups both in magnitude and rise time. The individual heat flux measurements provides an understanding of the spatial variation that goes into the average. The variation in heat flux is larger near the peak heat flux time and relatively small before the combustion event and later into the expansion stroke.

Figure 4.9 shows three subplots with data plotted as a function of crank angle. The data contained in this figure were all used as inputs to a new heat transfer correlation discussed in Chapter 6. Each of the different color lines on the plot represent a different SOI timing (the solid lines are plotted on the left axis and dotted lines on the right). The choice of SOI line color for crank angle data was consistent between the two chapters (for each operating condition) to simplify comparisons when needed. The top plot shows AHRR and in-cylinder pressure, which are standard engine research metrics. The middle plot shows $\langle T_{piston} \rangle$ and $T - \langle T_{piston} \rangle$, which is presented as a difference because it appears that way in the formulation

Table 4.1: Operating condition 1 (1700 rpm, 12.3 bar IMEPg) available thermocouple measurements and substitutions

Group	a	b		c		d		e		f		g		h	
Thermocouple #	8	7	9	6	10	5	11	4	12	3	13	2	14	1	15
On-plume		1	1	1	1	2	2	1	1	2	1	1	1	2	1
		2		2		4		2		3		2		3	
Split-plume		1	1	1	1	1	1	1	0	1	1	1	1	1	1
		2		2		2		1		2		2		2	
Off-plume	1	0	0	1	0	1	1	1	1	1	0	0	1	1	1
	1	Sub		1		2		2		1		1		2	

Total 41

Substitutions (shown in red text): Use on-plume group b for off-plume group b

of a heat transfer coefficient: $\langle \dot{q}'' \rangle = h(T - \langle T_{piston} \rangle)$, where T is the instantaneous gas temperature. The bottom plot shows spatially averaged heat flux, $\langle \dot{q}'' \rangle$, and the fuel rate of injection (ROI). The rise and maximum value of $\langle \dot{q}'' \rangle$ change significantly with each SOI. The more advanced SOI timings had in-cylinder pressure, in-cylinder temperature, and $\langle \dot{q}'' \rangle$ rise earlier and correspondingly had higher maximum values that decreased with later SOI. The heat flux falling tail is nearly the same for all SOIs which is not surprising given bulk gas temperature and pressure are nearly the same.

Figures 4.10 and 4.11 are different presentations of area-averaged heat flux data. Figure 4.10 shows contours of heat flux integrated with respect to time from -20 to 100 °ATDC for each SOI. The plots represent the energy deposited to the surface of the piston per unit area, *i.e.*, energy flux. The limits of integration where chosen because most thermocouple locations showed a positive heat flux starting around -20 °ATDC until 100 °ATDC (which is near EVO). The plots show that most of the energy flux is near the piston bowl. The gradients in energy flux are largest in the radial direction. The more advanced SOI timings show the highest magnitude of energy flux compared to the more retarded.

Figure 4.11 shows 12 contours from the result of the heat flux interpolation for an SOI timing of -16 °ATDC. Each frame shows the location of thermocouples in red (solid markers

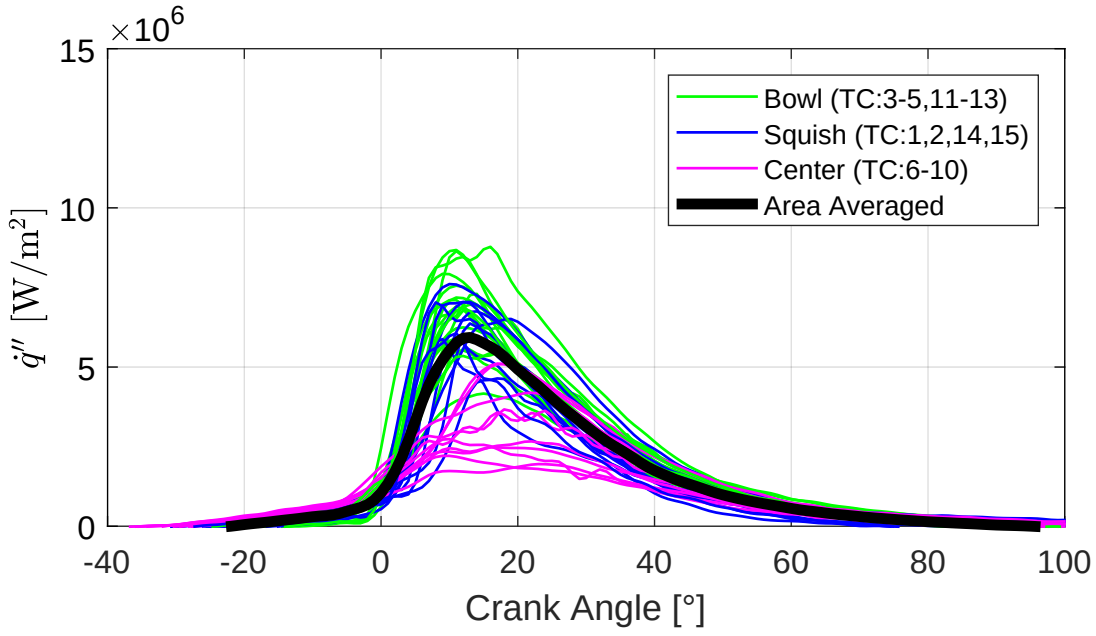


Figure 4.8: Operating condition 1 (1700 rpm, 12.3 bar IMEPg) SOI timing of -16 °ATDC area averaged and individual heat flux with line color indicating piston location

indicate data, open markers indicate substitutions) and two gray lines which represent the piston bowl edges. For each SOI timing, 720 contours (one per crank angle) were generated and area averaged as part of calculation of $\langle \dot{q}'' \rangle$ but because most of the action occurs during and after the combustion event only selected crank angles are presented. Additional contours of heat flux for all SOIs can be found in Appendix A.12. The heat flux usually first starts to rise in the piston bowl region on the spray-axis, which is presented as the center azimuthal angle on all contours, *i.e.*, middle of each plot. The high heat flux region is at the bowl edge and depending on operating condition spills outside (both toward the center and squish regions). For the presented SOI of -16 °ATDC in figure 4.11 the maximum $\langle \dot{q}'' \rangle$ occurs around 12 °ATDC. The contours after the peak trend to be more uniform compared to the contours before the peak heat flux timing.

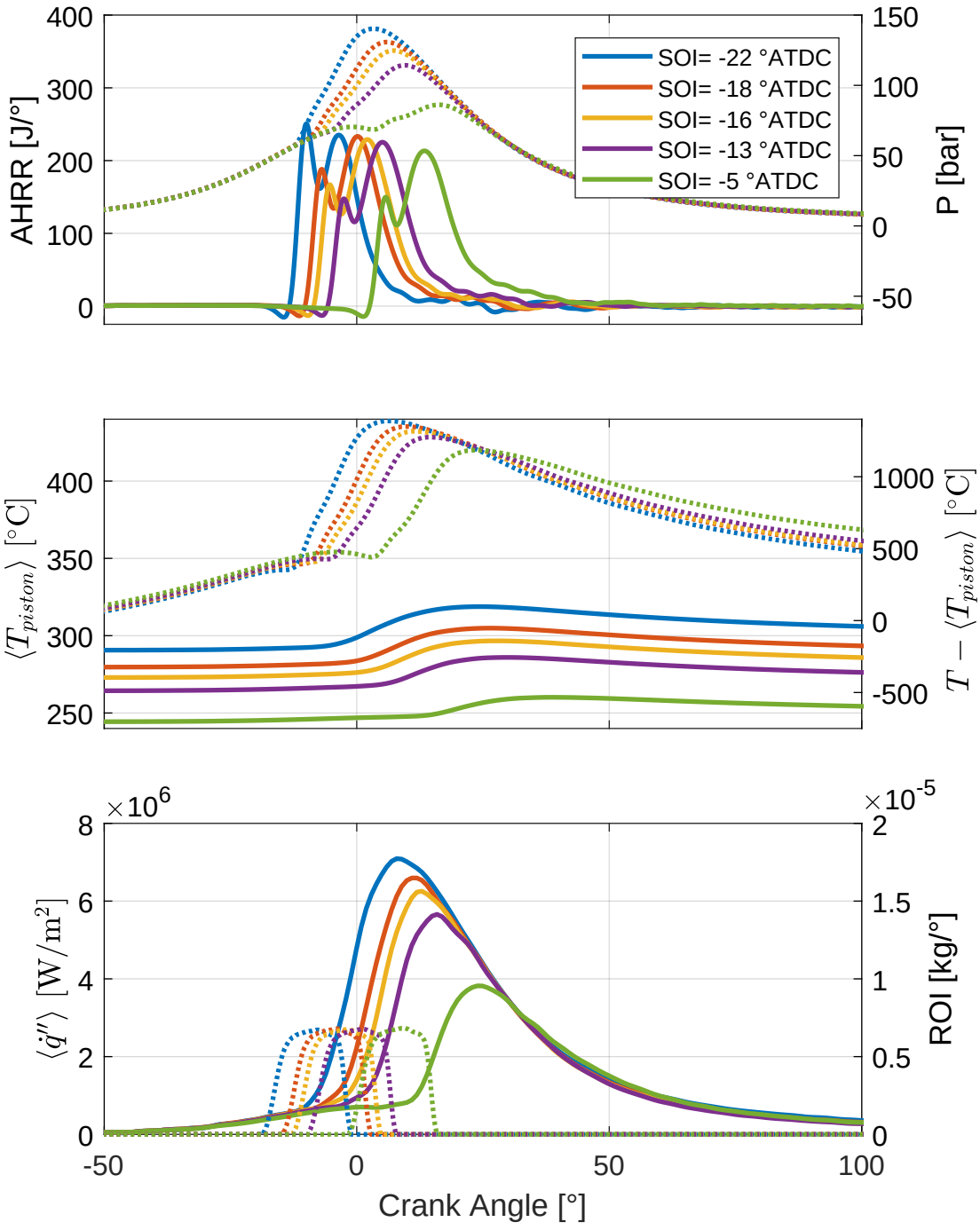


Figure 4.9: Operating condition 1 (1700 rpm, 12.3 bar IMEPg) high-speed crank angle measurements for all SOI (solid lines left axis, dotted lines right axis)

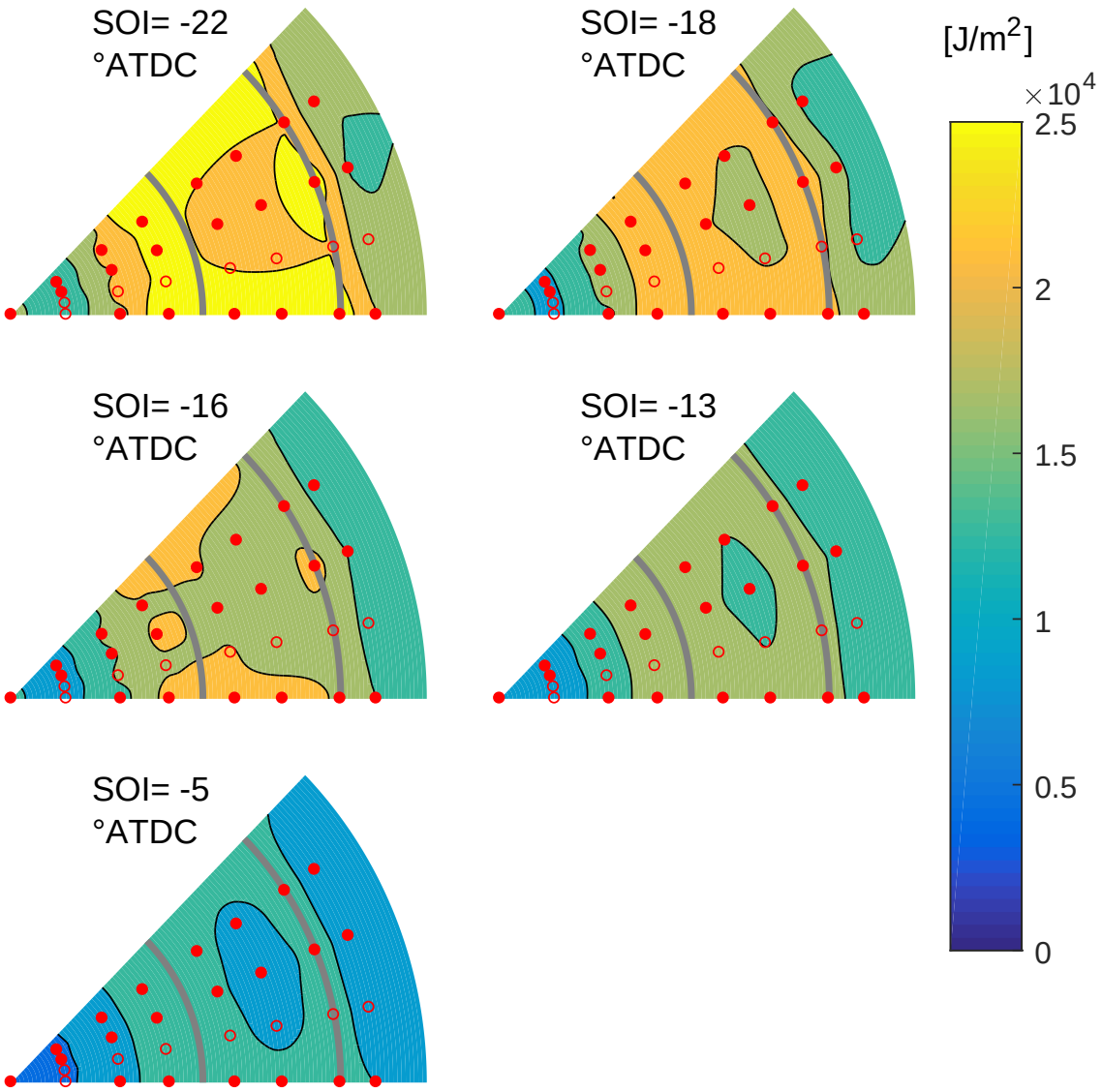


Figure 4.10: Operating condition 1 (1700 rpm, 12.3 bar IMEPg) contours of heat flux integrated w.r.t. time from -20 to 100 °ATDC (energy flux) for all SOI

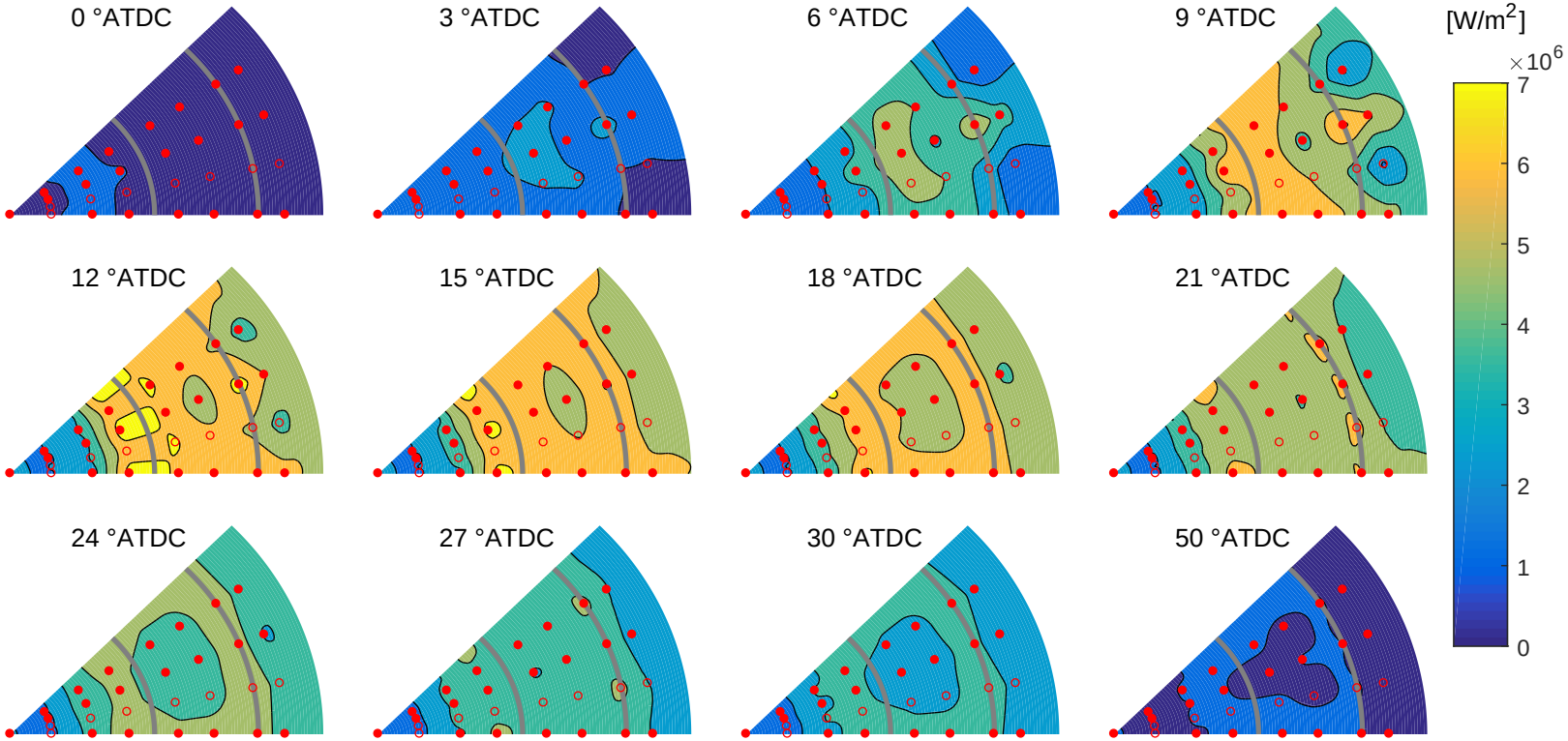


Figure 4.11: Operating condition 1 (1700 rpm, 12.3 bar IMEPg) SOI timing of -16 °ATDC contours of heat flux at selected crank angles

4.3.2 Operating Condition 2

Operating condition 2, which is at lower speed and higher load (1500 rpm, 23.8 bar IMEPg) than operating condition 1, showed very similar data trends. A total of 32 individual thermocouple measurements were available for this condition with two minor substitutions near the center of the piston (see table 4.2). Figure 4.12 shows individual heat flux traces using the same color scheme for the center/bowl/squish as figure 4.8. One of the individual measurements in the squish region seems delayed and lower in magnitude compared to the others which may have been due to an intermittent thermocouple. Because this thermocouple passed the other data validation checks, including statistical analysis in the crank angle domain and day-to-day repeatability (at lighter load), it was still included to avoid inadvertently adding analysis bias through manual selection of data. Ultimately, the quality of the data set was considered high because of the relatively large number of total measurements.

Operating condition 2 had the largest maximum $\langle \dot{q}'' \rangle$ at the most advanced SOI of all the operating conditions, which may have resulted from the lower engine speed. Other operating conditions that had higher load but lower maximum $\langle \dot{q}'' \rangle$ were at higher engine speed. Figure 4.13 shows that the in-cylinder pressure was significantly higher (nearly 250 bar) than operating condition 1 for this case. The resulting contours of energy flux (figure 4.14) and heat flux (figure 4.15) show about twice the magnitude of condition 1.

Table 4.2: Operating condition 2 (1500 rpm, 23.8 bar IMEPg) available thermocouple measurements and substitutions

Group	a	b		c		d		e		f		g		h	
Thermocouple #	8	7	9	6	10	5	11	4	12	3	13	2	14	1	15
On-plume		0	0	1	0	1	1	1	1	1	0	0	1	1	1
		Sub		1		2		2		1		1		2	
Split-plume		1	1	1	1	1	1	1	0	1	1	1	1	1	1
		2		2		2		1		2		2		2	
Off-plume	1	0	0	1	0	1	1	1	1	1	0	0	1	1	1
	1	Sub		1		2		2		1		1		2	

Total 32

Substitutions (shown in red text): Use split-plume group b for off-plume group and on-plume group b

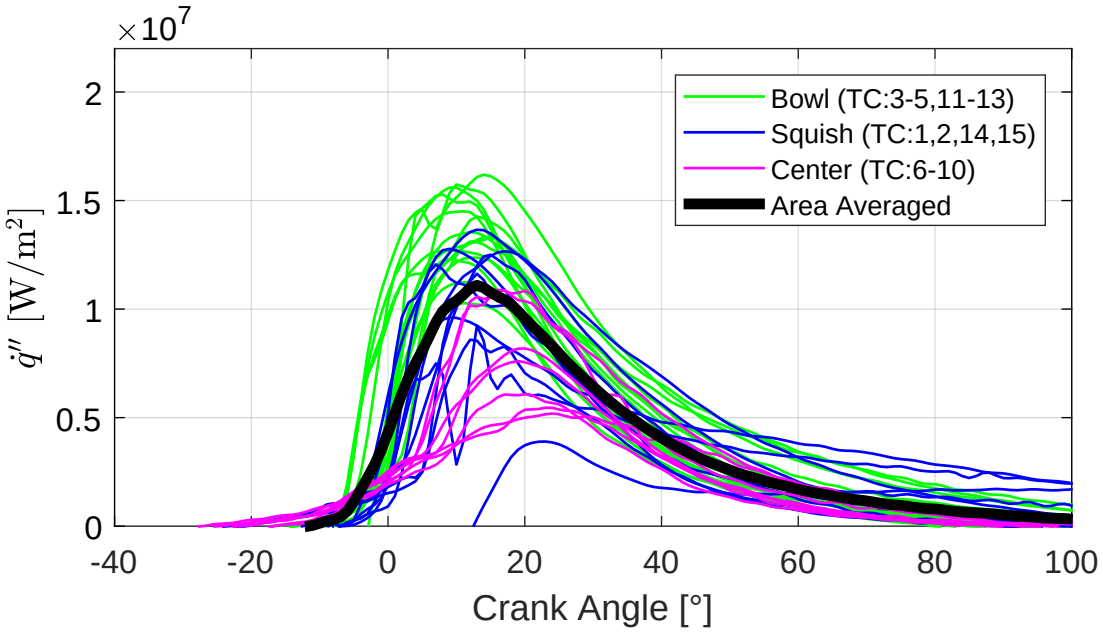


Figure 4.12: Operating condition 2 (1500 rpm, 23.8 bar IMEPg) SOI timing of -17 °ATDC area averaged and individual heat flux with line color indicating piston location

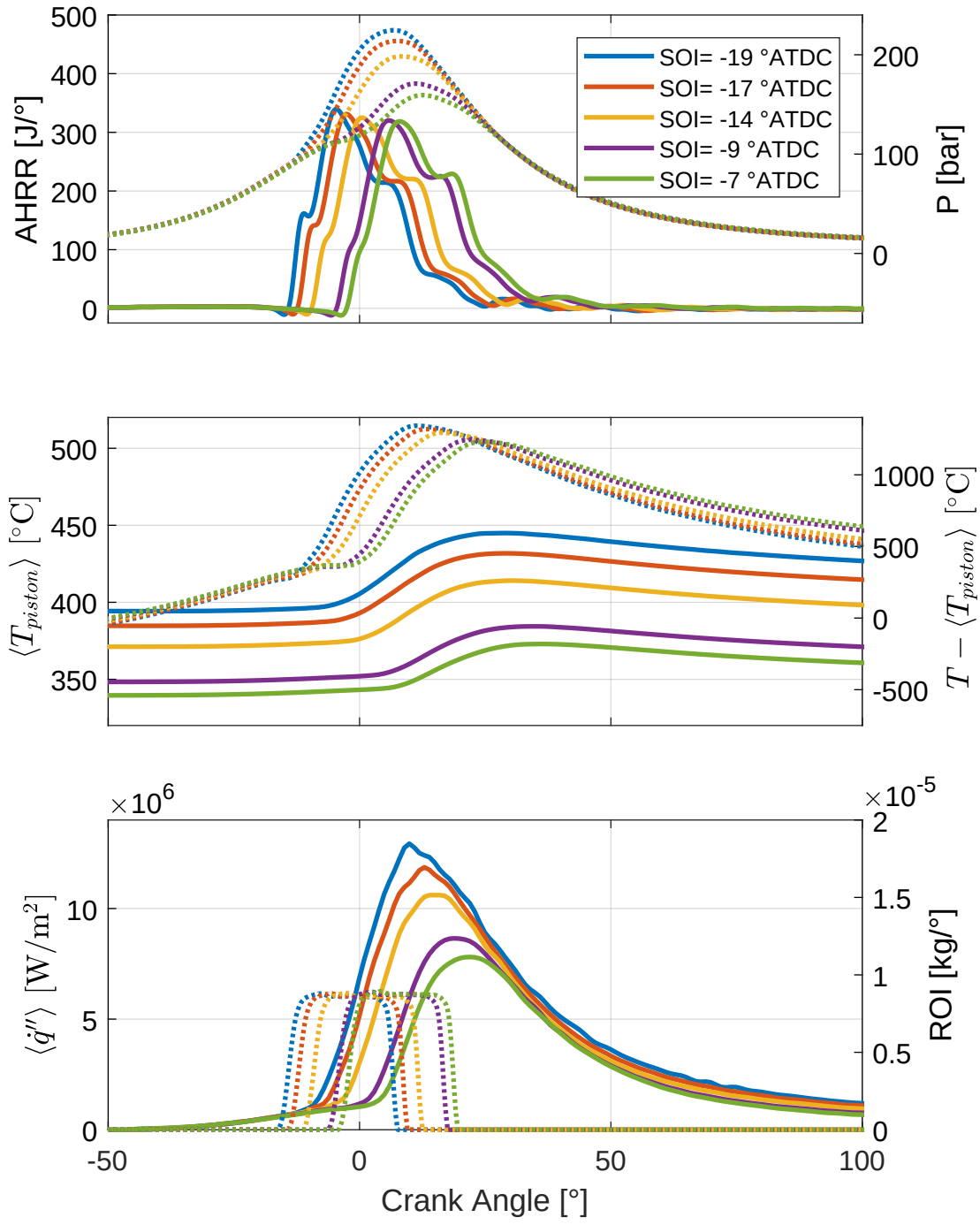


Figure 4.13: Operating condition 2 (1500 rpm, 23.8 bar IMEPg) high-speed crank angle measurements for all SOI (solid lines left axis, dotted lines right axis)

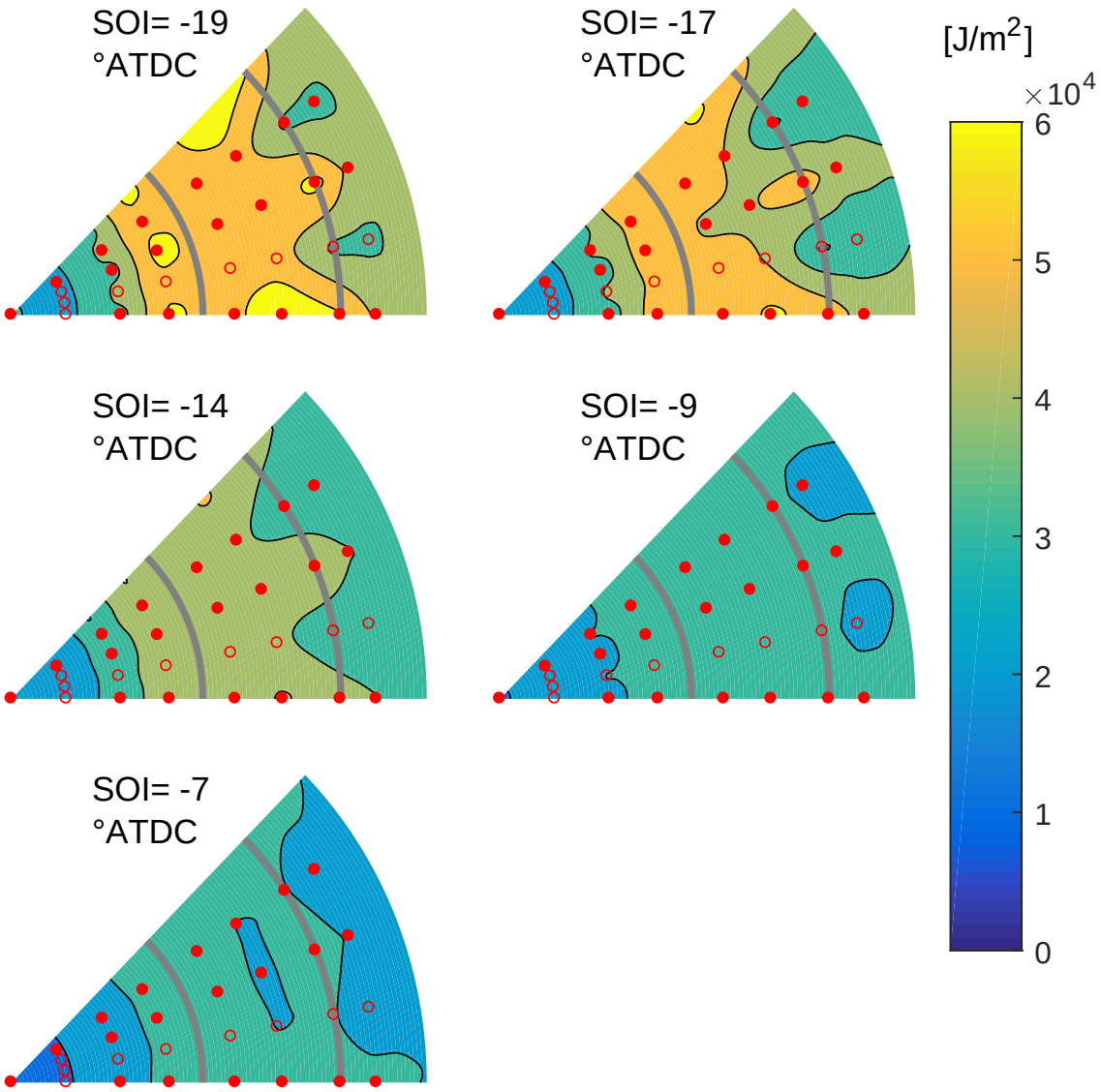


Figure 4.14: Operating condition 2 (1500 rpm, 23.8 bar IMEPg) contours of heat flux integrated w.r.t. time from -20 to 100 °ATDC (energy flux) for all SOI

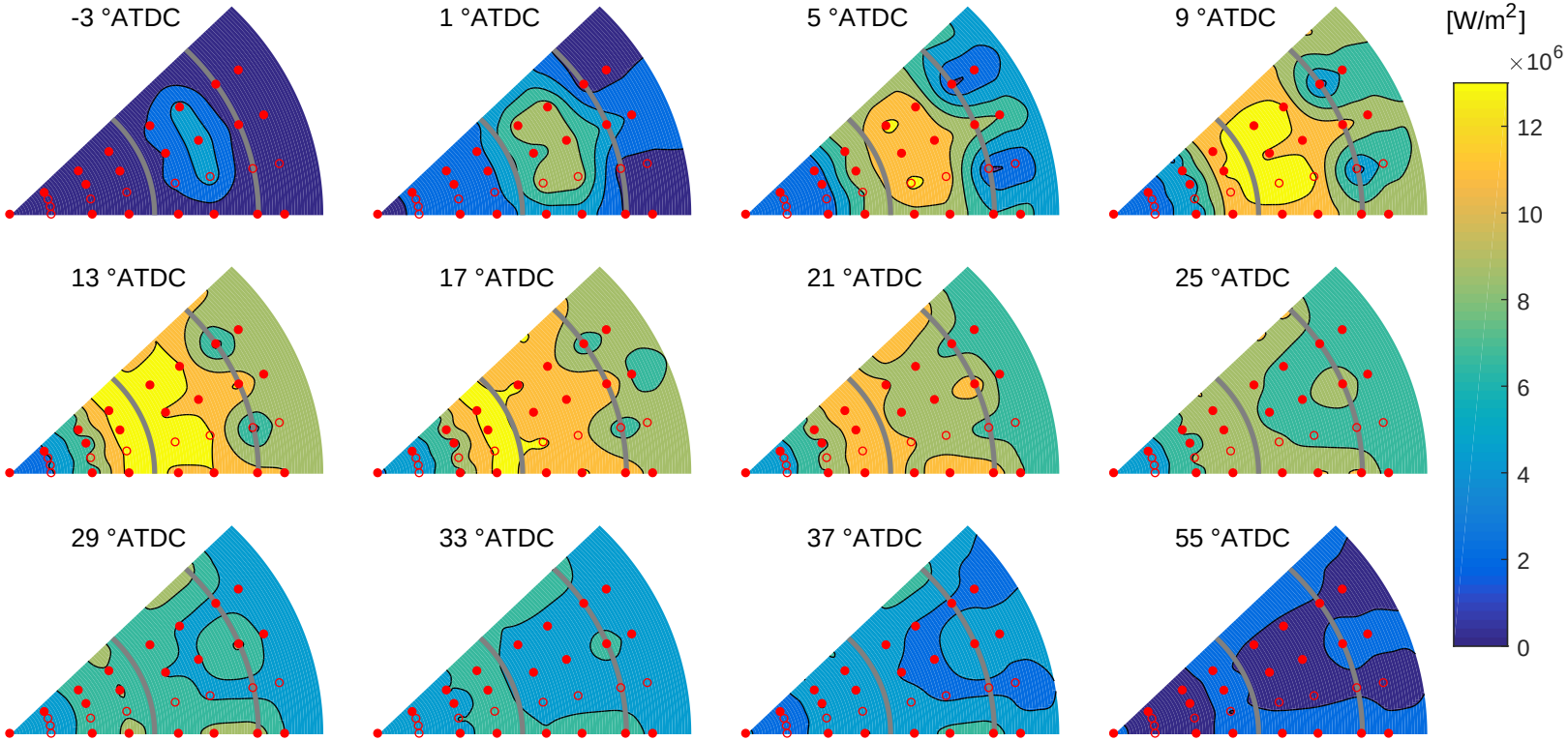


Figure 4.15: Operating condition 2 (1500 rpm, 23.8 bar IMEPg) SOI timing of -17 °ATDC contours of heat flux at selected crank angles

4.3.3 Operating Condition 3

Operating condition 3 (2500 rpm, 20.3 bar IMEPg) was the most extensive data set of all the operating conditions with a total 69 individual data points as shown in table 4.3 and figure 4.16. The same trends that were previously observed in crank angle measurements (figure 4.17), energy flux contours (figure 4.19) and heat flux contours (figure 4.20) were also observed at operating condition 3.

Operating condition 3 also included a limited data set where an intake manifold temperature sweep was conducted for a single SOI of -25 °ATDC. Intake temperature was increased from 49 to 93 °C. A large number of thermocouple substitutions were required for these tests because only one injector spray location was run (same as operation condition 4, see Appendix A.11 table A.5). The thermodynamic data for the intake temperature sweep, figure 4.18, shows very minor differences. A small increase in piston temperature was observed for the higher intake temperature conditions but this impact was relatively small compared to the impact of SOI timing.

Table 4.3: Operating condition 3 (2500 rpm, 20.3 bar IMEPg) available thermocouple measurements and substitutions

Group	a	b		c		d		e		f		g		h	
Thermocouple #	8	7	9	6	10	5	11	4	12	3	13	2	14	1	15
On-plume		1	1	1	1	2	2	1	1	2	1	0	1	1	2
		2		2		4		2		3		1		3	
Split-plume		2	2	2	2	3	3	2	1	3	2	1	2	3	2
		4		4		6		3		5		3		5	
Off-plume	2	1	1	2	1	2	2	1	1	2	1	1	2	2	1
	2	2		3		4		2		3		3		3	

Total 69

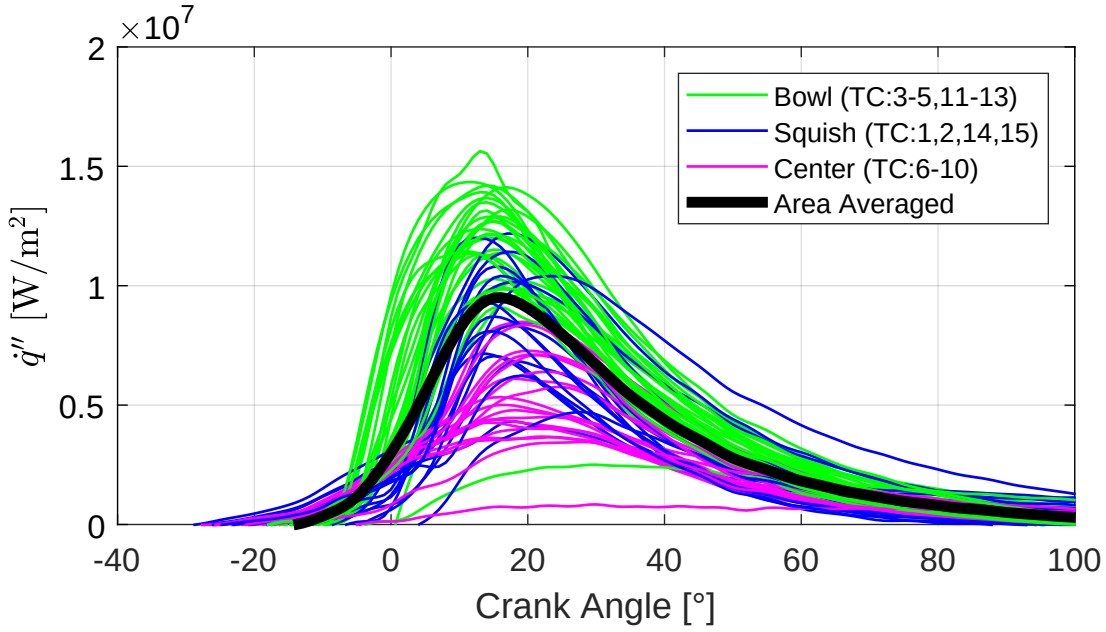


Figure 4.16: Operating condition 3 (2500 rpm, 20.3 bar IMEPg) SOI timing of -25 °ATDC area averaged and individual heat flux with line color indicating piston location

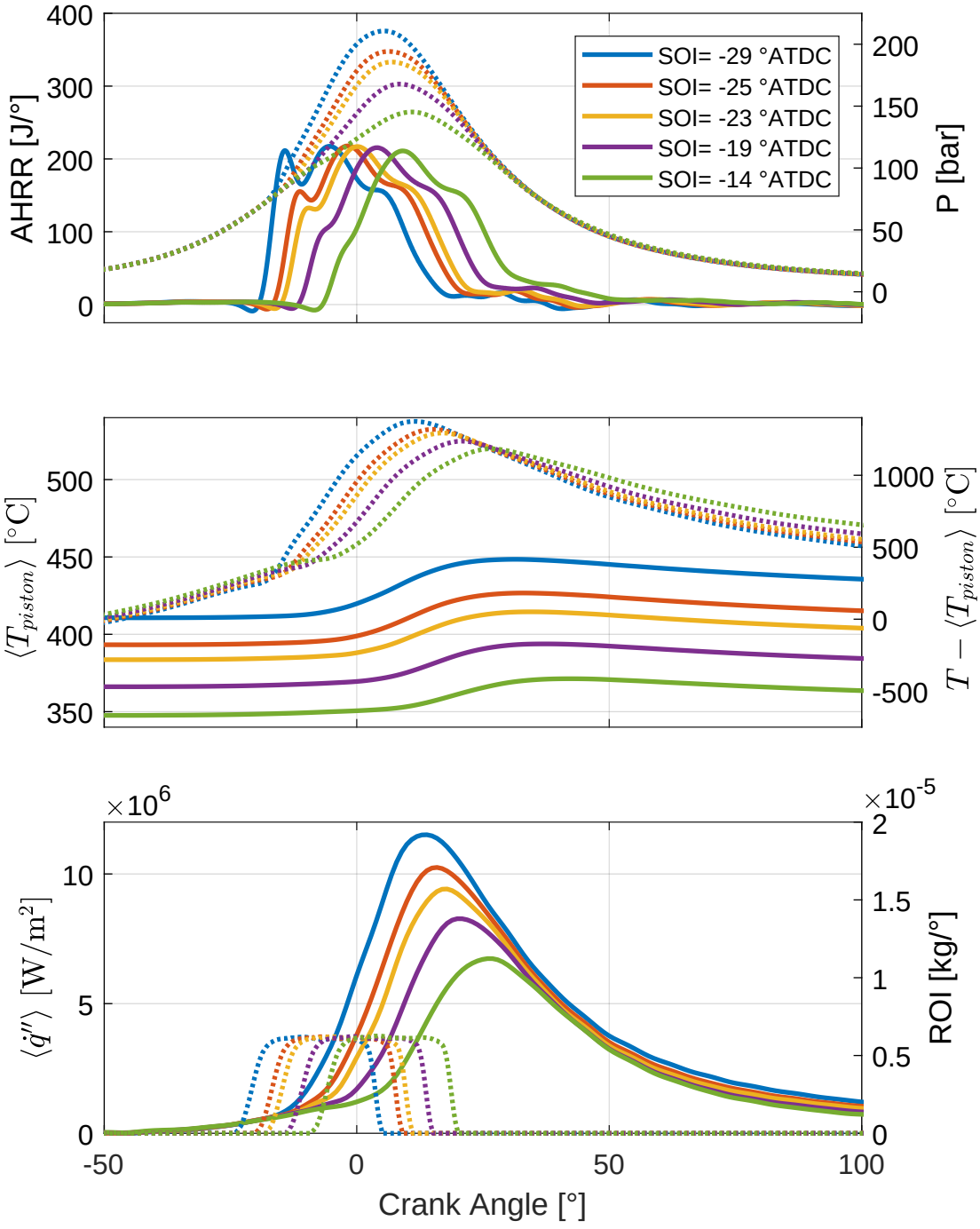


Figure 4.17: Operating condition 3 (2500 rpm, 20.3 bar IMEPg) high-speed crank angle measurements for all SOI (solid lines left axis, dotted lines right axis)

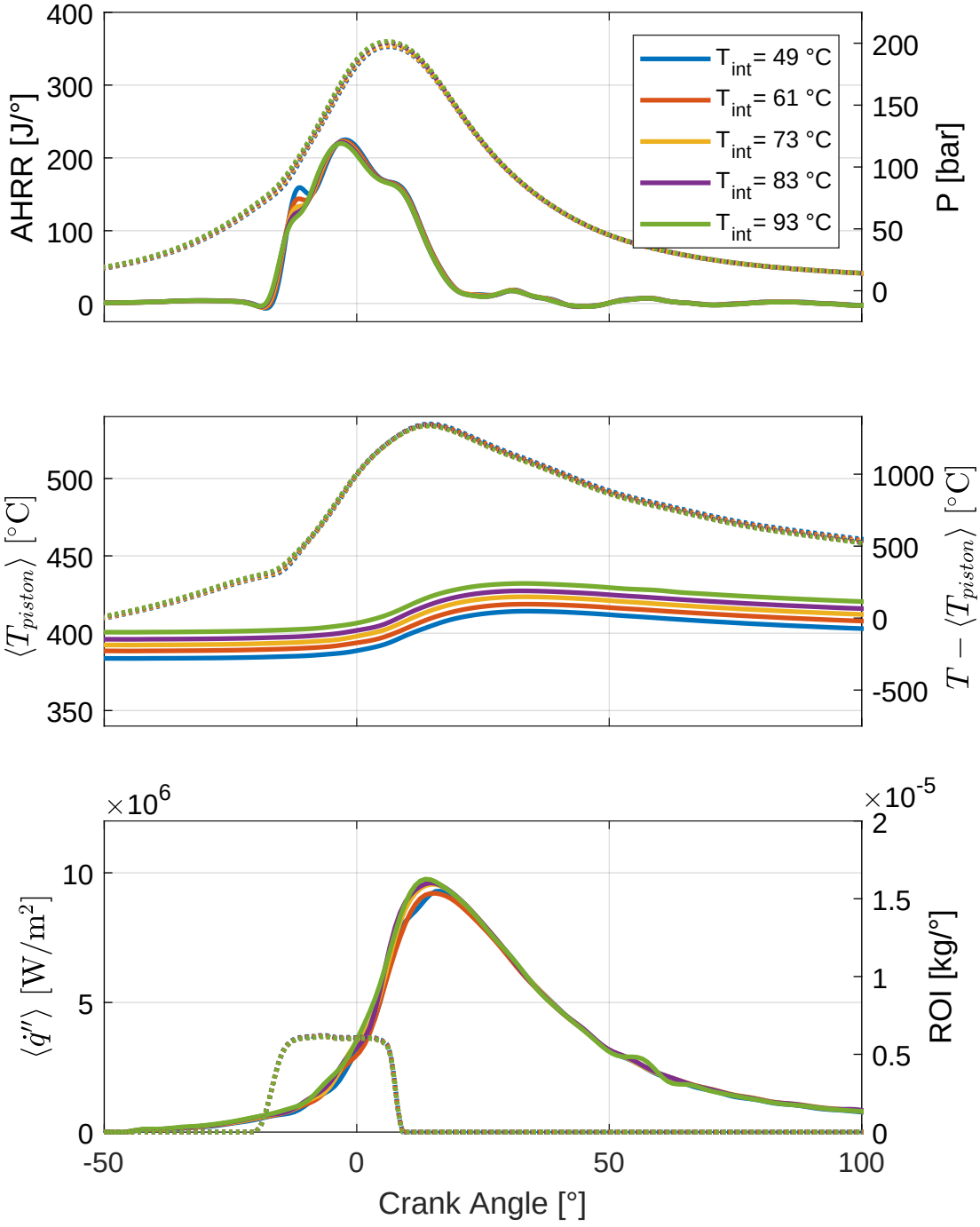


Figure 4.18: Operating condition 3 (2500 rpm, 20.3 bar IMEPg) high-speed measurements for intake manifold temperature sweep

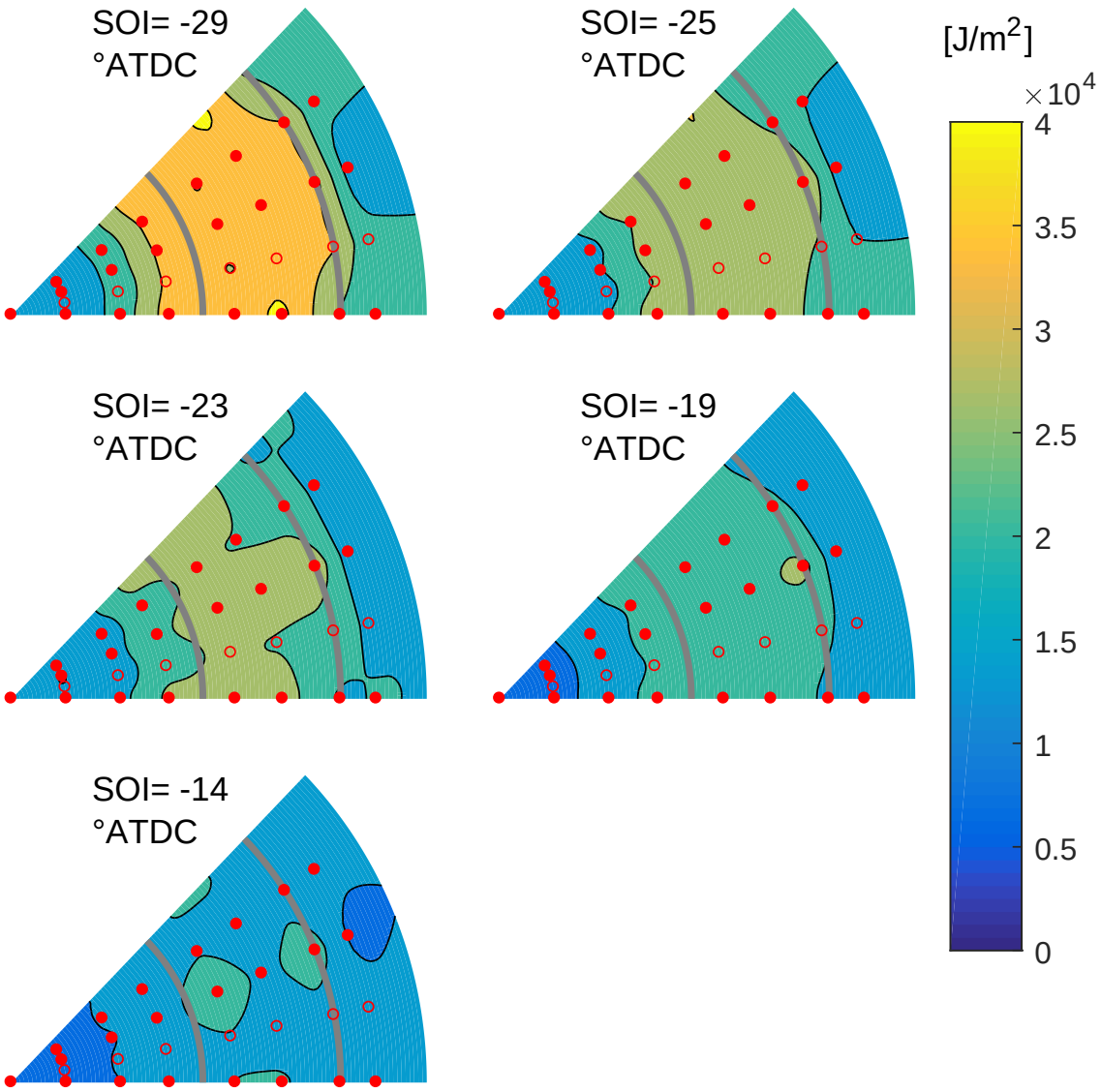


Figure 4.19: Operating condition 3 (2500 rpm, 20.3 bar IMEPg) contours of heat flux integrated w.r.t. time from -20 to 100 °ATDC (energy flux) for all SOI

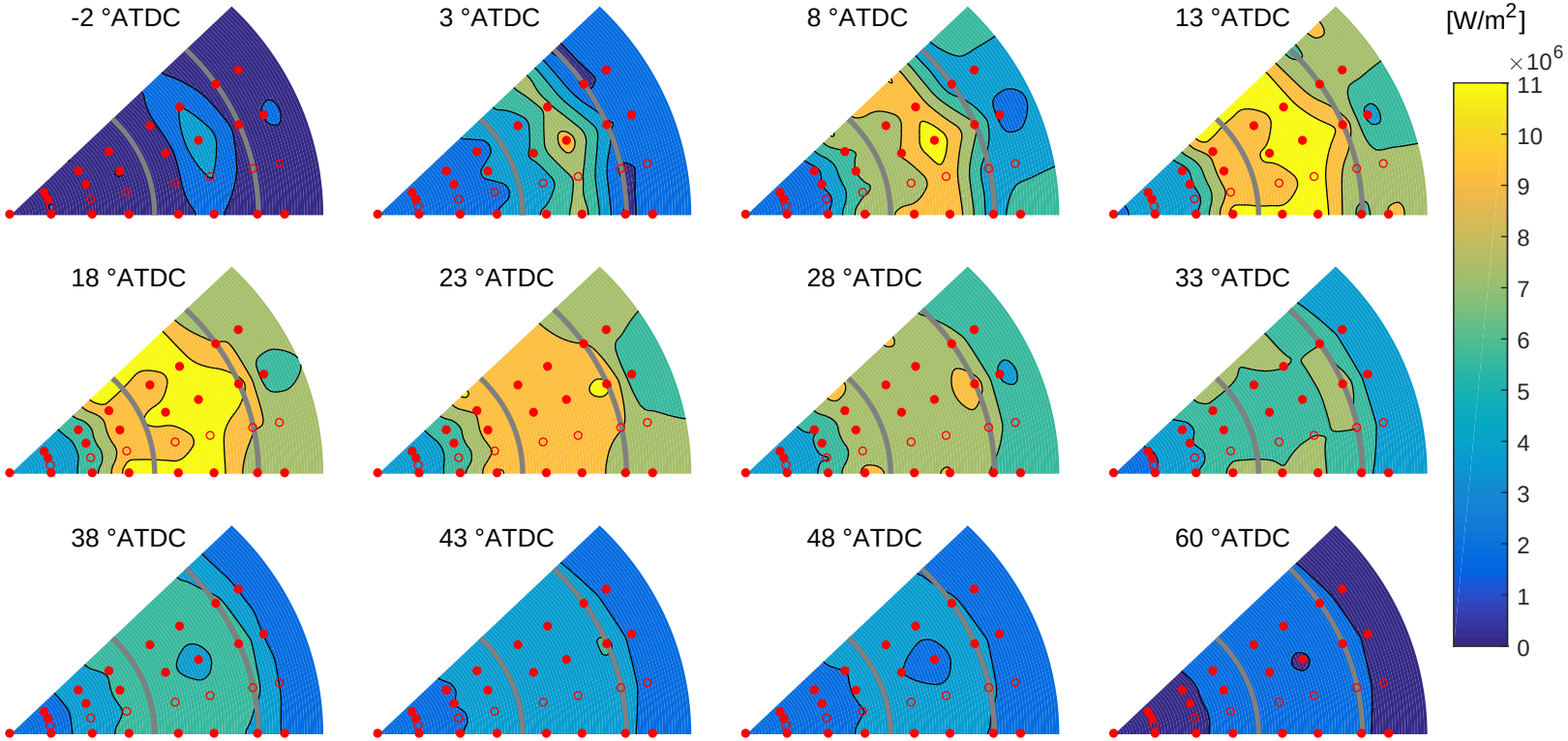


Figure 4.20: Operating condition 3 (2500 rpm, 20.3 bar IMEPg) SOI timing of -25 °ATDC contours of heat flux at selected crank angles

4.3.4 Operating Condition 4

Only a single set of data with a limited number of operational thermocouples was acquired for operating condition 4. This data set was not used in the heat transfer correlation development but was included in other figures. Plots similar to the other operating conditions in this chapter are include in Appendix A.11.

4.3.5 Operating Condition 5

Operation condition 5 (2750 rpm, 29.7 bar IMEPg) was a high-speed and high-output operating condition with a very long injection duration. A total of 25 individual heat flux measurements were available. Table 4.4 shows that six thermocouple substitutions were needed. Thermocouple group e (bowl) and g (bowl lip) were not available for any spray location so the thermocouple group to the left (d and f, respectively) for each spray location was used. These substitutions were selected based on analyzing the other operating conditions and selecting the groups that best matched. Figure 4.21 shows each of the heat flux measurements that have larger differences compared to the other operating conditions. First, the overall variability near the maximum heat flux was larger; for some cases the maximum measured heat flux in the bowl was nearly twice the area-averaged value. Both the center and squish regions had similar heat flux magnitudes, which is surprising given the long injection event is targeting the squish region at later crank angles.

Figure 4.22 shows some interesting trends in the crank-angle resolved data. The most advanced SOI had $T - \langle T_{piston} \rangle$, that was nearly constant at the maximum value for around 30 crank angles. The most retarded SOI had a similar trend where in-cylinder pressure was nearly constant for about 10 crank angles. The AHRR showed a speed up near the end of injection for all SOIs.

Figures 4.23 and 4.24 show many similar trends observed in the other operating conditions despite this operating condition having a significantly longer injection duration. Much of the heat flux and energy deposition was still contained in the bowl region.

Table 4.4: Operating condition 5 (2750 rpm, 29.7 bar IMEPg) available thermocouple measurements and substitutions

Group	a	b		c		d		e		f		g		h	
Thermocouple #	8	7	9	6	10	5	11	4	12	3	13	2	14	1	15
On-plume		1	1	0	1	1	1	0	0	1	1	0	0	1	0
		2		1		2		Sub		2		Sub		1	
Split-plume		1	1	0	1	1	1	0	0	1	1	0	0	1	0
		2		1		2		Sub		2		Sub		1	
Off-plume	1	1	1	0	1	1	1	0	0	1	1	0	0	1	0
	1	2		1		2		Sub		2		Sub		1	

Total 25

Substitutions (shown in red text): Use on-plume group d for on-plume group e, Use on-plume group f for on-plume group g, Use split-plume group d for split-plume group e, Use split-plume group f for split-plume group g, Use on-plume group d for on-plume group e, Use on-plume group f for on-plume group g,

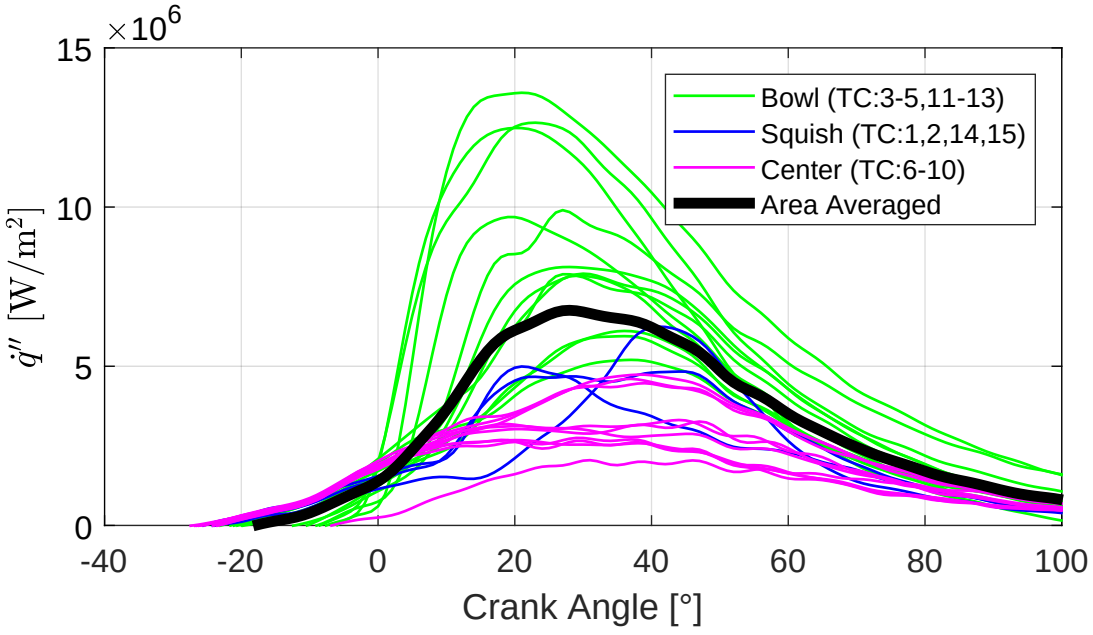


Figure 4.21: Operating condition 5 (2750 rpm, 29.7 bar IMEPg) SOI timing of -21 °ATDC area averaged and individual heat flux with line color indicating piston location

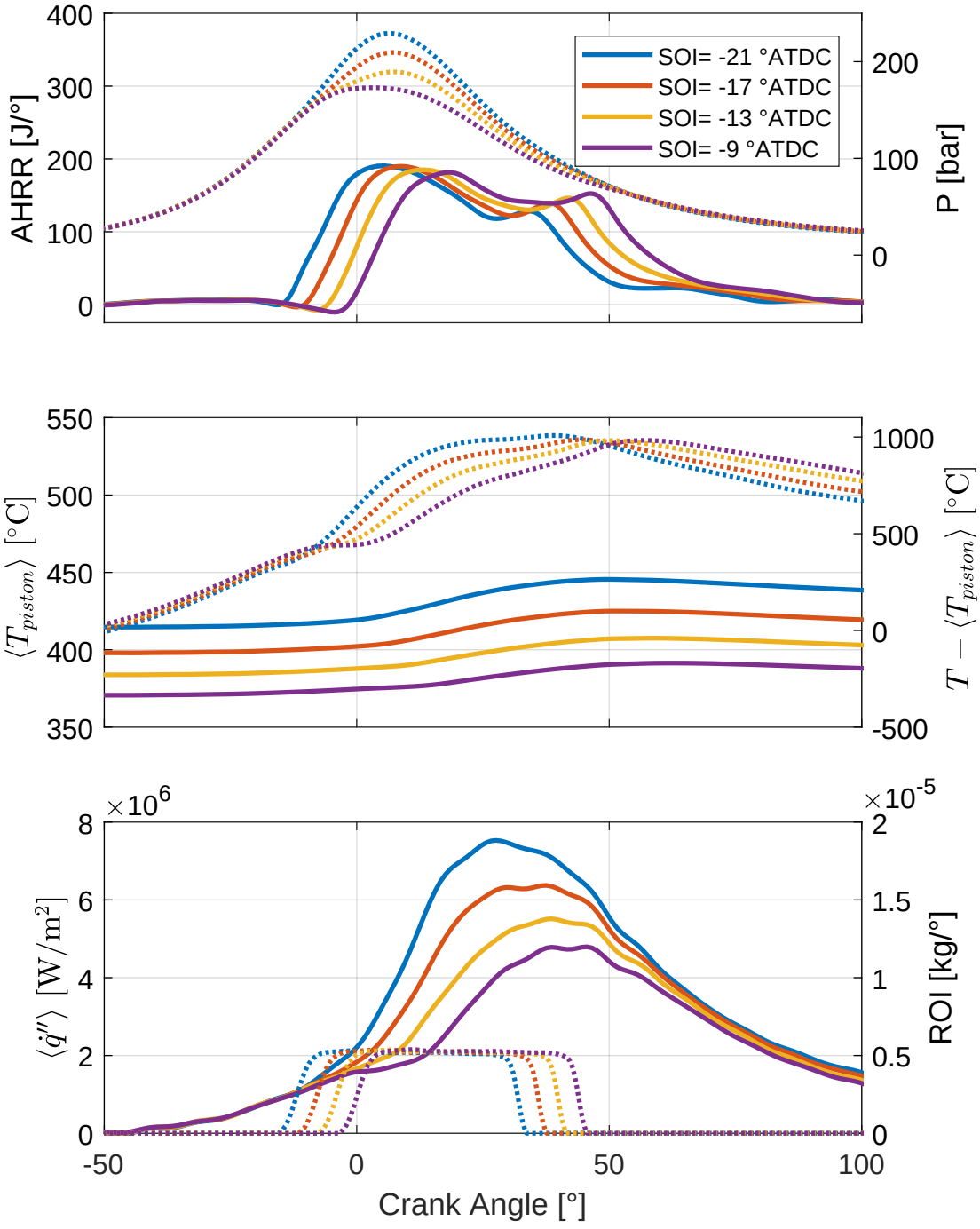


Figure 4.22: Operating condition 5 (2750 rpm, 29.7 bar IMEPg) high-speed crank angle measurements for all SOI (solid lines left axis, dotted lines right axis)

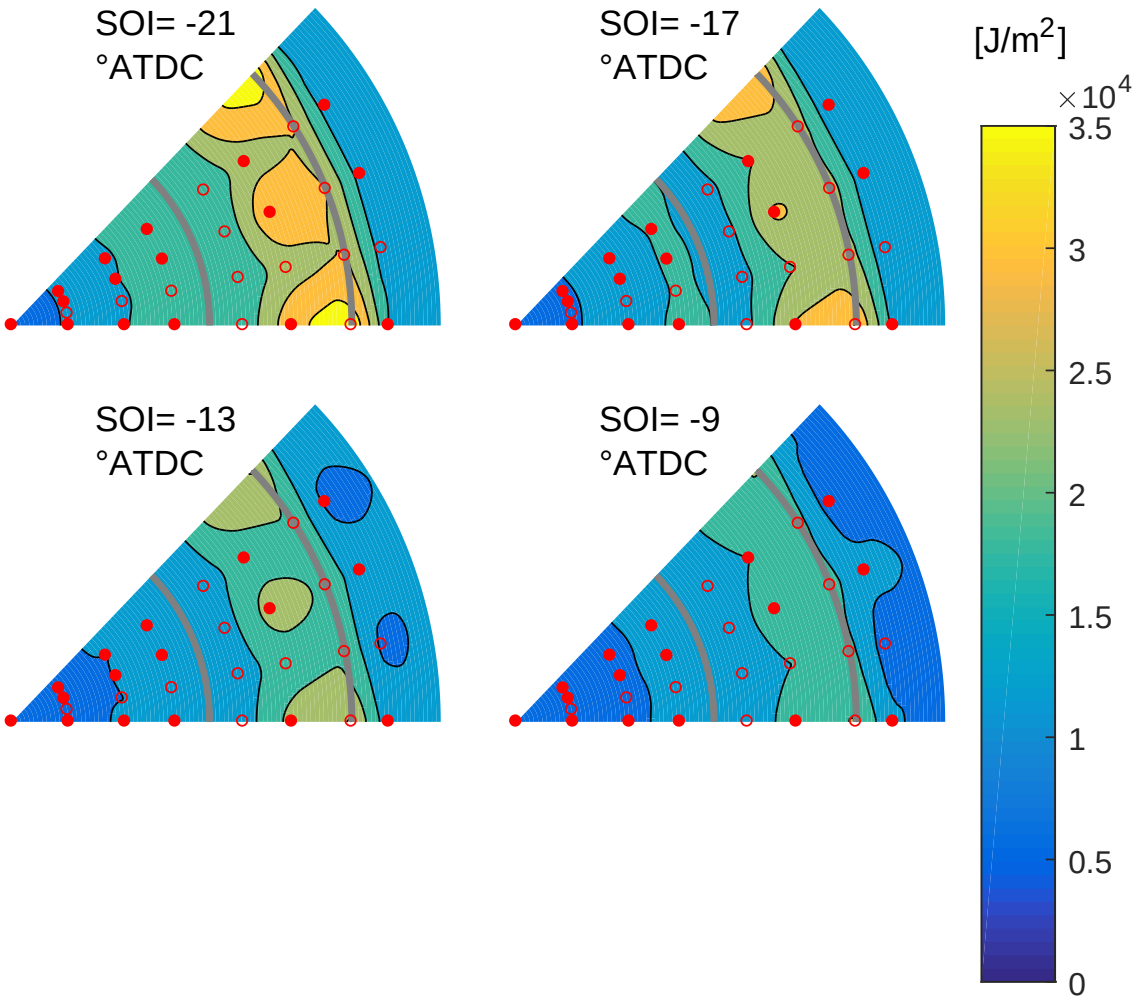


Figure 4.23: Operating condition 5 (2750 rpm, 29.7 bar IMEPg) contours of heat flux integrated w.r.t. time from -20 to 100 °ATDC (energy flux) for all SOI

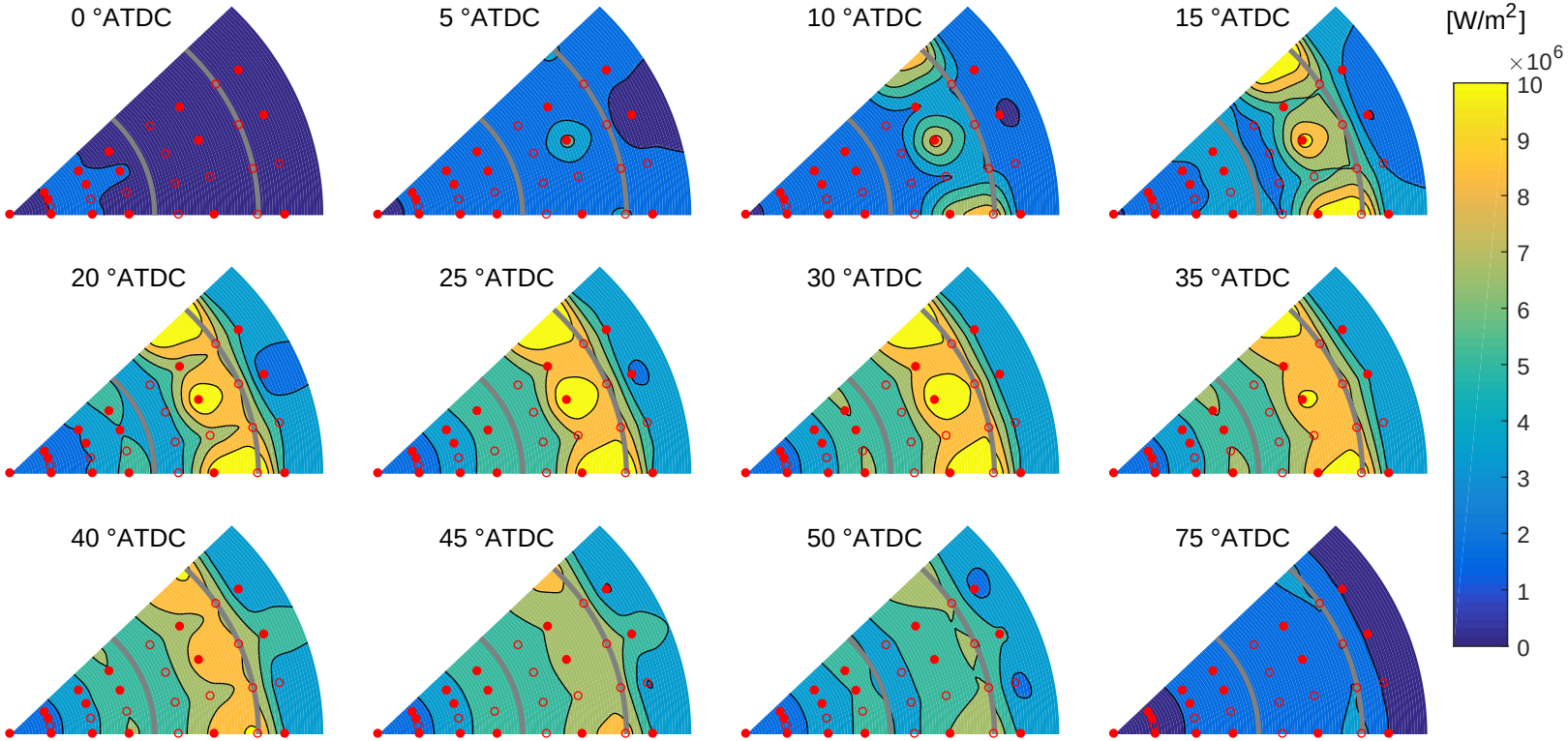


Figure 4.24: Operating condition 5 (2750 rpm, 29.7 bar IMEPg) SOI timing of -21 °ATDC contours of heat flux at selected crank angles

4.4 Comparison of Local and Global Heat Transfer

Comparison of global heat transfer metrics derived from the local piston thermocouple data to independent, global engine measurements of heat transfer were made. Although each of the individual assumptions related to calculating $\langle \dot{q}'' \rangle$ was previously discussed and individually seemed reasonable, further validation was performed. The spatially averaged local heat flux, $\langle \dot{q}'' \rangle$, was integrated over the full engine cycle to find the spatially averaged heat transfer, $\langle Q \rangle$, (see equation 4.5). Figure 4.25 shows a comparison of $\langle Q \rangle$ (based on piston heat flux measurements)to $\dot{Q}_{gas}$ (based on global and in-cylinder pressure measurements). Each operating condition represents a SOI sweep (or intake manifold temperature sweep in the case of condition 3 IMT). Operating condition 3 IMT and 4 were shown with open markers because these data are considered lower quality; there are relatively few available thermocouple and heat flux data sets, which may have biased $\langle Q \rangle$. Overall the agreement between the two metrics is reasonable.

When comparing between operating conditions the average value of each grouping (with different color markers) seems to correctly capture the trend of following the 1:1 line. When looking at each operating condition individually two different trends are observed. For conditions 1, 2 and 3 (standard output) a linear increasing trend was observed, where the most advanced SOI had the largest values of $\langle Q \rangle$ and $\dot{Q}_{gas}$ and the most retarded SOI had the smallest. Although the trend is linear the rate of increase of $\langle Q \rangle$ with respect to $\dot{Q}_{gas}$ is greater than the expected 1:1 line. Operating conditions 4 and 5 (very-high output) did not show a strong SOI trend for both $\dot{Q}_{gas}$ and $\langle Q \rangle$ with the data more tightly grouped. The dependence of $\langle Q \rangle$ on $\dot{Q}_{gas}$ seemed to be negatively correlated which was opposite of the standard output conditions. Both of the very-high output cases had very long injection events (with spray targeting toward the liner) which means $\langle Q \rangle$ may have been underestimated because measurement locations only on the piston were included. Interestingly, the negatively correlated data disappeared when a similar comparison was made using heat transfer calculated from a heat transfer correlation later in Chapter 6 (see figure 6.17), which

supports idea that local heat flux was not completely captured for these two operating conditions.

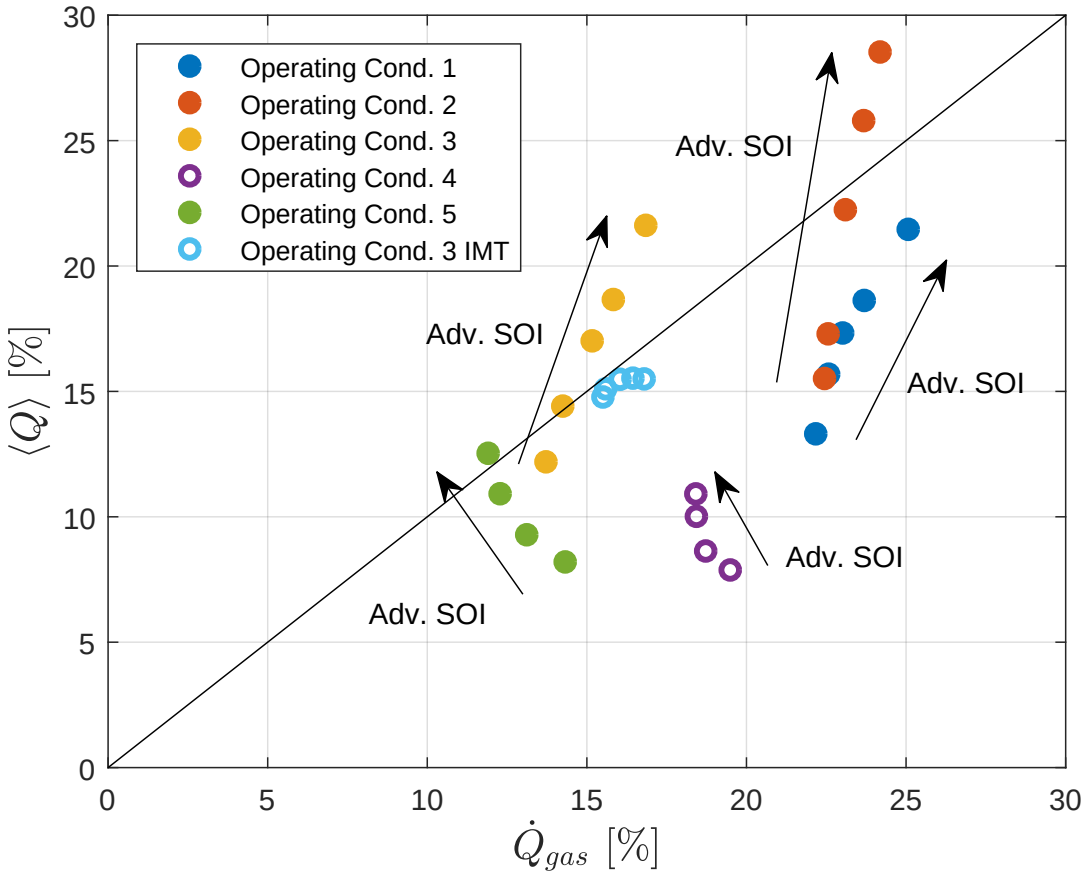


Figure 4.25: Comparison of local ($\langle Q \rangle$) and global ($\dot{Q}_{gas}$) heat transfer metrics for all operating conditions. Arrows show direction of advancing SOI (open markers used for higher uncertainty data)

Figure 4.26 shows the location of maximum $\langle \dot{q}'' \rangle$ as a function of location of maximum in-cylinder gas temperature. Overall there is strong agreement over all operating conditions which provides confidence that two independent data acquisition systems were synced properly and that the interpolation method used to generate $\langle \dot{q}'' \rangle$ was able to correctly locate the maximum $\langle \dot{q}'' \rangle$.

Operating condition 5 had the maximum location of $\langle \dot{q}'' \rangle$ earlier in the engine cycle than the peak in-cylinder temperature. Figure 4.22 showed that the difference between in-cylinder

temperature and piston temperature was nearly constant for approximately 30 crank angles. This constant temperature makes locating a maximum difficult and is also a reminder that this operating condition had significantly different in-cylinder temperature trajectory, which may have a complicating effect on heat transfer.

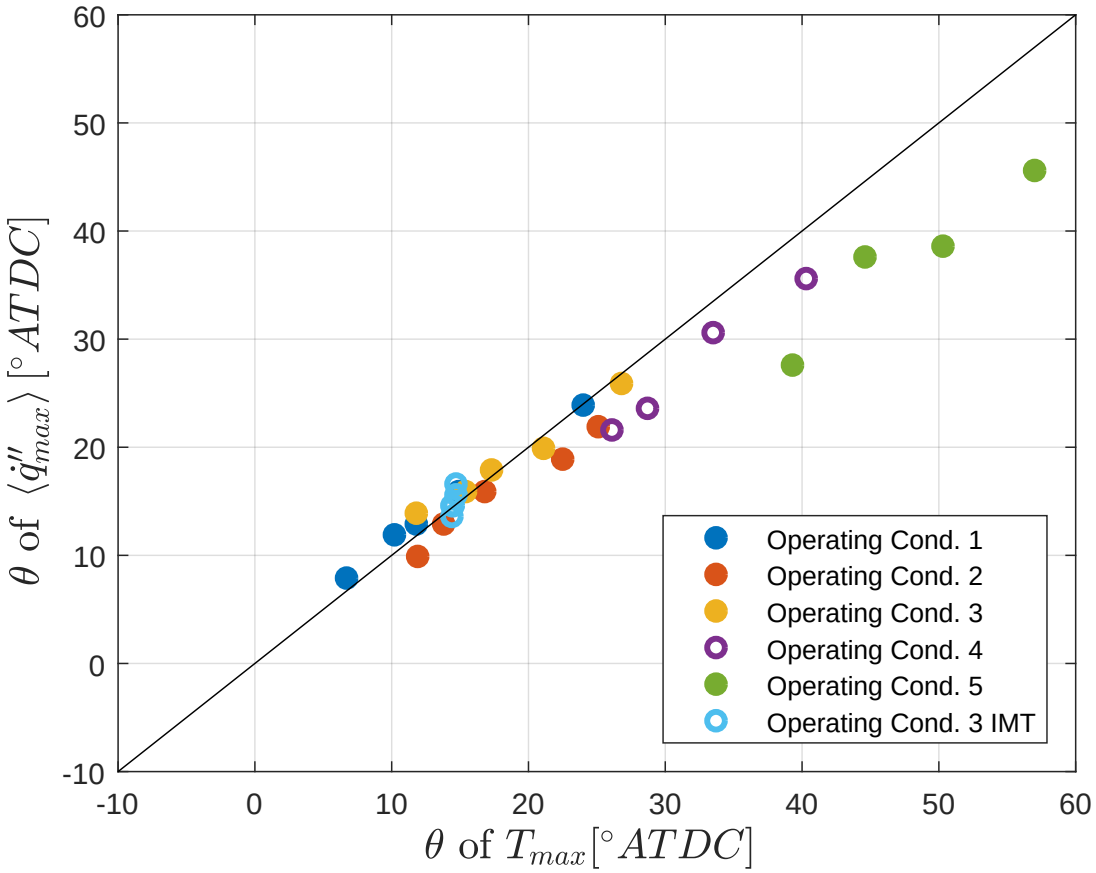


Figure 4.26: Comparison of location of maximum heat flux and maximum bulk gas temperature for all operating conditions (open markers used for higher uncertainty data)

Initial inspection of $\langle \dot{q}'' \rangle$ and later analysis in developing a heat transfer correlation in Chapter 6 showed a delayed onset in the rise of $\langle \dot{q}'' \rangle$ compared to the start of combustion (SOC) for some cases. The SOC is defined as the first crank angle with AHRR > 10 J/°, which for all cases occurs after the last zero crossing before the pre-mixed combustion spike. The location of heat flux rise, *i.e.*, θ of $\langle \dot{q}''_{rise} \rangle$, is defined as first crank angle to have $\langle \dot{q}'' \rangle > 7e5$ W/m^2. This value was chosen based on inspection of $\langle \dot{q}'' \rangle$ for all cases that had deviation

from the motoring portion of $\langle \dot{q}'' \rangle$ in the range of $5e5$ to $6.5e5$ W/m^2. Because the piston temperature and heat flux only has a one crank angle degree resolution this method was found to be the simplest and most robust definition. The delay of θ of $\langle \dot{q}''_{rise} \rangle$ is defined as the difference between the location of heat flux rise and SOC.

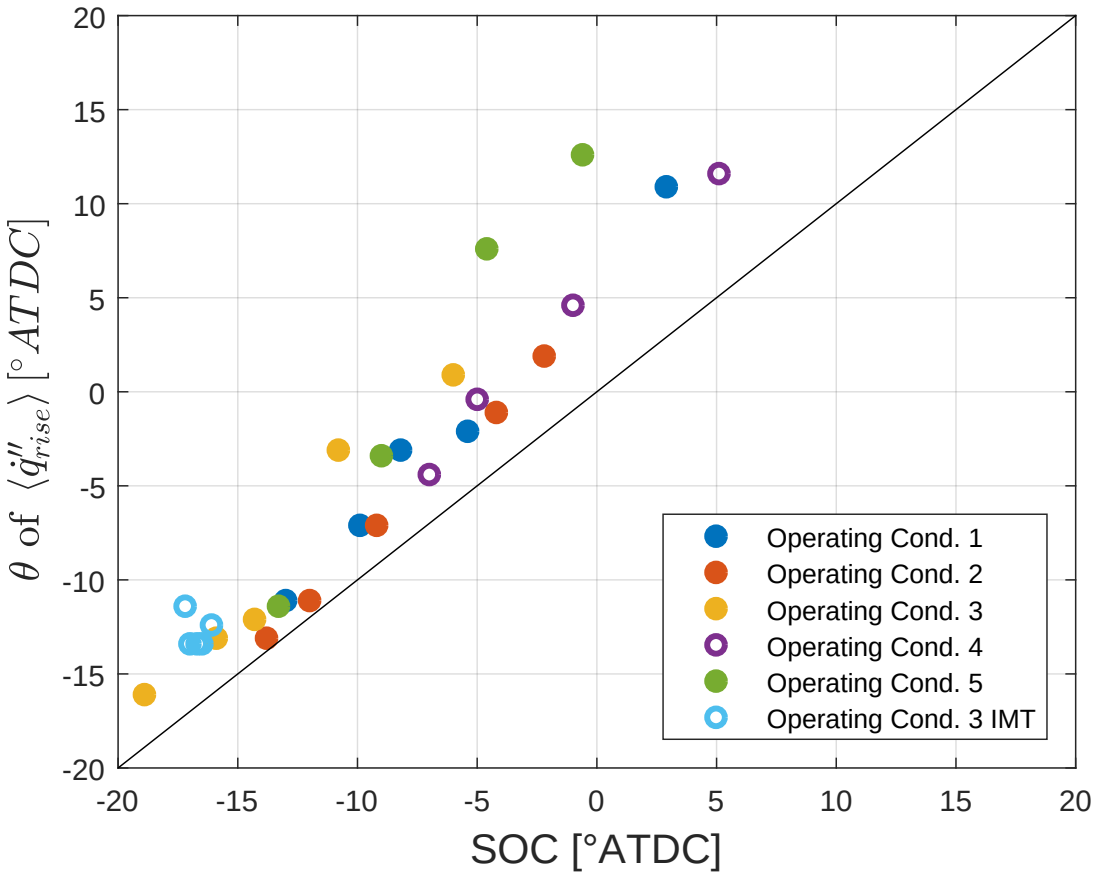


Figure 4.27: Comparison of location of heat flux rise and start of combustion for all operating conditions (open markers used for higher uncertainty data)

Figure 4.27 shows that the location of heat flux rise generally follows SOC but deviates for cases with later SOC. Operating condition 1, with an SOI of -5 °ATDC, was one of the data points with a larger deviation (upper right of figure 4.27). Additionally, operating condition 1 was run at 1700 rpm, which is a lower speed with longer time available for heat transfer. For this case all the individual heat flux, average heat flux and AHRR are plotted in figure 4.28. The heat flux delay for this case is significant. Further inspection shows that each of the

individual heat flux lines rises relatively close to the area averaged value which demonstrates that the observed delay is not an artifact of interpolation or other data processing method.

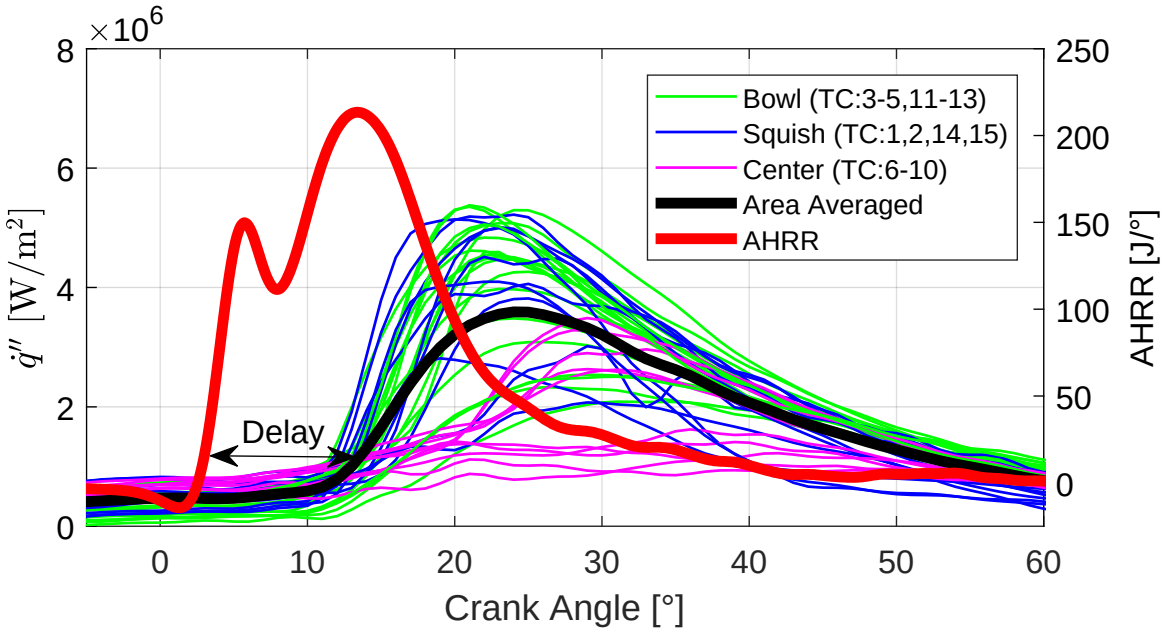


Figure 4.28: Operating condition 1 (1700 rpm, 12.3 bar IMEPg) SOI timing of -5 °ATDC area averaged, individual heat flux (with line color indicating piston location) and AHRR

Heat flux delay is further explored in figure 4.29. The bottom plot shows the delay in crank angles, which is a slightly different presentation of figure 4.27. The top plot shows heat flux delay in time, which seems to reduce the scatter in the data compared to crank angle domain. Development of a heat transfer correlation in Chapter 6 investigates dimensionless terms related to this observed delay, therefore knowing which domain the data best correlates is helpful.

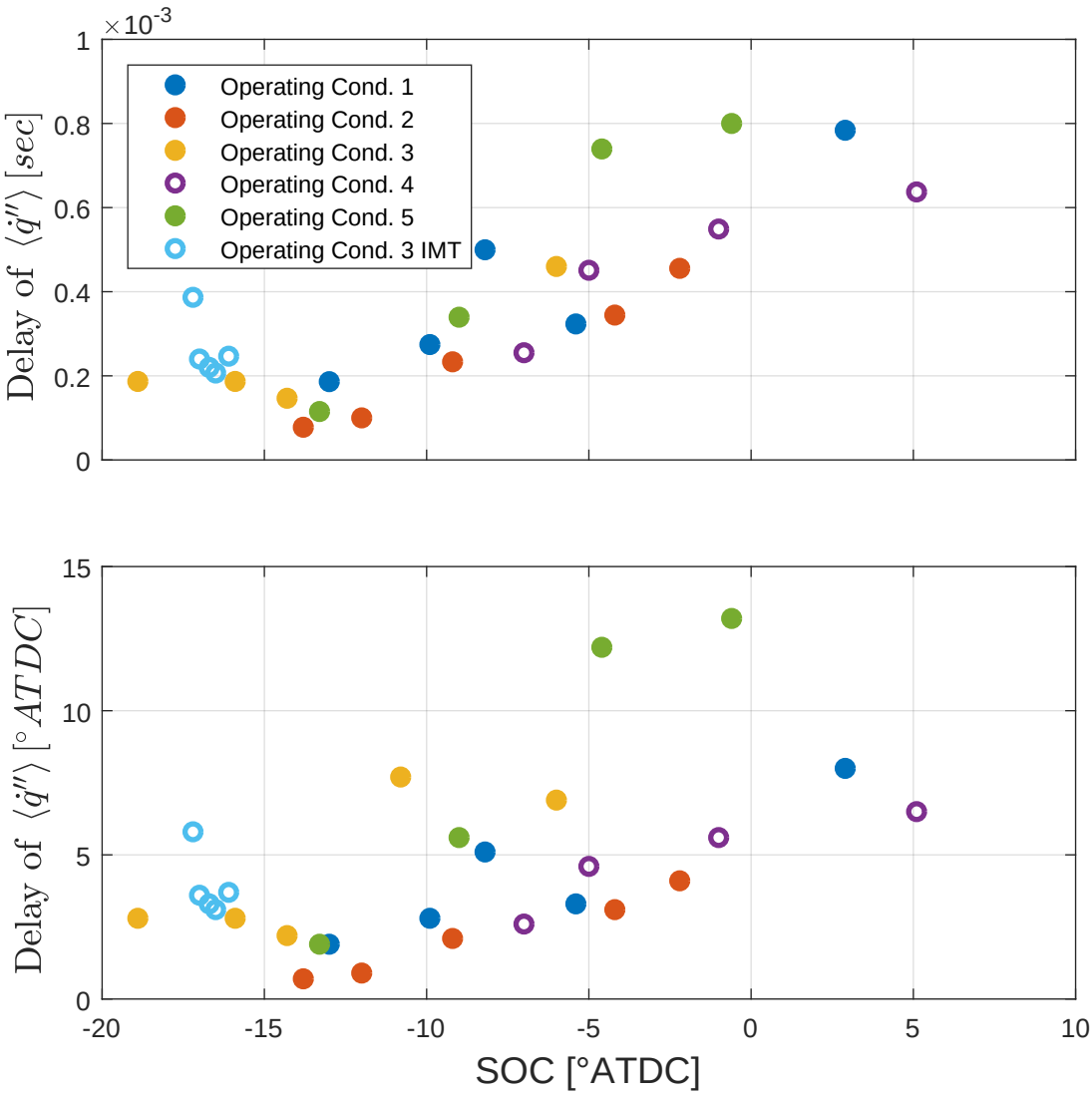


Figure 4.29: Comparison of heat flux delay in units of time (top) and crank angle (bottom) as function of start of combustion for all operating conditions (open markers used for higher uncertainty data)

4.5 Summary and conclusion

1. Local heat transfer, based on fast-response thermocouple data, combined with an appropriate spatial interpolation method and integrated over the cycle have relatively good agreement with independent, engine-out global thermodynamic heat transfer measurements and quantities based on in-cylinder pressure across a range of engine

operating conditions. These comparisons provide the basis for further investigating the subtleties of local heat flux through heat transfer correlation development.

2. Spatially averaged heat flux data, $\langle \dot{q}'' \rangle$, for operating conditions 1, 2, 3 and 5 are of high quality with a large number of individual thermocouple measurements available. The spatial variation of $\dot{q}''$ during the combustion event for operating condition 5 is higher than for other other operating conditions and as such, overall uncertainty in $\langle \dot{q}'' \rangle$ is higher for this case. The number of individual data points available for area averaging in operating condition 4 and the operating condition 3 intake manifold temperature sweep was not considered sufficient to reliably generate $\langle \dot{q}'' \rangle$ so these conditions should be considered for reference and not included in further heat transfer correlation development.

3. The spatial distribution of temporally integrated heat flux were dominated by radial position, and azimuthal location relative to the injector spray plume has a minor effect. The highest intensity of heat flux, and therefore integrated heat flux, was typically contained in the piston bowl.

4. Spatial gradients in instantaneous heat flux between on- and off-axis injector spray plumes (azimuthal direction) was strongest during the initial onset of heat flux rise and nearly disappeared later is the expansion stroke. On-axis spray locations typically showed the first rise in heat flux.

5. The start of injection command had a strong effect on $\langle \dot{q}'' \rangle$. As the injection timing was advanced, the initial rise of $\langle \dot{q}'' \rangle$ advanced and the maximum value of $\langle \dot{q}'' \rangle$ increased by nearly a factor of two (when compared to the most retarded timing tested). Advancing the injection timing increased the maximum in-cylinder pressure and temperature which are strong driving factors in $\langle \dot{q}'' \rangle$.

6. The intake temperature sweep showed virtually no influence on $\langle \dot{q}'' \rangle$ and a limited effect on mean piston temperature. For an increase of intake temperature of 44 °C, an area-

and time-averaged piston temperature increased roughly 20 °C. Both of these changes were small in comparison to the maximum difference in temperature between the piston and gas, which is greater than 1000 °C.

7. A delayed onset of the rise of $\langle \dot{q}'' \rangle$ was observed for later start of injection timings. It was found that the delay correlated slightly better in the time domain than in the crank angle domain. The individual data at each thermocouple location showed that the delay was not an artifact of the selected interpolation method. Any delay introduced by the thermocouples or telemetry system is believed to have been minimal.

5 Impact of Thermal Barrier Coating Roughness

This chapter focuses on data from four pistons where *global* thermodynamic data were collected, *i.e.*, none of these pistons were instrumented with thermocouples. The pistons included: 1) Metal, 2) 0.185mm TBC, 3) 0.325mm TBC and 4) 0.325mm TBC Polished (nomenclature from table 3.7) where coating thickness and surface roughness were varied. The same five operating conditions used in Chapter 4 were run with some additional SOI timings. Supplemental heat flux data from Chapter 4 using Co-axial Metal 1 and Co-axial Metal 2 pistons were also utilized in this chapter to help explain engine performance trends that may be related to heat transfer (see Section 5.2.1.1).

5.1 Thermal Barrier Coating

5.1.1 Architecture

A multi-layered architecture was used to help manage interfacial stresses that result from a mis-match in the coefficient of thermal expansion between the metal substrate and thermal barrier coating. The three-layer coating architecture and target thickness are shown in figure 5.1. The metallic bond coat consisted of a nickel chromium aluminum (NiCrAl) alloy; Metco 443NS thermal spray powder was used. The gradient layer was a mixture of the bond coat and the YSZ thermal barrier top coat (Saint-Gobain #204), which features an 8 percent stablized yttria with uniform chemistry. Measured properties of each layer and additional coating processing details are given in Appendix A.5. Two different thicknesses of TBC were investigated, 0.055 and 0.210 mm. The target design was to keep the bond coat and gradient layer thickness constant and change the top thermal barrier coating thickness giving *total* coating thicknesses of 0.185 and 0.325 mm.

The radiative properties of the TBCs were not quantified. Work by Ge *et al.* showed that pure YSZ systems show transmittance in the 1-8 μm wavelength range but for systems

with a small percent Nickel included in the TBC the transmittance drops to nearly zero [33]. The TBCs investigated in this study all include a 5 % NiCrAl alloy in the top TBC layer therefore the optical properties of the TBCs are not expected to be significantly different from the base metal piston.

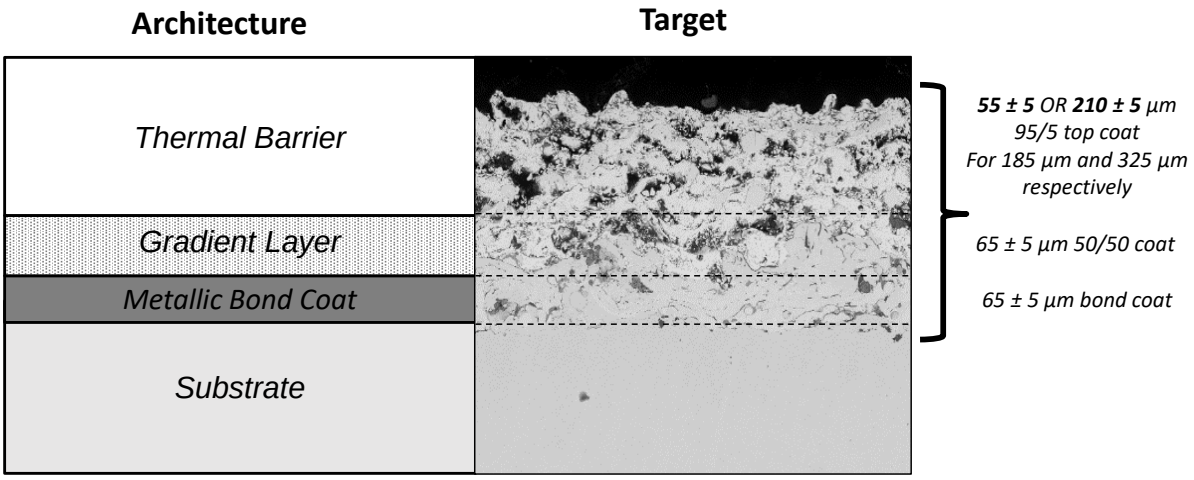


Figure 5.1: Thermal barrier coating architecture

5.1.2 Surface Roughness

The spray process results in a surface that has a significantly higher surface roughness than the baseline metal piston. An "as-sprayed" and "polished" TBC were tested to understand the impact of surface roughness on engine performance and emissions. To quantify the difference in the surface, an optical profilometer was utilized to measure variations in surface geometry. Figure 5.2 shows 3D contours for as-sprayed, polished, and metal pistons. From these data, one can find Ra= 11.8, 6.0, and 1.6 μm, respectively, where Ra is arithmetical mean deviation of the assessed profile. For the same samples and locations a histogram of height is shown in figure 5.3. The as-sprayed and metal samples show a relatively symmetric distribution, although the metal sample has a much smaller standard deviation. The polished sample, which was shifted so that the maximum value was at zero, shows a skewed distribution. It is

Table 5.1: Piston Nomenclature

Piston Nomenclature	Total Coating Thickness [mm]	Ra [μm]	Compression Ratio [-]
Metal	N/A	1.6	14.0
0.185mm TBC	0.185	11.8	14.3
0.325mm TBC	0.325	11.8	14.5
0.325mm TBC Polished	<0.325	6.0	14.5

similar to the as-sprayed sample for negative values but for positive values the distribution cuts off sharply similar to the metal piston. Both figures illustrate that the polishing process is only able to remove TBC material in the areas with the largest height, resulting in a plateau-hone-type finish.

Table 5.1 gives the nomenclature used to describe the different engine configurations. The same base metal piston design was used for every engine build, which meant the compression ratio varied slightly when a TBC was added. The "0.325mm TBC"and the "0.325 TBC Polished" were assumed to have the same compression ratio because only a small amount of material was removed in the polishing process. Figure A.2 in Appendix A.5 show the three TBC coated pistons after they were run.

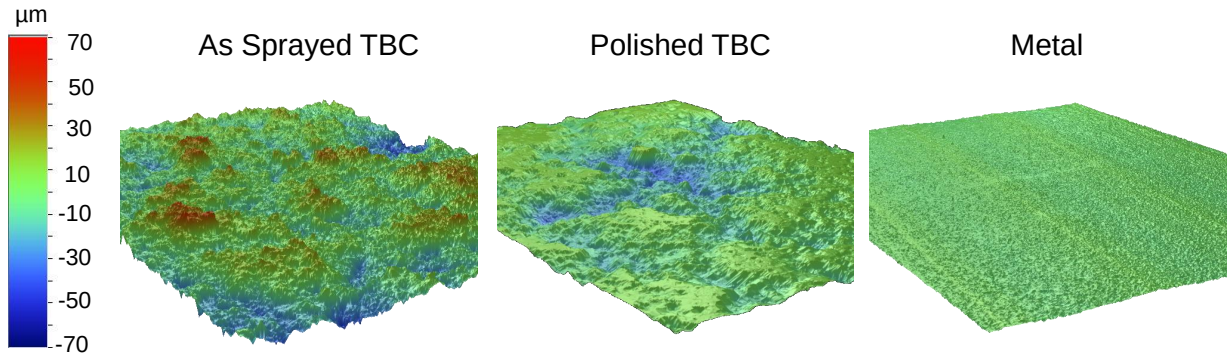


Figure 5.2: 3D Contour of 1.16 by 0.87 mm portion of piston for an as sprayed TBC, polished TBC and stock metal piston

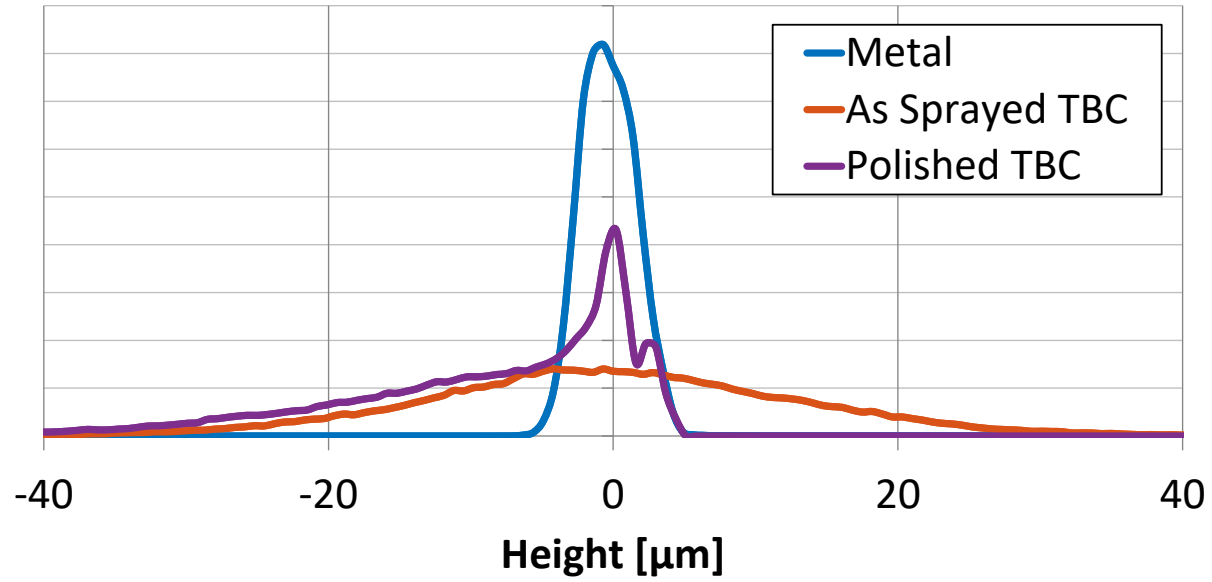


Figure 5.3: Histogram of height for an as sprayed TBC, polished TBC and stock metal piston

5.2 Results

The experimental results are presented for the standard output conditions (1-3) first, and then for the very high-output operating conditions (4 and 5). The observed trends are similar for these groupings. For each case, pressure and AHRR are presented only for the SOI timing with maximum gross indicated thermal efficiency (ITEg). The final section focuses on the normalized heat rejection results for conditions 3 and 5.

5.2.1 Standard Output: Operating Conditions 1-3

Initial experiments using the two different thickness as-sprayed TBCs (0.325 and 0.185 mm) did not see any positive improvement in performance for operating conditions 1-3. Data from operating condition 3 is given in figure 5.4. For the most retarded injection timings most of operating conditions showed an increase in FSN. $\dot{Q}_{gas}$ also trended higher for these TBCs when compared to the metal baseline. These results motivated the investigation of the role of TBC surface roughness on the spray/mixing process and if the local gas-side thermal boundary layer was being impacted by the change in surface roughness.

A third TBC coated piston (not previously run in the engine) with the same as-sprayed thickness as the previous 0.325 mm TBC was polished using a hand sanding procedure where an ascending silicon carbide sandpaper grit was used until the desired surface roughness was achieved. Care was taken to polish the piston surfaces as evenly as possible and limit the total amount of material removed. Subsequently, it may have been possible to achieve a lower Ra value but additional as-sprayed thickness would need to be added before polishing to avoid removing too much TBC.

The reduced roughness piston was then run over all operating conditions and SOI timings and compared to the previous metal baseline and TBC results, see figures 5.5-5.12. The increases in FSN observed with the 0.185 and 0.325 mm as-sprayed TBC pistons was reversed to values similar the metal baseline. Similarly, $\dot{Q}_{gas}$ which also trended higher for the as-sprayed TBCs was reduced back to values equal to or less than the metal baseline.

The polished 0.325 mm TBC showed an increase in ITEg for most of the SOI timings at all standard output operating conditions. For these operating conditions the most retarded injection timings showed little difference in ITEg when compared to the metal baseline. The increase in ITEg was accompanied by an increase in late-cycle AHRR in the 10-30 °ATDC range. The increase in AHRR may be related to an instantaneous reduction in heat transfer. This trend will be explored further using piston heat flux data in Section 5.2.1.1. Overall, when examining the full AHRR none of the TBCs tested resulted in a significant change in ignition delay and the resulting pre-mixed burn was mostly unchanged.

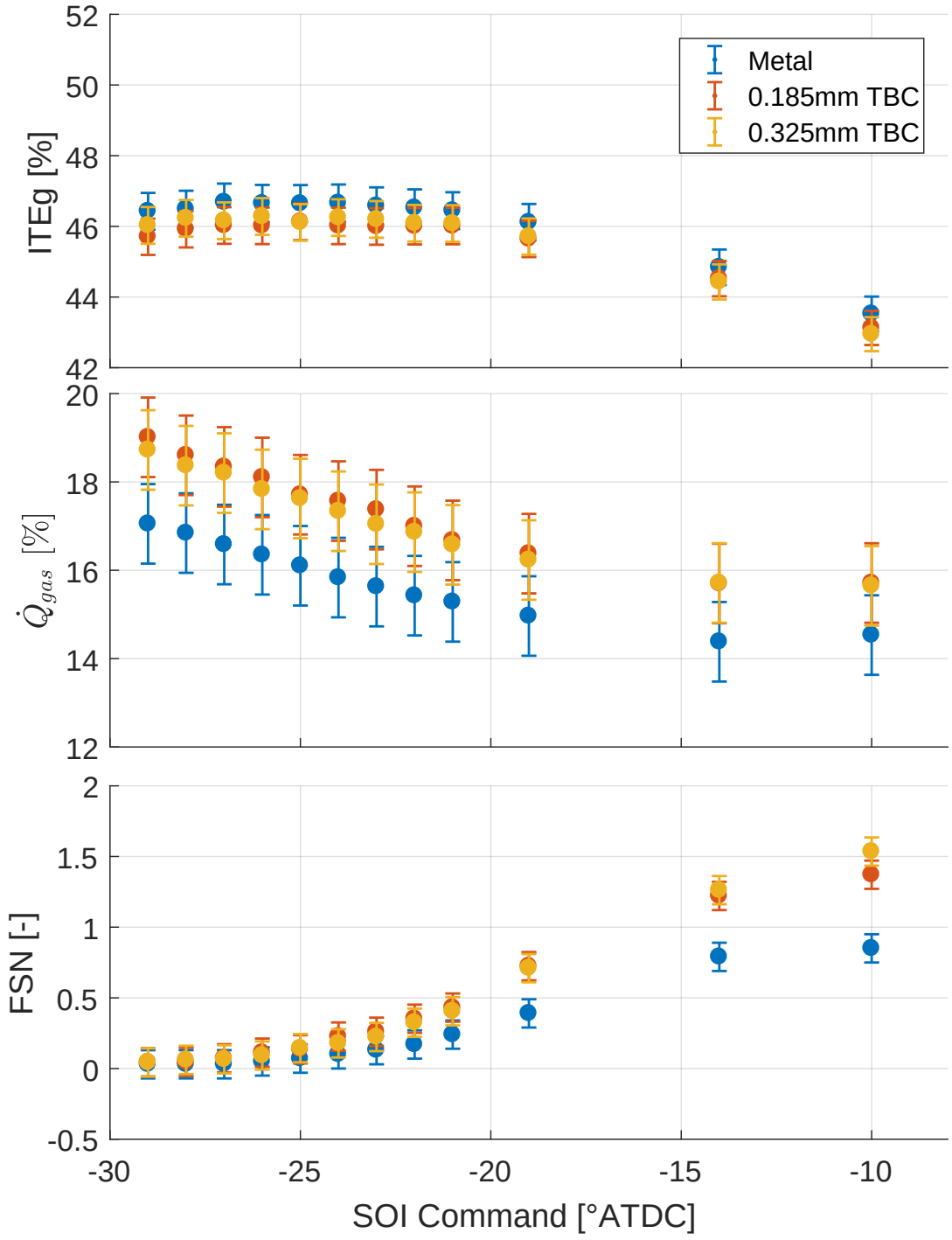


Figure 5.4: Initial experiments operating condition 3 (2500 rpm, 20.3 bar IMEPg) ITEg, $\dot{Q}_{gas}$ and FSN

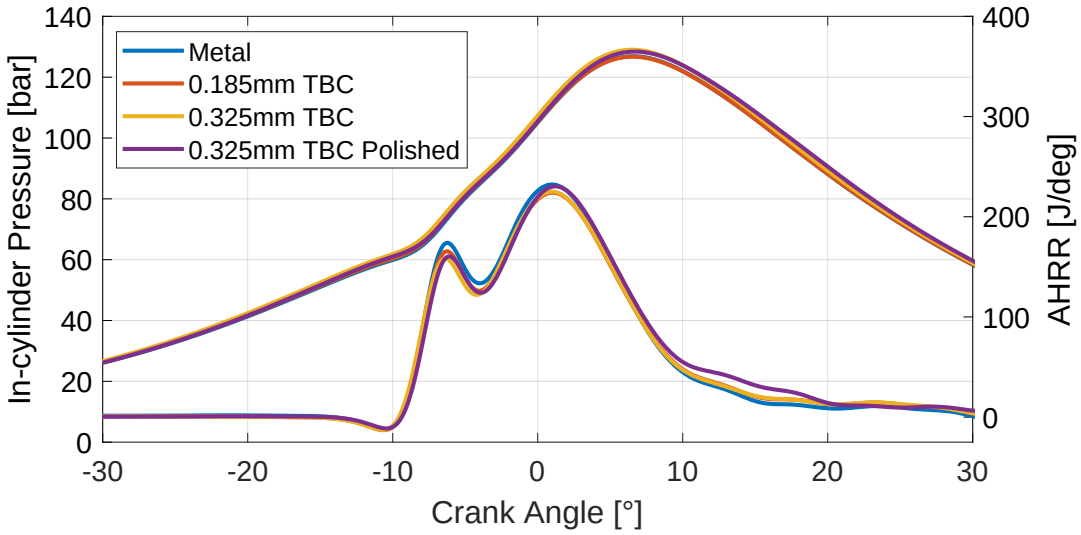


Figure 5.5: Operating condition 1 (1700 rpm, 12.3 bar IMEPg) in-cylinder pressure and AHRR for SOI timing of -17 °ATDC

Figures 5.5 and 5.6 show results for condition 1 which was the lowest IMEPg case. The previously discussed trends in ITEg and FSN for the standard operating conditions are less apparent for this part-load operating condition. Specifically, FSN was mostly unchanged when comparing any of the TBCs to the metal baseline which may be related to the higher air-fuel ratio (AFR) that was selected for this operating condition. A percent change of ITEg of 3.3 % (relative) for the polished TBC was visible for the SOI timing of -17 °ATDC which just barely exceeds the limits of the error bars.

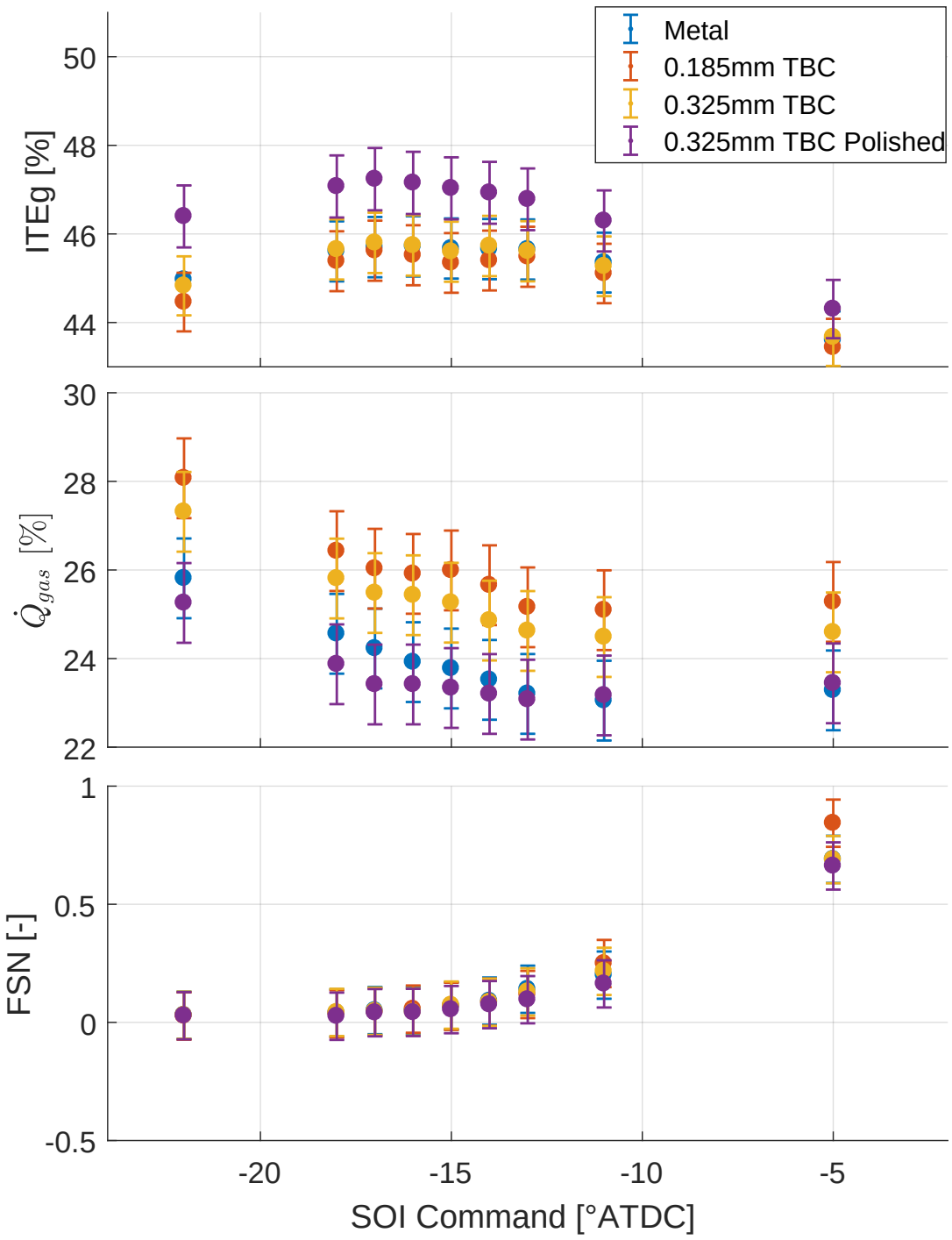


Figure 5.6: Operating condition 1 (1700 rpm, 12.3 bar IMEPg) ITEg, $\dot{Q}_{gas}$ and FSN

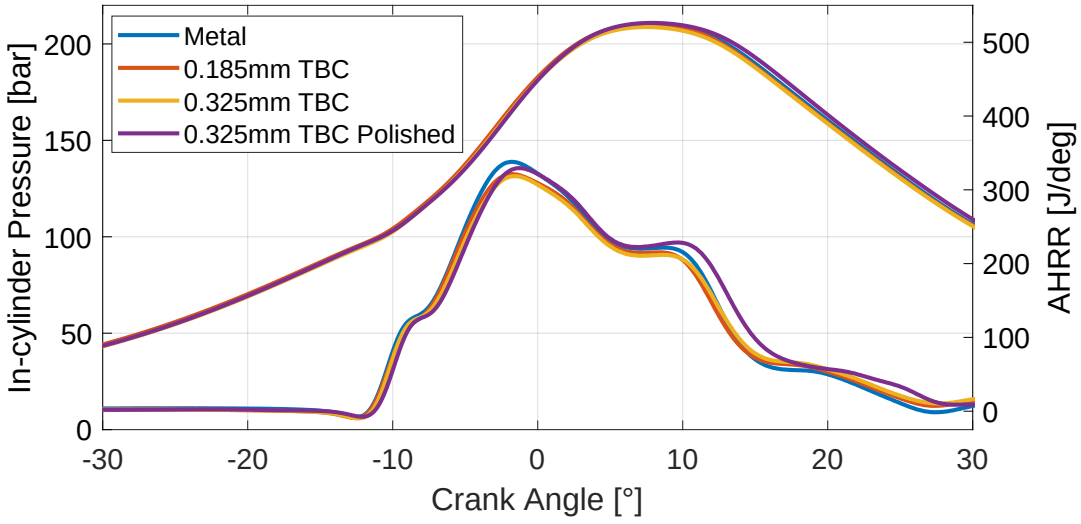


Figure 5.7: Operating condition 2 (1500 rpm, 23.8 bar IMEPg) in-cylinder pressure and AHRR for SOI timing of -16 °ATDC

Results for operating conditions 2 and 3, which represent a peak torque and rated power operating point for a commercially available diesel engine, are shown in figures 5.7-5.12. These operating conditions showed similar trends in ITEg, $\dot{Q}_{gas}$, and FSN when comparing the TBC pistons to the metal baseline. For both conditions, the polished piston showed an increased ITEg greater than 3.5 % (relative). This increased efficiency corresponds to a decrease in $\dot{Q}_{gas}$.

Figures 5.9 and 5.10 show the AHRR and in-cylinder pressure for SOI command of -25 °ATDC and -10 °ATDC, respectively. The additional late-cycle heat release that was observed for the polished TBC at -25 °ATDC (figure 5.9) was nearly eliminated for the -10 °ATDC case (figure 5.10). Corresponding to the additional AHRR, an increase in ITEg at -25 °ATDC relative to the retarded and as-sprayed TBC pistons is seen in figure 5.11. As injection timing was retarded, the ITEg reduced to values similar to the metal baseline and correspondingly the additional late-cylce heat release abated as seen in figure 5.10. These two SOI cases were chosen as an example data set of a larger trend to demonstrate the linkage between additional late-cycle heat release and an increase in ITEg. Other operating conditions that showed a reduction of ITEg to the metal baseline value for retarded SOI also showed a reduction in

late-cycle heat release back to the metal baseline values. This trend will be explored further in the following section (Section 5.2.1.1) by analyzing trends in local piston heat flux.

For operating condition 3, the measured NO_x, CO and HC emission results are shown in figure 5.12. The incomplete products of combustion (CO and HC) were generally quite low with η_c greater than 99 %. Overall the dominant trend in NO_x was related to the SOI timing; similar trends were seen for the other operating conditions.

Overall, for the standard output operating conditions, there was a clear impact of TBC surface roughness on engine performance and smoke. Although smoke was reduced to values similar to the metal baseline for the polished TBC, this observation does not necessarily mean that other surface effects, such as a modified fluid boundary layer, are not present. This work did not explore if reducing the TBC surface roughness further would cause an additional decrease in smoke or increase ITEg. If the initial increase in smoke using the as-sprayed TBC was strictly related to decreased fuel spray mixing (from additional spray-wall iteration), further reducing the surface roughness may not have any additional impact. Similarly, if the increase in ITEg was related to an instantaneous reduction in heat transfer it is not clear if reducing surface roughness would further impact efficiency. Figure 5.2 shows that the actual surface area of the polished TBC was still larger than the metal baseline, which could impact the fluid boundary layer and subsequently heat transfer. The next section will compare how changes in the AHRR that were observed on the polished 0.325mm TBC compare to measurements of instantaneous area averaged heat flux on a metal (non-coated) piston.

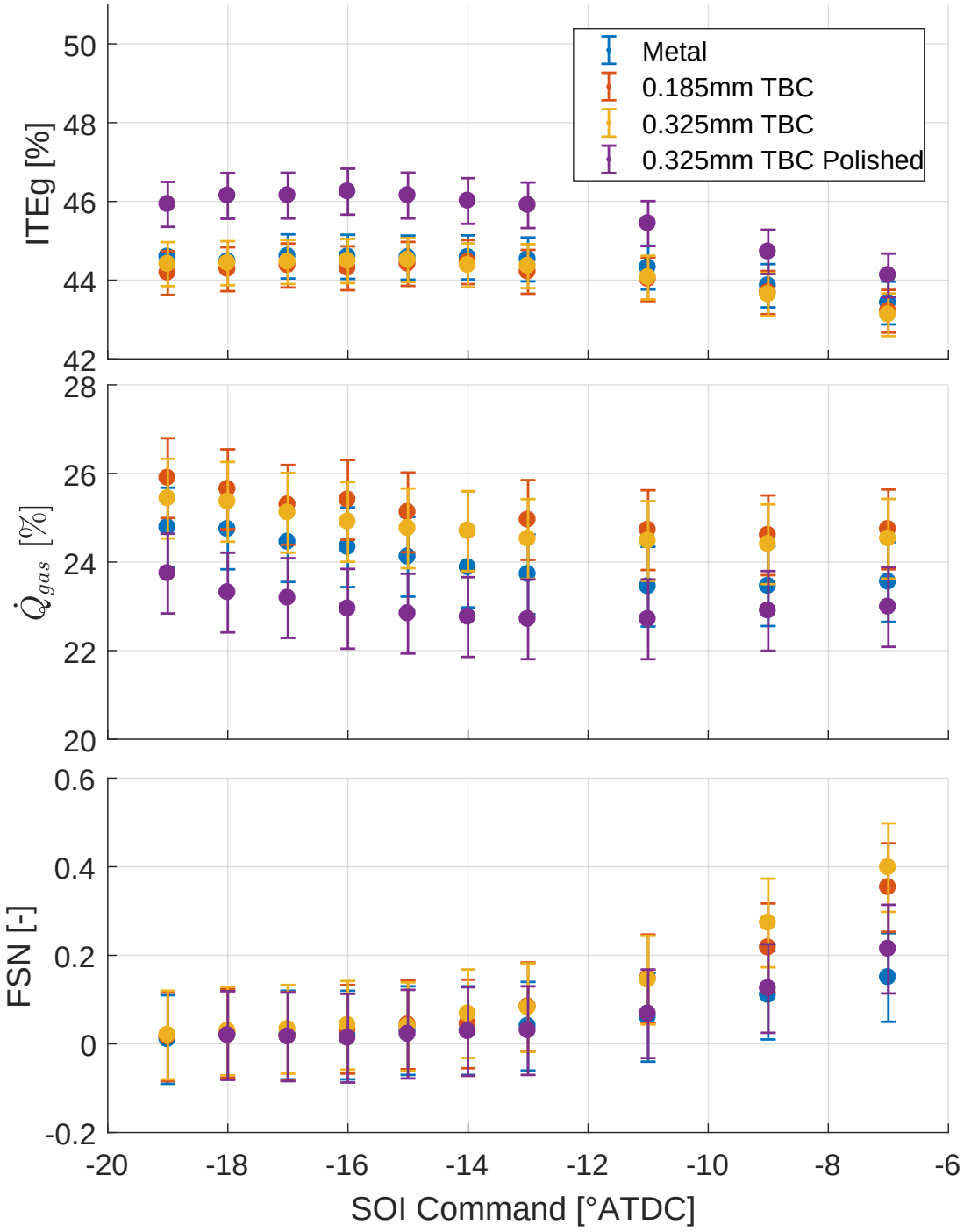


Figure 5.8: Operating condition 2 (1500 rpm, 23.8 bar IMEPg) ITEg, $\dot{Q}_{gas}$ and FSN

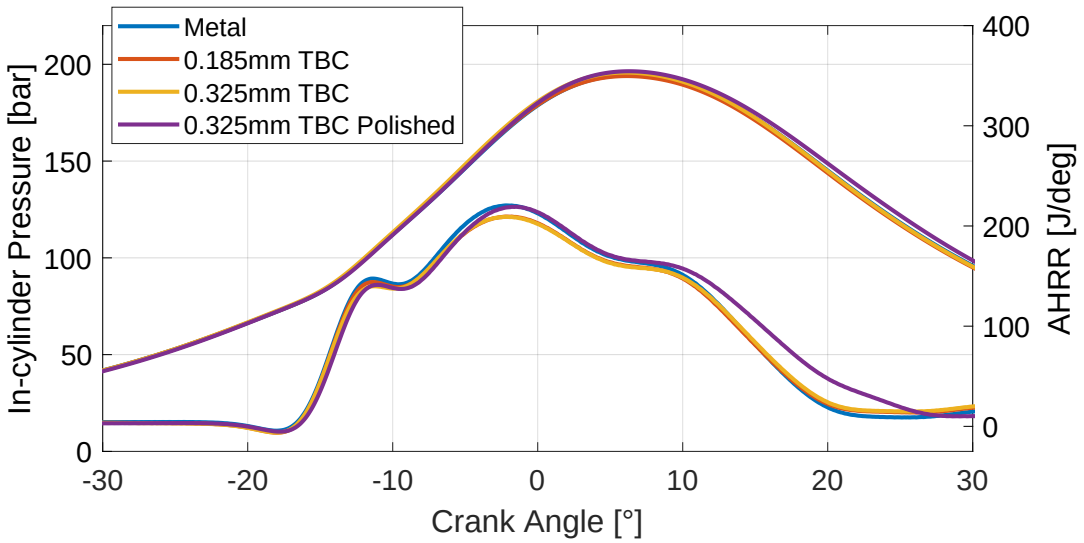


Figure 5.9: Operating condition 3 (2500 rpm, 20.3 bar IMEPg) in-cylinder pressure and AHRR for SOI timing of -25 °ATDC

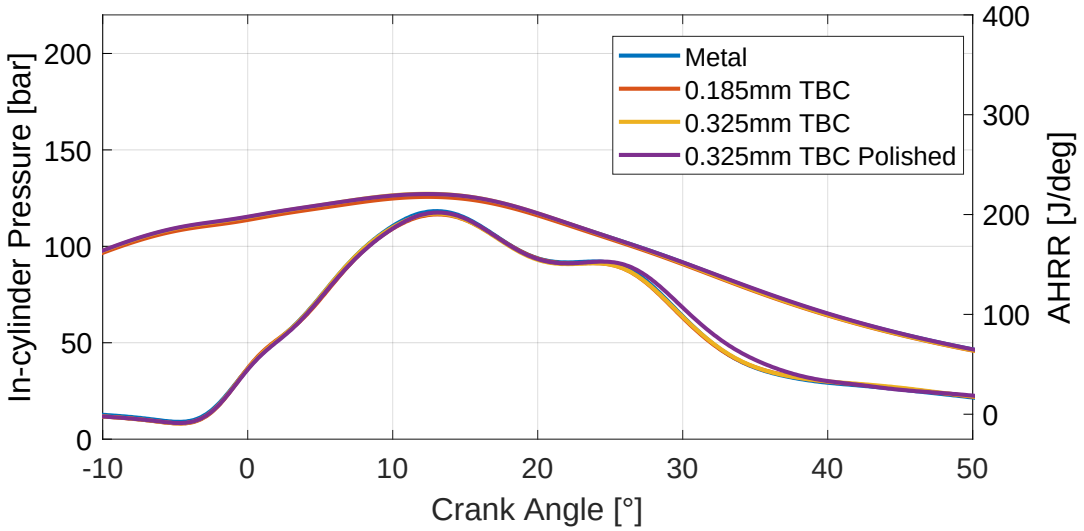


Figure 5.10: Operating condition 3 (2500 rpm, 20.3 bar IMEPg) in-cylinder pressure and AHRR for SOI timing of -10 °ATDC

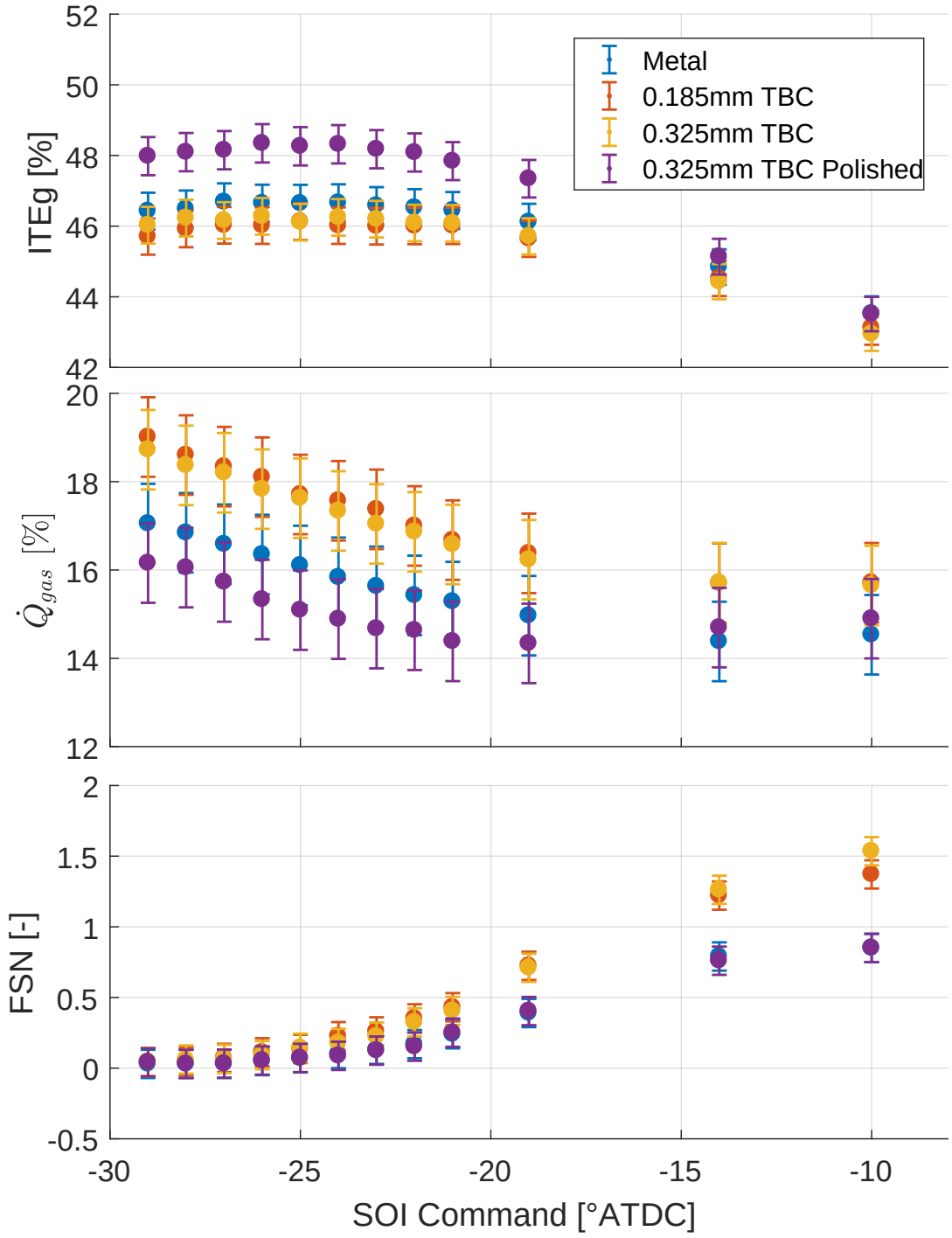


Figure 5.11: Operating condition 3 (2500 rpm, 20.3 bar IMEPg) ITEg, $\dot{Q}_{gas}$ and FSN

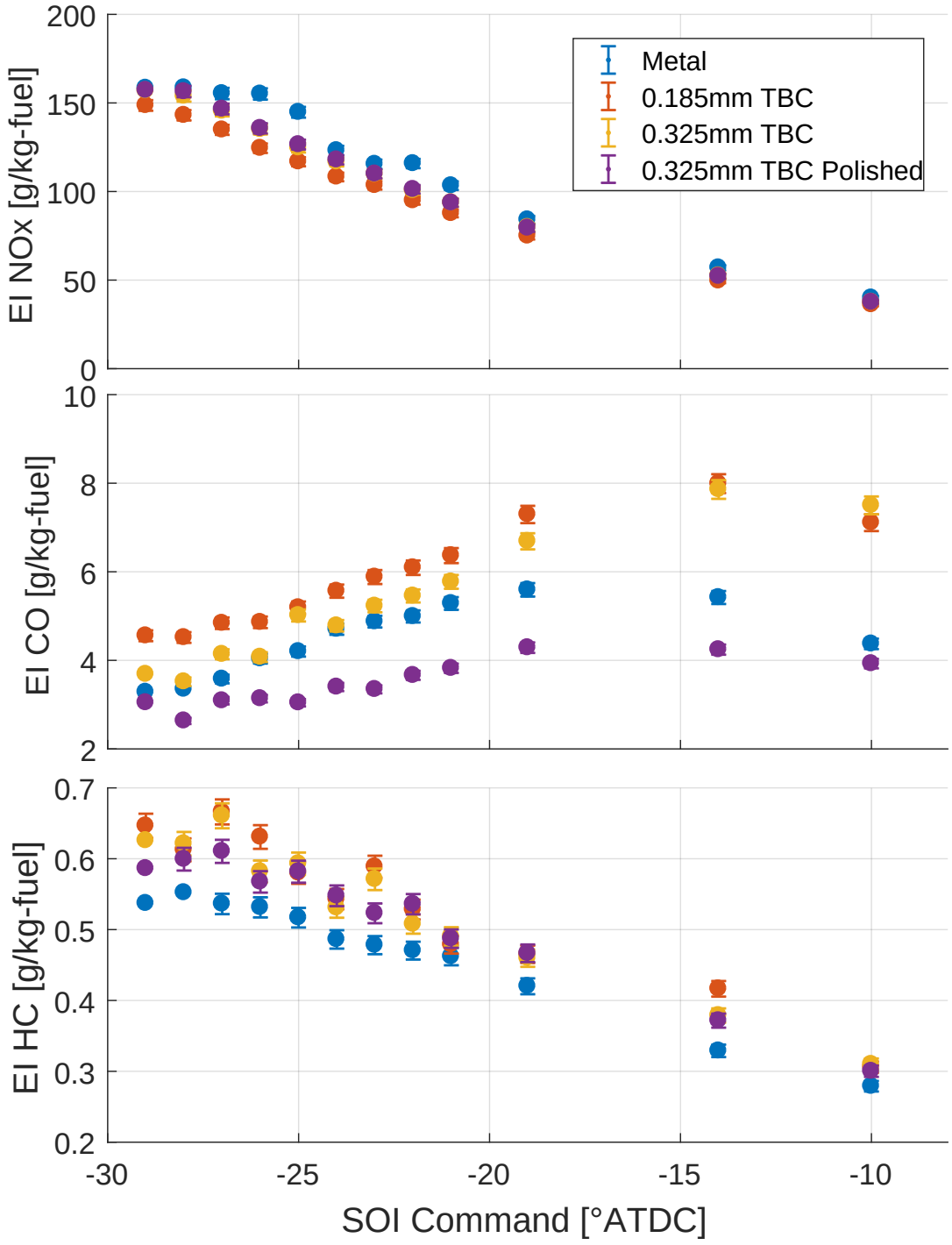


Figure 5.12: Operating condition 3 (2500 rpm, 20.3 bar IMEPg) NO_x, CO and HC emission indexes

5.2.1.1 Comparison of Metal Piston Heat Flux to Changes in AHRR

Operating conditions 1-3 all showed an increase in ITEg for the more advanced SOIs when comparing 0.325mm TBC polished to the metal baseline. When the SOI was retarded the ITEg of 0.325mm TBC polished closely matches the metal baseline for these operating conditions. The increase in ITEg was also associated with additional late-cycle AHRR (see figure 5.9 and 5.10). The maximum spatially averaged heat flux, $\langle \dot{q}''_{max} \rangle$, from the metal thermocouple instrumented piston experiments in Chapter 4 also appears to occur near the end of combustion, as previously shown in figures 4.9, 4.13 and 4.17. The change observed in AHRR is quantified by $\Delta AHRR_{max}$ which is defined as the maximum difference between the AHRR for 0.325mm TBC polished and the metal baseline. Figure 5.13 shows good agreement between the crank angle of $\Delta AHRR_{max}$ and the crank angle of $\langle \dot{q}''_{max} \rangle$. This agreement supports the hypothesis that the TBC may be reducing heat transfer during portions of the cycle when heat flux is largest

Next, the change in ITEg is compared to the intensity of the heat flux. The absolute change in ITEg, $\Delta ITEg$ is defined as the difference between the ITEg for 0.325mm TBC polished and the metal baseline. $\Delta ITEg$, was plotted as a function of $\langle \dot{q}''_{max} \rangle$ for operating conditions 1-3 in figure 5.14. The dependence of $\Delta ITEg$ on $\langle \dot{q}''_{max} \rangle$ is not clear. Each of the individual operating conditions shows a similar trend. The earlier SOIs, which have lower $\langle \dot{q}''_{max} \rangle$, show the smallest $\Delta ITEg$. As timing is advanced and $\langle \dot{q}''_{max} \rangle$ increases, $\Delta ITEg$ increases until a local maximum is found.

When comparing operating condition 1 to conditions 2 and 3 similar values of $\Delta ITEg$ are found at much lower $\langle \dot{q}''_{max} \rangle$ (approximately half). Using the magnitude of heat flux as a prediction of change in efficiency does not work well.

The agreement between the location of $\langle \dot{q}''_{max} \rangle$ and location of $\Delta AHHH_{max}$ in figure 5.13 motivates investigating the spatial variation of heat flux at $\langle \dot{q}''_{max} \rangle$. Figure 5.15 shows contours of heat flux, $\dot{q}''$, at the crank angle, θ, where $\langle \dot{q}''_{max} \rangle$ occurs. Each row displays a different operating condition (top row condition 1, middle row condition 2 and bottom row condition

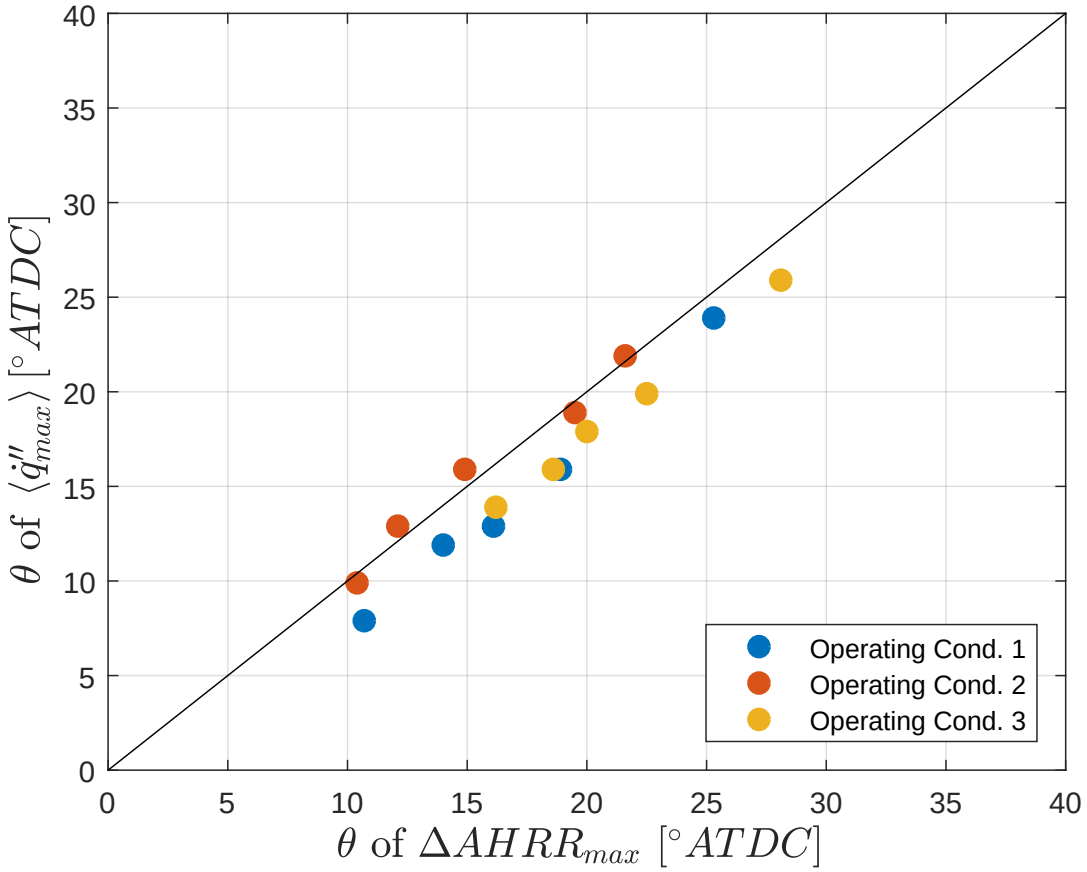


Figure 5.13: Operating conditions 1, 2 and 3 comparison of location of $\langle \dot{q}''_{max} \rangle$ to location of $\Delta AHHH_{max}$

3). Each of the columns shows a different SOI which are ordered from most advanced on the left (which showed an increase in $\Delta ITEg$) to most retarded on the right (which showed small changes in $\Delta ITEg$). The maximum values of $\dot{q}''$ for operating condition 1 are about half of conditions 2 and 3. The more advanced SOI cases on the left show a higher intensity of heat flux in the bowl (between gray lines) relative to the most retarded SOI cases on the right for that operating condition which have a more uniform spatial variation. This observation may suggest that the largest benefit from a TBC is realized in the piston bowl region at conditions where heat flux is largely contained in the bowl.

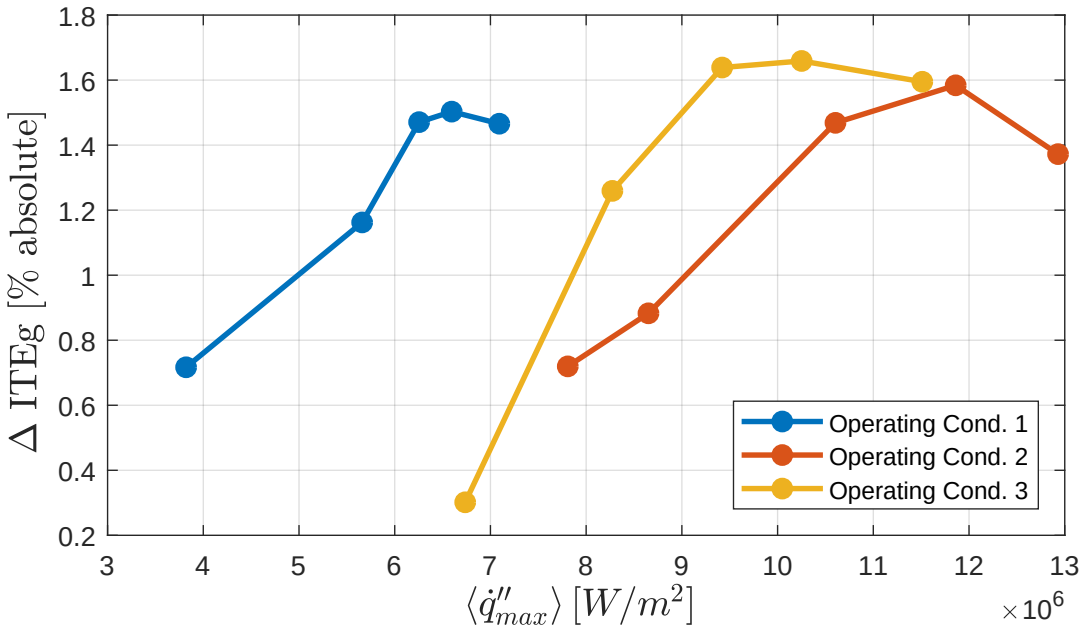


Figure 5.14: Operating conditions 1, 2 and 3 comparison of change in ITEg as function of $\langle \dot{q}''_{max} \rangle$

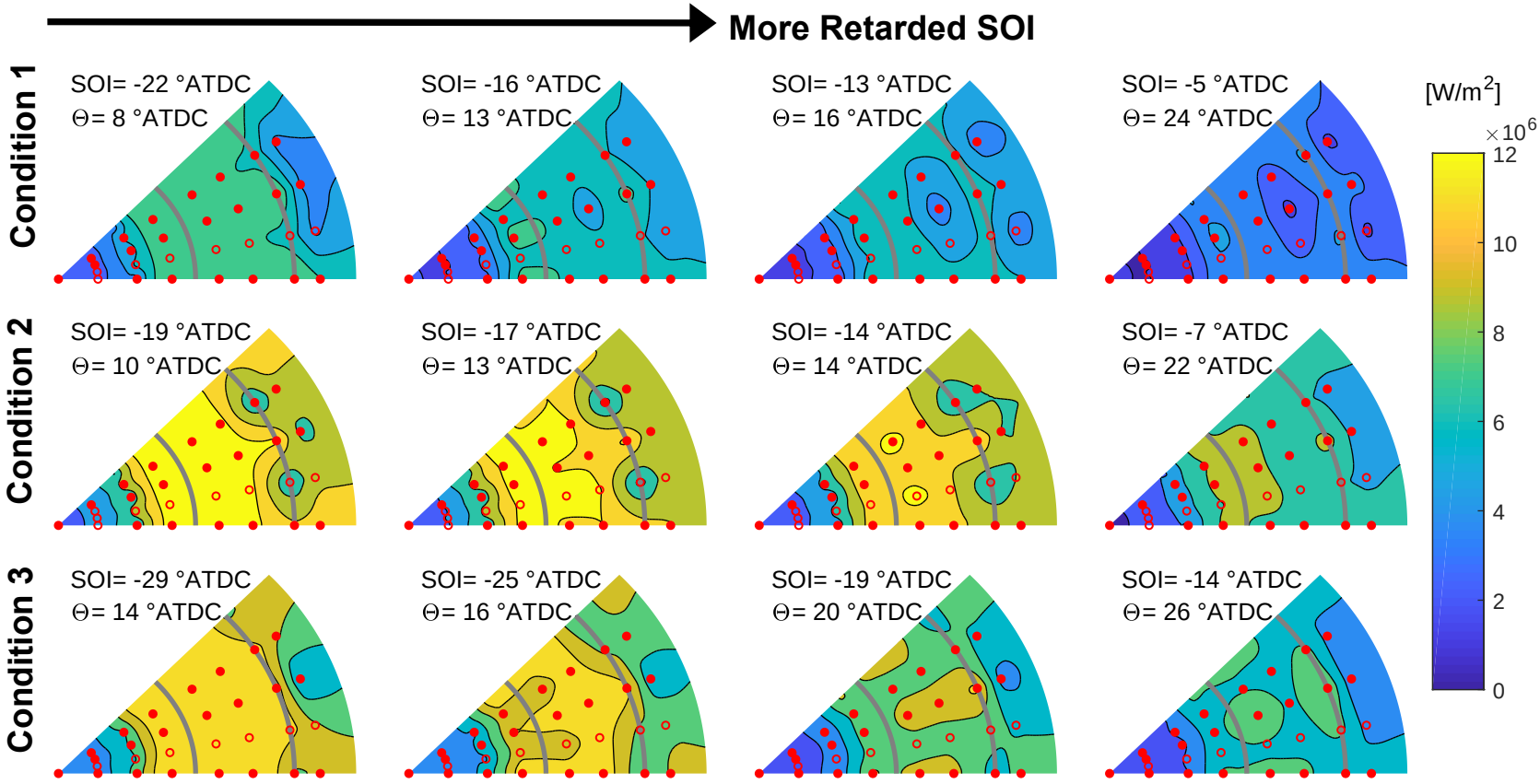


Figure 5.15: Operating conditions 1, 2 and 3 contours of heat flux at crank angle with maximum $\langle \dot{q}'' \rangle$

5.2.2 Very High-Output: Operating Conditions 4 & 5

Operating conditions 4 and 5 represent very high-output conditions of possible future diesel engines. These conditions differ from the previous operating conditions in that IMEPg is approximately 50 % higher than conditions 2 and 3. To achieve these loads, the injection duration was increased which resulted in end-of-injection timings late into the expansion stroke, resulting in significantly longer burn durations as shown in figures 5.16 and 5.18.

Figures 5.16 and 5.17 show results for operating condition 4. Overall, the effect of any of the TBCs was smaller than for operating conditions 1-3 and was often near the limits of the error bars. Similar to the standard output conditions, FSN trended higher for some of the SOI timings when comparing as-sprayed TBCs to the metal baseline. This effect was exaggerated for SOI timings that previously trended higher for the metal baseline (see local maximum around -6 to -8 °ATDC in bottom plot figure 5.17). For the more advanced injection timings ITEg increased slightly for the polished TBC when compared to the metal and as-sprayed TBCs. For the same injection timings the increase in ITEg corresponded with a reduction in $\dot{Q}_{gas}$. The trend in ITEg and $\dot{Q}_{gas}$ reduced as injection timing was retarded.

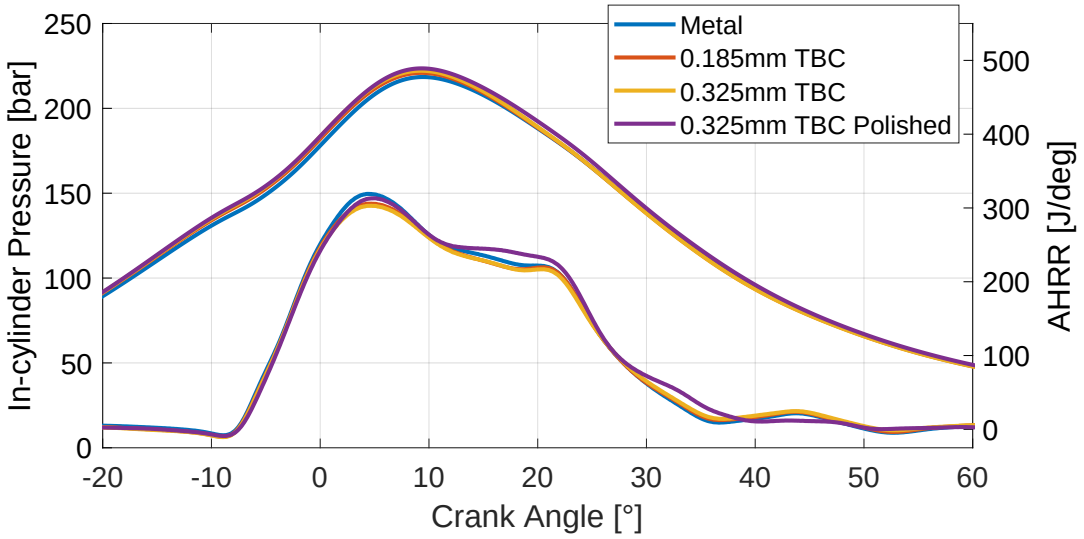


Figure 5.16: Operating condition 4 (1700 rpm, 30.3 bar IMEPg) in-cylinder pressure and AHRR for SOI timing of -12 °ATDC

Figures 5.18 and 5.19 show results for the highest power output case, operating condition 5. This condition has an extremely long injection duration with positive AHRR extending beyond 60 °ATDC. Because of this, the in-cylinder thermodynamic conditions are significantly changing through the combustion event; pressure alone is changing by a factor of greater than four from the time of peak pressure to 60 °ATDC. The AHRR exhibits a speed-up near 35 °ATDC that corresponds roughly with the end of injection event.

Condition 5 does not show statistically significant changes to ITEg or $\dot{Q}_{gas}$ for any of the TBC pistons tested, but does show a trend of increased FSN for as-sprayed 0.185 and 0.325 mm TBC pistons. A change in late-cycle heat release was also visible when comparing the polished TBC to the other pistons; additional AHRR between 10-30 °ATDC was observed but fluctuations above and below the metal baseline make it unclear if the instantaneous heat transfer or the combustion process are being changed by the polished TBC.

When looking at both very high-output cases, the impact of TBCs on ITEg, $\dot{Q}_{gas}$ and FSN was minimal. The long injection duration for these operating conditions may reduce the impact a piston TBC has on these parameters. Specifically, injector spray targeting for these conditions may direct high temperature gas away from the piston surface limiting its impact. Further investigation using an injector with a larger flow area may allow the combustion event to be tailored in a way where fuel injection was better contained within the piston bowl to allow this hypothesis to be tested.

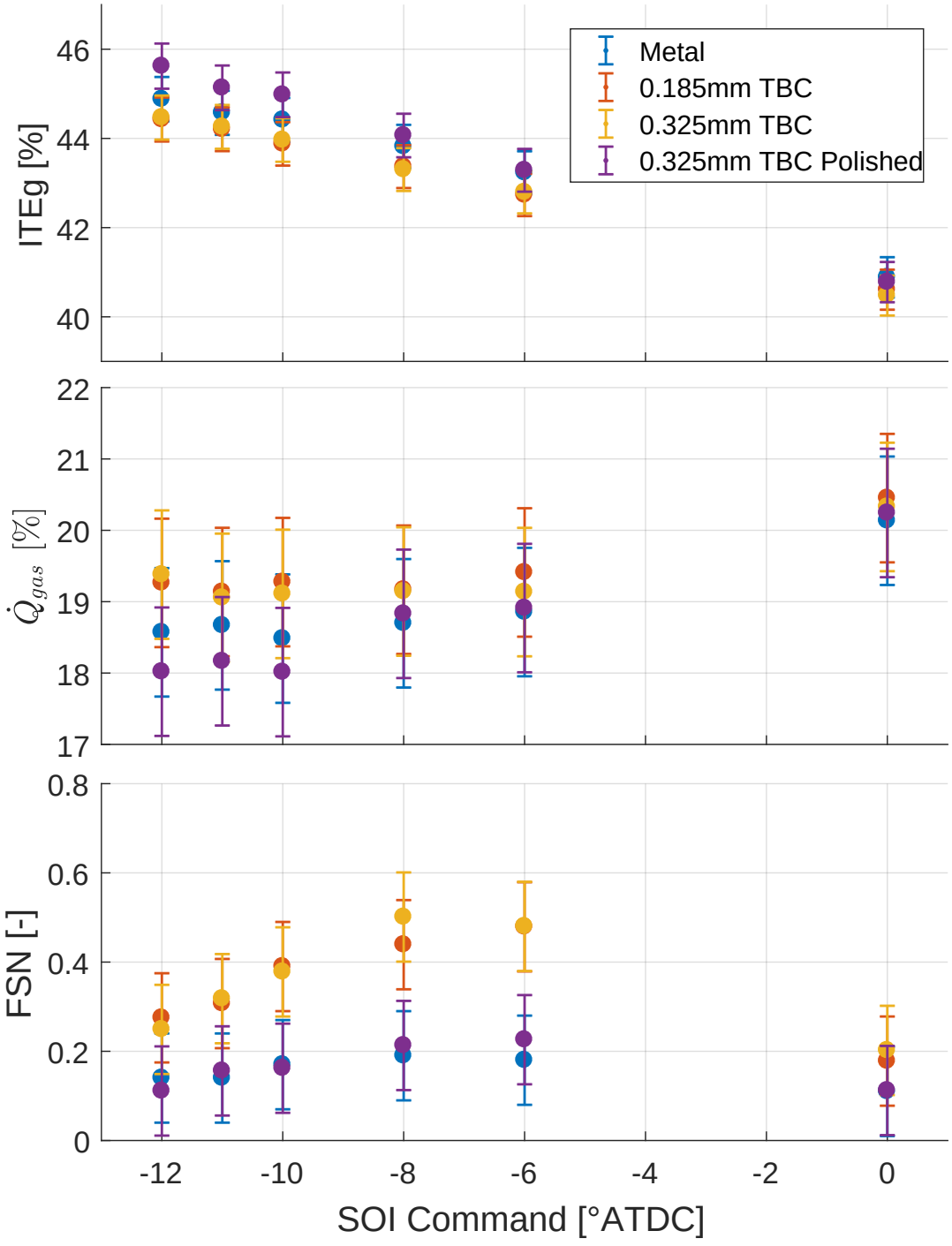


Figure 5.17: Operating condition 4 (1700 rpm, 30.3 bar IMEPg) ITEg, $\dot{Q}_{gas}$ and FSN

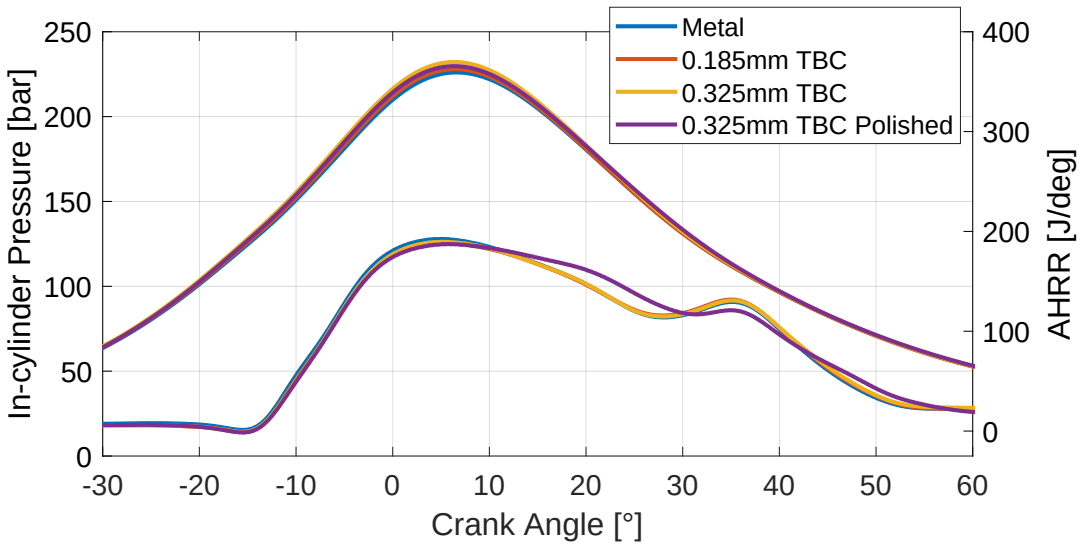


Figure 5.18: Operating condition 5 (2750 rpm, 29.7 bar IMEPg) in-cylinder pressure and AHRR for SOI timing of -21 °ATDC

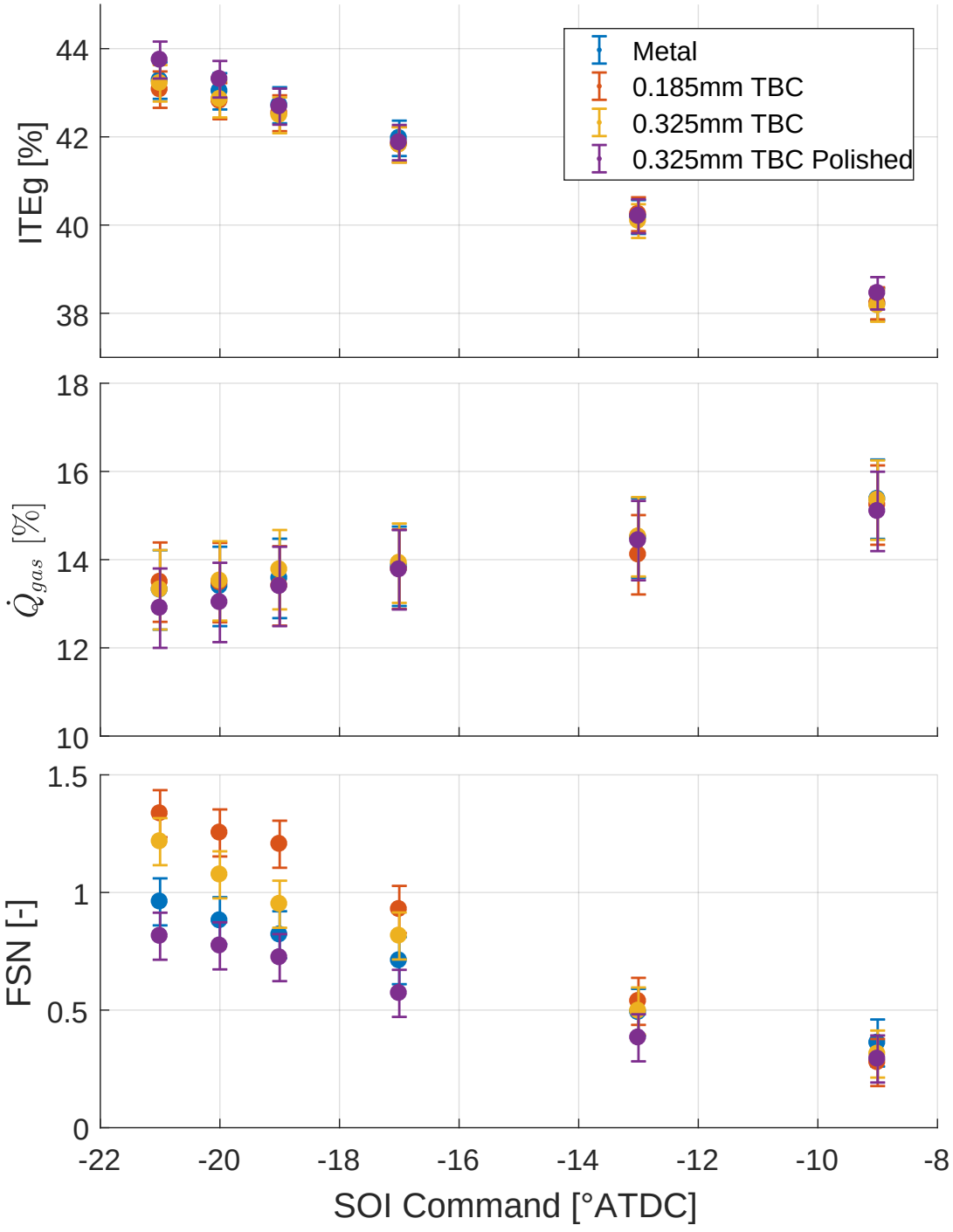


Figure 5.19: Operating condition 5 (2750 rpm, 29.7 bar IMEPg) ITEg, $\dot{Q}_{gas}$ and FSN

5.2.3 Rated Power Heat Transfer

The maximum heat rejection of an engine, in units of power, typically occurs at the maximum brake power output condition, rated power, becoming the design constraint on the system. Minimizing engine heat rejection, specifically $\dot{Q}_{global}$, normalized by $\dot{W}_b$ on a multi-cylinder engine will lead to vehicle integration benefits by reducing radiator size and cooling fan power. The previous discussion on the challenges of using $\dot{Q}_{global}$ on a single-cylinder engine have motivated presentation of a second dimensionless value of $\dot{Q}_{gas}/\dot{W}_{i,g}$ which should be a better representation of *in-cylinder* heat transfer and more applicable to a single-cylinder engine.

The two normalized heat transfer metrics for operating conditions 3 and 5 are shown in figures 5.20 and 5.21, respectively. Both normalized metrics show similar trends for the operating conditions presented; the major difference between them was in magnitude.

Figure 5.20 shows higher normalized heat transfer for the two as-sprayed TBCs when compared to the metal baseline for the $\dot{Q}_{global}/\dot{W}_b$ metric. The polished TBC shows a lower value of $\dot{Q}_{gas}/\dot{W}_{i,g}$ for the more advanced timings. A local minimum for all pistons tested was found near an SOI command of -21 °ATDC, which was slightly shifted from the maximum ITEg timing of -25 °ATDC (see figure 5.11) for this operating condition.

Figure 5.21 shows that there are no statistically significant differences in normalized heat transfer observed for any of the pistons at operating condition 5. The most advanced SOI timing showed the lowest values and was also the location of highest ITEg; excessive peak in-cylinder pressure prevented earlier injection timings. If timing was able to be advanced further, a local minimum similar to that observed in figure 5.20 would be expected. Additionally, when comparing normalized heat transfer for the two operating conditions, the high-output condition has a lower minimum value. These observations may be attributed to the very long injection duration and long AHRR for condition 5. The long injection duration leads to spray targeting outside the piston bowl where piston heat transfer may have less of an impact. Additionally, a significant portion of the injection event occurs later in the expansion

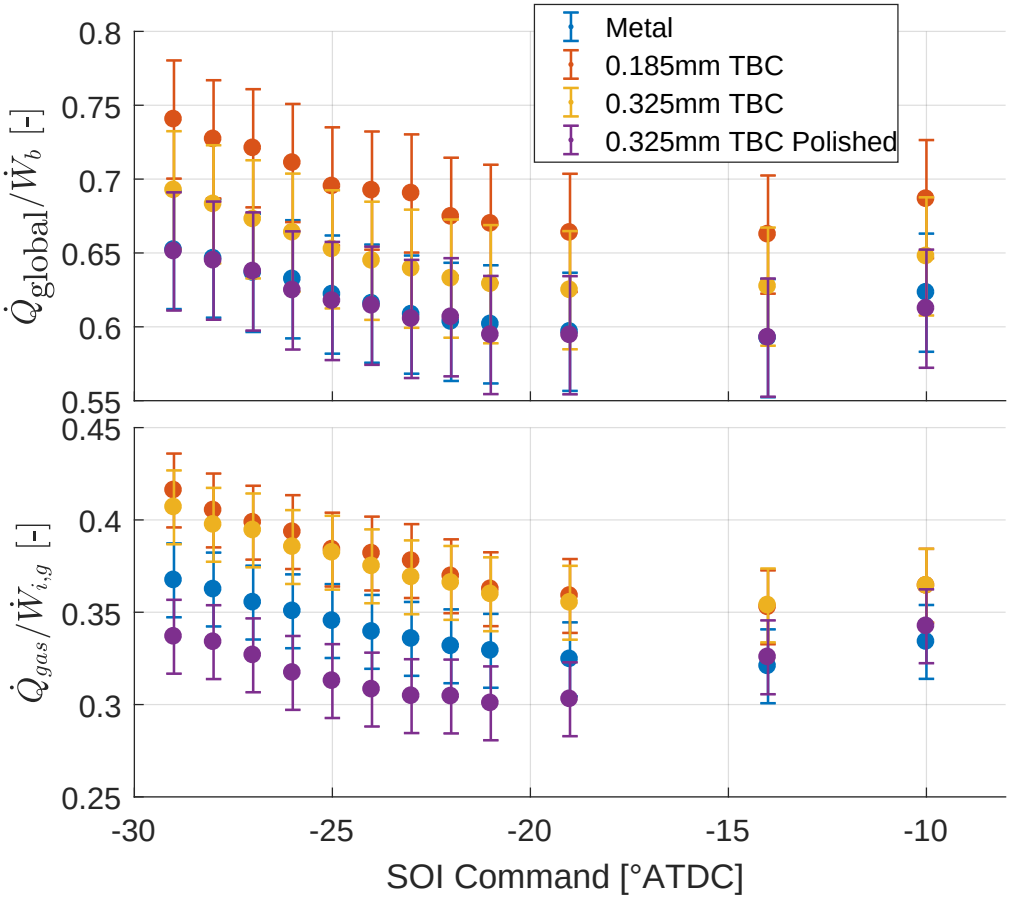


Figure 5.20: Operating condition 3 (2500 rpm, 20.3 bar IMEPg) normalized heat transfer

stroke where the in-cylinder pressure is rapidly falling which may contribute to reduced heat transfer.

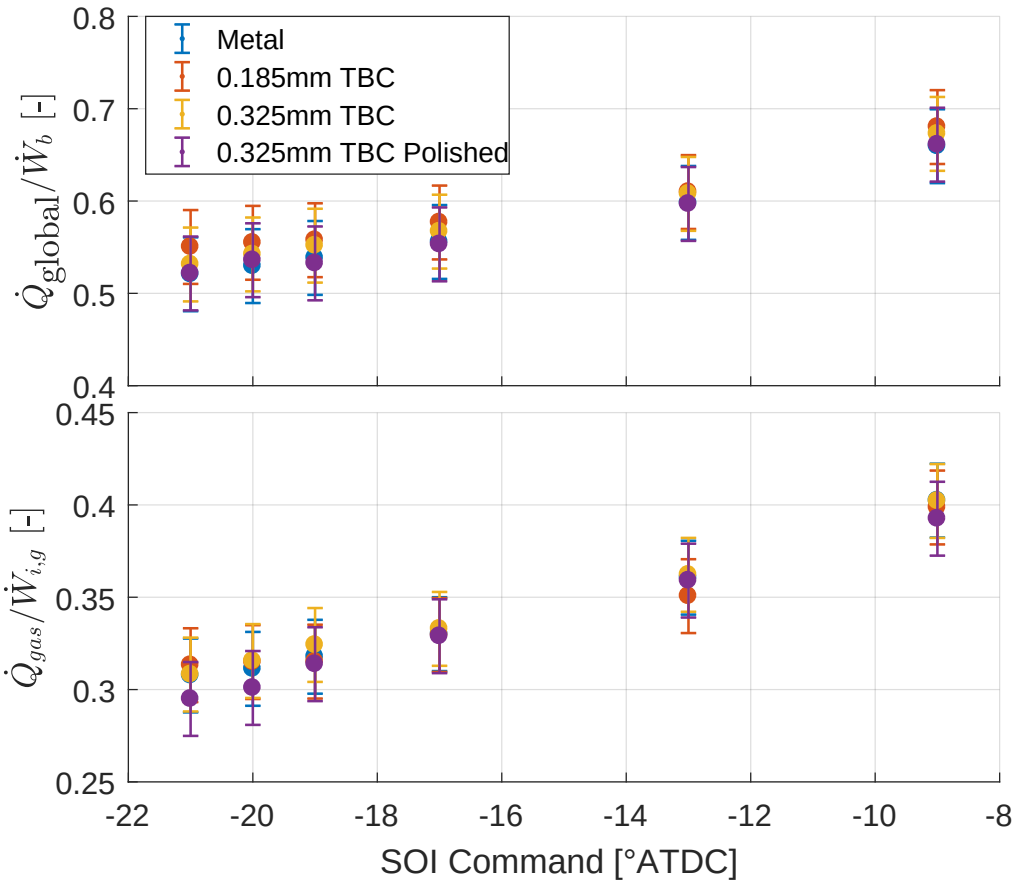


Figure 5.21: Operating condition 5 (2750 rpm, 29.7 bar IMEPg) normalized heat transfer

5.3 Summary and conclusion

In this work, the impact of TBC thickness and surface roughness was investigated under very high-output diesel operating conditions. TBCs were applied to the piston crown of a single-cylinder research engine, with results compared to a metal piston baseline. An SOI sweep was conducted for five operating conditions, and in-cylinder pressure and AHRR along with exhaust emission measurements were analyzed to understand global engine behavior. From this work the following observations and conclusions are drawn:

1. The heat transfer normalized by power for the very high-output conditions (4 and 5) showed statistically insignificant differences between any of the TBCs or the metal baseline. Similarly, no statistical change in ITEg or $\dot{Q}_{gas}$ was observed for either of these cases. For both of these operating conditions a very long injection duration was used that causes a portion of the spray targeting to be outside the piston bowl, potentially reducing the impact the TBCs have on heat transfer.

2. The *polished* TBC showed an increased ITEg when compared to the metal baseline for operating conditions 1-3, which are representative of traditional engine loads, at SOI timings near maximum ITEg. Increases in ITEg corresponded with additional late-cycle AHRR and a reduction in $\dot{Q}_{gas}$. For retarded SOIs, no change between any of TBCs and metal baseline was observed. The additional late-cycle AHRR corresponded with the crank angle of maximum spatially averaged piston heat flux (metal piston). Contours of piston heat flux at these crank angles may suggest that the change in ITEg is related to the heat flux in the piston bowl.

3. The *rough* (as-sprayed) TBCs for operating conditions 1-3 showed, in reference to the metal piston, showed no statistically significant change in ITEg or $\dot{Q}_{gas}$. A slight (sometimes not statistically significant at retarded SOI) increase in ITEg was observed when comparing the polished 0.325 mm TBC to either of the two as-sprayed TBCs. The polished 0.325 mm TBC also had a lower $\dot{Q}_{gas}$ when compared to either the 0.325 mm as-sprayed or 0.185 mm as-sprayed TBC pistons.

4. For most cases, pistons with higher surface roughness TBCs showed increased exhaust smoke when compared to the metal baseline. This effect was most pronounced at retarded SOI timings that had elevated FSN. When the coating was polished, the FSN for all operating conditions and SOI timings was similar to the metal baseline and less than the as-sprayed coating. It is possible that the increased surface roughness of the

TBC impacted the spray mixing process, causing local increases in equivalence ratio and subsequently additional engine-out smoke.

5. For all operating conditions and SOI timings, incomplete products of combustion (CO and HC) were low with η_c greater than 99 %. Overall the dominant trend in NO_x was related to the SOI timing and was not impacted by the higher wall temperature with TBCs. Additionally, no significant combustion phasing change was observed at constant SOI for all the TBC pistons.

6. Although this work focused on performance evaluation, a practical observation was that none of the TBCs tested had visually observable durability issues despite the high-output operating conditions tested.

6 Engine Heat Transfer Correlation for High-output Operating Conditions

The chapter will focus on developing an instantaneous spatially averaged heat transfer correlation. Data from Chapter 4 using Co-axial Metal 1 and Co-axial Metal 2 pistons (nomenclature from table 3.7) will be used; specifically, spatially averaged heat flux, $\langle \dot{q}'' \rangle$, and spatially averaged piston temperature, $\langle T_{piston} \rangle$, will be used in calculating a heat transfer coefficient. Different functional forms of instantaneous spatially averaged heat transfer correlations will be explored and compared to the experimental data.

6.1 Motivation based on Experimental Data

Instantaneous spatially averaged heat transfer correlations developed to date are typically based on the non-dimensional Reynolds analogy of boundary layer theory: $Nu = CRe^m$ where C and m are empirical constants. Spatially averaged heat flux, $\langle \dot{q}'' \rangle$, which was calculated for a range of operating conditions (see Chapter 4), was used to estimate an instantaneous, spatially averaged heat transfer coefficient:

$$\langle h \rangle = \frac{\langle \dot{q}'' \rangle}{T - \langle T_{piston} \rangle} \tag{6.1}$$

Initially, plotting Nu as function of Re may provide some understanding of the functional dependence. Both Nu and Re require a length scale to be defined; which for this analysis is taken as the engine bore, B. Ideal gas properties of air are used for conductivity, k, and dynamic viscosity, μ, and will be defined in Section 6.4.2.1. The spatially averaged heat transfer coefficient, $\langle h \rangle$, is used to find Nu which is written as:

$$\langle Nu \rangle = \frac{\langle h \rangle B}{k} \tag{6.2}$$

The $\langle\ \rangle$ braces are used for $\langle h \rangle$ and $\langle Nu \rangle$ to again emphasize that they are calculated based on values that were spatially interpolated and averaged.

Reynolds number includes density, ρ, which was found using the ideal gas law with measured in-cylinder and temperature estimated based on closed-cycle analysis. For an engine, characteristic velocity, v, is most challenging to define. The complex in-cylinder flow-field is established by the intake port geometry and piston motion. Additionally, engines are run over a range of speeds, which introduces an additional dynamic that may need to be considered. A range of definitions for v can be found in the literature [17, 42, 96] but for this initial analysis the simplest form, the mean piston speed, $\bar{S_p}$, was taken.

The definition for Re can now be given:

$$Re = \frac{\rho v B}{\mu} \tag{6.3}$$

Figure 6.1 shows $\langle Nu \rangle$ as a function of Re for engine operating conditions 1, 2, 3 and 5. Operating condition 4 and intake manifold temperature (IMT) sweep for condition 3 were not used in the heat transfer correlation development due to thermocouple failures, see Section 4.3. These two additional data sets were used later for correlation validation with knowledge that the uncertainty in the data was higher. Each of the plots in figure 6.1 include data for a start of injection (SOI) sweep. Each of the lines can be followed starting in the bottom left, which is -40 °ATDC, in a counter-clockwise direction through the cycle to 100°ATDC (see top plot for direction), which again is the bottom left of the figure. The open circle marker on the figures denotes the start of combustion (SOC), and the $\times$ marker denotes the end of combustion (EOC). The SOC is defined as the first crank angle with AHRR $>$ 10 J/°; EOC is defined as the crank angle of 90 percent burn. Linear axes were chosen to make the counter-clockwise path clear even though log axes would better highlight a power-law dependence.

Overall the operating conditions show similar trends each with three distinct regions: before SOC, during combustion and after EOC; each with a unique slope as shown in operating

condition 2 of figure 6.1. Additionally the most advanced SOI typically shows the maximum $\langle Nu \rangle$ and Re. A somewhat linear trend is seen before SOC and after EOC but during the combustion event a unique power-law dependence of $\langle Nu \rangle$ on Re was not observed. These figures show that for an engine, the $Nu = CRe^m$ formulation may be an oversimplification of a more complex phenomenon.

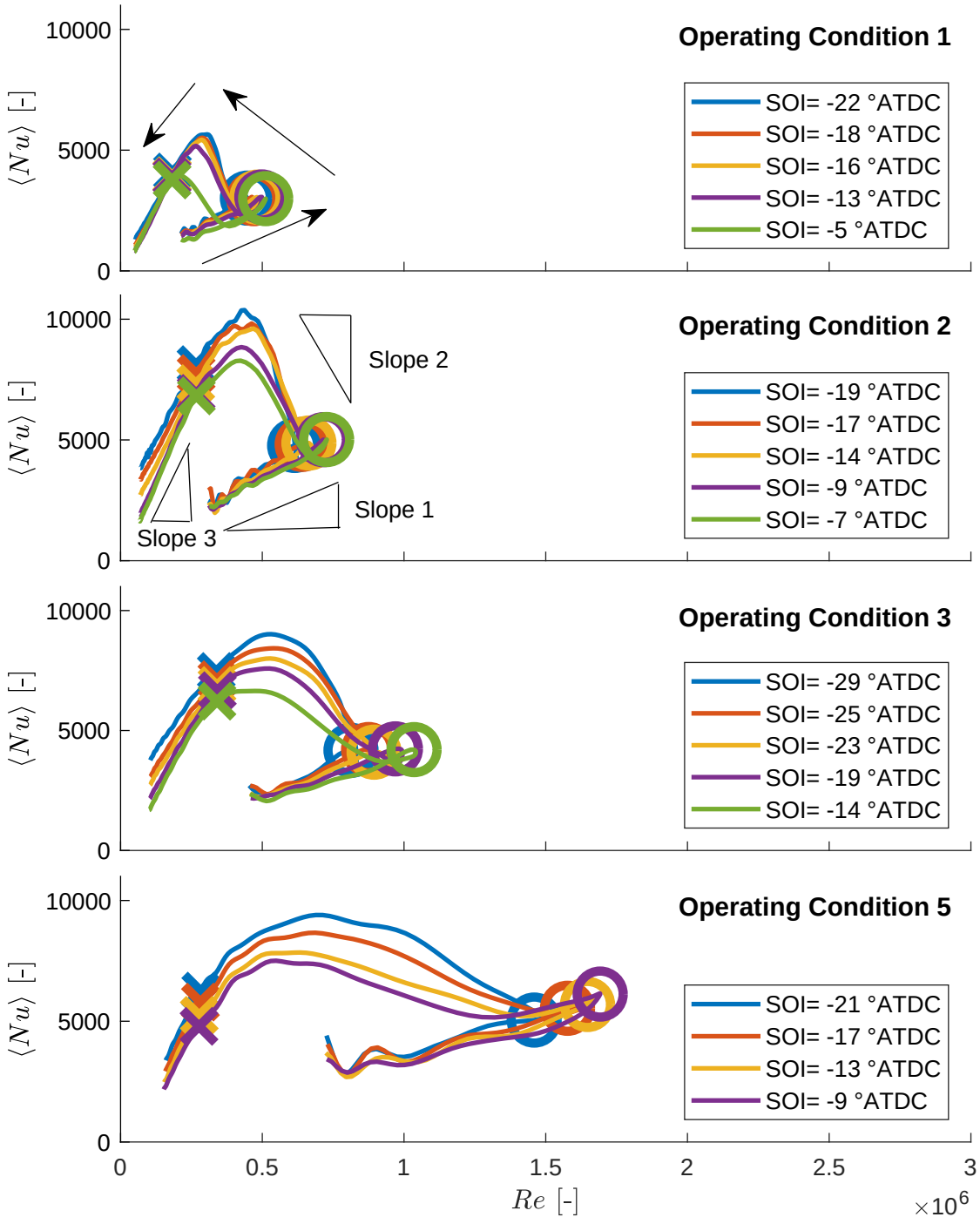


Figure 6.1: Operating conditions 1, 2, 3 and 5 $\langle Nu \rangle$ as a function of Re using mean piston speed as velocity (open circle markers show SOC and $\times$ markers show EOC). In general, the trajectory follows a counterclockwise path.

6.2 Dimensional Analysis

Dimensional analysis can be used to explore the functional form that governs the convective heat transfer process in an engine. For time-varying spatially averaged correlations a *quasi-steady* assumption at each crank-angle, θ, must be made which means a heat transfer coefficient is independently generated for each θ. Applying dimensional analysis requires judicious selection of variables. A similar analysis by Heywood [41] provides some understanding of the impact of variable selection on the final non-dimensional form. For this analysis the heat transfer coefficient, h, is considered the dependent variable. Engine bore, B, and axial cylinder length (*i.e.*, distance from piston crown to cylinder head), z, which varies with θ, are included as geometric variables. In-cylinder gas properties conductivity, k, dynamic viscosity, μ, specific heat, c_p, and density, ρ are considered the important gas properties for the analysis. A characteristic velocity, v and temperature, T, are included and represent the average in-cylinder flow and temperature conditions. The chemical energy release rate per unit volume $\dot{q}_{ch}$ and engine speed, N are engine operating specific variables that may impact the heat transfer. Equation 6.4 shows that the $j = 11$ selected variables can be written as a function and set equal to zero.

$$f(h, B, z, k, \mu, c_p, \rho, v, T, \dot{q}_{ch}, N) = 0 \tag{6.4}$$

Dimensional analysis based on the Buckingham Pi theorem states that a dimensionally homogeneous equation of j variables can be reduced to a relationship of $j - r$ independent dimensionless products where r is the number of reference dimensions required to describe the variables. For the case shown in equation 6.4, $r = 4$ with mass, length, time, and temperature taken as the independent dimensions. Equation 6.5 shows seven resulting non-dimensional groups:

$$f\left(\frac{hB}{k}, \frac{\rho v B}{\mu}, \frac{c_p \mu}{k}, \frac{c_p T}{v^2}, \frac{NB}{v}, \frac{z}{B}, \frac{\dot{q}_{ch}}{\rho c_p N T}\right) = 0 \tag{6.5}$$

The first three terms of equation 6.5 can be recognized as the well known Nusselt, Reynolds and Prandtl numbers, respectively. c_pT/v^2 is similar to the Mach number because c_pT is proportional to the sound speed squared ($c^2 = \gamma RT \propto c_pT$). For engine flows the velocity is typically much less than the speed of sound and it can be assumed the dependence on c_pT/v^2 is minimal therefore the term can be eliminated. Similarly the Prandtl number dependence is small over the range of temperatures and pressures expected in an engine and can be omitted.

If v is taken as the mean piston speed, $\bar{S}_p$, and $\bar{S}_p = 2LN$, NB/v becomes half the bore/stroke ratio, $B/2L$ which is a geometric feature of an engine. It should be noted that many heat transfer correlations, including the one proposed as part of this work, use a more complex interpretation of v so strictly speaking this assumption is only useful for theoretical development. The z/B term is also identified as a function of engine geometric features.

The final remaining term of equation 6.5, $\dot{q}_{ch}/\rho c_p NT$, is related to the combustion event. $\dot{q}_{ch}$ in the numerator is positive and non-zero only during a portion of the cycle when the combustion event is taking place. ρ, c_p, and T in the denominator all change as a function of the in-cylinder conditions.

The non-dimensional groups can thus be restated as:

$$f\left(\overbrace{\frac{hB}{k}}^{Nu}, \overbrace{\frac{\rho v B}{\mu}}^{Re}, \overbrace{\frac{B}{L}, \frac{z}{B}}^{Geometry}, \frac{\dot{q}_{ch}}{\rho c_p NT}\right) = 0 \tag{6.6}$$

Equation 6.6 includes the Nu, Re, two engine geometry terms and $\dot{q}_{ch}/\rho c_p NT$. Previous engine heat transfer correlations have been based on correlations of turbulent flow in pipes and fit the basic functional form: $Nu = CRe^m Pr^n$ with various definitions for length, velocity and gas properties. Most correlations drop the Pr dependence and experimentally find a best fit for m. The engine geometry terms become part of the leading constant C and are expected to change for different engine configurations. For all the existing correlations reviewed, $\dot{q}_{ch}/\rho c_p NT$ has been eliminated without further justification. The lack of dependence of power-law Nu on Re during the combustion event (see figure 6.1), and the identification of

$\dot{q}_{ch}/\rho c_p NT$ in the dimensional analysis, supports investigation into inclusion of $\dot{q}_{ch}/\rho c_p NT$ in a heat transfer correlation.

6.3 Comparison of Existing Heat Transfer Correlations to Experiments

To establish a baseline level of performance the commonly cited Woschni correlation [96] was used to generate temporally varying heat transfer coefficients and compared to experimental results, $\langle h \rangle$. The Woschni correlation is given by:.

$$h = C_3 B^{m-1} P^m T^{0.75-1.62m} v^m \tag{6.7}$$

with velocity defined by:

$$v = C_1 \bar{S}_p + C_2 \frac{V_d T_r}{P_r V_r}(P - P_m) \tag{6.8}$$

where $C_1 = 2.28 + 0.308 \cdot \text{swirl}$ and V_d is displacement volume, and the sub-script r is for a known reference point in cycle, such as IVC. $P - P_m$ is the difference between the in-cylinder pressure during combustion and motoring.

Table 6.1 shows the values of the constants (from Heywood [41]) used for this initial case (correlation 1). This table was used to organize further correlation development including an optimized Woschni correlation, and a new heat transfer correlation. Tabulated values in table 6.1 include the equation number, constants (C_1-C_7, and m), the average error, ϵ, (see equation 6.9) and comments on the correlation to help summarize the finding of this section. The dashed line on figures 6.2-6.5 shows the results of Woschni (correlation 1) for two injection timings at the four different operating conditions.

Overall the Woschni correlation does a poor job predicting h. For all the cases the maximum value of h is less than $\langle h \rangle$ and the portion of the expansion stroke after the peak of

h is severely underestimated for all operating conditions. For figure 6.3, which has the lowest engine speed (1500 rpm) of all operation conditions, the location of maximum h and $\langle h \rangle$ match relatively well. As engine speed is increased to 1700 rpm for operating condition 1 (see figure 6.2), then further for operating conditions 3 and 5 (see figures 6.4 and 6.5) a phasing issue develops with h. In the two higher speed cases h peaks earlier than $\langle h \rangle$. The phasing between h and $\langle h \rangle$ is worse at retarded injection timing. Some of later injection events, such as SOI = -9 °ATDC in figure 6.5, show a local minimum in $\langle h \rangle$ before the maximum, which is not captured by h.

All the previous correlations developed, which were based on dimensional analysis, have dimensionless engine geometry terms that ultimately get included as experimentally calibrated constants. As such, it is implied that a limited amount of correlation tuning is required for different engine geometries. Using the functional form of the Woschni equation a new set of constants (see correlation 2 table 6.1) were generated by minimizing the least squares error between h and $\langle h \rangle$. A detailed discussion of the method used to generate constants will be described in detail in Section 6.4.3. Not all constants should have geometric dependence included as part of the formulation, but to get the best fit, all constants were included in the optimization.

The dotted lines on figures 6.2-6.5 show the results of the optimized Woschni correlation (correlation 2). On average the optimized Woschni correlation is a better fit when average error, ϵ, is compared: 1353 W/m^2-K for correlation 1 compared to 741 W/m^2-K for correlation 2. The mean error is defined by:

$$\epsilon = \sum_{\theta=\theta_1}^{\theta_n} |h - \langle h \rangle| \tag{6.9}$$

which is calculated for the θ in the range the constants were optimized (-40 to 100 °ATDC) and is also averaged across the 19 unique SOI / operating conditions combinations.

The same phasing problems that were observed in the base Woschni correlation are still observed in the optimized Woschni correlation. Because the coefficients were optimized across

a range of operating conditions some operating conditions now are overestimated (see figure 6.2) and other still underestimated (see figure 6.5). Operating condition 5 shown in figure 6.5, which has the highest speed and load, still shows a poor fit when the overall phasing between h and $\langle h \rangle$ is compared. Other authors [14, 16] have compared additional correlations but because they are generally limited to the function form of $Nu = CRe^m$ the resulting shape and phasing of h is similar to Woschni.

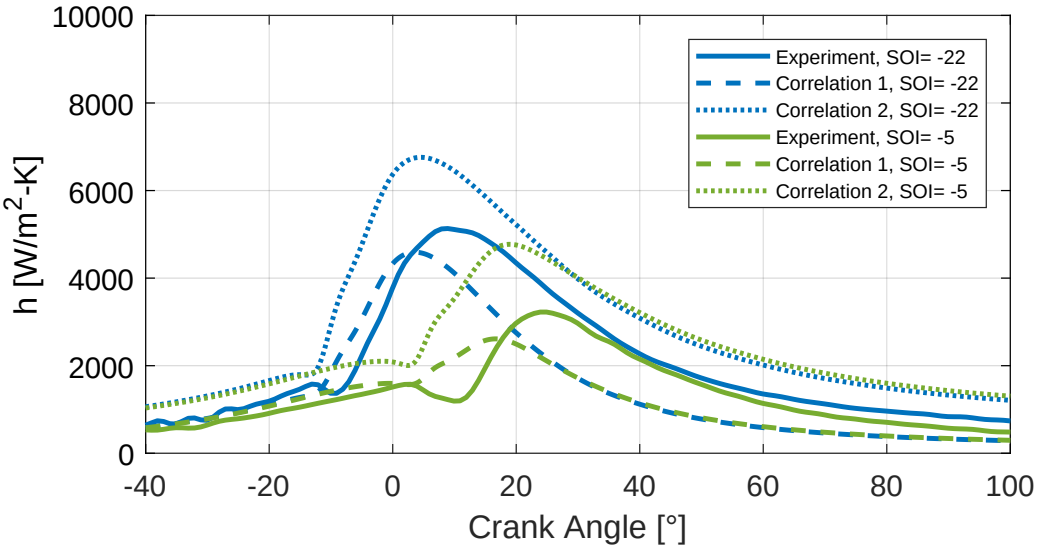


Figure 6.2: Operating condition 1 (1700 rpm, 12.3 bar IMEPg), SOI of -22 and -5 °ATDC, comparing experimental data $\langle h \rangle$, correlation 1 (Woschni), and correlation 2 (Woschni optimized)

Figure 6.6 shows $\langle Nu \rangle$ as a function of Re for engine operating conditions 1, 2, 3 and 5 using the definition of velocity from correlation 1 (Woschni, see equation 6.8). This figure shows the same experimental data ($\langle Nu \rangle$) as figure 6.1 using a different velocity definition for Re. Again, the open circle marker on the figures denotes SOC, and the $\times$ marker denotes EOC with engine cycle progressing in the counter-clockwise direction. Linear axes were chosen to make the counter-clockwise path clear. The power-law dependence of used in many correlations may be better displayed on a log-axis which would make the slope of the line

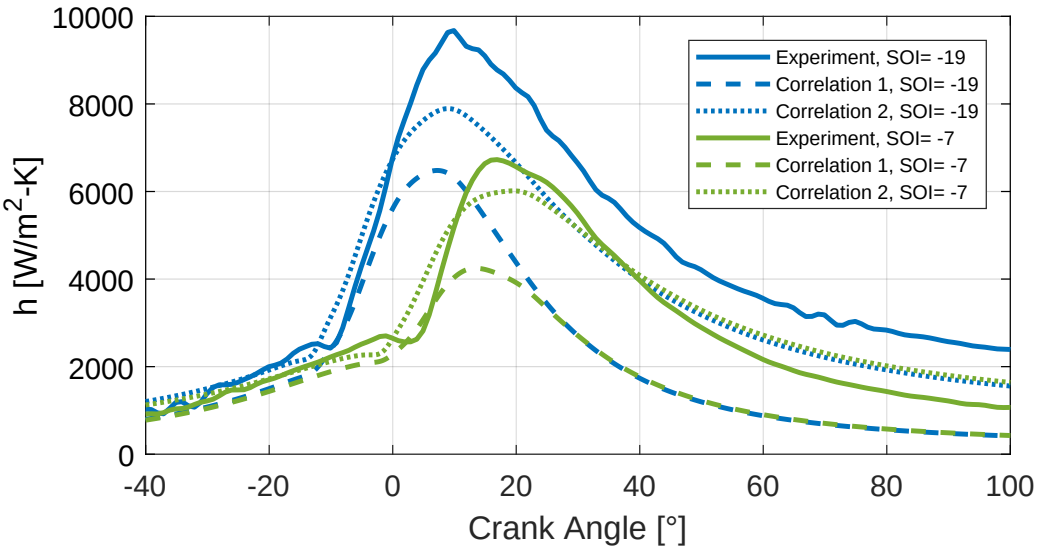


Figure 6.3: Operating condition 2 (1500 rpm, 23.8 bar IMEPg), SOI of -19 and -7 °ATDC, comparing experimental data $\langle h \rangle$, correlation 1 (Woschni), and correlation 2 (Woschni optimized)

equal to the exponent but because the exponent is typically chosen to be a value close to one, the power-law trend should be easily observed on a linear axis. The very abrupt change in trend that was observed at SOC in figure 6.1 is now somewhat smoothed out for operating conditions 1, 2 and 3 (top 3 plots figure 6.6); operating condition 5 still shows an abrupt change. Additionally, in figure 6.6 the slope of the data before SOC and after EOC are more similar to each other than figure 6.1, which should lend itself to better fitting of data to a $Nu = CRe^m$ power-law correlation. Despite the noted improvements to the data trends, all of the plots have significant scatter which makes finding a single set of correlation constants difficult.

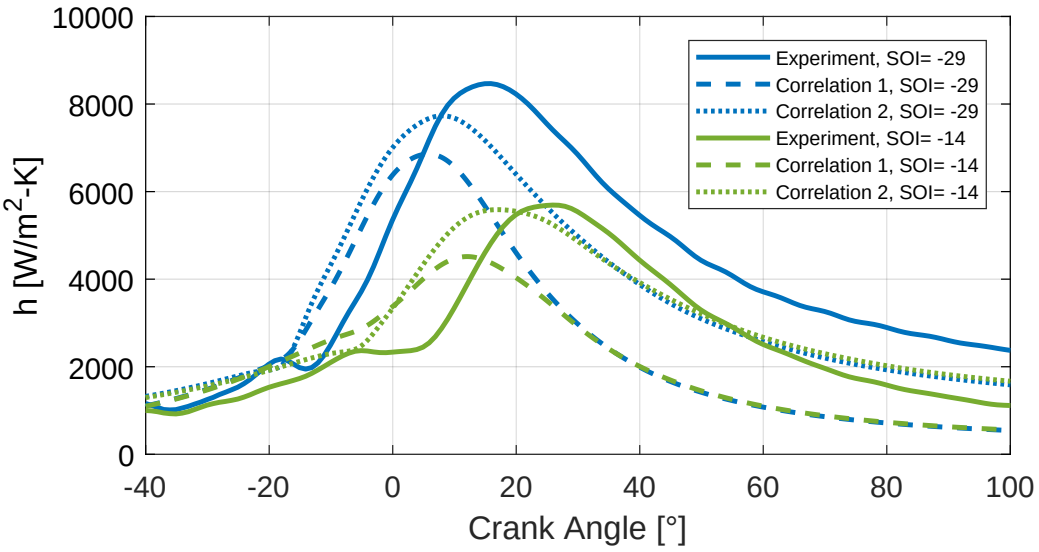


Figure 6.4: Operating condition 3 (2500 rpm, 20.3 bar IMEPg), SOI of -29 and -14 °ATDC, comparing experimental data $\langle h \rangle$, correlation 1 (Woschni), and correlation 2 (Woschni optimized)

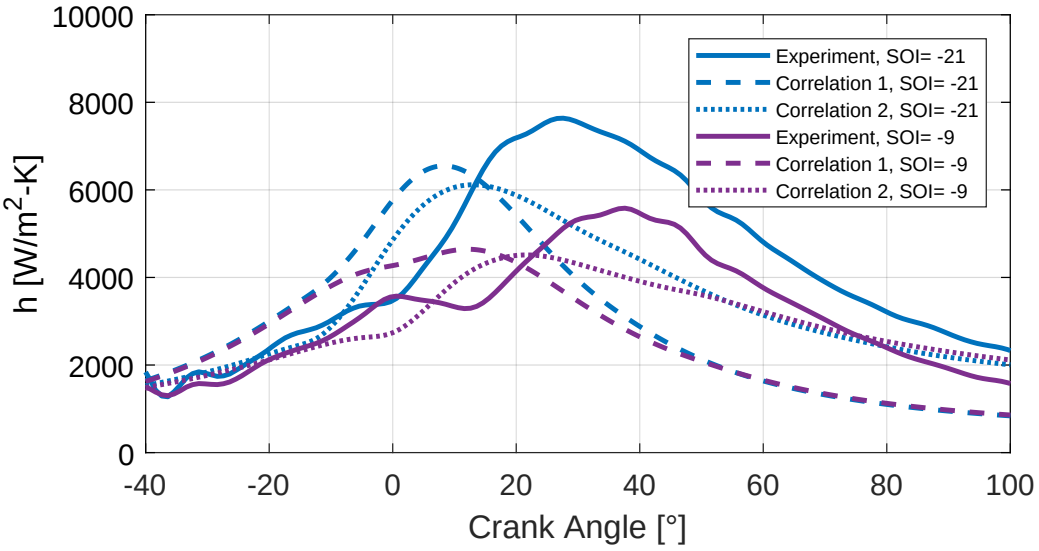


Figure 6.5: Operating condition 5 (2750 rpm, 29.7 bar IMEPg), SOI of -21 and -9 °ATDC, comparing experimental data $\langle h \rangle$, correlation 1 (Woschni), and correlation 2 (Woschni optimized)

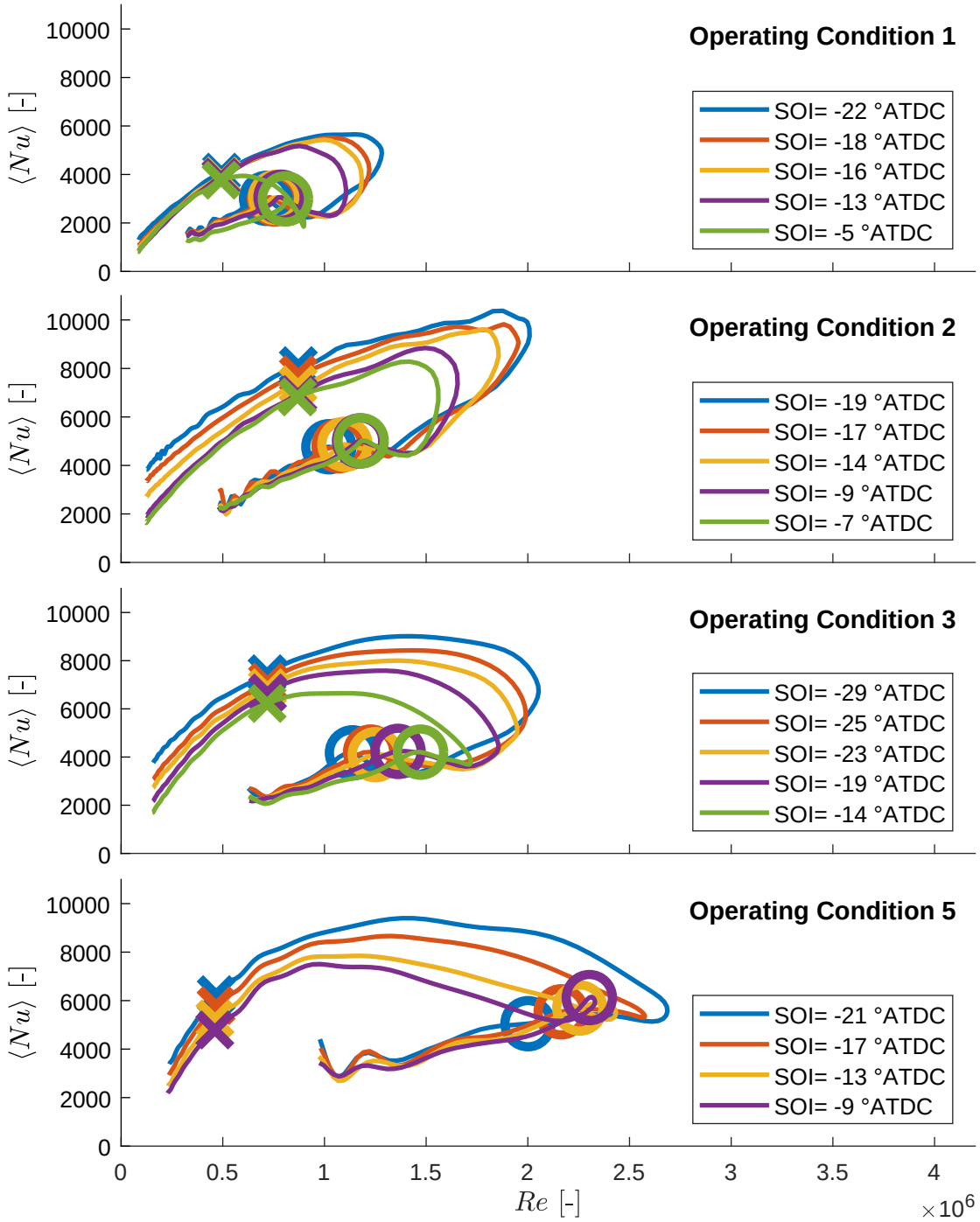


Figure 6.6: Operating conditions 1, 2, 3 and 5 $\langle Nu \rangle$ as a function of Re using velocity from correlation 1 (Woschni) (open circle markers show SOC and $\times$ markers show EOC)

6.4 Investigation into a New Heat Transfer Correlation

The shortcomings of the existing correlations motivated the need to evaluate the underlying assumption that Nu is only a function of Re for time-varying spatially averaged engine heat transfer correlations. The dimensional analysis conducted suggested the dimensionless term, $\dot{q}_{ch}/\rho c_p NT$, may need to be included the correlation. Additionally, the comparison of $\langle h \rangle$ to existing correlations showed the largest disagreement at the operating condition 5, which has the highest load and speed with a long injection event (40.5 crank angles). Because many other diesel engine phenomena are controlled by the injection event the fuel rate-of-injection (ROI) was included as a component of the Re velocity term. The use of both the ROI and $\dot{q}_{ch}/\rho c_p NT$ in a new heat transfer correlation was investigated in this section.

To evaluate equation heat transfer correlations a definition for v must be given:

$$v = C_4 \bar{S}_p + C_5 + C_6 e^{C_7(\theta - \theta_{EOI})} \int_{\theta_{SOI}}^{\theta} \frac{dm_{fuel}}{d\theta} d\theta \tag{6.10}$$

Equation 6.10 includes a number of different terms and constants; each are further evaluated (and some eliminated) in this section. Because an optimized set of coefficients was generated for each correlation, if a term has limited influence the coefficients will reflect that. Generally speaking, adding additional terms only helps improve the correlation fit compared to the input data due to additional degrees of freedom in the solution. The following terms were included: mean piston speed, $C_4 \bar{S}_p$, constant C_5, integrated fuel mass injection rate, $C_6 \int_{\theta_{SOI}}^{\theta} \frac{dm_{fuel}}{d\theta} d\theta$, which also includes an exponential decay, $e^{C_7(\theta - \theta_{EOI})}$, which begins decaying at the end of injection (EOI), to account for dissipation of the injected momentum. Before EOI C_7 is set to zero which means the exponential has no impact to velocity.

6.4.1 Proposed Dimensionless Form

The dimensionless form of the proposed heat transfer correlation is based on modification of the existing correlations in the form of: $Nu = CRe^m$. A new multiplicative term, $f(\dot{q}_{ch}/\rho c_p NT)$, refereed to hereafter as the combustion multiplier, is added to the correlation:

$$Nu = CRe^m f\left(\frac{\dot{q}_{ch}}{\rho c_p NT}\right) \tag{6.11}$$

Dimensional analysis does not provide the functional form of $f(\dot{q}_{ch}/\rho c_p NT)$ as such, a combination of engineering judgment and experimental data were used to develop the function.

6.4.2 Proposed Dimensional Form

The dimensionless form provides the most fundamental form of the correlation, but for practical engineering applications a dimensional equation with well-defined inputs is required. By substituting back the definition of Nu and Re and using the ideal gas law a dimensional form of equation 6.11 can be developed:

$$h = [CB^{m-1}\bar{R}^{-m}]v^m P^m T^{-m} k\mu^{-m} f\left(\frac{\dot{q}_{ch}}{\rho c_p NT}\right) \tag{6.12}$$

It is useful to further investigate $\dot{q}_{ch}/\rho c_p NT$. $\dot{q}_{ch}$ is the chemical energy release rate per unit volume and has SI units of [J/s-m^3]. Many engine-related phenomena occur in the crank-angle domain therefore it is common to calculate the apparent heat release rate (AHRR) with units of [J/°]. $\dot{q}_{ch}$ can be written in terms of AHRR, N, and V:

$$\dot{q}_{ch} = \frac{AHRR \cdot N \cdot 360}{V} \tag{6.13}$$

where $N \cdot 360$ is used to convert AHRR to units [J/s].

Substituting equation 6.13 for $\dot{q}_{ch}$ and using the Ideal Gas law, $\rho = P/\bar{R}T$:

$$\frac{\dot{q}_{ch}}{\rho c_p N T} \approx 360 \bar{R} \frac{AHRR}{P V c_p} \tag{6.14}$$

The approximate symbol, $\approx$, is used is used because AHRR is only an estimate for chemical energy release rate and has sensitivities associated with its calculation. Dimensionless chemical energy release rate is now given by definition:

$$\tilde{q}_{ch}[\text{-}] \equiv 360[^\circ] \bar{R}[\text{kJ/kg-K}] \frac{AHRR[\text{J}/^\circ]}{P[\text{Pa}] V[\text{m}^3] c_p[\text{kJ/kg-K}]} \tag{6.15}$$

Because AHRR is only a simplified estimate for the chemical energy release rate, at some crank angles AHRR can be slightly negative (*e.g.*, near SOI from evaporative cooling). Only positive values of $\tilde{q}_{ch}$ where considered and any negative values were set to zero. Figure 6.7 shows typical values of $\tilde{q}_{ch}$ for operating conditions 1-5 at the most advanced SOI. The shape of $\tilde{q}_{ch}$ as a function of crank angle is similar to the AHRR (see Section 4.3).

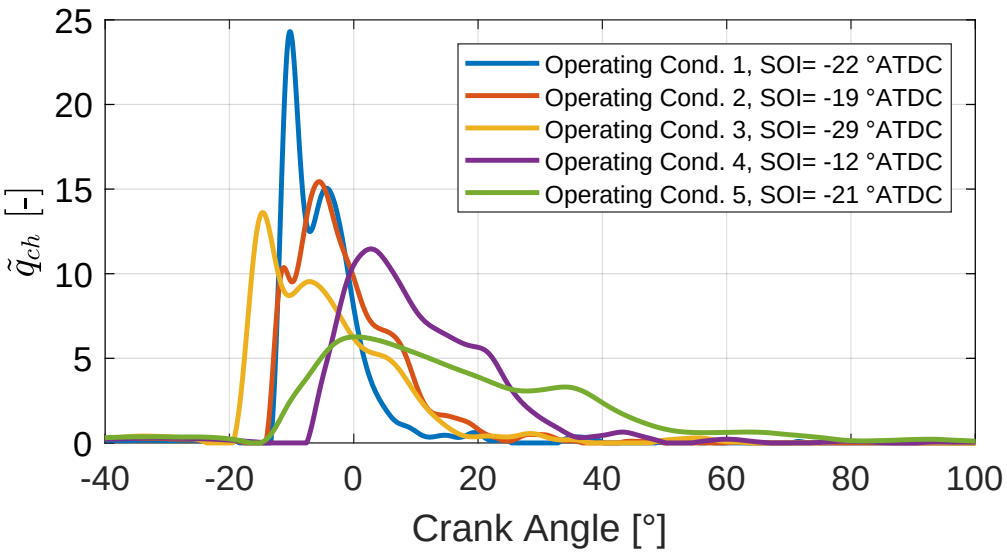


Figure 6.7: Operating condition 1-5, typical values of $\tilde{q}_{ch}$, most advanced SOI shown for each operating condition

The most retarded SOI from operating condition 3 (SOI= -14 °ATDC) is now shown in figure 6.8 which shows $\tilde{q}_{ch}$, measured heat transfer coefficient ($\langle h \rangle$) and h from correlation 2 (Woschni optimized) as a function of crank angle. The slight lag and decrease of h in the measurement (near -5 °ATDC) corresponds well with positive values of $\tilde{q}_{ch}$. As such, this motivates investigation into functions, $f(\tilde{q}_{ch})$, that attenuate h during portions of the cycle where $\tilde{q}_{ch}$ is positive.

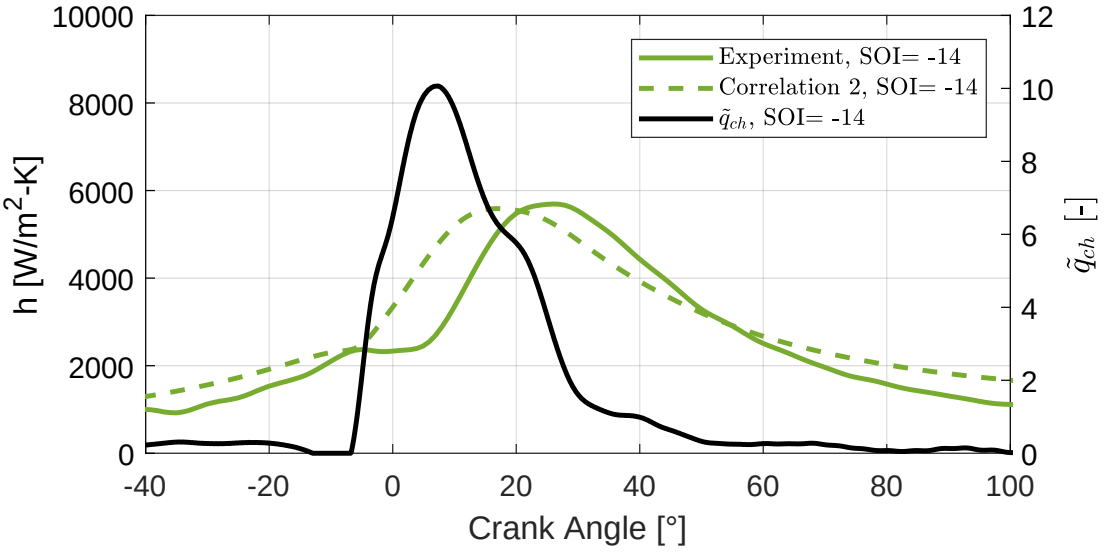


Figure 6.8: Operating condition 3 (2500 rpm, 20.3 bar IMEPg), SOI= -14 °ATDC comparing $\tilde{q}_{ch}$ to measured heat transfer coefficient, $\langle h \rangle$, and correlation 2 (Woschni optimized)

Substituting $\tilde{q}_{ch}$ back into 6.12 and combining the leading variables, $[CB^{m-1}\bar{R}^{-m}]$ into a single constant C_1:

$$h = C_1 v^m P^m T^{-m} k \mu^{-m} f\left(\tilde{q}_{ch}\right) \tag{6.16}$$

The dimensional analysis conducted requires definition of variables in units but does not specify exactly how each is interpreted in relation to measured engine parameters. Precise definitions for each of the non-constant terms must given. In-cylinder pressure is a widely

available measurement and captures the dynamics of the engine cycle and is used for definition of pressure. The instantaneous in-cylinder volume, V is calculated based on known geometric features of an engine and the measurement of crank position. In-cylinder temperature is non-uniform and cannot be directly measured; therefore an average in-cylinder temperature based on the ideal gas law, $T = PV/m_{trap}\bar{R}$ is used. Calculation of temperature is sensitive to in-cylinder trapped mass, m_{trap} but because the dynamics within the cycle are captured by P and V the relative change in T is accurate enough for use in the correlation. Similarly, AHRR is a calculated quantity, primarily based on in-cylinder pressure and volume, that has its own sensitivities based on definitions of gas properties. The definition and data processing details of P, V, T and AHRR were given in Section 3.1.

6.4.2.1 Gas Properties

Using properties of air, curve fits were generated for k, μ and c_p using Engineering Equation Solver (EES) [48]. EES has built-in functions for fluid thermodynamic and transport properties which have been compiled from many sources. For k and μ power-law curve fits in the range of 300-2000 K were generated as a function of temperature only. The real gas properties for k and μ in EES were implemented with the equations provided by Lemmon and Jacobsen [54]. Real gases allow variation in both temperature and pressure but because changes to k and μ are typically less than 5 percent over the pressure range of interest (for a fixed temperature), pressure dependence was eliminated by evaluating all cases at 130 bar. Some of the operating conditions have bulk temperature near 2100 K so extrapolation of the power-law fit is necessary but should produce reasonable values. Equations 6.17 and 6.18 show the power-law fit used for conductivity and viscosity, respectively. The data that were used to generate these equations and the resulting fit is shown in figure 6.9.

$$k \text{ [W/m-K]} = 0.000604295 \cdot T^{0.687791} \tag{6.17}$$

$$\mu \text{ [kg/m-s]} = 6.00579\text{E-}07 \cdot T^{0.622048} \tag{6.18}$$

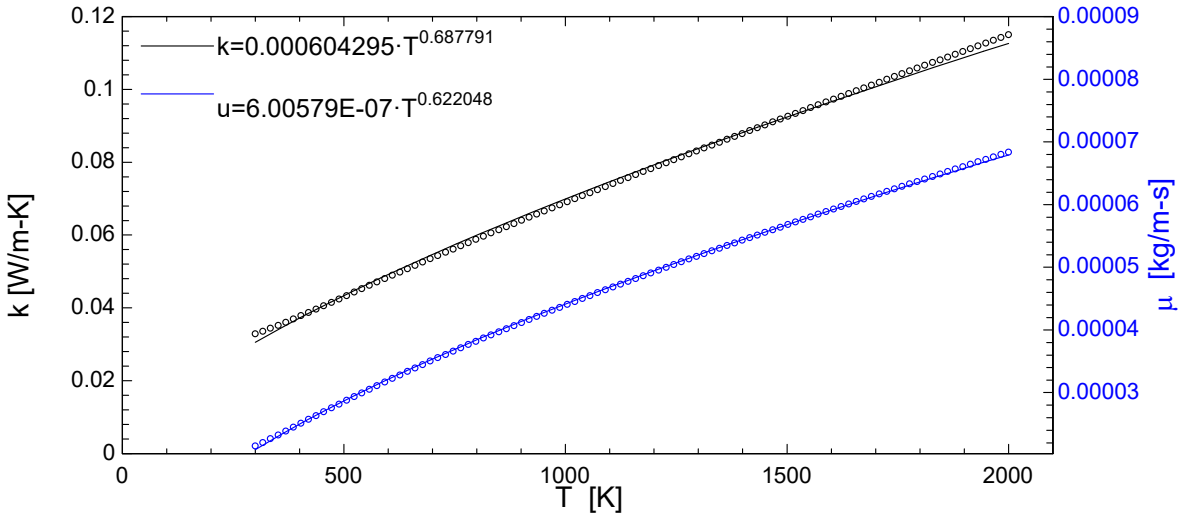


Figure 6.9: Conductivity, k, and viscosity, μ as a function of temperature using real air properties at 130 bar

An equation for specific heat, c_p, was generated in a similar way as k and μ but a fourth-order polynomial was fit to the data in the range of 300 to 2500 K. NASA ideal gas properties assuming a mixture of 21 percent O_2 and 79 percent N_2 were used [55]. Equation 6.19 shows the polynomial fit and figure 6.10 shows both the data and fit.

$$\begin{aligned} c_p \text{ [KJ/kg-K]} = 0.965761 + 0.000084381 \cdot T + 2.02410\text{E-}07 \cdot T^2 \\ -1.29021\text{E-}10 \cdot T^3 + 2.21140\text{E-}14 \cdot T^4 \end{aligned} \tag{6.19}$$

6.4.3 Optimization of Constants

In order to fairly compare different variations of heat transfer correlations, an optimized set of constants for each correlation must be found. To do this a commercially available nonlinear least squares solver was used. The *lsqcurvefit* function included in the MATLAB Optimization

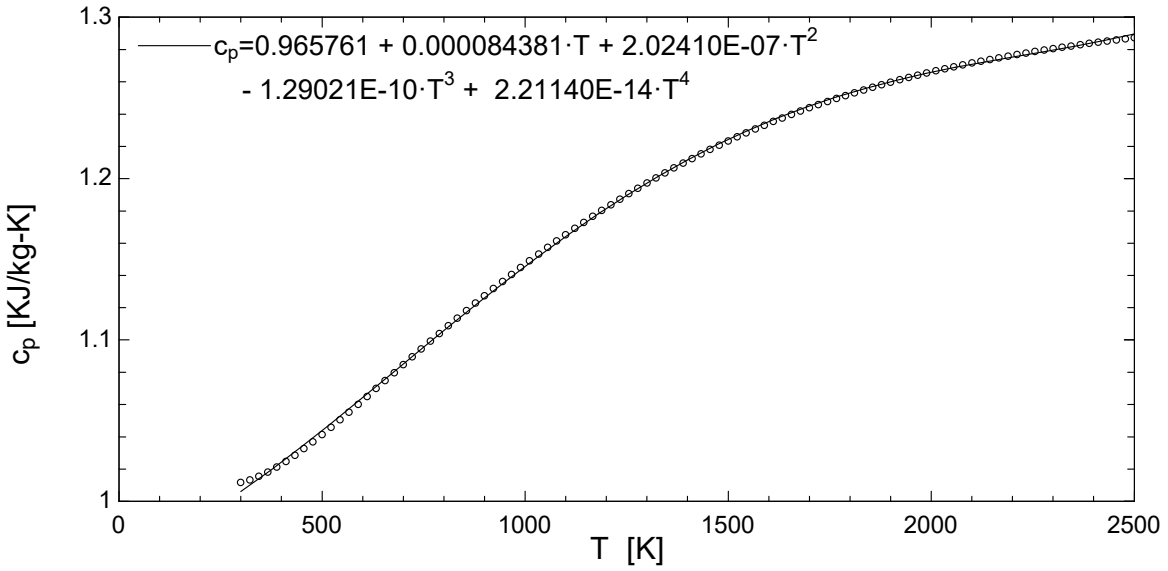


Figure 6.10: Specific heat, c_p as a function of temperature using ideal gas properties of 21 percent O_2 and 79 percent N_2

Toolbox was used to minimize the least squares error between the measured data, $\langle h \rangle$, and user-defined heat transfer correlation function such that: $min \sum_\theta (h(C_{1...n}, xdata_\theta) - \langle h \rangle)^2$, where $C_{1...n}$ were the n constants to be found and $xdata_\theta$ included all the input data required for the correlation (such as P, T, V, etc.). The least squares solver can solve both bounded and unbounded problems, but for all case tested bounds were provided to help with solver efficiency and eliminated unreasonable solutions. The documentation for the *lsqcurvefit* function states that bounded problems are solved using subspace trust-region method and is based on the interior-reflective Newton method described in [21, 22].

The correlation constants were generated using data from -40 to 100 °ATDC using 19 unique SOI / operating condition combinations. For the operating conditions tested $T - \langle T_{piston} \rangle$ become near zero around -50 °ATDC which caused $\langle h \rangle$ in equation 6.1 to approach infinity. As such it's not reasonable to calculate $\langle h \rangle$ near this cross-over point.

6.4.4 Combustion Multiplier

The functional form of the combustion multiplier, $f(\tilde{q}_{ch})$, is not known so a function with the following attributes was sought:

1. $f(0) = 1$, which eliminates the combustion multiplier impact on h when AHRR is zero
2. $0 < f(\tilde{q}_{ch}) \leq 1$, with negative dependence of $f(\tilde{q}_{ch})$ on $\tilde{q}_{ch}$ (as $\tilde{q}_{ch}$ increases $f(\tilde{q}_{ch})$ decreases)
3. $\lim_{\tilde{q}_{ch} \to \infty} f(\tilde{q}_{ch}) = C$, which is a horizontal asymptote at a defined constant
4. The total number of constants included in the formulation should be kept to a minimum.

Two functional forms for $f(\tilde{q}_{ch})$ were selected and evaluated. The first includes only one constant, C_2, and has some of the desired attributes.

$$f_1(\tilde{q}_{ch}) \equiv (1 - C_2\tilde{q}_{ch}) \tag{6.20}$$

$f_1(\tilde{q}_{ch})$ is not bound to $0 < f(\tilde{q}_{ch}) \leq 1$ and does not have an a horizontal asymptote but in practice proper selection of C_2 may limit the output of the function to reasonable values. Because this function only includes one constant, which is the minimum needed, it was substituted into 6.16 and evaluated:

$$h = C_1 v^m P^m T^{-m} k \mu^{-m} (1 - C_2\tilde{q}_{ch}) \tag{6.21}$$

Using equation 6.21 and 6.10 a set of coefficients was generated and is listed as correlation 3 in table 6.1. Correlation 3 has a mean error of 454.0 W/m^2-K. Overall, the fit to the data is relatively good but has some undesirable features. Figure 6.11 shows that for operating condition 1 at the most advanced SOI there is a large dip in h near -10 °ATDC. This dip coincides with the combustion pre-mixed spike and is driven by $f_1(\tilde{q}_{ch})$. Other operating

conditions also show this feature and motivated the investigation of a different function for the combustion multiplier.

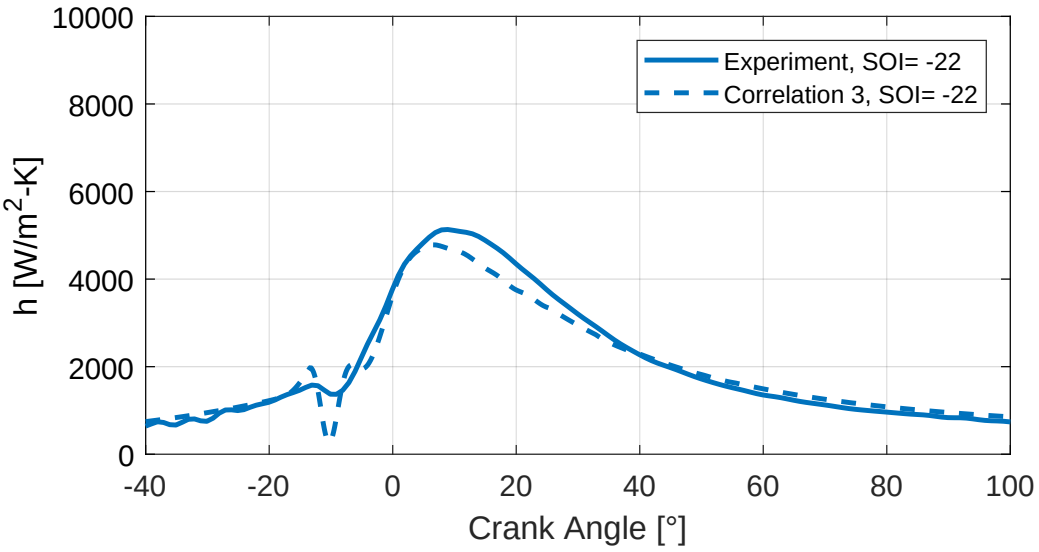


Figure 6.11: Operating condition 1 (1700 rpm, 12.3 bar IMEPg), SOI of -22 °ATDC, comparing experimental data $\langle h \rangle$ and correlation 3 (combustion multiplier 1)

A second functional form for $f(\tilde{q}_{ch})$ was selected:

$$f_2(\tilde{q}_{ch}) \equiv \frac{(C_2\tilde{q}_{ch} + C_3)}{(\tilde{q}_{ch} + C_3)} \tag{6.22}$$

Substituting back into equation 6.16:

$$h = C_1 v^m P^m T^{-m} k \mu^{-m} \frac{(C_2\tilde{q}_{ch} + C_3)}{(\tilde{q}_{ch} + C_3)} \tag{6.23}$$

Equation 6.22 has all the desired attributes that were described for $f(\tilde{q}_{ch})$. Figure 6.12 shows sample cases for the function $f_2(\tilde{q}_{ch})$. The function includes two constants, C_2 and C_3. As shown, the function asymptotes to C_2 at large $\tilde{q}_{ch}$ and $f_2(0) = 1$. The constant C_3 changes how fast the function approaches the asymptote.

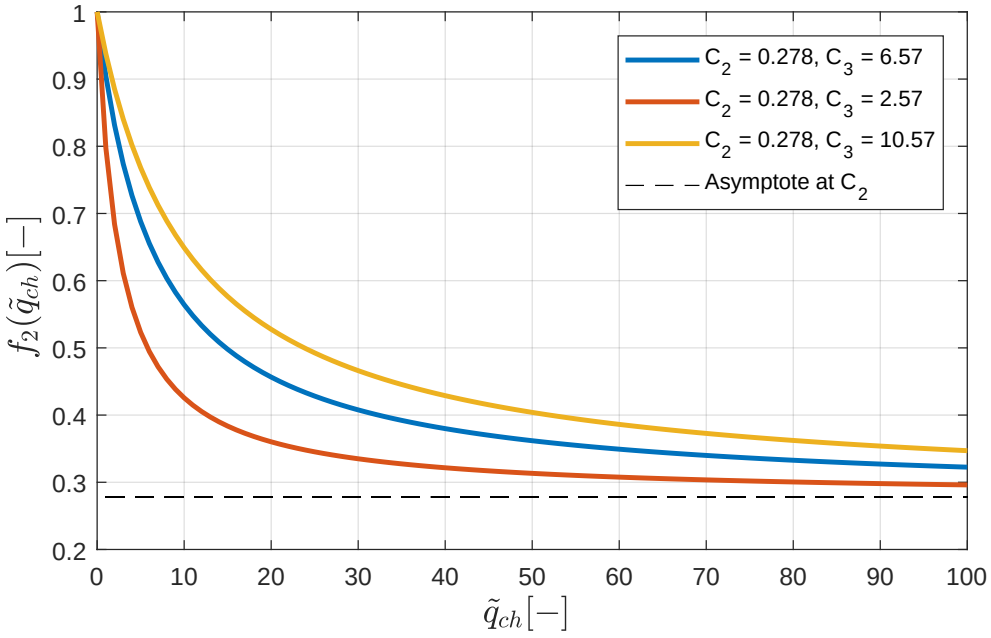


Figure 6.12: Examples of $f_2(\tilde{q}_{ch})$

The formulation of v in equation 6.10 had an exponential decay term, but C_7 was positive (see C_7, correlation 3 in table 6.1); the original intent of the term was to capture dissipation in velocity which requires C_7 to be negative. Further correlation development eliminates the exponential decay term by setting $C_7 = 0$.

Using equation 6.23 and 6.10 correlations 4 and 5 were developed; correlation 4 fit all the constants, except C_7 which was set to zero to eliminate the decay term. Correlation 5 turned off the combustion multiplier by setting $C_2 = 1$ and $C_3 = 0$. Figure 6.13 shows the results for correlation 4 and 5 for operating condition 3. Both correlations produce an acceptable fit to the experimental data. The large dip in correlation 3 was eliminated. The error for correlation 4 was 428.7 W/m^2-K compared to 574.7 W/m^2-K for correlation 5. The increased error in correlation 5 was driven by the phasing issue that was observed in existing heat transfer correlations in Section 6.3, *i.e.*, the correlation formulation has reverted back to $Nu = CRe^m$. For most cases correlation 5 rises earlier and produces a peak heat flux advanced compared to $\langle h \rangle$.

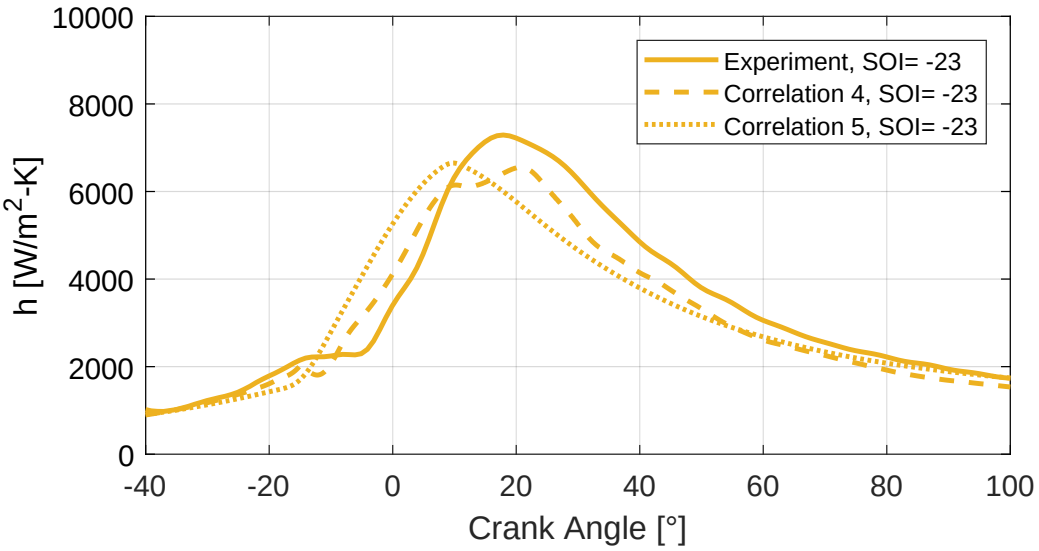


Figure 6.13: Operating condition 3 (2500 rpm, 20.3 bar IMEPg), SOI of -23 °ATDC, comparing experimental data $\langle h \rangle$, correlation 4 ($f_2(\tilde{q}_{ch})$) and correlation 5 (combustion multiplier off)

6.4.5 Velocity Term

Further investigation of the velocity term based on equations 6.23 and 6.10 was explored. The ultimate goal was to understand the impact of each of the individual components of v and eliminate any that did not provide a significant contribution. The theoretical development presented took v as the mean piston speed, $\bar{S}_p$, which allowed additional simplification of the engine geometry terms; the transient nature of the injection, ignition and combustion process requires a more complex definition.

Each of the three components of equation 6.10 were individually turned off in correlations 6 through 8, and each plotted in figure 6.14. In correlation 6 the integrated fuel mass injection rate term, $C_6 e^{C_7(\theta - \theta_{EOI})} \int_{\theta_{SOI}}^{\theta} \frac{dm_{fuel}}{d\theta} d\theta$, was eliminated by selecting $C_6 = 0$. Correlation 6 produced a poor overall fit with a large amount of error. The constant term C_5 was set to zero in correlation 7, which produced a good fit with low error. Correlation 7 did not, however, correctly match the compression portion of cycle for the low speed case shown in

figure 6.14. Correlation 8 eliminated the mean piston speed term, $C_4\bar{S}_p$ by setting $C_4 = 0$.The fit was good, with error nearly equal to correlation 4, which had a more general form of v. The problem in the compression portion of the cycle observed in correlation 7 was eliminated and produced a better overall fit.

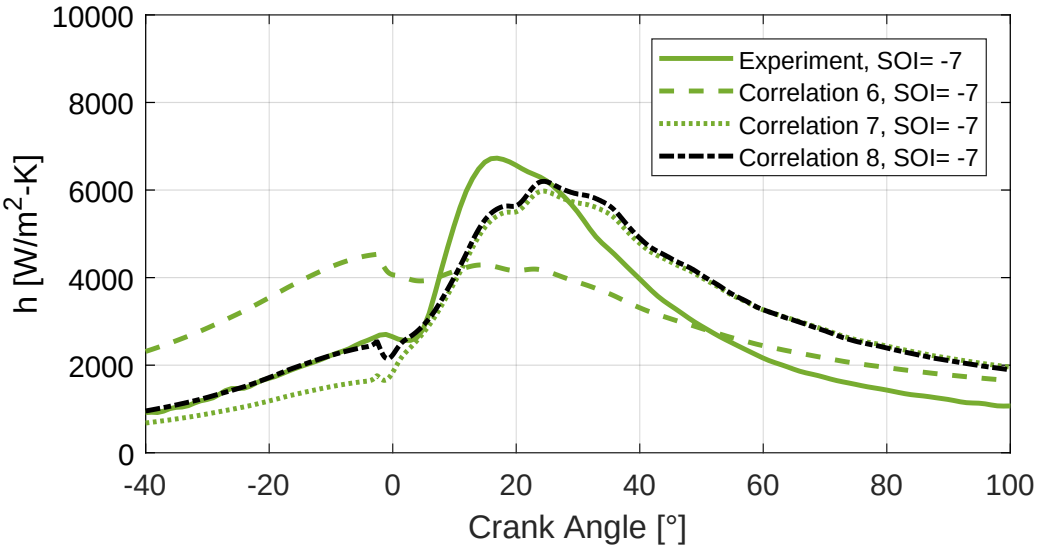


Figure 6.14: Operating condition 2 (1500 rpm, 23.8 bar IMEPg), SOI of -7 °ATDC, comparing experimental data $\langle h \rangle$, correlation 7 (velocity- no constant term) and correlation 8 (no $\bar{S}_p$)

6.4.6 Comparison of Cases Tested

Figure 6.15 and table 6.1 summarize intermediate steps in heat transfer correlation development.

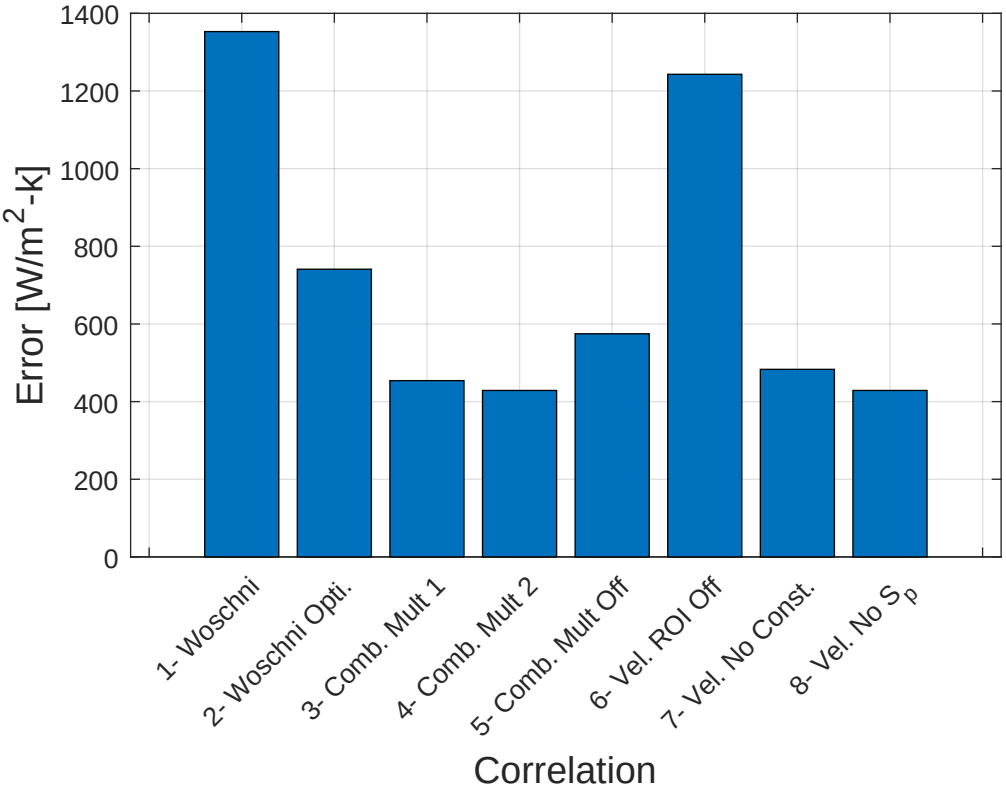


Figure 6.15: Comparison of error for all correlations developed as part intermediate steps

Table 6.1: Summary of intermediate steps in heat transfer correlation development

#	Description	Eq.	C_1	C_2	C_3	C_4	C_5	C_6	C_7	m	Error [W/m^2-K]	Comments
1	Woschni	6.7, 6.8	2.67	0.0032	3.26	N/A	N/A	N/A	N/A	0.8	1353	Overall poor fit
2	Woschni Optimized	6.7 6.8	81.52	1.22	0.62	N/A	N/A	N/A	N/A	0.306	741	Both over- and under- prediction depending on condition
3	Combustion Multiplier 1	6.21, 6.10	0.0403	0.0371	N/A	4.437e-14	5.306	2.0529e5	0.0040	0.6457	454.0	Produces large dips for some cases
4	Combustion Multiplier 2	6.23, 6.10	2.916e-4	0.2787	6.5659	8.551e-10	41.42	1.227e6	0	0.8052	428.7	Good fit, many constants
5	Combustion Multiplier Off	6.23, 6.10	0.4487	1	0	4.44e-14	1.185	5.220e4	0	0.5636	574.7	Fair fit, phasing is off
6	Velocity- ROI Off	6.23, 6.10	1.259	0.6434	12.7	0.1616	8.584	0	0	0.5014	1243	Poor fit
7	Velocity- No Const.	6.23, 6.10	0.0987	0.3328	6.6113	0.0104	0	3.618e3	0	0.7427	483.1	Good fit for most, compression problem at low engine speed
8	Velocity- No $\bar{S}_p$	6.23, 6.10	0.0343	0.2787	6.5651	0	0.1109	3.2865e3	0	0.8051	428.7	Good fit

Table includes correlation number, short description of correlation, equations used, constants, error, and comments on the performance of the correlation compared to $\langle h \rangle$. Correlation constants, C_1-C_7 should only be compared when the same equations were used. m was always used as the exponent such that: $Nu = CRe^m$. Constants with red text were provided as fixed inputs. Error is calculated by equation 6.9.

(Woschni, Eq. 6.7) $h = C_3 B^{m-1} P^m T^{0.75-1.62m} v^m$, (Woschni Velocity Eq. 6.8) $v = C_1 \bar{S}_p + C_2 \frac{V_d T_r}{P_r V_r}(P - P_m)$

(Eq. 6.21) $h = C_1 v^m P^m T^{-m} k \mu^{-m} (1 - C_2 \tilde{q}_{ch})$

(Eq. 6.23) $h = C_1 v^m P^m T^{-m} k \mu^{-m} \frac{(C_2 \tilde{q}_{ch} + C_3)}{(\tilde{q}_{ch} + C_3)}$

(Eq. 6.10) $v = C_4 \bar{S}_p + C_5 + C_6 e^{C_7(\theta - \theta_{EOI})} \int_{\theta_{SOI}}^{\theta} \frac{dm_{fuel}}{d\theta} d\theta$

6.5 New Heat Transfer Correlation

The development of a new heat transfer correlation in the previous section provided insight into the advantages and disadvantages of various functional forms of h and v. It was found that including a cumulative fuel injection term in v provided a significant benefit to the correlation fit. An additional improvement, specifically in relation to correlation phasing (rise, peak and decay), was observed when a multiplicative term of $f_2(\tilde{q}_{ch})$ was included in h. Two correlations, one that includes $f_2(\tilde{q}_{ch})$ and another that does not, are proposed as a final summary to the development work.

Equation 6.24 is the final proposed heat transfer correlation with velocity defined by equation 6.25. These equations are functionally the same as equations 6.10 and 6.23 but a was used for constant terms. The previous definition for velocity (equation 6.10) had the $\bar{S}_p$ term and exponential decay term eliminated. Table 6.2 includes two sets of constants; the first set, *final correlation 1*, is the same as correlation 8 in Section 6.4 but the ratio of a_1 with v has been adjusted (described next). The second set of constants, *final correlation 2* eliminates $f(\tilde{q}_{ch})$ by selecting $a_2 = 1$ and $a_3 = 0$.

Final correlation 1 provides a better overall fit than *final correlation 2* but it includes the additional complexity of requiring $\tilde{q}_{ch}$. Calculation of $\tilde{q}_{ch}$ requires *a priori* knowledge of the in-cylinder pressure (to calculate AHRR). Because time-varying spatially averaged heat correlations are often used in reduced-order engine simulations, including a set of coefficients that eliminates $\tilde{q}_{ch}$ may be useful to some investigators. Depending on the required accuracy of the simulation it may be possible to initialize the problem using *final correlation 2* and iteratively solve using *final correlation 1*.

$$h[\mathrm{W/m^2K}] = a_1 v^m P^m T^{-m} k \mu^{-m} \frac{(a_2 \tilde{q}_{ch} + a_3)}{(\tilde{q}_{ch} + a_3)} \tag{6.24}$$

$$v = a_4 + a_5 \int_{\theta_{SOI}}^{\theta} \frac{dm_{fuel}}{d\theta} d\theta \tag{6.25}$$

Table 6.2: Constants for final heat transfer correlations

	a_1	a_2	a_3	a_4	a_5	m	Error [W/m^2-K]
Final Correlation 1	0.00340	0.278	6.57	1.97	58300	0.805	428.7
Final Correlation 2	0.337	1	0	1.97	86700	0.564	573.6

The choice of a_1 was arbitrary because a_1 is multiplicative with C_4 and C_5 in v (*i.e.* there is an extra constant). To give v in equation 6.25 physical units, correlation 8 was re-solved using a constrained optimization using information from correlation 7 which included mean piston speed (units of m/s). The constrained optimization resulted in $a_4 = 1.97$ which was used in both final correlation 1 and 2.

It is worth noting that equation 6.24 reduces to the Woschni correlation by selecting $m = 0.8$, assuming $k \propto T^{0.75}$ and $\mu \propto T^{0.62}$, eliminating $f_2(\tilde{q}_{ch})$ by selecting $a_2 = 1$ and $a_3 = 0$. Woschni used a different definition for v (see equation 6.8), which was based on $\bar{S}_p$ and a difference between fired and motored pressure, $(P - P_m)$. The intent of the $(P - P_m)$ term was to capture additional velocity from the combustion process, which is similar to $\int_{\theta_{SOI}}^{\theta} \frac{dm_{fuel}}{d\theta} d\theta$ in equation 6.25 but differs because $(P - P_m)$ decreases into the expansion stroke where as $\int_{\theta_{SOI}}^{\theta} \frac{dm_{fuel}}{d\theta} d\theta$ is cumulative. It is also possible that $\int_{\theta_{SOI}}^{\theta} \frac{dm_{fuel}}{d\theta} d\theta$ is capturing in-cylinder radiation effects that are present but can not be decoupled from convection in $\langle \dot{q}'' \rangle$. In-cylinder radiation is a complex phenomenon but it would not be unreasonable to assume that the amount of radiation scales with the amount of fuel injected, which would be captured in the proposed velocity term.

To arrive at equation 6.25 a systematic approach of eliminating components of v was conducted, which resulted in removal of the $\bar{S}_p$ dependence. The theoretical development in Section 6.2 assumed $v = \bar{S}_p$ so completely eliminating this term was surprising but justified based on the data. In a practical sense the implication of removing $\bar{S}_p$ dependence is that engine speed does not impact h, and v is based strictly on engine geometry (before the

injection event). Constant term, a_4, in equation 6.25 is expected to change for different engines and different intake charge preparation (*e.g.*, swirl ratio).

Figure 6.16 shows the relative change (from -40 °ATDC) in each of the components of final correlation 1. The pressure dependence, P^m, shows the largest maximum in percent change compared to the other factors. Additionally, it dynamically changes throughout the cycle first increasing and then later decreasing to a negative relative change. The temperature dependence, T^{-m}, and viscosity dependence μ^{-m} both show a similar negative percent change throughout the cycle. The conductivity dependence, k, is nearly opposite the viscosity and temperature dependence which is not surprising because both gas properties use a power-law fit to temperature: $k \propto T^{0.687791}$ and $\mu \propto T^{0.622048}$. The total combined temperature dependence, which include the exponent m, can be expressed as $T^{0.687791-1.622048m}$ which simplifies further for $m = 0.805$ and $m = 0.564$ in final correlation 1 and 2 as $T^{-0.61796}$ and $T^{-0.22704}$, respectively. The velocity dependence, v^m, increases throughout the injection event and then remains constant after the end of injection. The negative dependence of $f(\tilde{q}_{ch})$ directly competes with $\int_{\theta_{SOI}}^{\theta} \frac{dm_{fuel}}{d\theta} d\theta$ in the velocity term. In a mixing-limited combustion regime, $\tilde{q}_{ch}$ is ultimately linked to the $\frac{dm_{fuel}}{d\theta}$. The early portion of the injection and ignition event was typically dominated by $f(\tilde{q}_{ch})$, which quickly rises and then later in the injection event was overcome by $\int_{\theta_{SOI}}^{\theta} \frac{dm_{fuel}}{d\theta} d\theta$.

To validate that the new heat transfer correlation can capture the correct trends in the thermodynamically determined heat loss, the predicted heat transfer was used to estimate a total heat transfer similar to equation 4.5 except measured heat flux, $\langle \dot{q}'' \rangle$, was replaced with $h(T - \langle T_{piston} \rangle)$:

$$Q_h = \int_{t=0}^{t=t_{cycle}} A_\theta h(T - \langle T_{piston} \rangle) dt \tag{6.26}$$

The limits of integration in equation 6.26 are shown as $t = 0$, which corresponds to -360 °ATDC, and $t = t_{cycle}$ which corresponds to 360 °ATDC. Because the correlation constants were calibrated over in the range of -40 to 100 °ATDC the correlation is used outside the range

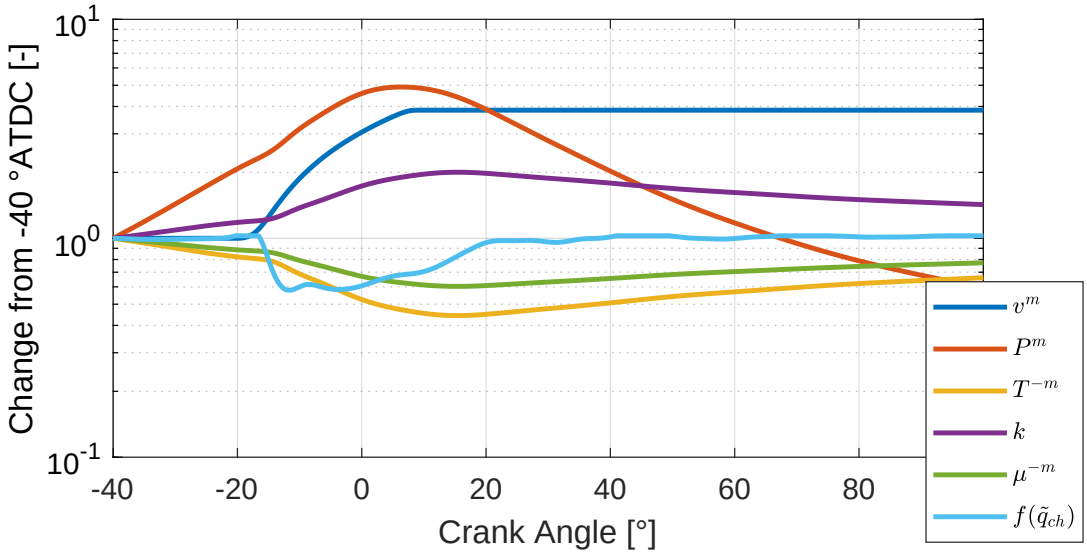


Figure 6.16: Operating condition 3 (2500 rpm, 20.3 bar IMEPg), SOI of -25 °ATDC, comparing typical dependence of each component of final correlation 1 (shown as ratio of value at -40 °ATDC)

it was developed. Additionally, a different estimate for bulk temperature was needed during the open portion of the cycle. For crank angles before intake valve close (IVC) temperature was estimated as the greater of the intake temperature or the temperature from extending the closed-cycle anylsis $T = PV/m_{trap}\bar{R}$ to crank angles before IVC. Similarly, for crank angles after exhaust valve open (EVO) the greater of exhaust temperature or extended closed-cycle temperature was used. Overall, the impact of both correlation extrapolation and bulk temperature selection is small because the small temperature difference between the piston and gas results in a small addition to Q_h.

Figure 6.17 shows a comparison between Q_h and $\dot{Q}_{gas}$ for all operating conditions tested using *final correlation 1*. The agreement between the two values is good over the wide range of conditions. Conditions 4 and 3 IMT were not used to develop the correlation constants, so these data demonstrate the correlation's prediction ability at different operating points. Because $\dot{Q}_{gas}$ includes additional heat transfer during the open portion of the cycle and

exhaust ports Q_h is expected to fall slightly below the 1:1 line. A comparison can also be made to figure 4.25 which plots the $\langle Q \rangle$ in a similar way. The overall agreement for the correlation in figure 6.17 is better over the full range of conditions, both of which provide confidence in the correlation and suggests $\langle \dot{q}'' \rangle$ may have errors within each SOI sweep but, on average, the local temperature data is of high quality and represents the combustion chambers contribution to overall engine heat transfer.

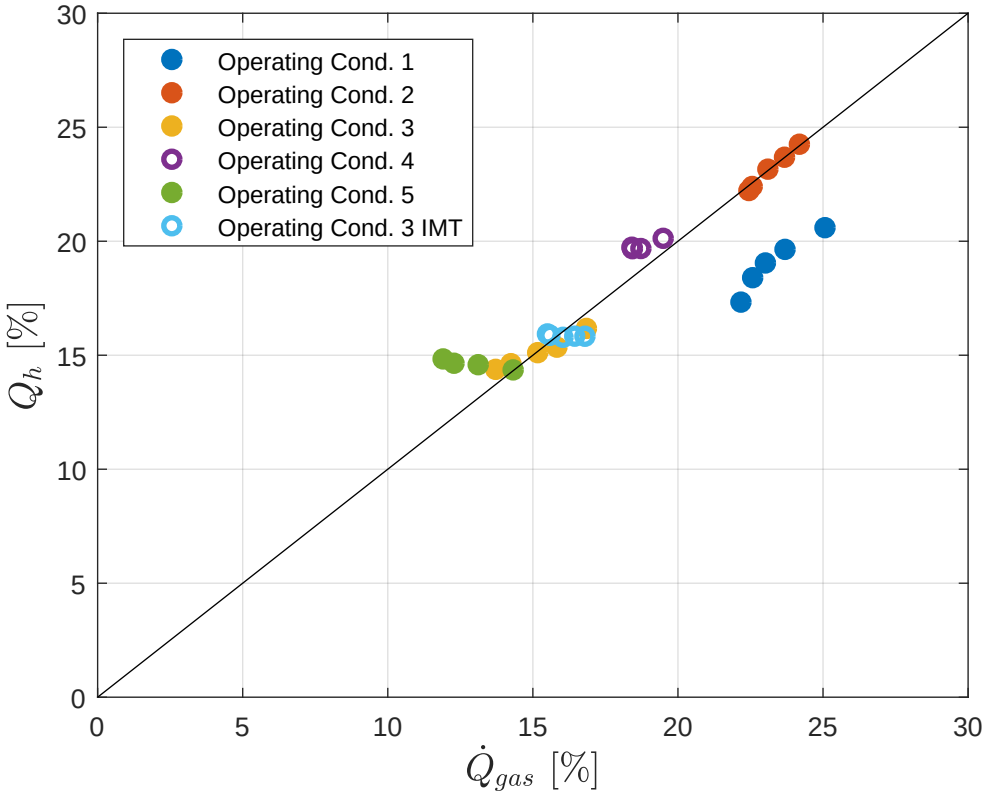


Figure 6.17: Comparison of Q_h and $\dot{Q}_{gas}$ for final correlation 1

Figures 6.18-6.23 show *final correlation 1* for operating conditions 1-5 including condition 3 IMT. All cases show relatively good agreement across all the operating conditions and SOIs. Condition 4 (figure 6.22) shows a relatively large disagreement late in the expansion stroke, which may be related to the thermocouple substitution due to failures (which was the reason the data were not included in the correlation development). Interestingly Q_h in figure 6.17 agrees better for operating condition 4 than $\langle Q \rangle$ in figure 4.25, which suggests the correlation

is a better estimate for h than the measured $\langle h \rangle$ data for this particular operating condition. A similar set of figures for *final correlation 2* can be found in Appendix A.13.

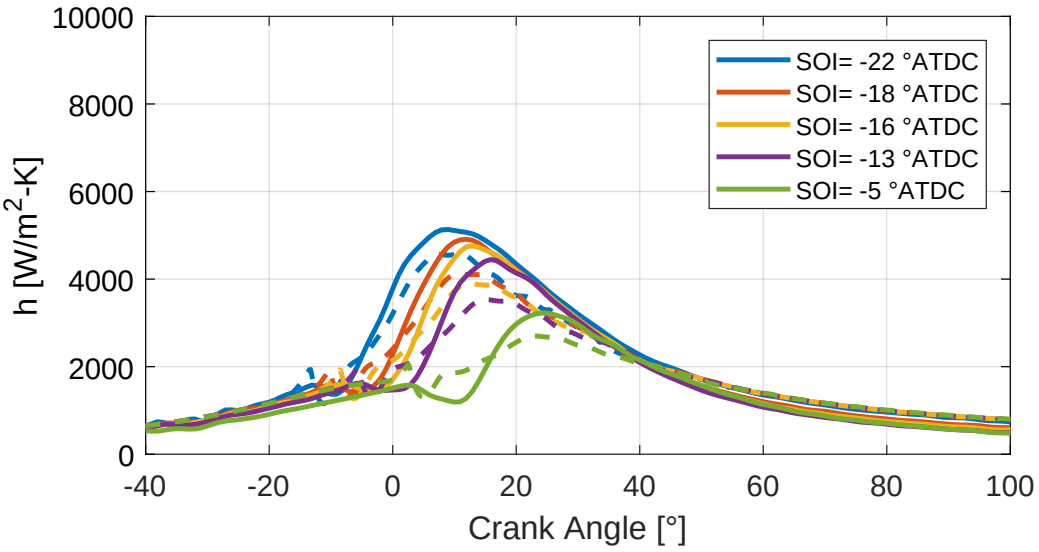


Figure 6.18: Operating condition 1 (1700 rpm, 12.3 bar IMEPg), SOI sweep, comparing experimental data $\langle h \rangle$ (solid lines) and final correlation 1 (dashed lines)

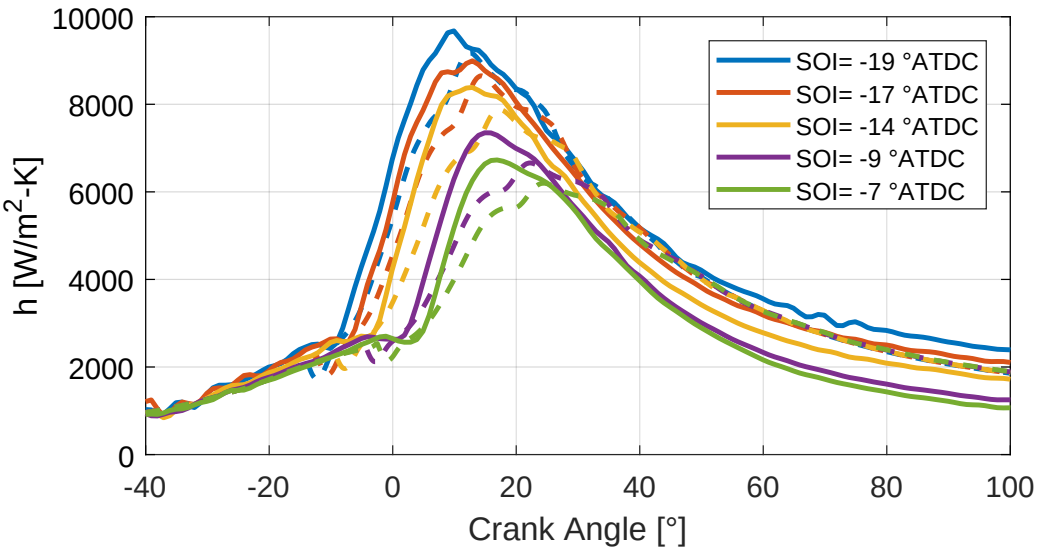


Figure 6.19: Operating condition 2 (1500 rpm, 23.8 bar IMEPg), comparing experimental data $\langle h \rangle$ (solid lines) and final correlation 1 (dashed lines)

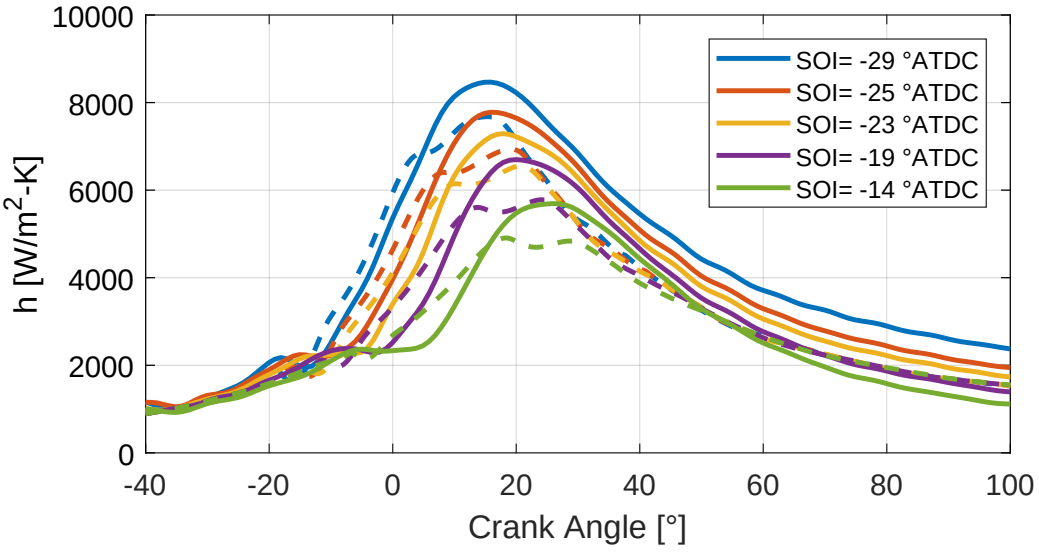


Figure 6.20: Operating condition 3 (2500 rpm, 20.3 bar IMEPg), comparing experimental data $\langle h \rangle$ (solid lines) and final correlation 1 (dashed lines)

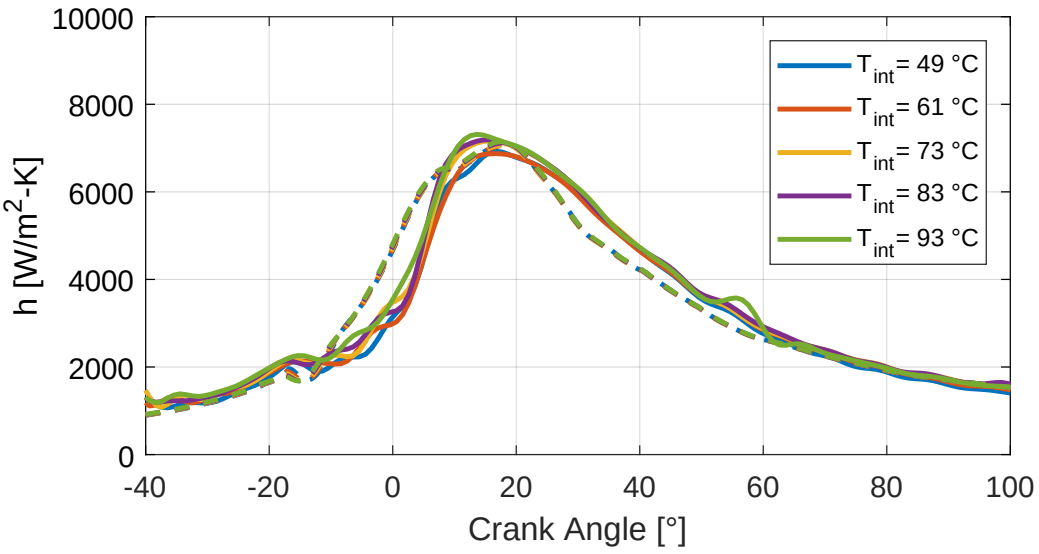


Figure 6.21: Operating condition 3 IMT (2500 rpm, 20.3 bar IMEPg), comparing experimental data $\langle h \rangle$ (solid lines) and final correlation 1 (dashed lines)

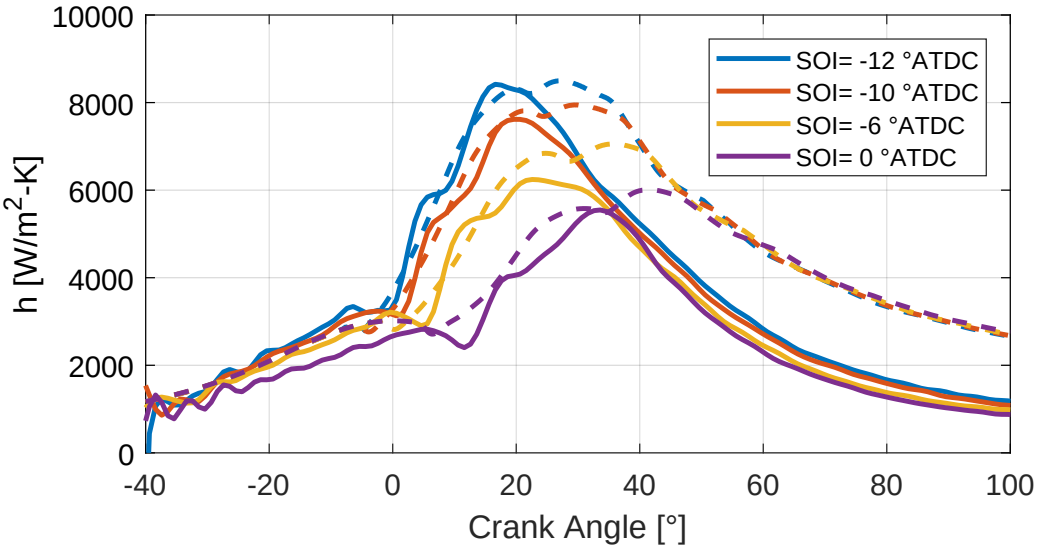


Figure 6.22: Operating condition 4 (1700 rpm, 30.3 bar IMEPg), comparing experimental data $\langle h \rangle$ (solid lines) and final correlation 1 (dashed lines)

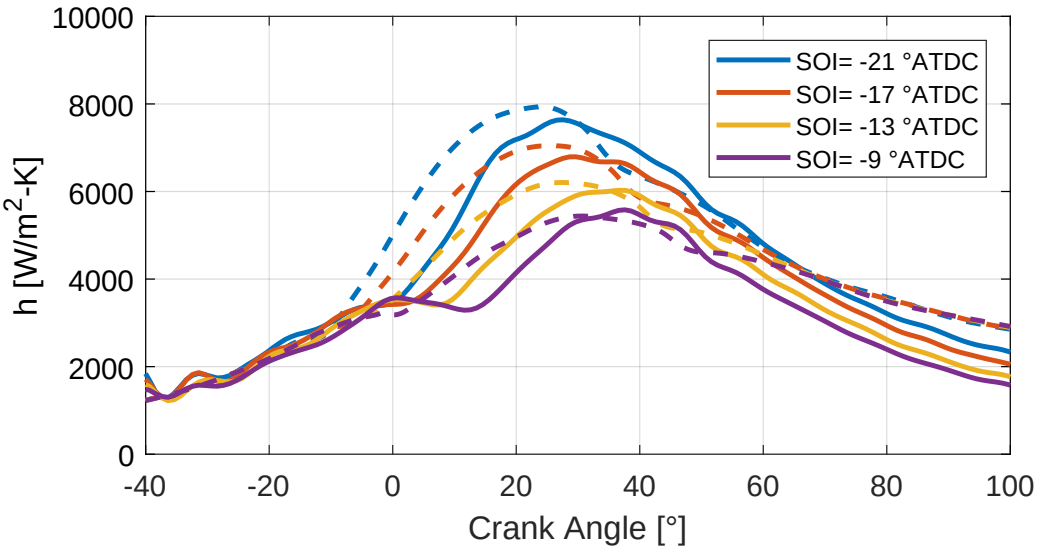


Figure 6.23: Operating condition 5 (2750 rpm, 29.7 bar IMEPg), comparing experimental data $\langle h \rangle$ (solid lines) and final correlation 1 (dashed lines)

6.5.1 Comparison of Dimensionless Values

The plots of $\langle Nu \rangle$ as a function of Re in the beginning of this chapter (figures 6.1 and 6.6) were regenerated for final correlation 1 and 2 in figures 6.25 and 6.24, respectively. SOC is again marked with an open circle and EOC with an $\times$. The result from using the velocity of final correlation 2 is shown first (figure 6.24) because it is the simpler of the two correlations. When figure 6.24 is compared back to figure 6.6 (Woschni velocity) the most noticeable improvement are for the portions of the cycle before SOC and after EOC; the data are more tightly grouped (see bottom left of each plot). This improvement can mostly be attributed to improvements in the velocity term, which now scales with the total quantity of fuel injected. For all the operating conditions during the combustion event the dependence of $\langle Nu \rangle$ on Re is still not clear with $\langle Nu \rangle$ first slightly decreasing after SOC then rapidly increasing.

Figure 6.25 shows $\langle Nu \rangle$ as a function of $Re \cdot f_2(\tilde{q}_{ch})$ (rather than just Re) using velocity from final correlation 1. Compared to final correlation 2 in figure 6.24 additional improvement to the data during the combustion event are observed. Operating conditions 1 and 2 now collapse to a single line across the entire set of data. For operating conditions 3 and 5 during combustion event the data do not fully collapse to a single power-law fit, but are improved from final correlation 2. Overall, when the independent variable $Re \cdot f(\tilde{q}_{ch})$ is used rather than just Re all operating conditions produce a more condensed trend.

Figure 6.26 shows all of the data from figure 6.25 but all on the same axes. Overall, most of the data collapse to a single line. At high values of $Re \cdot f_2(\tilde{q}_{ch})$, data from operating condition 5 seems to be slightly lower than the overall trend. Individual heat flux at each measurement location as well the average heat flux was plotted in figure 4.21 for operating condition 5 and show that this particular operating condition had larger variation in heat flux, especially during SOC when compared to the other operating conditions. Additionally, fewer total measurements were available for averaging. The higher uncertainty in operating condition 5 heat flux during SOC may suggest that the outlying data in figure 6.26 may be an artifact of limited data available for this operating condition.

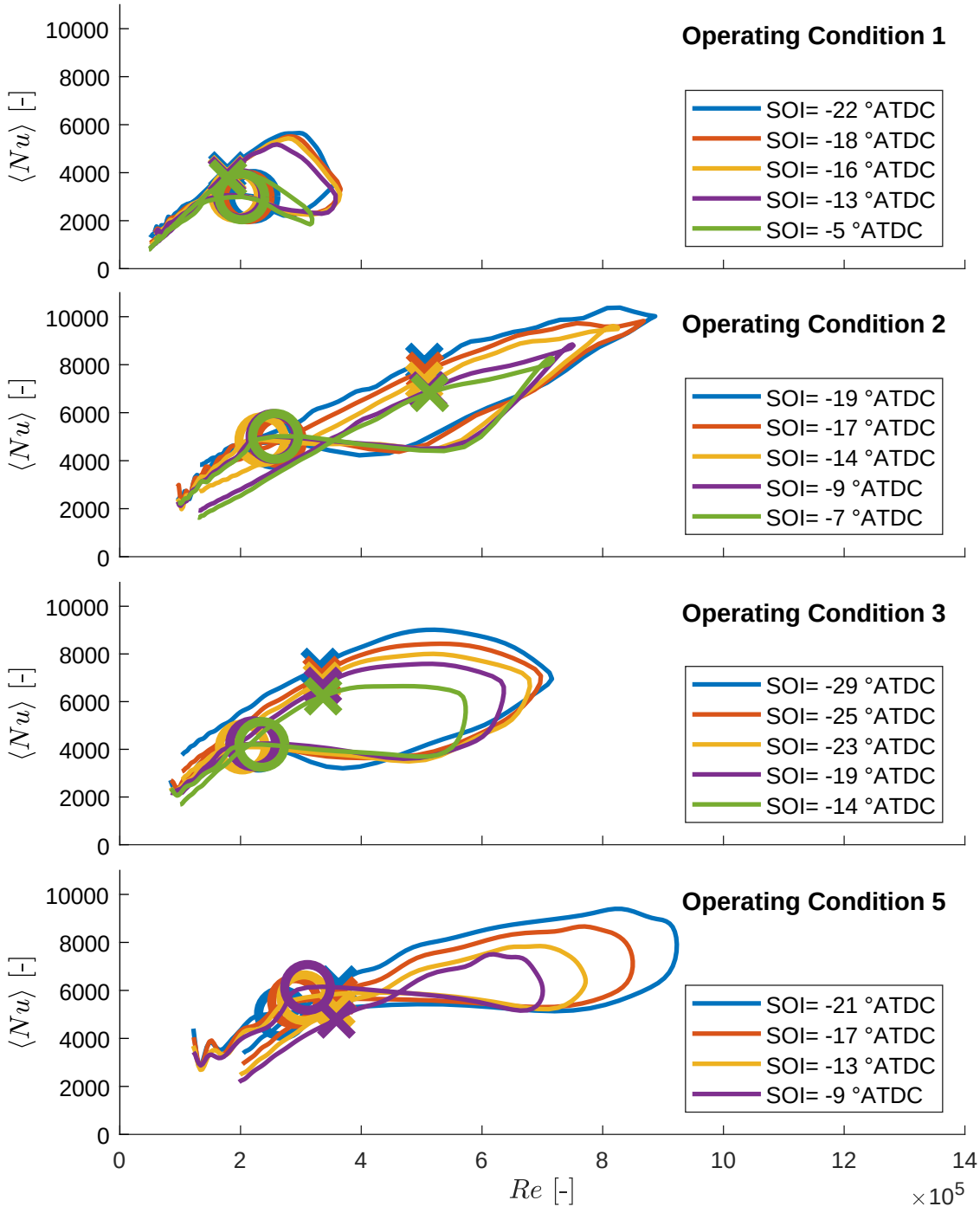


Figure 6.24: Operating conditions 1, 2, 3 and 5 $\langle Nu \rangle$ as a function of Re using velocity from final correlation 2 (open circle markers show SOC and $\times$ markers show EOC)

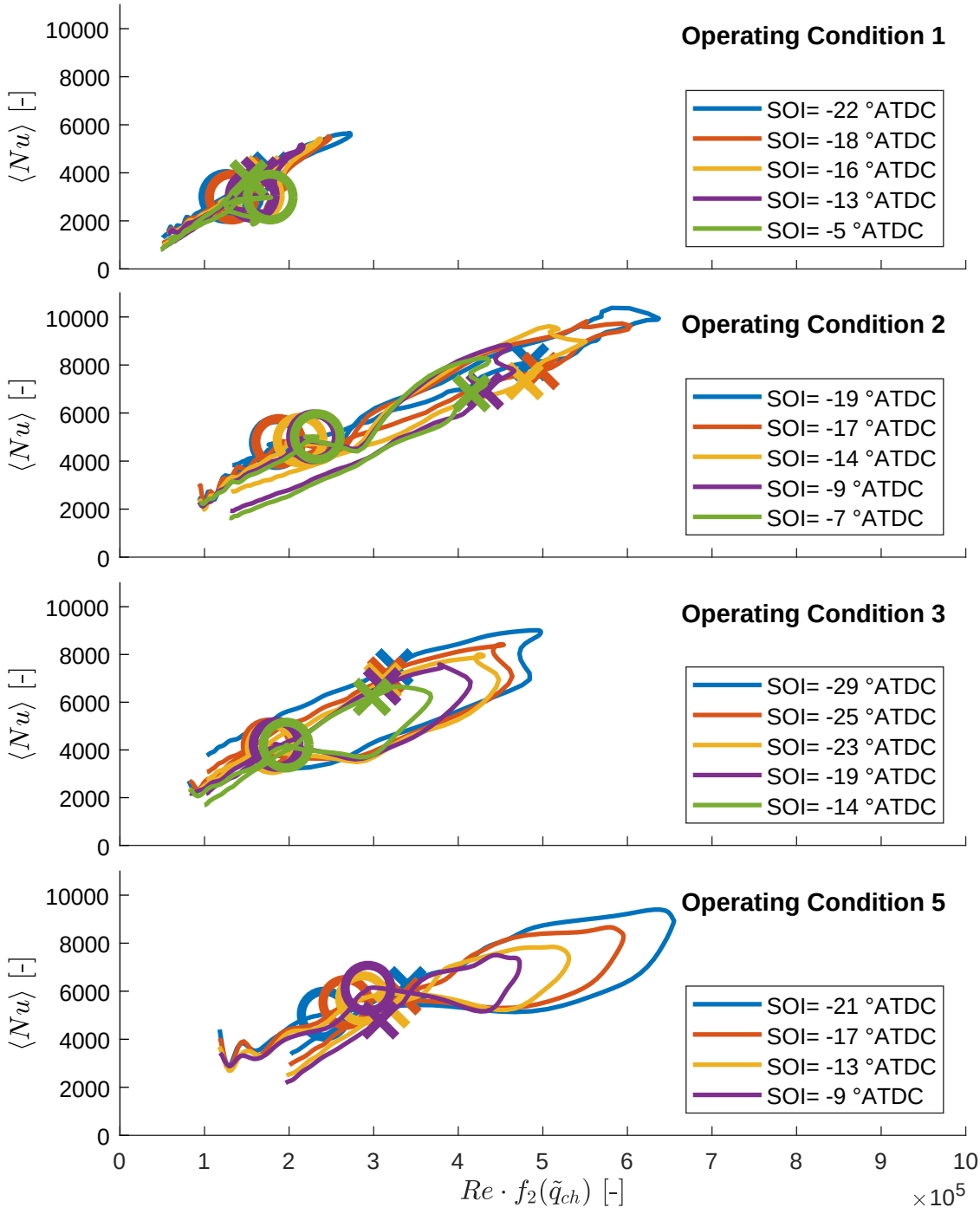


Figure 6.25: Operating conditions 1, 2, 3 and 5 $\langle Nu \rangle$ as a function of $Re \cdot f(\tilde{q}_{ch})$ using velocity from final correlation 1 (open circle markers show SOC and $\times$ markers show EOC)

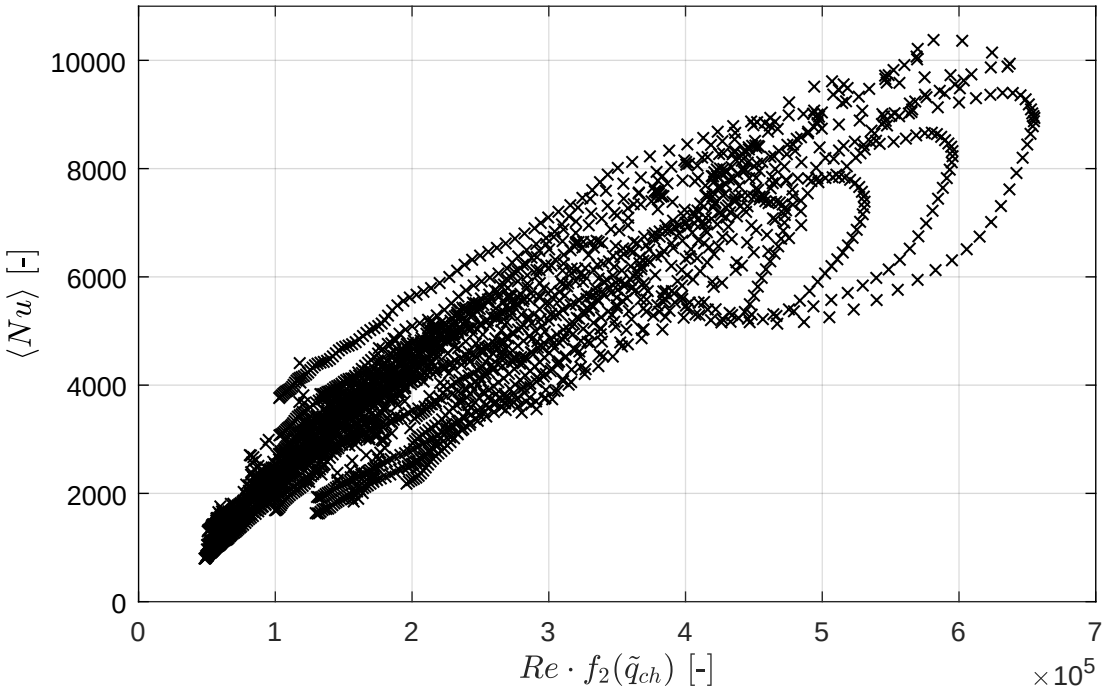


Figure 6.26: Operating conditions 1, 2, 3 and 5 $\langle Nu \rangle$ as a function of $Re \cdot f(\tilde{q}_{ch})$ using velocity from final correlation 1 all on same axes

6.6 Summary and conclusion

1. A new engine heat transfer correlation was developed for high-output diesel operating conditions. The correlation was based on a new dimensionless form: $Nu = CRe^m f(\tilde{q}_{ch})$. Including dimensionless chemical energy release rate, $\tilde{q}_{ch}$, in the correlations provided the best fit to experimental data and was consistent with the dimensional analysis.

2. Various dimensional forms of the heat transfer correlation were investigated including different functional forms for $f(\tilde{q}_{ch})$ and v. A non-linear squares solver was used to find the optimum coefficients for each specific case, which allowed error between functional forms to be compared. A heat transfer correlation with form: $h = a_1 v^m P^m T^{-m} k \mu^{-m} \frac{(a_2 \tilde{q}_{ch} + a_3)}{(\tilde{q}_{ch} + a_3)}$ was found to be the best fit to the data using the least number of constants.

3. A new definition of velocity, $v = a_4 + a_5 \int_{\theta_{SOI}}^{\theta} \frac{dm_{fuel}}{d\theta} d\theta$, included a cumulative fuel mass term (*i.e.*, integrated rate of injection) and a constant term. Including a mean piston speed term, $\bar{S_p}$, as many of previous correlations have, was investigated but ultimately not pursued because the experimental data did not support such a term.

4. Cumulative local heat transfer (found from the new correlation) and global thermodynamic measurements agreed well over all the operating conditions investigated. When additional operating conditions, which were not used to develop the model, were tested the model appears to become predictive.

5. Additional physics was included in the new correlation by the addition of $\tilde{q}_{ch}$, but no additional information was needed to calculate this term. AHRR and other terms are only a function of P, T and V, which are already needed for the correlation. Because time-varying spatially averaged heat transfer correlations are often used in reduced-order engine simulation, calculating $\tilde{q}_{ch}$ may be inconvenient; as such, a second correlation that eliminated $f(\tilde{q}_{ch})$ was developed. This second correlation should provide more accurate results than existing correlations, but was less accurate than the full correlation.

7 Summary and Recommendations

This chapter provides a summary of the results and discusses directions for future work.

7.1 Summary

A high-output single-cylinder research engine was used to acquire data over a range of operating conditions, some at very high-output (IMEPg greater than 30 bar). The engine was configured with several pistons, some that included thermal barrier coatings. For some of the experiments, pistons instrumented with fast-response thermocouples were used to acquire instantaneous surface temperature, from which a temporally varying heat flux could be calculated. *Local* heat transfer, based on the piston surface temperature measurements, were compared to *global* heat transfer, based on thermodynamic measurements on the engine. Spatially averaged heat flux was used to develop a new instantaneous spatially averaged heat transfer correlation. A summary of results for each specific section is given next.

7.1.1 Metal Piston Heat Flux Measurements in a High-output Diesel Engine

Two pistons were instrumented with co-axial fast-response surface thermocouples and run to quantify the spatial and temporal variation of piston heat flux. Both the pistons used were stock metal pistons, *i.e.*, they had no applied coating. For each operating condition three fuel injectors with varying spray axis orientation relative to a thermocouple axis were used to investigate variation of heat flux on and off the spray's axis. The following conclusions can be drawn from this study:

1. Local heat transfer, based on fast-response thermocouple data, combined with an appropriate spatial interpolation method and integrated over the cycle have relatively good agreement with independent, engine-out global thermodynamic heat transfer

measurements and quantities based on in-cylinder pressure across a range of engine operating conditions. Spatially averaged heat flux data, $\langle \dot{q}'' \rangle$, are of high quality and to the author's knowledge, this work is the first time local heat transfer, based on fast-response thermocouples, were shown to agree with global thermodynamic heat transfer over a range of operating conditions.

2. The spatial distribution of temporally integrated heat flux were dominated by radial position, and azimuthal location relative to the injector spray plume has a minor effect. The highest intensity of heat flux, and therefore integrated heat flux, was typically contained in the piston bowl.

3. Spatial gradients in instantaneous heat flux between on- and off-axis injector spray plumes (azimuthal direction) was strongest during the initial onset of heat flux rise and nearly disappeared later is the expansion stroke. On-axis spray locations typically showed the first rise in heat flux.

4. The start of injection command had a strong effect on $\langle \dot{q}'' \rangle$. As the injection timing was advanced, the initial rise of $\langle \dot{q}'' \rangle$ advanced and the maximum value of $\langle \dot{q}'' \rangle$ increased by nearly a factor of two (when compared to the most retarded timing tested). Advancing the injection timing increased the maximum in-cylinder pressure and temperature which are strong driving factors in $\langle \dot{q}'' \rangle$.

5. The intake temperature sweep showed virtually no influence on $\langle \dot{q}'' \rangle$ and a limited effect on mean piston temperature. For an increase of intake temperature of 44 °C, an area- and time-averaged piston temperature increased roughly 20 °C. Both of these changes were small in comparison to the maximum difference in temperature between the piston and gas, which is greater than 1000 °C.

6. A delayed onset of the rise of $\langle \dot{q}'' \rangle$ was observed for later start of injection timings. It was found that the delay correlated slightly better in the time domain than in the crank

angle domain. The individual data at each thermocouple location showed that the delay was not an artifact of the selected interpolation method. Any delay introduced by the thermocouples or telemetry system is believed to have been minimal.

7.1.2 Impact of Thermal Barrier Coating Roughness

Global thermodynamic data were collected from four pistons, *i.e.*; none of these pistons were instrumented with thermocouples. Thermal barrier coatings (TBC) of various thickness and surface roughness were applied to the piston crown. Three variations of pistons coated with a graded-layer TBC were tested. The conclusions from the TBC testing can be summarized as:

1. The heat transfer normalized by power for the very high-output conditions (4 and 5) showed statistically insignificant differences between any of the TBCs or the metal baseline. Similarly, no statistical change in efficiency (ITEg) or heat transfer ($\dot{Q}_{gas}$) was observed for either of these cases. For both of these operating conditions a very long injection duration was used that causes a portion of the spray to be targeted outside the piston bowl, potentially reducing the impact the TBCs have on heat transfer.

2. The *polished* TBC showed an increased ITEg when compared to the metal baseline for traditional engine loads (operating conditions 1-3). Increases in ITEg corresponded with additional late-cycle AHRR and a reduction in $\dot{Q}_{gas}$. The additional late-cycle AHRR corresponded with the crank angle of maximum spatially averaged piston heat flux (on instrumented metal pistons). Contours of piston heat flux at these crank angles may suggest that the change in ITEg is related to the heat flux in the piston bowl.

3. The *rough* (as-sprayed) TBCs for traditional engine loads (operating conditions 1-3), in reference to the metal piston, showed no statistically significant change in ITEg or heat transfer from the gas, $\dot{Q}_{gas}$. For most cases, pistons with higher surface roughness TBCs showed increased exhaust smoke when compared to the metal baseline. This effect was most pronounced at retarded SOI timings that had elevated FSN. When the

coating was polished, the FSN for all operating conditions and SOI timings was similar to the metal baseline and less than the as-sprayed coating.

7.1.3 Engine Heat Transfer Correlation for High-output Operating Conditions

A new instantaneous spatially averaged heat transfer correlation was developed on the based surface heat flux acquired on two instrumented metal pistons. Spatially averaged heat flux, $\langle \dot{q}'' \rangle$, and spatially averaged piston temperature, $\langle T_{piston} \rangle$, were used to calculate a heat transfer coefficient. Different functional forms of heat transfer correlations were explored and compared to the experimental data. The conclusions based on the heat transfer correlation development can summarized as:

1. A new engine heat transfer correlation was developed for high-output diesel operating conditions. The correlation was based on a new dimensionless form: $Nu = CRe^m f(\tilde{q}_{ch})$. Including dimensionless chemical energy release rate, $\tilde{q}_{ch}$, in the correlations provided the best fit to experimental data and was consistent with the dimensional analysis.

2. Various dimensional forms of the heat transfer correlation were investigated including different functional forms for $f(\tilde{q}_{ch})$ and v. A non-linear squares solver was used to find the optimum coefficients for each specific case, which allowed error between functional forms to be compared. A heat transfer correlation with form: $h = a_1 v^m P^m T^{-m} k \mu^{-m} \frac{(a_2 \tilde{q}_{ch} + a_3)}{(\tilde{q}_{ch} + a_3)}$ was found to be the best fit to the data using the least number of constants.

3. A new definition of velocity, $v = a_4 + a_5 \int_{\theta_{SOI}}^{\theta} \frac{dm_{fuel}}{d\theta} d\theta$, included a cumulative fuel mass term (*i.e.*, integrated rate of injection) and a constant term. Including a mean piston speed term, $\bar{S_p}$, as many of previous correlations have, was investigated but ultimately not pursued because the experimental data did not support such a term.

4. Cumulative local heat transfer (found from the new correlation) and global thermodynamic measurements agreed well over all the operating conditions investigated. When additional operating conditions, which were not used to develop the model, were tested the model appears to become predictive.

5. Additional physics was included in the new correlation by the addition of $\tilde{q}_{ch}$, but no additional information was needed to calculate this term. AHRR and other terms are only a function of P, T and V, which are already needed for the correlation. Because time-varying spatially averaged heat transfer correlations are often used in reduced-order engine simulation, calculating $\tilde{q}_{ch}$ may be inconvenient; as such, a second correlation that eliminated $f(\tilde{q}_{ch})$ was developed. This second correlation should provide more accurate results than existing correlations, but was less accurate than the full correlation.

7.2 Recommendations

Recommendations for each specific section of this work are given next.

7.2.1 Metal Piston Heat Flux Measurements in a High-output Diesel Engine

As part of this study, a large number of heat flux measurements were combined, interpolated and spatially averaged to find the spatially averaged heat flux, $\langle \dot{q}'' \rangle$. Based on experience from this study a number of recommendations are made:

1. In future work the locations of fast-response thermocouples can be optimized to make $\langle \dot{q}'' \rangle$ representative of the entire combustion chamber while minimizing the total number of measurements need. Based on result from this effort, fewer measurements are needed near the center of the piston and additional measurement are needed near the bowl, bowl lip and squish region (outer area of piston surface). For longer injection events that

have spray targeting outside the piston bowl additional measurements on the liner may provide useful data. On most engine hardware configurations, thermocouple placement is limited by packaging considerations, so focusing on optimizing thermocouple placement on the piston may be a more practical approach.

2. Comparison of local and global heat transfer should be made for other diesel engine geometries using a heat flux interpolation method similar to the one proposed as part of this work. Operating conditions should be selected to include a wide range of expected global heat transfer, which will allow the most robust comparison.

3. To reconstruct surface heat flux a co-axial design thermocouple is recommended for future experiments. The agreement of local heat transfer (based on co-axial thermocouple data) to global heat transfer demonstrates the functionality of these sensors. Experiments conducted using a prototype pair-wire thermocouple did not produce reasonable heat flux results (see Appendix A.10).

7.2.2 Impact of Thermal Barrier Coating Roughness

The impact of thermal barrier coating roughness on high-load diesel operation was explored using three piston TBC samples. It is recommended that future development work explore the following:

1. A thicker TBC, or an area on the piston with a thicker TBC should be explored. The thickest coating tested as part of this work was 0.325 mm but of that only 0.210 mm was TBC; the remaining thickness was a mixture of bond coat and TBC with thermal properties similar to the steel piston. Piston heat flux on a metal piston (no TBC) showed the highest intensity of heat flux in the piston bowl which motivates the need to insulate this particular region with a thicker TBC. Independently coating and evaluating the three distinct regions of the piston: 1) center, 2) bowl and 3) squish would help isolate the impact of each region.

2. It is recommended that additional experiments be run at constant compression ratio to isolate the impact from any other thermodynamic efficiency increase. This is of particular importance if total coating thickness is to increase compared to the total thickness in this effort.

3. To explore heat transfer for a piston coated with a TBC, low-speed thermocouples that are mounted subsurface to the metal are recommended. The low-speed subsurface thermocouple eliminate the durability problems typically encountered with the fast-response surface thermocouples. This configuration would allow piston temperature to be measured on a metal uncoated piston and allow a TBC to subsequently be added to the same piston, which would help eliminate uncertainty regarding thermocouple placement. This study attempted to use pair-wire type fast-response thermocouples at the metal-TBC interface but durability problems limited the amount of quality data acquired.

4. Further TBC development should be guided by reduced-order models. A one-dimensional conduction solver coupled to combustion and heat transfer model (such as the one proposed as part of this work) should provide guidance on TBC material properties and thickness.

7.2.3 Engine Heat Transfer Correlation for High-output Operating Conditions

The following work based on the engine heat transfer correlation development is recommended:

1. Additional experiments on the engine hardware of this study could provide additional fidelity to the final correlation. Specifically, experiments where in-cylinder swirl is changed would allow a better understanding of the velocity term. Additional experiments where multiple fuel injections are run would test the robustness of the integrated fuel

rate-of-injection term proposed as part of the velocity. Only single-injection events were tested in this study.

2. The heat transfer correlation proposed as part of this work should be tested on other engines where surface heat flux was acquired. Such testing would support validation of the proposed correlation and give understanding to the amount of coefficient tuning that is necessary. It may be possible to develop coefficient tuning method using only global thermodynamic data because of the strong agreement between global and local heat transfer in this work. Such a tuning method would allow calibration of the model to different types of engine hardware without the need for surface heat flux data.

3. The heat transfer correlation proposed as part of this work only focused on closed-cycle analysis. Further work using the data from the open portion of the cycle can be used to develop (or validate) other heat transfer models.

4. The heat transfer model developed should be integrated with a one-dimensional conduction solver and linked to a combustion model. The combined reduced-order model will allow parametric studies of materials (*e.g.* TBCs) and operating conditions that may reduce total engine heat transfer.

Bibliography

[1] A. Alkidas. Performance and Emissions Achievements with an Uncooled Heavy-duty, Single-cylinder Diesel Engine. *SAE Technical Paper 890144*, 1989.

[2] A. A. Amsden. KIVA-3V: A Block-structured KIVA Program for Engines with Vertical or Canted Valves. Technical report, Los Alamos National Lab., NM (United States), 1997.

[3] M. Andrie, S. Kokjohn, S. Paliwal, L. S. Kamo, A. Kamo, and D. Procknow. Low heat capacitance thermal barrier coatings for internal combustion engines. *SAE Technical Paper 2019-01-0228*, 2019.

[4] P. P. Andruskiewicz. *Analytical and experimental investigation of temperature-swing insulation on engine performance*. Doctoral dissertation, Universitat Politecnica De Valencia, 2017.

[5] C. Angelberger, T. Poinsot, and B. Delhay. Improving Near-wall Combustion and Wall Heat Transfer Modeling in SI Engine Computations. *SAE Technical Paper 972881*, 1997.

[6] W. Annand and T. Ma. Second Paper: Instantaneous Heat Transfer Rates to the Cylinder Head Surface of a Small Compression-ignition Engine. *Proceedings of the Institution of Mechanical Engineers*, 185(1):976–987, 1970.

[7] W. Annand et al. Heat Transfer in the Cylinders of Reciprocating Internal Combustion Engines. *Proceedings of the Institution of Mechanical Engineers*, 177(1):973–996, 1963.

[8] D. N. Assanis and E. Badillo. Transient Heat Conduction in Low-heat-rejection Engine Combustion Chambers. *SAE Technical Paper 870156*, 1987.

[9] D. N. Assanis and F. Friedmann. A telemetry linkage system for piston temperature measurements in a diesel engine. *SAE Technical Paper 910299*, 1991.

[10] D. N. Assanis, K. Wiese, E. Schwarz, and W. Bryzik. The Effects of Ceramic Coatings on Diesel Engine Performance and Exhaust Emissions. *SAE Technical Paper 910460*, 1991.

[11] J. V. Beck, B. Blackwell, and C. S. Clair Jr. *Inverse Heat Conduction Problems*. 1985.

[12] J. Benajes, J. Martin, A. Garcia, D. Villalta, A. Warey, V. Domenech, and A. Vassallo. An investigation of radiation heat transfer in a light-duty diesel engine. *SAE International Journal of Engines*, 8(5):2199–2212, 2015.

[13] D. Bendersky. A Special Thermocouple for Measuring Transient Temperatures. *Mechanical Engineering*, 75(2):117–121, 1953.

[14] G. Borman and K. Nishiwaki. Internal-combustion engine heat transfer. *Progress in energy and combustion science*, 13(1):1–46, 1987.

[15] J. Caton. Comparisons of thermocouple, time-averaged and mass-averaged exhaust gas temperatures for a spark-ignited engine. *SAE Technical Paper 820050*, 1982.

[16] J. A. Caton. Comparisons of global heat transfer correlations for conventional and high efficiency reciprocating engines. pages 327–337. American Society of Mechanical Engineers, 2011.

[17] J. Chang, O. Güralp, Z. Filipi, D. N. Assanis, T.-W. Kuo, P. Najt, and R. Rask. New Heat Transfer Correlation for an HCCI Engine Derived from Measurements of Instantaneous Surface Heat Flux. *SAE Technical Paper 2004-01-2996*, 2004.

[18] W. K. Cheng, V. W. Wong, and F. Gao. Heat Transfer Measurement Comparisons in Insulated and Non-insulated Diesel Engines. *SAE Technical Paper 890570*, 1989.

[19] W. Chi, S. Sampath, and H. Wang. Ambient and high-temperature thermal conductivity of thermal sprayed coatings. *Journal of Thermal Spray Technology*, 15(4):773–778, 2006.

[20] R. A. Churchill, J. E. Smith, N. Clark, and R. A. Turton. Low-heat Rejection Engines - a Concept Review. *SAE Technical Paper 880014*, 1988.

[21] T. F. Coleman and Y. Li. On the convergence of interior-reflective Newton methods for nonlinear minimization subject to bounds. *Mathematical programming*, 67(1-3):189–224, 1994.

[22] T. F. Coleman and Y. Li. An interior trust region approach for nonlinear minimization subject to bounds. *SIAM Journal on optimization*, 6(2):418–445, 1996.

[23] J. Dent and S. Sulaiman. Convective and Radiative Heat Transfer in a High Swirl Direct Injection Diesel Engine. *SAE Technical Paper 770407*, 1977.

[24] D. Dickey. The Effect of Insulated Combustion Surfaces on Direct Injection Diesel Engine Performance, Emissions and Combustion. *SAE Technical Paper 890292*, 1989.

[25] R. P. Durrett, P. M. Najt, P. P. Andruskiewicz IV, G. P. Hill, and T. A. Schaedler. Ceramic microsphere thermal barrier coating, August 7 2018. US Patent App. 10/040,723.

[26] R. P. Durrett, P. M. Najt, P. P. Andruskiewicz IV, T. A. Schaedler, G. P. Hill, J. H. Martin, and C. J. Ro. Internal combustion engine and method for coating internal combustion engine components, February 8 2018. US Patent App. 15/230,701.

[27] G. D. Ebersole, P. Myers, and O. Uyehara. The radiant and convective components of diesel engine heat transfer. *SAE Technical Paper 630148*, 1963.

[28] G. Eichelberg. Some New Investigations on Old Combustion Engine Problems. *Engineering*, 148(27):463–466, 1939.

[29] C. Finol and K. Robinson. Thermal Modelling of Modern Engines: a Review of Empirical Correlations to Estimate the In-cylinder Heat Transfer Coefficient. *Proceedings of the institution of mechanical engineers, part D: journal of automobile engineering*, 220(12): 1765–1781, 2006.

[30] P. Flynn, M. Mizusawa, O. A. Uyehara, and P. S. Myers. An experimental determination of the instantaneous potential radiant heat transfer within an operating Diesel engine. *SAE Transactions*, pages 95–126, 1972.

[31] K. Fukui, Y. Wakisaka, K. Nishikawa, Y. Hattori, H. Kosaka, and A. Kawaguchi. Development of Instantaneous Temperature Measurement Technique for Combustion Chamber Surface and Verification of Temperature Swing Concept. *SAE Technical Paper 2016-01-0675*, 2016.

[32] J. A. Gatowski. Evaluation of a Selectively-Cooled Single-Cylinder 05-L. Diesel Engine. *SAE Technical Paper 900693*, 1990.

[33] W. Ge, C. Zhao, and B. Wang. Thermal radiation and conduction in functionally graded thermal barrier coatings. Part I: Experimental study on radiative properties. *International Journal of Heat and Mass Transfer*, 134:101–113, 2019.

[34] E. Gingrich, J. Ghandhi, and R. Reitz. Experimental Investigation of Piston Heat Transfer in a Light Duty Engine Under Conventional Diesel, Homogeneous Charge Compression Ignition, and Reactivity Controlled Compression Ignition Combustion Regimes. *SAE International Journal of Engines*, 7(1):375–385, 2014.

[35] Z. Han and R. D. Reitz. A Temperature Wall Function Formulation for Variable-density Turbulent Flows with Application to Engine Convective Heat Transfer Modeling. *International journal of heat and mass transfer*, 40(3):613–625, 1997.

[36] P. Havstad, I. Garwin, and W. R. Wade. A Ceramic Insert Uncooled Diesel Engine. *SAE Technical Paper 860447*, 1986.

[37] T. Hendricks, J. Ghandhi, and J. Brossman. Instantaneous Local Heat Flux Measurements in a Small Utility Engine. In *ASME 2009 Internal Combustion Engine Division Spring Technical Conference*, pages 439–450. American Society of Mechanical Engineers, 2009.

[38] T. L. Hendricks. *Instantaneous Heat Flux Measurements in Internal Combustion Engines*. Doctoral dissertation, University of Wisconsin - Madison, 2011.

[39] T. L. Hendricks, D. A. Splitter, and J. B. Ghandhi. Experimental Investigation of Piston Heat Transfer Under Conventional Diesel and Reactivity-controlled Compression Ignition Combustion Regimes. *International Journal of Engine Research*, 15(6):684–705, 2014.

[40] C. Hennes, J. Lehmann, and T. Koch. Possibilities of Wall Heat Transfer Measurements at a Supercharged Euro VI Heavy-Duty Diesel Engine with High EGR-Rates, an In-Cylinder Peak Pressure of 250 Bar and an Injection Pressure up to 2500 Bar. *SAE Technical Paper 2019-24-0171*, 2019.

[41] J. B. Heywood. *Internal Combustion Engine Fundamentals*. McGraw-Hill, 1988.

[42] G. F. Hohenberg. Advanced Approaches for Heat Transfer Calculations. *SAE Technical Paper 790825*, 1979.

[43] IR-Telemetrics. Specialty Thermocouples. URL `https://irtelemetrics.com/products/specialty-thermocouples`.

[44] S. Jaichandar and P. Tamilporai. Low Heat Rejection Engines - an Overview. *SAE Technical Paper 2003-01-0405*, 2003.

[45] R. Kamo and W. Bryzik. Adiabatic Turbocompound Engine Performance Prediction. *SAE Technical Paper 780068*, 1978.

[46] R. Kamo and W. Bryzik. Cummins/TACOM Advanced Adiabatic Engine. *SAE Technical Paper 840428*, 1984.

[47] R. Kamo, N. S. Mavinahally, L. Kamo, W. Bryzik, and E. E. Schwartz. Injection Characteristics that Improve Performance of Ceramic Coated Diesel Engines. *SAE Technical Paper 1999-01-0972*, 1999.

[48] S. Klein. Engineering Equation Solver (Version 10.644-3D). URL `http://www.fchartsoftware.com/ees/`.

[49] B. Knight. The Problem of Predicting Heat Transfer in Diesel Engines. In *Proceedings of the Institution of Mechanical Engineers, Conference Proceedings*, volume 179, pages 99–115. SAGE Publications, 1964.

[50] T. Kogo, Y. Hamamura, K. Nakatani, T. Toda, A. Kawaguchi, and A. Shoji. High Efficiency Diesel Engine with Low Heat Loss Combustion Concept-Toyota's Inline 4-Cylinder 2.8-Liter ESTEC 1GD-FTV Engine. *SAE Technical Paper 2016-01-0658*, 2016.

[51] H. Kosaka, Y. Wakisaka, Y. Nomura, Y. Hotta, M. Koike, K. Nakakita, and A. Kawaguchi. Concept of "Temperature Swing Heat Insulation" in Combustion Chamber Walls, and Appropriate Thermo-Physical Properties for Heat Insulation Coat. *SAE International Journal of Engines*, 6(2013-01-0274):142–149, 2013.

[52] B. E. Launder and D. Spalding. The Numerical Computation of Turbulent Flows. *Computer Methods in Applied Mechanics and Engineering*, 3(2):269–289, 1974.

[53] T. LeFeuvre, P. S. Myers, and O. A. Uyehara. Experimental Instantaneous Heat Fluxes in a Diesel Engine and their Correlation. *SAE Technical Paper 690464*, 1969.

[54] E. W. Lemmon and R. T. Jacobsen. Viscosity and thermal conductivity equations for nitrogen, oxygen, argon, and air. *International journal of thermophysics*, 25(1):21–69, 2004.

[55] B. J. McBride, M. J. Zehe, and S. Gordon. NASA Glenn coefficients for calculating thermodynamic properties of individual species, 2002.

[56] MEDTHERM CORP. Coaxial Surface Thermocouple Probes, Bulletin 500, 2006.

[57] S. Memme. *The influence of thermal barrier coating surface roughness on spark-ignition engine performance and emissions*. Master's thesis, University of Toronto, 2012.

[58] S. A. Miers, C. L. Anderson, J. R. Blough, and M. K. Inal. Impingement identification in a high speed diesel engine using piston surface temperature measurements. *SAE transactions*, pages 845–851, 2005.

[59] Y. Miyairi, T. Matsuhisa, T. Ozawa, H. Oikawa, and N. Nakashima. Selective Heat Insulation of Combustion Chamber Walls for a DI Diesel Engine with Monolithic Ceramics. *SAE Technical Paper 890141*, 1989.

[60] C. H. Moore and J. L. Hoehne. Combustion Chamber Insulation Effect on the Performance of a Low Heat Rejection Cummins V-903 Engine. *SAE Technical Paper 860317*, 1986.

[61] S. Moser, R. O'Donnell, M. Hoffman, E. Jordan, T. Powell, and Z. Filipi. Experimental Investigation of Low Cost, Low Thermal Conductivity Thermal Barrier Coating on HCCI Combustion, Efficiency, and Emissions. *SAE Technical Paper*, 2020.

[62] M. P. Musculus. Measurements of the influence of soot radiation on in-cylinder temperatures and exhaust NOx in a heavy-duty DI diesel engine. *SAE transactions*, pages 845–866, 2005.

[63] NATO. Logistics Handbook, 2007.

[64] NATO. NATO-AFLP-3747, Guide Specification (Minimum Quality Standards) for Aviation Turbine Fuels (F-24, F-27, F-34, F-35, F-37, F-40 and F-44), 2016.

[65] N. Nishikawa, T. Hijii, A. Kawaguchi, R. Yatsuduka, F. Shimizu, Y. Wakisaka, and H. Kosaka. Internal Combustion Engine and Method for Manufacturing the Same, August 23 2011. US Patent App. 13/817,966.

[66] NIST/SEMATECH. e-Handbook of Statistical Methods. URL `http://www.itl.nist.gov/div898/handbook/`.

[67] W. Nusselt. *Der Wärmeübergang in der Verbrennungskraftmaschine*. Verlag d. Vereines deutscher Ingenieure, 1923.

[68] R. O'Donnell. *Experimental and Analytical Techniques for Evaluating the Impact of Thermal Barrier Coatings on Low Temperature Combustion*. Doctoral dissertation, Clemson University, 2018.

[69] R. O'Donnell, T. Powell, M. Hoffman, E. Jordan, and Z. Filipi. Inverse analysis of in-cylinder gas-wall boundary conditions: Investigation of a yttria-stabilized zirconia thermal barrier coating for homogeneous charge compression ignition. *Journal of Engineering for Gas Turbines and Power*, 139(10):102808, 2017.

[70] R. N. O'Donnell, T. R. Powell, Z. S. Filipi, and M. A. Hoffman. Estimation of thermal barrier coating surface temperature and heat flux profiles in a low temperature combustion engine using a modified sequential function specification approach. *Journal of Heat Transfer*, 139(4):041201, 2017.

[71] T. Oguri and S. Inaba. Radiant heat transfer in diesel engines. *SAE Transactions*, pages 127–147, 1972.

[72] V. D. Overbye, J. E. Bennethum, O. Uyehara, and P. Myers. Unsteady Heat Transfer in Engines. *SAE Technical Paper 610041*, 1961.

[73] T. Powell. *Impacts of Thermal Barrier Coating Morphology and Catalytic Properties on Low Temperature Combustion Engine In-Cylinder Processes.* Doctoral dissertation, Clemson University, 2018.

[74] T. Powell, R. O'Donnell, M. Hoffman, and Z. Filipi. Impact of a yttria-stabilized zirconia thermal barrier coating on hcci engine combustion, emissions, and efficiency. *Journal of Engineering for Gas Turbines and Power*, 139(11):111504, 2017.

[75] C. Raffa, E. Schwarz, and J. Tasdemir. Combat Vehicle Engine Selection Methodology Based On Vehicle Integration Considerations. *SAE Technical Paper 2005-01-1545*, 2005.

[76] B. Rosner. Percentage points for a generalized ESD many-outlier procedure. *Technometrics*, 25(2):165–172, 1983.

[77] S. Sampath, W. Smith, T. Jewett, and H. Kim. Synthesis and characterization of grading profiles in plasma sprayed NiCrAlY-zirconia FGMs. In *Materials science forum*, volume 308, pages 383–388. Trans Tech Publ, 1999.

[78] S. Sasaki, H. Masuda, H. Kou, and H. Takahashi. A transient heating technique for measuring the thermal diffusivity of metals. *International journal of thermophysics*, 19 (1):259–279, 1998.

[79] P. Schihl. On the Availability of Commercial Off-the-Shelf (COTS) Heavy-Duty Diesel Engines for Military Ground Vehicle Use. *SAE International Journal of Engines*, 2(1): 1520–1527, 2009.

[80] M. F. Shabir, S. Authars, S. Ganesan, R. Karthik, and S. K. Madhan. Low Heat Rejection Engines - Review. *SAE Technical Paper 2010-01-1510*, 2010.

[81] K. Sihling and G. Woschni. Experimental Investigation of the Instantaneous Heat Transfer in the Cylinder of a High Speed Diesel Engine. *SAE Technical Paper 790833*, 1979.

[82] G. Sitkei and G. Ramanaiah. A Rational Approach for Calculation of Heat Transfer in Diesel Engines. *SAE Technical Paper 720027*, 1972.

[83] S. Skeen, J. Manin, L. Pickett, K. Dalen, and A. Ivarsson. Quantitative spatially resolved measurements of total radiation in high-pressure spray flames. *SAE Technical Paper 2014-01-1252*, 2014.

[84] Southwest Research Institute. Research Need for More Compact Intermittent Combustion Propulsion Systems for Army Combat Vehicles- Volume I, 1995.

[85] Southwest Research Institute. Research Need for More Compact Intermittent Combustion Propulsion Systems for Army Combat Vehicles- Volume II, 1995.

[86] V. Srinivasan, M. Friis, A. Vaidya, T. Streibl, and S. Sampath. Particle injection in direct current air plasma spray: salient observations and optimization strategies. *Plasma Chemistry and Plasma Processing*, 27(5):609–623, 2007.

[87] F. Struwe and D. E. Foster. In-cylinder measurement of particulate radiant heat transfer in a direct injection diesel engine. *SAE transactions*, pages 293–313, 2003.

[88] C. F. Taylor. *The Internal-combustion Engine in Theory and Practice: Thermodynamics, Fluid Flow, Performance*, volume 2. MIT press, 1985.

[89] C. F. Taylor and T.-Y. Toong. Heat Transfer in Internal-combustion Engines. American Society of Mechanical Engineers, 1957.

[90] U.S. Department of Defense. MIL-DTL-83133J, Detail Specification: Turbine Fuel, Aviation, Kerosene Type, JP-8 (NATO F-34), NATO F-35, and JP-8+100 (NATO F-37), 2015.

[91] A. Vaidya, V. Srinivasan, T. Streibl, M. Friis, W. Chi, and S. Sampath. Process maps for plasma spraying of yttria-stabilized zirconia: An integrated approach to design, optimization and reliability. *Materials Science and Engineering: A*, 497(1-2):239–253, 2008.

[92] Y. Wakisaka, H. Kosaka, M. Inayoshi, Y. Hotta, K. Nakakita, S. Iida, and Y. Nomura. Internal Combustion Engine, August 08 2008. International Patent App. PCT/JP2008/064304.

[93] Y. Wakisaka, M. Inayoshi, K. Fukui, H. Kosaka, Y. Hotta, A. Kawaguchi, and N. Takada. Reduction of Heat Loss and Improvement of Thermal Efficiency by Application of "Temperature Swing" Insulation to Direct-Injection Diesel Engines. *SAE International Journal of Engines*, 9(2016-01-0661), 2016.

[94] V. W. Wong, W. Bauer, R. Kamo, W. Bryzik, and M. Reid. Assessment of Thin Thermal Barrier Coatings for IC Engines. *SAE Technical Paper 950980*, 1995.

[95] G. Woschni. Die Berechnung der Wandverluste und der thermischen Belastung der Bauteile von Dieselmotoren MTZ 31 (1970) 12. *Nr*, 12:491.

[96] G. Woschni. A Universally Applicable Equation for the Instantaneous Heat Transfer Coefficient in the Internal Combustion Engine. *SAE Technical Paper 670931*, 1967.

[97] G. Woschni, W. Spindler, and K. Kolesa. Heat Insulation of Combustion Chamber Walls-A Measure to Decrease the Fuel Consumption of IC Engines? *SAE Technical Paper 870339*, 1987.

[98] Z. Yan, B. Gainey, J. Gohn, D. Hariharan, J. Saputo, C. Schmidt, F. Caliari, S. Sampath, and B. Lawler. The Effects of Thick Thermal Barrier Coatings on Low-Temperature Combustion. *SAE Technical Paper 2020-01-0275*, 2020.

[99] H. Yun and W. Mirsky. Schlieren-streak measurements of instantaneous exhaust gas velocities from a spark-ignition engine. *SAE Transactions*, pages 3143–3158, 1974.

A Appendix

A.1 Lower Heating Value

For a constant flow system where fuel and air enter, combust and exit, the First Law can be written as:

$$\frac{dU}{dt} = \dot{Q} - \dot{W} + \sum \dot{m}h \tag{A.1}$$

where the summation is over all inlet and outlet locations. For a steady, isothermal system with no work extraction, heat is lost to the environment and is represented by $-\dot{Q}$. The First Law can then be written as:

$$-\dot{Q} = \sum_{inlet} \dot{m}_i h_i - \sum_{outlet} \dot{m}_i h_i \tag{A.2}$$

where the summation index, i, is over the species present. For the special case where the temperature is chosen as the reference temperature of 298.15K one finds:

$$-\frac{\dot{Q}}{\dot{m}} = y_{fuel}\Delta h_{f,fuel} - \sum_{outlet} y_i \Delta h_{f,i} \tag{A.3}$$

where $\Delta h_{f,i}$ is the standard enthalpy of formation of species, i and the standard enthalpy of formation of the fuel is $\Delta h_{f,fuel}$. The lower heating value (LHV) is defined not on a mass of mixture basis but rather a mass of fuel basis so equation A.3 can be divided by the fuel mass fraction which is the definition of LHV:

$$LHV \equiv -\frac{\dot{Q}}{y_{fuel}\dot{m}} = \Delta h_{f,fuel} - \frac{1}{y_{fuel}} \sum_{outlet} y_i \Delta h_{f,i} \tag{A.4}$$

Because the LHV is found assuming a stoichiometric air-fuel mixture with H_2O, CO_2, and N_2 as the products, the summation symbol is shown with the word *ideal* to emphasize that the products are complete combustion products.

$$LHV \equiv -\frac{\dot{Q}}{y_{fuel}\dot{m}} = \Delta h_{f,fuel} - \frac{1}{y_{fuel}} \sum_{ideal,prod} y_i \Delta h_{f,i} \tag{A.5}$$

A.2 Combustion Efficiency

When the reactions are incomplete because the mixture is rich or thermodynamic conditions did not allow for complete combustion there will be less energy release than ideal stoichiometric case in equation A.5. The combustion efficiency can be defined as the ratio of actual energy release to the ideal amount of energy release:

$$\eta_c \equiv \frac{\Delta h_{f,fuel} - \frac{1}{y_{fuel}} \sum_{actual,prod} y_i \Delta h_{f,i}}{\Delta h_{f,fuel} - \frac{1}{y_{fuel}} \sum_{ideal,prod} y_i \Delta h_{f,i}} = \frac{\left[\frac{\dot{Q}}{y_{fuel}\dot{m}}\right]_{actual}}{\left[\frac{\dot{Q}}{y_{fuel}\dot{m}}\right]_{ideal}} = \frac{\left[\frac{\dot{Q}}{y_{fuel}\dot{m}}\right]_{actual}}{LHV} \tag{A.6}$$

A.3 Global Energy Balance

For a control volume that surrounds the entire engine, with inlet and outlet streams i, where brake work, $\dot{W}_b$, is crossing the boundary, and heat transfer to the surrounding, $\dot{Q}_s$, includes convection to the air and radiation, the First Law can be written as:

$$0 = -\dot{Q}_s - \dot{W}_b + \sum_{inlet} \dot{m}_i y_i h_i - \sum_{outlet} \dot{m}_i y_i h_i \tag{A.7}$$

where m_i is the mass flow, y_i is mass fraction, and h_i enthalpy. Expanding enthalpy in terms of heat of formation, $\Delta h_{f,i}$, and sensible enthalpy, h_i^s:

$$0 = -\dot{Q}_s - \dot{W}_b \sum_{inlet} \dot{m}_i y_i (\Delta h_{f,i} + h_i^s) - \sum_{outlet} \dot{m}_i y_i (\Delta h_{f,i} + h_i^s) \tag{A.8}$$

Referring to the outlet as products and isolating the sensible enthalpy of the air, oil and coolant streams:

$$\begin{aligned} 0 = -\dot{Q}_s - \dot{W}_b + \dot{m}_{air} h_{air}^s + \dot{m}_{fuel}(h_{fuel}^s + \Delta h_{f,fuel}) - \dot{m}_{exh} \sum_{prod} y_i h_i^s - \dot{m}_{exh} \sum_{prod} y_i \Delta h_{f,i} \\ + \dot{m}_{oil}(h_{oil,in}^s - h_{oil,out}^s) + \dot{m}_{cool}(h_{cool,in}^s - h_{cool,out}^s) \end{aligned} \tag{A.9}$$

where the only reactant with non-zero enthalpy of formation is the fuel, which along with the product heats of formation can be written in terms of lower heating value, LHV (see Appendix A.1), and the combustion efficiency, η_c (see Appendix A.2). It is worth noting that both exhaust gas recirculation (EGR) and friction are internal to the system.

$$\begin{aligned} 0 = \dot{Q}_s + \dot{W}_b + \dot{m}_{exh} \sum_{prod} y_i h_i^s - \dot{m}_{air} h_{air}^s - \dot{m}_{fuel}(h_{fuel}^s + \eta_c LHV) \\ + \dot{m}_{oil}(h_{oil,out}^s - h_{oil,in}^s) + \dot{m}_{cool}(h_{cool,out}^s - h_{cool,in}^s) \end{aligned} \tag{A.10}$$

Equation A.10 can also be rewritten in terms of measured variables, which are highlighted in red. By inspection the grouping of each the oil and coolant terms represents *intentional* cooling of the engine and are identified by $\dot{Q}_{oil}$ and $\dot{Q}_{cool}$ respectively.

$$\dot{Q}_{global} = \dot{Q}_s + \overbrace{\dot{m}_{oil}(h^s_{oil,out}(T_{oil,out}) - h^s_{oil,in}(T_{oil,in}))}^{\dot{Q}_{oil}} + \overbrace{\dot{m}_{cool}(h^s_{cool,out}(T_{cool,out}) - h^s_{cool,in}(T_{cool,in}))}^{\dot{Q}_{cool}}$$
$$= \overbrace{\dot{m}_{fuel}(\eta_c LHV + h^s_{fuel}T_{fuel})}^{\dot{E}_{fuel}} - \dot{W}_b - \overbrace{\left((\dot{m}_{air} + \dot{m}_{fuel})(h^s_{exh}(T_{exh}) - h^{ref}_{exh}) - \dot{m}_{air}(h^s_{air}(T_{air}) - h^{ref}_{air})\right)}^{\dot{E}_{exh}} \tag{A.11}$$

The first term, $\dot{Q}_s$, represents convective and radiative heat transfer from the engine to the surroundings (which will be positive in practice). It will depend on surface area and temperature of the engine along with the temperature and other conditions of the surroundings. The heat transfer to the oil and coolant, $\dot{Q}_{oil}$, and $\dot{Q}_{cool}$ are found by measuring the mass flow and the temperature rise of each stream. On the right-hand side of the equation the terms grouped under $\dot{E}_{fuel}$ represent the energy delivered to the system through the fuel. The work done by the system is refereed to as brake power, $\dot{W}_b$. It is convenient to group the intake and exhaust flow stream terms and refer to them as $\dot{E}_{exh}$ which is sensible enthalpy flow of the exhaust minus that of the intake, which is typically small in comparison. A mass balance shows that the exhaust mass flow rate is equal to the combination of air and fuel. Strictly speaking η_c and $\dot{W}_b$ are not directly a measured quantity but can be calculated or measured through various methods.

The left-hand side of equation A.11 represents the total heat loss from the gas with friction added, which for this work, is defined as global heat transfer, $\dot{Q}_{global}$. The right-hand side of the equation can be used to solve for the $\dot{Q}_{global}$ and $\dot{Q}_{oil}$ and $\dot{Q}_{cool}$ can be used as a check to make sure $\dot{Q}_s$ losses are within reason. One of the difficulties of this energy balance method is that the exhaust temperature measurement is made downstream of where the exhaust exits the engine and is subject to periodic fluctuations in flow. Because of these reasons, the exhaust temperature reported is slightly less than the true value [15] and, therefore, over-estimates the engine heat transfer.

A.4 Heat Transfer from AHRR

A common *ad hoc* method to calculate heat transfer is to integrate the AHRR found in equation 3.7:

$$\oint AHRR \mathrm{d}\theta = \oint \dot{Q}_{ch} \mathrm{d}\theta - \oint \dot{Q}_w \mathrm{d}\theta \tag{A.12}$$

The $\oint \dot{Q}_{ch} \mathrm{d}\theta$ term can be equated to the fuel energy delivered per cycle modified by a combustion efficiency, *i.e.* $\eta_c m_{fuel} LHV$, where m_{fuel} is fuel mass per cycle.

$$Q_w \equiv \int \dot{Q}_w \mathrm{d}\theta = \eta_c m_{fuel} LHV - \int_{IVC}^{EVO} AHRR \mathrm{d}\theta \tag{A.13}$$

The value found in equation A.13 can then be normalized by the fuel energy per cycle, $m_{fuel} LHV$, which allows comparison to other heat transfer metrics normalized by fuel power, $\dot{m}_{fuel} LHV$. This method suffers from the limitations associated with heat release analysis

that include noise due to in-cylinder pressure oscillations and the inherent assumption that the combustion process can be reduced to a single homogeneous zone. The limits of integration shown in equation A.13 are constrained to the closed portion of the cycle (IVC to EVO) where the AHRR analysis is valid; the open portion of the cycle cannot be account for therefore this method underestimates the total heat transfer. Figure A.1 shows a comparison between $Q_w$and $\dot{Q}_{gas}$ as a function of $\dot{Q}_{global}$ for all operation conditions presented in this work. $\dot{Q}_{gas}$ is less than $\dot{Q}_{global}$ which is consistent with the elimination of friction from $\dot{Q}_{gas}$. Additionally, Q_w trends lower than $\dot{Q}_{gas}$ which is in agreement given this method is only constrained to the portion of the engine cycle. Q_w was not reported in this work, but was compared to the other reported values for data quality checks.

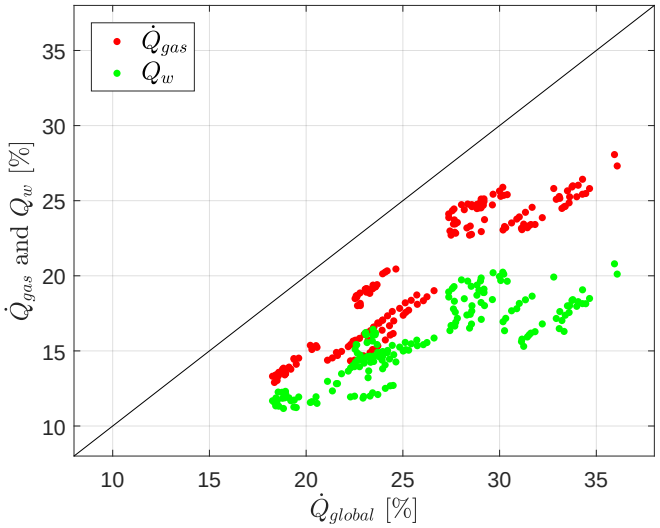


Figure A.1: Comparison of different heat transfer metrics

A.5 Thermal Barrier Coating Processing and Properties

All coatings were fabricated using an argon-hydrogen direct current atmospheric plasma spray process (Oerlikon Metco 3MB) with a 7 mm nozzle and a 1.85 mm 90 ° injector. Carrier gas flow rates were optimized on a per-run basis following principles reported by Srinivasan *et al.* [86]. Coatings were produced using gas flowrates of 45 and 8 NLPM of argon and hydrogen respectively, with 550 A of current at 30 kW of power, with choice of parameters selected using the framework of process maps based on a two-level three factor design of experiment as described by Vaidya *et al.* [91]. Piston surfaces were prepared for coating by first grit blasting at 80 psi at 125 mm using 24 mesh alumina grit, followed by the removal of entrained grit and organics with acetone before being rinsed in purified deionized water and dried with compressed air.

A functionally graded ceramic-metallic coating [77] was deposited in three layers: a NiCrAl bond coat (Oerlikon Metco 443NS) to increase adhesion and resist high temperature oxidation, a graded ceramic-metallic layer for increased mechanical compliance and reduced interfacial stresses of NiCrAl and yttria-stabilized zirconia (Saint-Gobain Coating Solutions SG204), and an insulating thermal barrier top coat. Specific layer compositions can be found in table A.1, with a diagrammatic depiction and microstructure available in figure 5.1. Despite the inclusion of relatively high thermal conductivity metallics the thermal conductivity of these coatings, as measured using a laser flash method, are much lower than traditional bulk ceramics due to their high defect concentrations and unique microstructures and morphologies [19].

Coating thickness and microstructural uniformity were ensured across the piston geometry by using a three-step coating development process. Parts were fixtured in a revolving carousel and rotated at 300 rpm while the plasma spray torch, controlled by a 6-axis robot traversed the piston geometry with the spray plume held normal to profile contours. Thickness was controlled by varying the torch velocity in each unique geometric section. First, tool-path optimization was performed with matching bowl contour steel strips that were coated with the three-layer system described above. The thickness was measured both by micrometer and cross-sectioned samples in a scanning electron microscope (SEM). Second, coatings were produced on piston blanks that mimicked both the geometry and thermal mass of actual parts for microstructural evaluation, which was preformed on cross-sectioned vacuum-cured mounts in an SEM. Finally, optimized coatings were produced the on piston crown with final thickness confirmed using non-destructive eddy current testing.



Figure A.2: Post testing TBC pistons from left to right: 0.185 mm as-sprayed, 0.325 mm as-sprayed, 0.325 mm polished

Table A.1: Coating layer properties

Layer	Composition	Density [kg/m^3]	Thermal Diffusivity [cm^2/s]	Thermal Conductivity [W/m-K]	Specific Heat [kJ/kg-K]
Thermal Barrier	443NS (5%) SG204 (95%)	4713	0.0042	0.77	387.5
Gradient Layer	443NS (30%) SG204 (70%)	3886	0.0403	0.85	385.1
Metallic Bond Coat	443NS (100%) SG204 (0%)	6255	0.0173	4.07	152.6

A.6 Piston Thermocouple Locations

Figures A.3, A.4 and A.5 show the location of fast-response thermocouples installed in the piston relative to other salient engine features. These figures all have the same orientation as viewed from above the engine looking from the gear-train side of the engine toward the dynamometer. Thermocouple numbers are given in descending order from left to right. The intake system has a quiescent and tangential port which allow the engine to have variable swirl ratio. The swirl direction in all images is clockwise. Exact location of thermocouples can be found in appendix A.7.

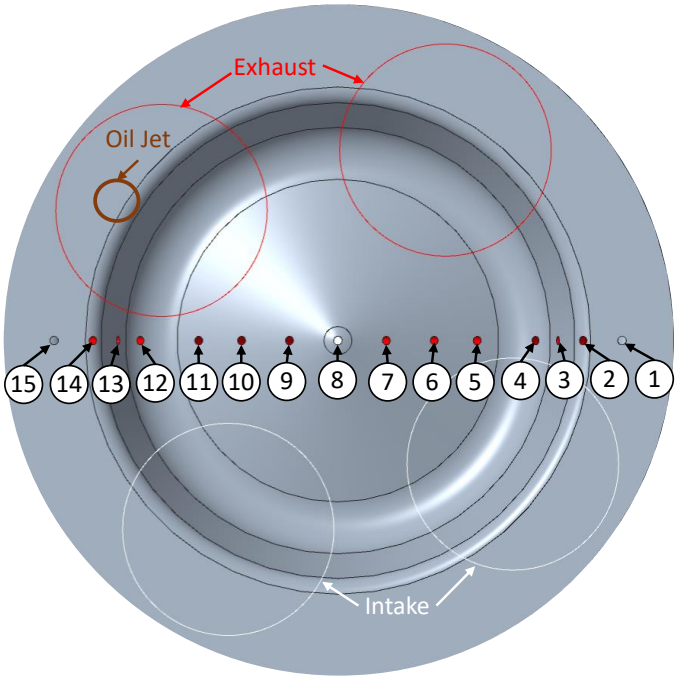


Figure A.3: Piston thermocouple locations with oil cooling jet (underside), intake valves (cylinder head), and exhaust valves (cylinder head) superimposed

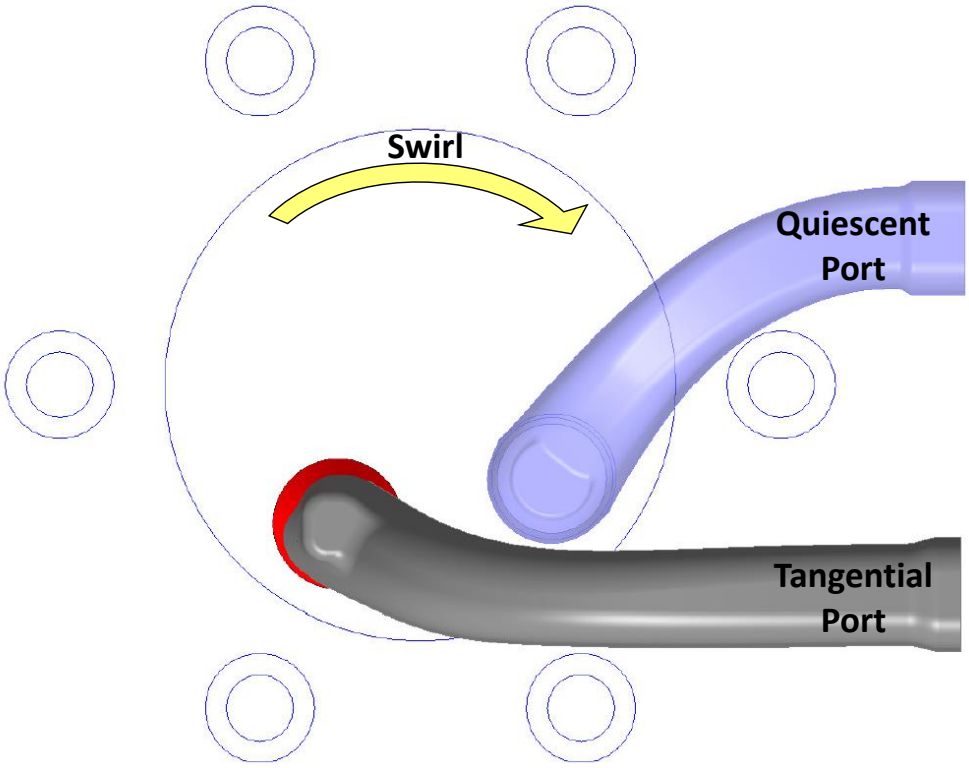


Figure A.4: Single-cylinder engine intake port layout

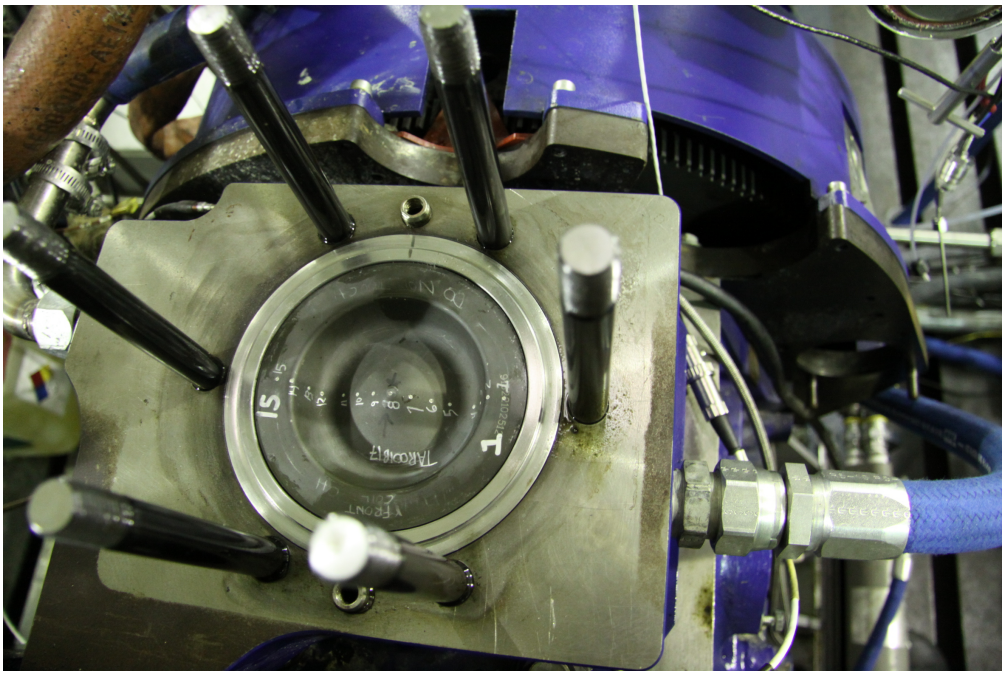
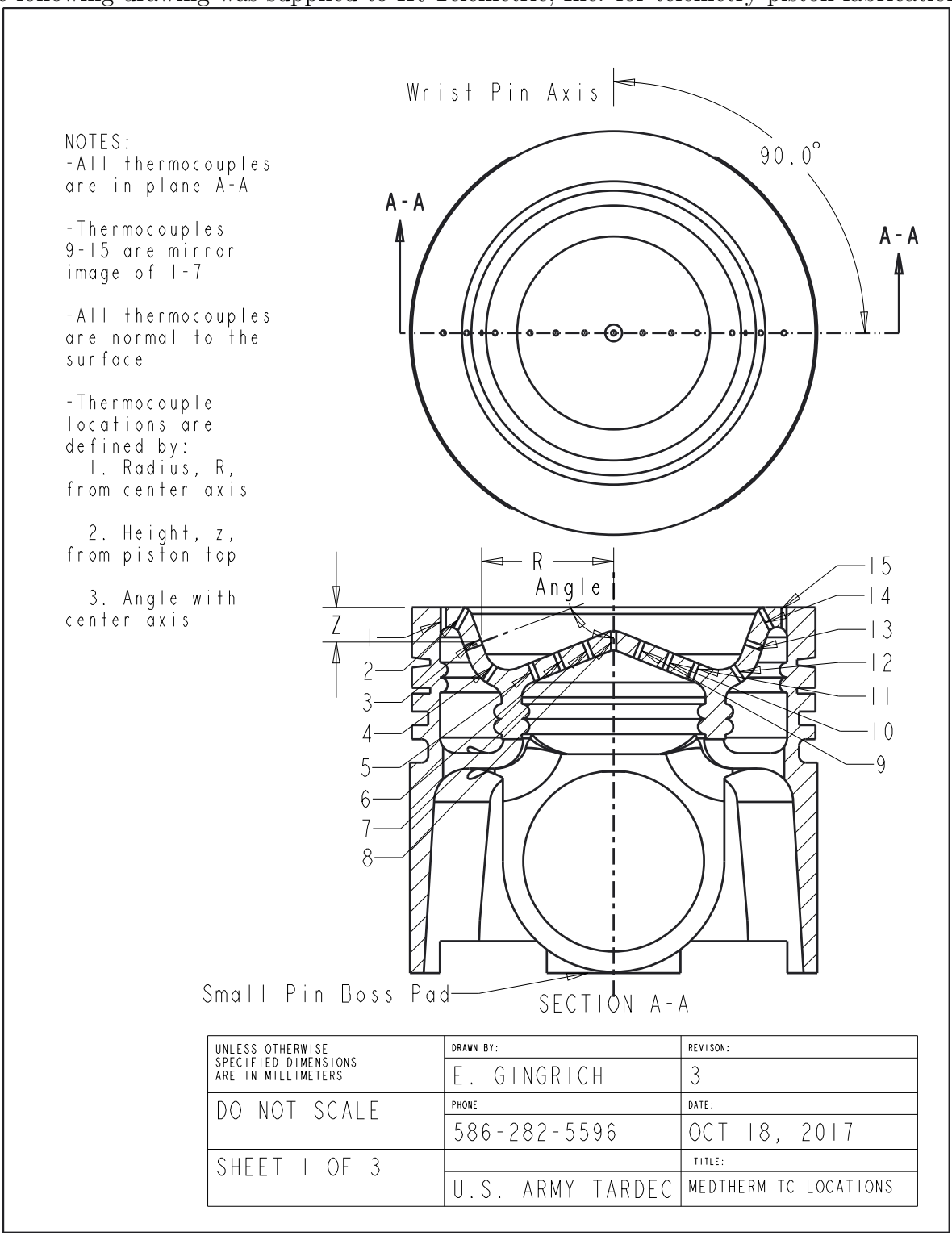


Figure A.5: Telemetry piston installed in engine

A.7 Piston Thermocouple Drawing

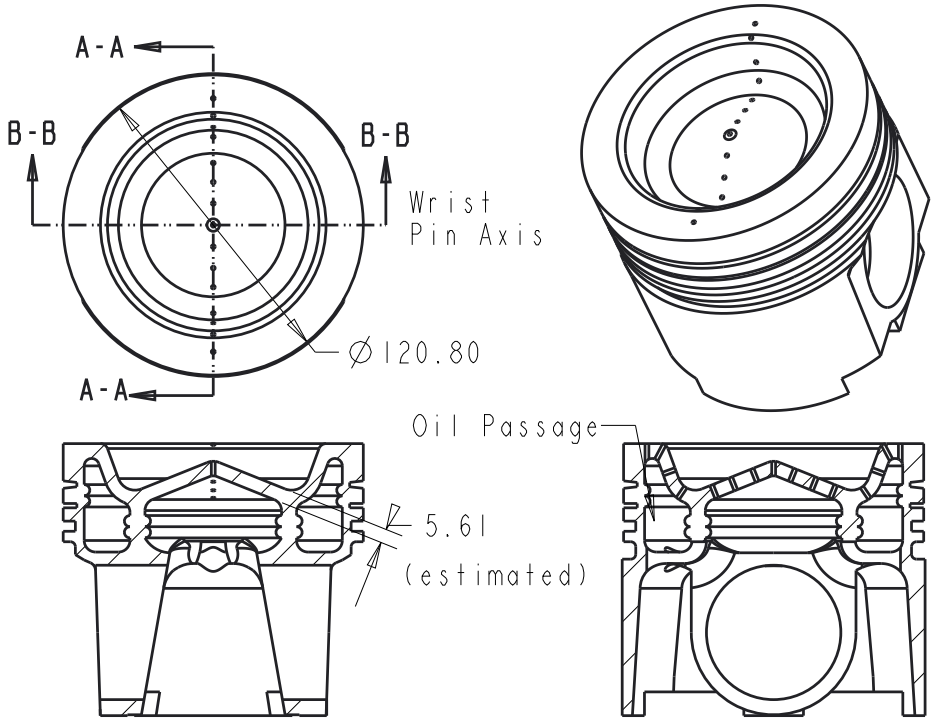
The following drawing was supplied to IR Telemetric, Inc. for telemetry piston fabrication.

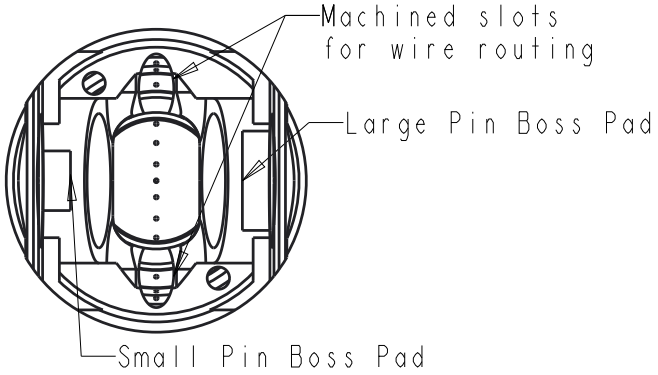


TC	R (mm)	Z (mm)	Angle (deg)	Contour Fit	Medtherm Part Number
1	51.0	0.0	VERTICAL	NO	TCS-061-JU-0.100-CR-12-10960
2	44.0	-0.35	27.8	YES	TCS-061-JU-0.100-12-10960
3	39.5	-10.4	70.0	NO	TCS-061-JU-0.100-CR-12-10960
4	35.5	-17.5	34.2	NO	TCS-061-JU-0.100-CR-12-10960
5	25.0	-17	-21.9	NO	TCS-061-JU-0.100-CR-12-10960
6	17.3	-13.6	-21.9	NO	TCS-061-JU-0.100-CR-12-10960
7	8.7	-10.1	-21.9	NO	TCS-061-JU-0.100-CR-12-10960
8	0.0	-7.0	VERTICAL	NO	TCS-061-JU-0.100-CR-12-10960
9	-8.7	-10.1	21.9	NO	TCS-061-JU-0.100-CR-12-10960
10	-17.3	-13.6	21.9	NO	TCS-061-JU-0.100-CR-12-10960
11	-25.0	-17.0	21.9	NO	TCS-061-JU-0.100-CR-12-10960
12	-35.5	-17.5	-34.2	NO	TCS-061-JU-0.100-CR-12-10960
13	-39.5	-10.4	-70.0	NO	TCS-061-JU-0.100-CR-12-10960
14	-44.0	-0.35	-27.8	YES	TCS-061-JU-0.100-12-10960
15	-51.0	0.0	VERTICAL	NO	TCS-061-JU-0.100-CR-12-10960

Medtherm Thermocouple Description:
-0.061in diameter J-Type Triaxial Surface thermocouple probe (Ungrounded junction)
-All probes except TC2 & TC14 with Chromium plating
-36 AWG single thermocouple wires, Teflon insulated
-Probes should be flush mounted with press-fit
-Total probe lenth must be limited to piston wall thickness of approximately 5mm (see sheet 3).

UNLESS OTHERWISE SPECIFIED DIMENSIONS ARE IN MILLIMETERS	DRAWN BY:	REVISON:
	E. GINGRICH	3
DO NOT SCALE	PHONE	DATE:
	586-282-5596	OCT 18, 2017
SHEET 2 OF 3		TITLE:
	U.S. ARMY TARDEC	MEDTHERM TC LOCATIONS





UNLESS OTHERWISE SPECIFIED DIMENSIONS ARE IN MILLIMETERS	DRAWN BY:	REVISON:
	E. GINGRICH	3
DO NOT SCALE	PHONE	DATE:
	586-282-5596	OCT 18, 2017
SHEET 3 OF 3		TITLE:
	U.S. ARMY TARDEC	MEDTHERM TC LOCATIONS

A.8 Injector Spray Locations

A Bosch CRIN3-18 high-pressure common-rail fuel injector was used in all experiments. The injector specifications are given in table A.2. Three different nozzle geometries were used where the only feature that differed between the nozzles was the spray plume location relative the thermocouple axis. Figure 4.2 shows the location of the spray plumes relative to the thermocouple axis for injectors $\epsilon = 22.5°$, $\epsilon = 11.25°$ and $\epsilon = 0.0°$. The ϵ designation is an angle used by Bosch to specify nozzle rotation relative to a reference feature on the nozzle. Additional angles, including the positioning of the injector in the head, are needed to determine the actual spray location in the engine. The resulting angles relative to the thermocouple axis are shown but the details of the intermediate reference angles have been omitted.

Table A.2: Fuel injector specifications

Manufacture	Bosch
Type	CRIN3-18
Holes	8
Orifice Diameter [μm]	167
Included Angle [°]	147
Maximum Pressure [bar]	2000

Post-testing optical imaging of two different TBC pistons was conducted. Figure A.6 shows a semi-transparent optical image overlaid and aligned to a solid model of the piston and thermocouples. These particular pistons were only run with the $\epsilon = 22.5°$ injector and had a TBC color that contrasted well with soot witness marks. Injector spray locations are shown in red and the thin blue circles are used to estimate the center of mass of the soot witness marks. This crude analysis shows that spray plumes have rotated in the direction of the swirl motion with an angle of around 7.5°. This analysis was conducted on the piston shown in left side of figure A.6 and the same witness marks circles were overladed on the right side of figure A.6 for additional confirmation. The location of spray plumes for the $\epsilon = 22.5°$ injector is approximately 2.0° off the piston thermocouple axis and subsequently will be refereed to as the "On-plume" injector. Table A.3 summarizes the different nozzle geometries and the adopted nomenclature.

Table A.3: Fuel injector nomenclature

Bosch Angle [°]	Thermocouple Axis Angle [°]	Nomenclature
$\epsilon = 22.5$	-5.5	On-plume
$\epsilon = 11.25$	5.75	Split-plume
$\epsilon = 0.0$	17.0	Off-plume

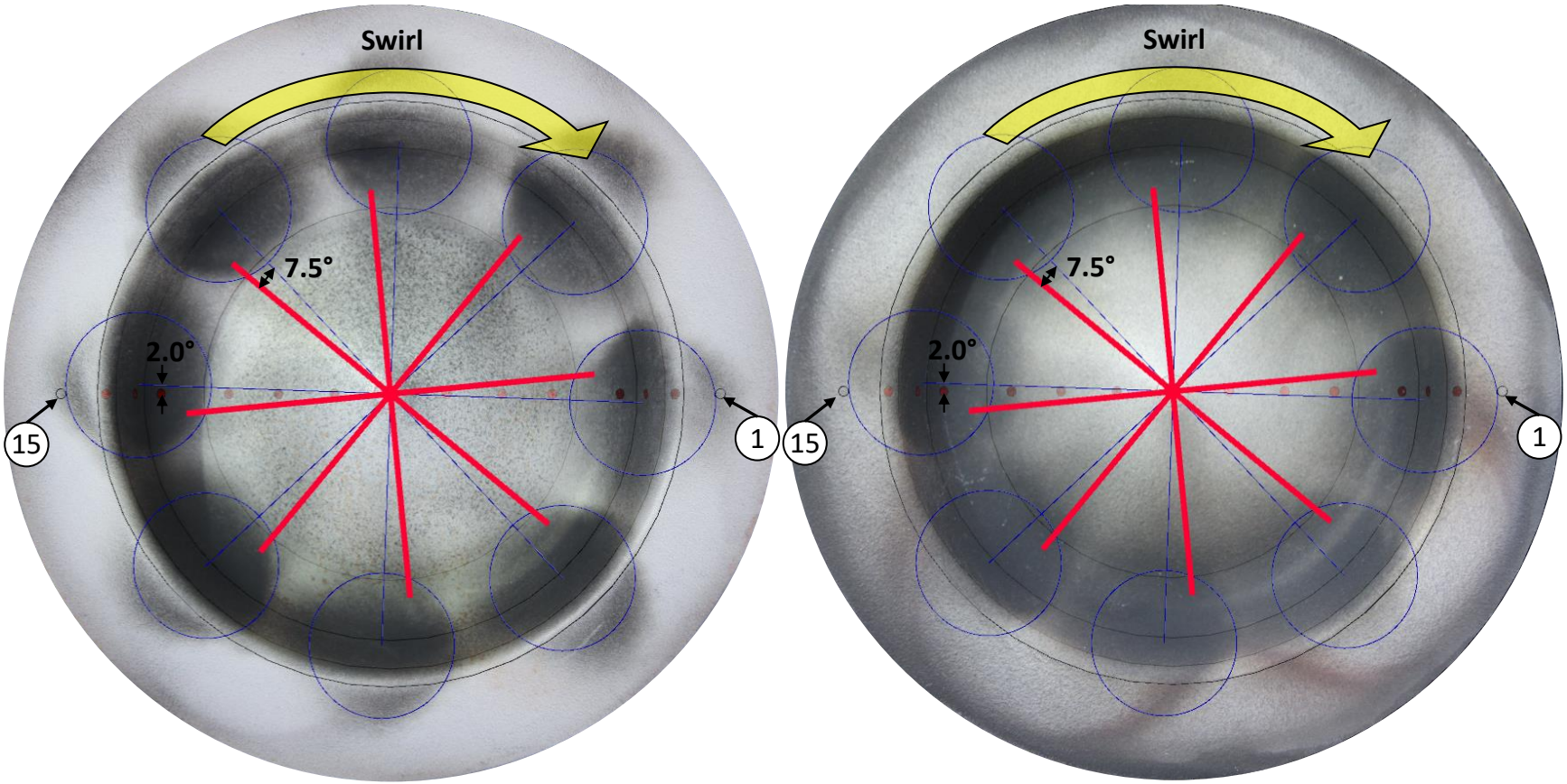


Figure A.6: Soot witness marks on pistons run with $\epsilon = 22.5°$ injector where red lines represent injector spray targeting and blue represent soot witness mark estimated center of mass. The center of mass is approximately 2.0° off the piston thermocouple axis and 7.5° off each spray plume location.

A.9 Thermocouple Functionality

Four thermocouple instrumented pistons were run as part of this work. Co-axial Metal 1 and Co-axial Metal 2 pistons (nomenclature from table 3.7) were the same design (duplicate hardware) and used MEDTHERM co-axial thermocouples. These two pistons provided high quality heat flux data that are discussed in all three results chapters 4, 5 and 6. Pair-wire Metal and Pair-wire TBC used a pair-wire type fast-response thermocouple installed at the same locations as Co-axial Metal 1 and Co-axial Metal 2. The original goal of these two pistons was to reconstruct surface heat flux on a piston with a TBC and compare to a metal piston. Results from these pistons were limited by excessive thermocouple failures and poor transient temperature response.

Table A.4 shows the functionality of each of the 15 thermocouples for each of the four instrumented pistons. Functionality was checked by comparing temperature and heat flux data at a reference motored and fired case run at the start and end of each day of data acquisition. If data at any one of the thermocouple locations became non-repeatable, data from that day and every subsequent day were eliminated from further anylsis. Co-axial Metal 1 and Co-axial Metal 2 had the majority of thermocouples make it though all testing. Co-axial Metal 1 had all failures occur on the first day of testing, where Co-axial Metal 2 had all thermocouples function through the first day of testing with failures occurring as testing progressed.

Pair-wire Metal and Pair-wire TBC are shown with a single column in table A.4 because the quality of this data was much lower than Co-axial Meal 1 and Co-axial Metal 2, which made day-to-day functionality checks more challenging. Overall, five thermocouples in Pair-wire Metal were considered repeatable and four in Pair-wire TBC. Appendix A.10 will discuss observations in heat flux for Pair-wire Metal and make a limited comparison between Pair-wire Metal and Pair-wire TBC.

Table A.4: Thermocouple functionality as a function of date for instrumented pistons

	Co-axial Metal 1						Co-axial Metal 2						Pair-wire Metal		Pair-wire TBC
Date	20180625	20180626	20180628	20180629	20180702		20180717	20180718	20180723	20180724	20180725		All		All
Injector	On-plume	On-plume	Off-plume	Off-plume	Split-plume		Split-plume	Off-axis	On-plume	Off-plume	Split-plume		All		All
1	Good	Good	Good	Good	Good		Good	Good	Good	Good	Good		Bad		Good
2	Bad	Bad	Bad	Bad	Bad		Good	Bad	Bad	Bad	Bad		Bad		Good
3	Good	Good	Good	Good	Good		Good	Good	Good	Good	Good		Bad		Bad
4	Good	Good	Good	Good	Good		Good	Bad	Bad	Bad	Bad		Bad		Bad
5	Good	Good	Good	Good	Good		Good	Good	Good	Good	Good		Bad		Bad
6	Good	Good	Good	Good	Good		Good	Good	Bad	Bad	Bad		Good		Bad
7	Bad	Bad	Bad	Bad	Bad		Good	Good	Good	Good	Good		Good		Bad
8	Good	Good	Good	Good	Good		Good	Good	Good	Good	Good		Bad		Bad
9	Bad	Bad	Bad	Bad	Bad		Good	Good	Good	Good	Good		Good		Bad
10	Bad	Bad	Bad	Bad	Bad		Good	Good	Good	Good	Good		Bad		Bad
11	Good	Good	Good	Good	Good		Good	Good	Good	Good	Good		Bad		Bad
12	Good	Good	Good	Good	Good		Good	Bad	Bad	Bad	Bad		Good		Good
13	Bad	Bad	Bad	Bad	Bad		Good	Good	Good	Good	Good		Bad		Good
14	Good	Good	Good	Good	Good		Good	Good	Bad	Bad	Bad		Good		Bad
15	Good	Good	Good	Good	Good		Good	Bad	Bad	Bad	Bad		Bad		Bad

A.10 Pair-wire Thermocouple Results

Figure A.7 show an example of a pair-wire thermocouple similar to the ones used in Pair-wire Metal and Pair-wire TBC pistons. The image includes an optional embedded junction (and disconnected surface junction), which were not included on pair-wire thermocouples as part of this effort. When compared to a co-axial thermocouple design (see figure 2.3) some design differences exist that may impact heat flux results. First the thermocouple materials are formed into two wires which terminate at the surface of the sensor. The two wires are encompassed with Magnesium oxide (MgO) which is a thermal insulator (compared to most metals). The junction is formed over the MgO using Platinum which is laser welded onto the two wires. The outer body of the sensor is constructed of 304 stainless steel. The large range of materials and their associated thermal properties makes selection of a single set of material properties, which is required for to calculate heat flux in equation 3.3, difficult.

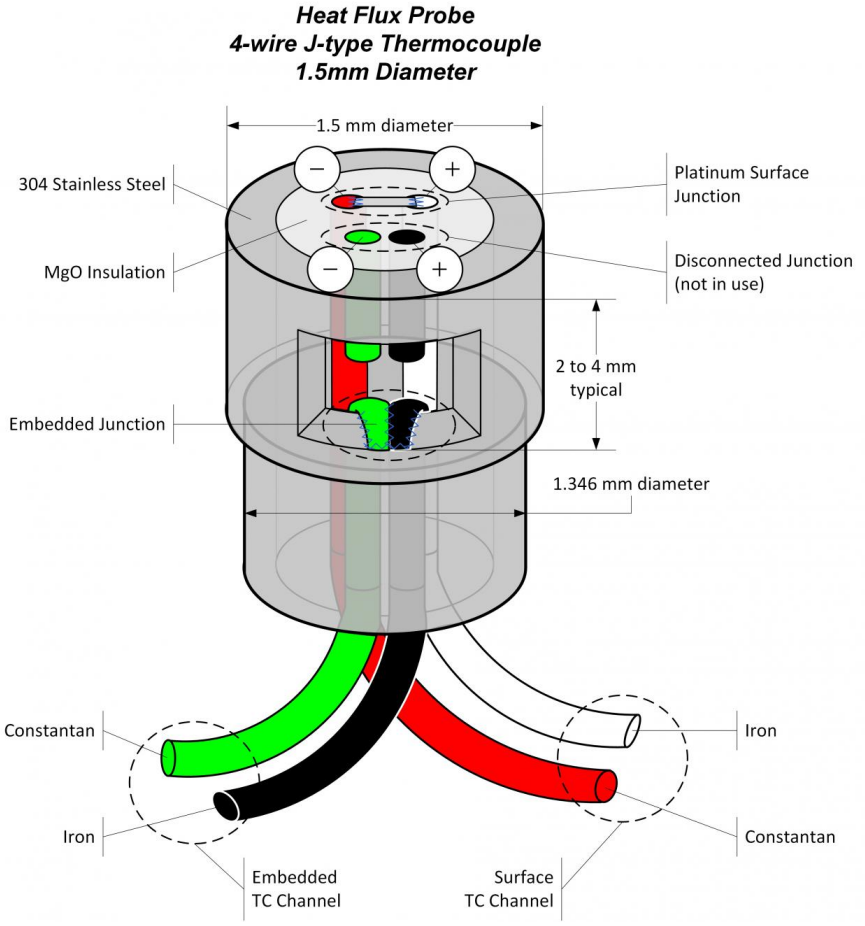


Figure A.7: Example of pair-wire type thermocouple taken from [43]

Figure A.8 shows a comparison of heat flux between Co-axial Metal 1 and Pair-wire Metal pistons at thermocouple location 6 (near center of piston) and 14 (bowl lip). The comparison is made at operating condition 3 (2500 rpm, 20.3 bar IMEPg) SOI timing of -25 °ATDC using the on-plume injector spray orientation. The pair-wire thermocouples both show a

higher heat flux than the corresponding co-axial thermocouple location. The same thermal properties of Constantan, which were used for the co-axial thermocouples, were also used in the pair-wire type sensor. Based on the knowledge of the sensor constitution, a different selection of thermal properties, more similar to MgO may have been more appropriate. The selection of thermal properties primarily functions to adjust the magnitude of heat flux without significant changes to the overall shape.

An additional trend observed in Pair-wire Metal piston data is also seen in figure A.8 at thermocouple 14. For this location, and others with relatively high heat flux, a negative dip in the data were observed on the falling edge of the heat flux. This dip was only observed using the pair-wire type sensors. FEA modeling work by Hendricks [38] showed that the a similar dip in the data may be related to two-dimensional conduction effects within the sensor, which may be exacerbated by the large amount of thermal insulator material (MgO) present in the pair-wire thermocouples.

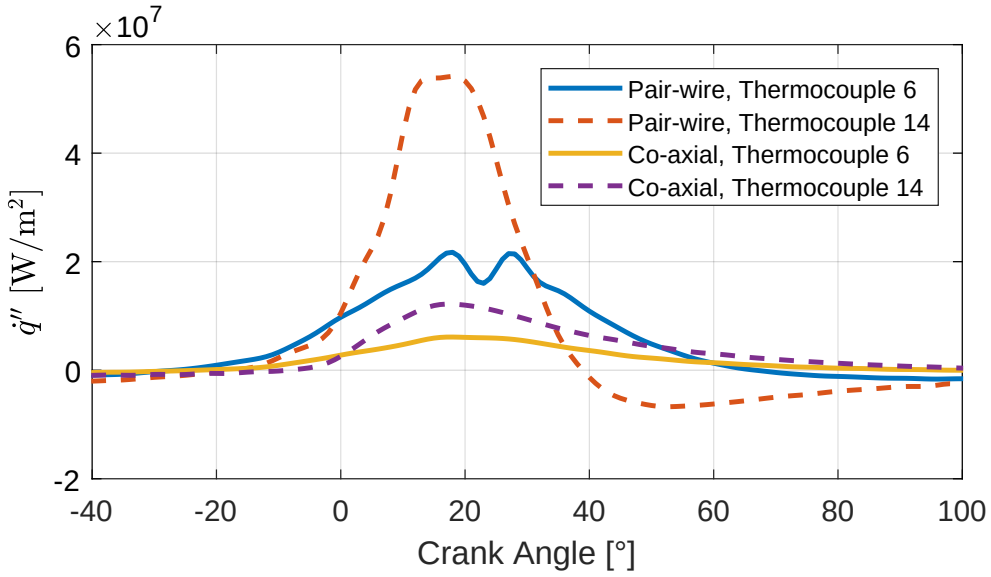


Figure A.8: Operating condition 3 (2500 rpm, 20.3 bar IMEPg) SOI timing of -25 °ATDC comparison of heat flux from co-axial and pair-wire type thermocouples

Figure A.9 shows temperature data for the Pair-wire TBC piston. The comparison is made at operating condition 3 (2500 rpm, 20.3 bar IMEPg) SOI timing of -25 °ATDC using the on-plume injector spray orientation. Due to the many problems with the pair-wire sensors and additional complexity of a sub-surface temperature measurement, heat flux was not calculated. Because the temperature measurement for this piston in now sub-surface (flush mounted with metal but below the TBC) the transient response was expected to be delayed and attenuated. Thermocouples 1 and 12 show no transient response; only a steady measurement. Thermocouple 2 and 13 show a transient response but the crank angle phasing of the temperature increase does not appear to be the same for these measurements.

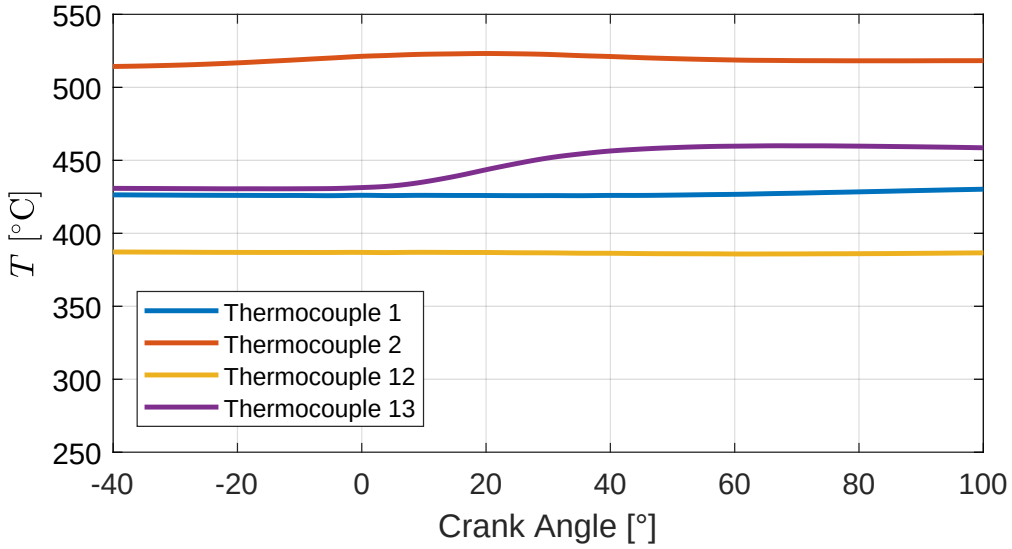


Figure A.9: Operating condition 3 (2500 rpm, 20.3 bar IMEPg) SOI timing of -25 °ATDC sub-surface temperature for Pair-wire TBC piston

Figure A.10 compares the mean temperature, $\bar{T}$, for Co-axial Metal 1, Pair-wire Metal, and Pair-wire TBC pistons at thermocouple 12, which is the only location where repeatable data was available for all the pistons (see table A.4). Pair-wire Metal and Pair-wire TBC mean temperature data were similar to each other, but about 25 °C higher than Co-axial Metal 1. For thermocouple locations where a comparison could be made, the pair-wire type sensor typically gave a higher mean temperature than the co-axial type sensor.

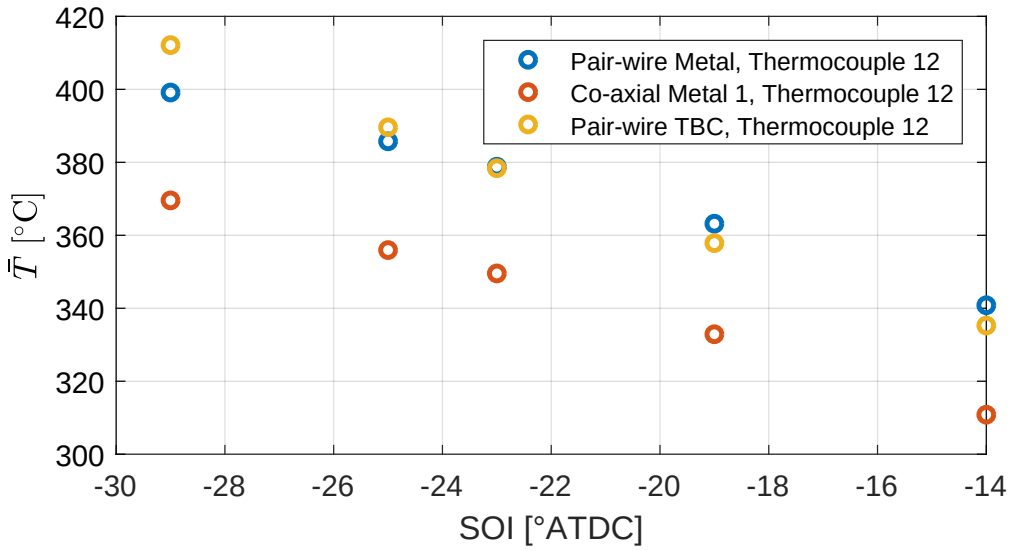


Figure A.10: Operating condition 3 (2500 rpm, 20.3 bar IMEPg) comparison of mean temperature at thermocouple 12 using Pair-wire Metal, Co-axial Metal 1 and Pair-wire TBC piston

A.11 Heat Flux Results- Operating Condition 4

Only a single set of data with a limited number of operational thermocouples was acquired for operating condition 4. This data was not used for heat transfer correlation development but was used in other figures for reference. Figures similar to other operating conditions in section 4.3 are shown below.

Table A.5: Operating condition 4 (1700 rpm, 30.3 bar IMEPg) available thermocouple measurements and substitutions

Group	a	b		c		d		e		f		g		h	
Thermocouple #	8	7	9	6	10	5	11	4	12	3	13	2	14	1	15
On-plume		0	0	0	0	0	0	0	0	0	0	0	0	0	0
		Sub		Sub		Sub		Sub		Sub		Sub		Sub	
Split-plume	1	1	1	0	1	1	1	0	0	1	1	0	0	1	0
	1	2		1		2		Sub		2		Sub		1	
Off-plume		0	0	0	0	0	0	0	0	0	0	0	0	0	0
		Sub		Sub		Sub		Sub		Sub		Sub		Sub	

Total 9

Substitutions (shown in red text): Use split-plume group d for split-plume group e, Use split-plume group f for split-plume group g, Use all location split-plum (including previous substitutions) for on-plume and off-plume

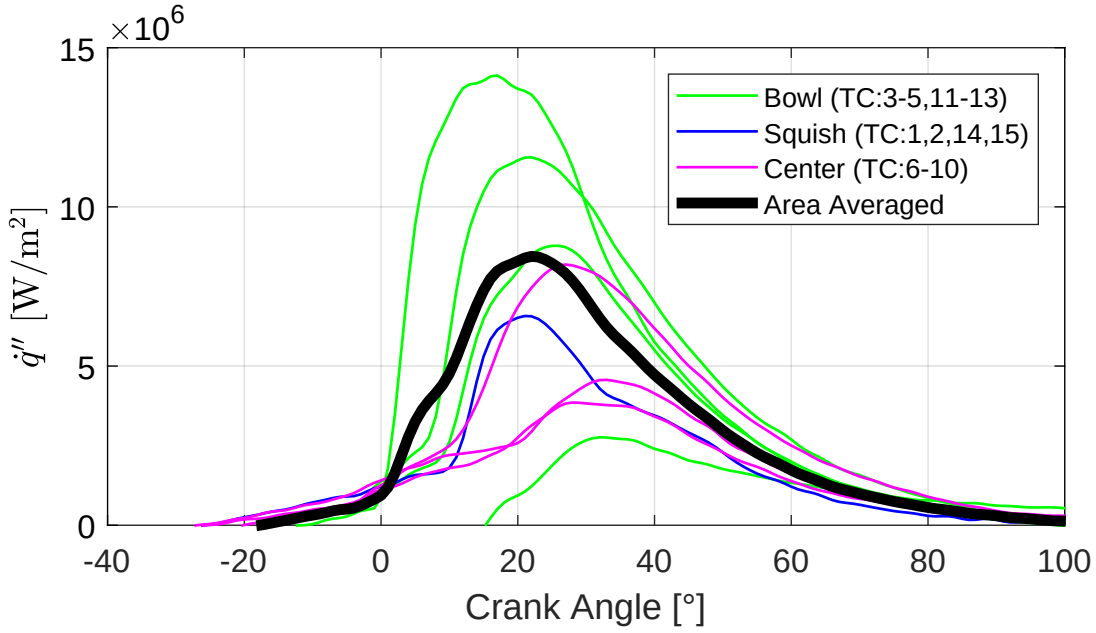


Figure A.11: Operating condition 4 (1700 rpm, 30.3 bar IMEPg) SOI timing of -12 °ATDC area averaged and individual heat flux with line color indicating piston location

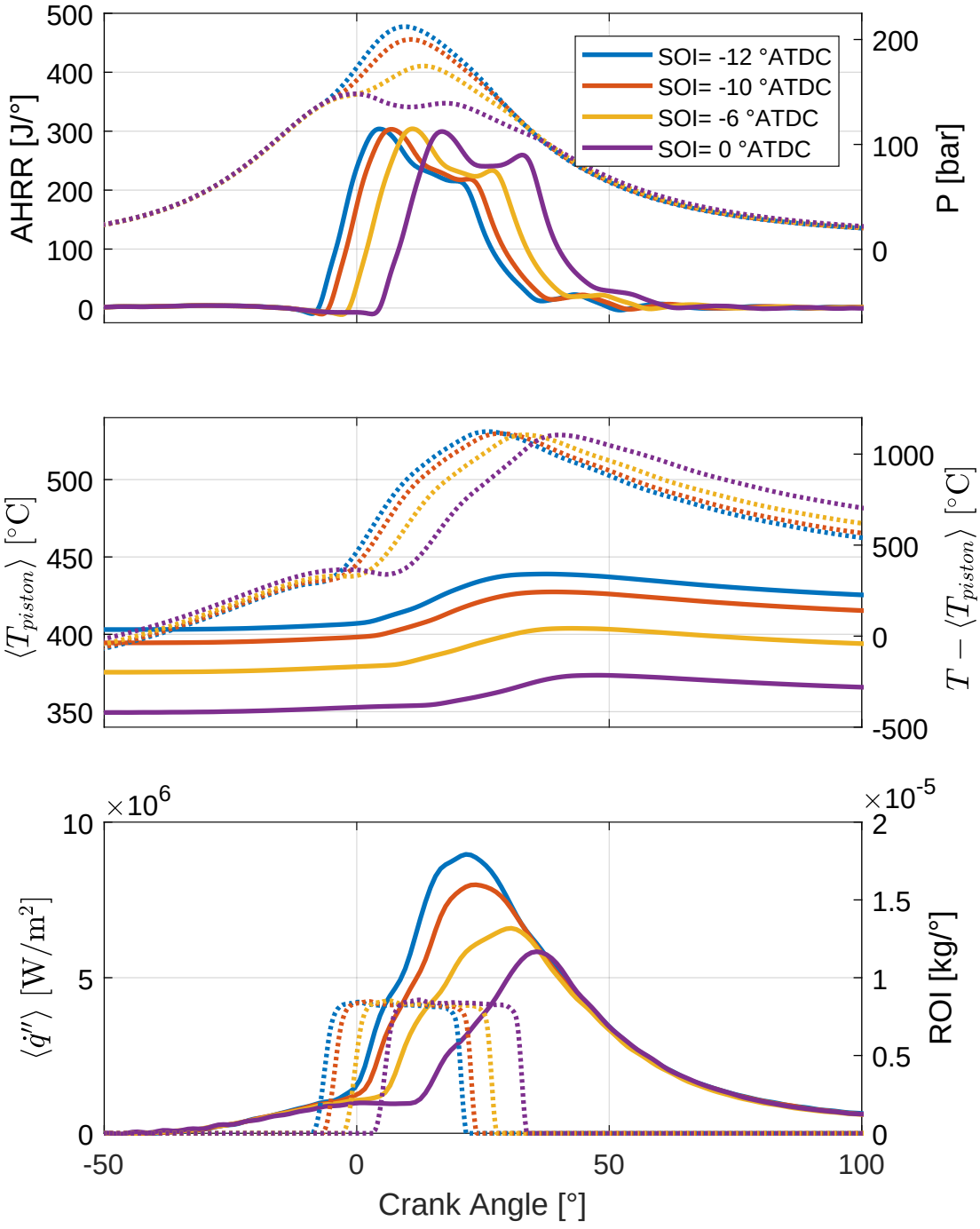


Figure A.12: Operating condition 4 (1700 rpm, 30.3 bar IMEPg) high-speed crank angle measurements for all SOI (solid lines left axis, dotted lines right axis)

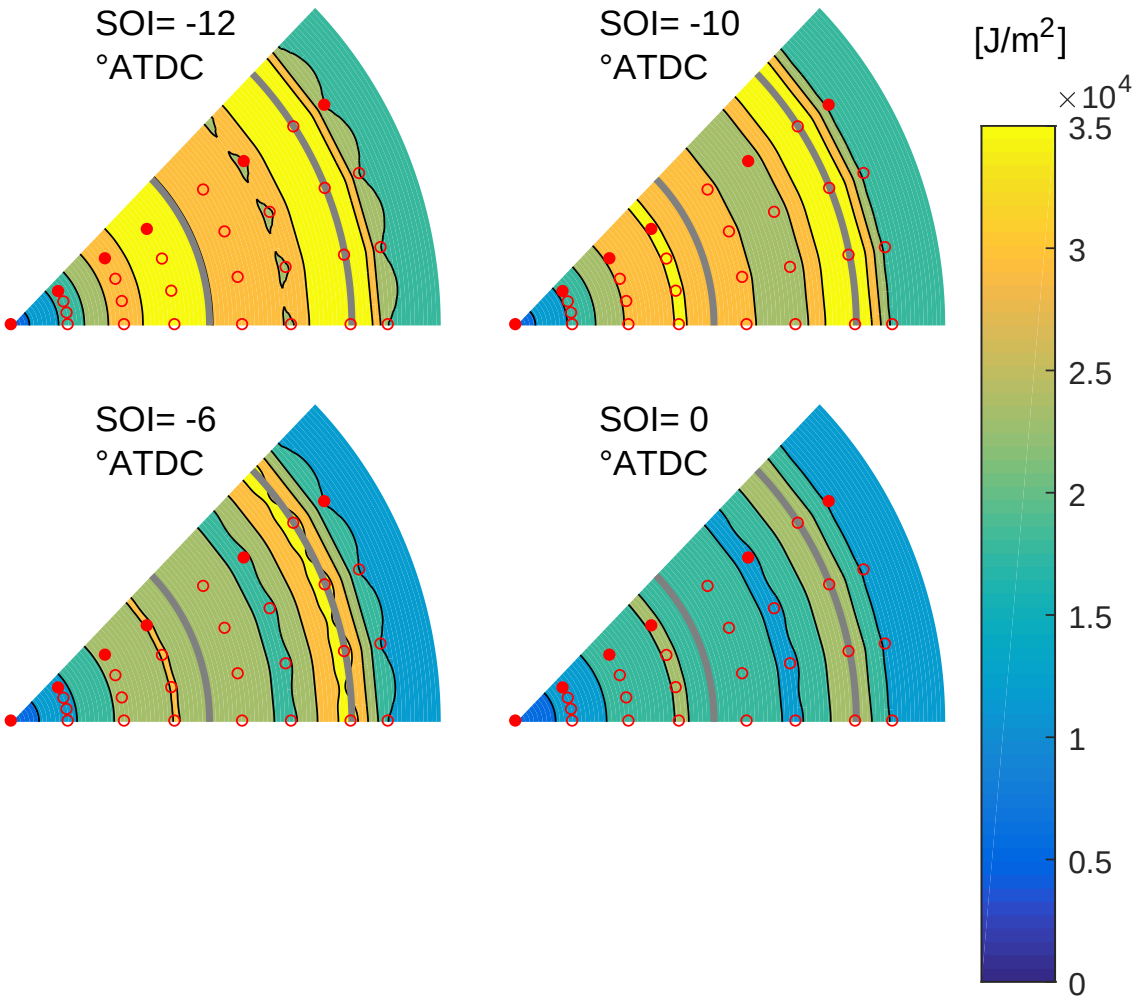


Figure A.13: Operating condition 4 (1700 rpm, 30.3 bar IMEPg) contours of heat flux integrated w.r.t. time from -20 to 100 °ATDC (energy flux) for all SOI

A.12 Heat Flux Contours for all Conditions

Heat flux contours were generated for all operating conditions and SOI. The same crank angles and color scale was used for all plots allowing comparisons between conditions to be made.

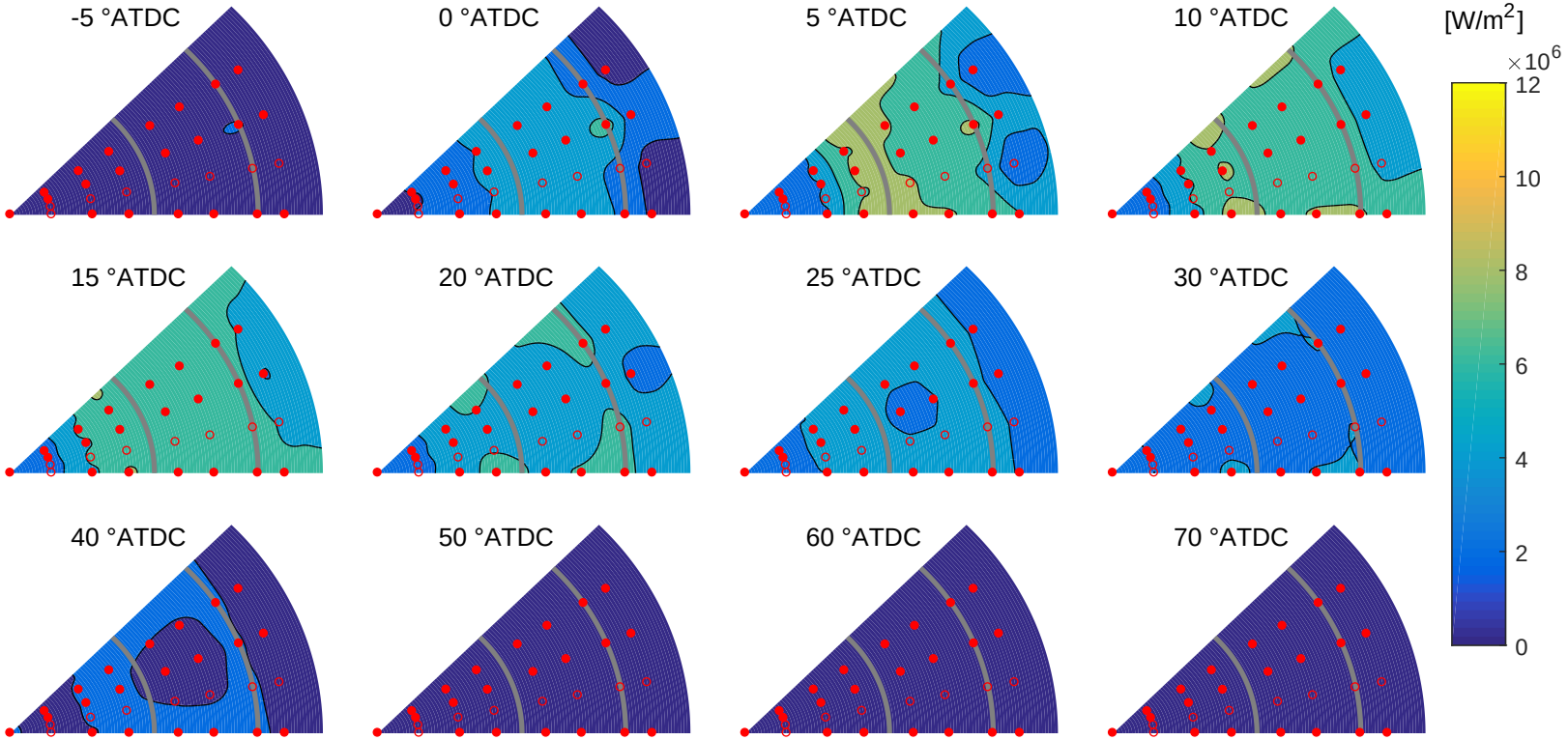


Figure A.14: Operating condition 1 (1700 rpm, 12.3 bar IMEPg) SOI timing of -22 °ATDC

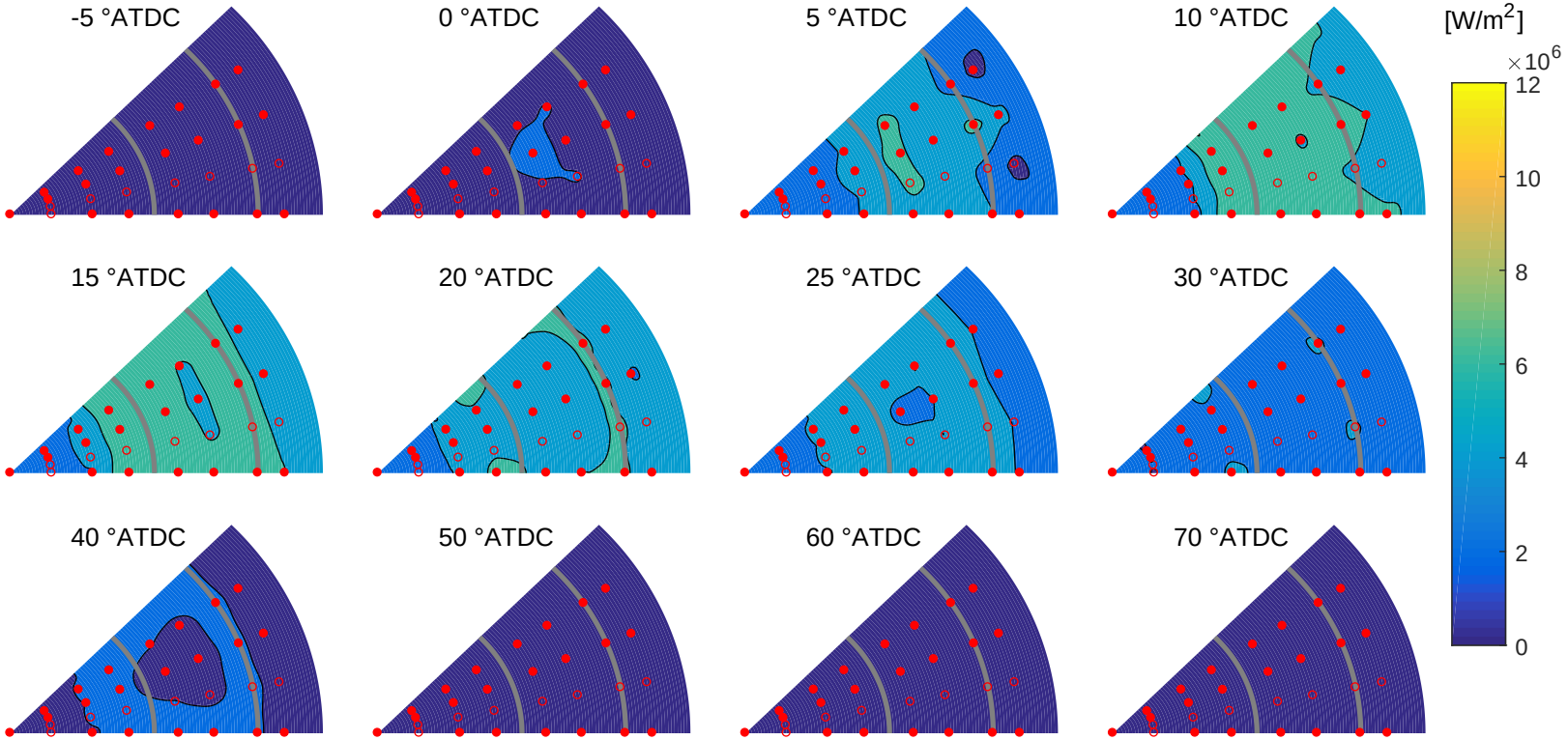


Figure A.15: Operating condition 1 (1700 rpm, 12.3 bar IMEPg) SOI timing of -18 °ATDC

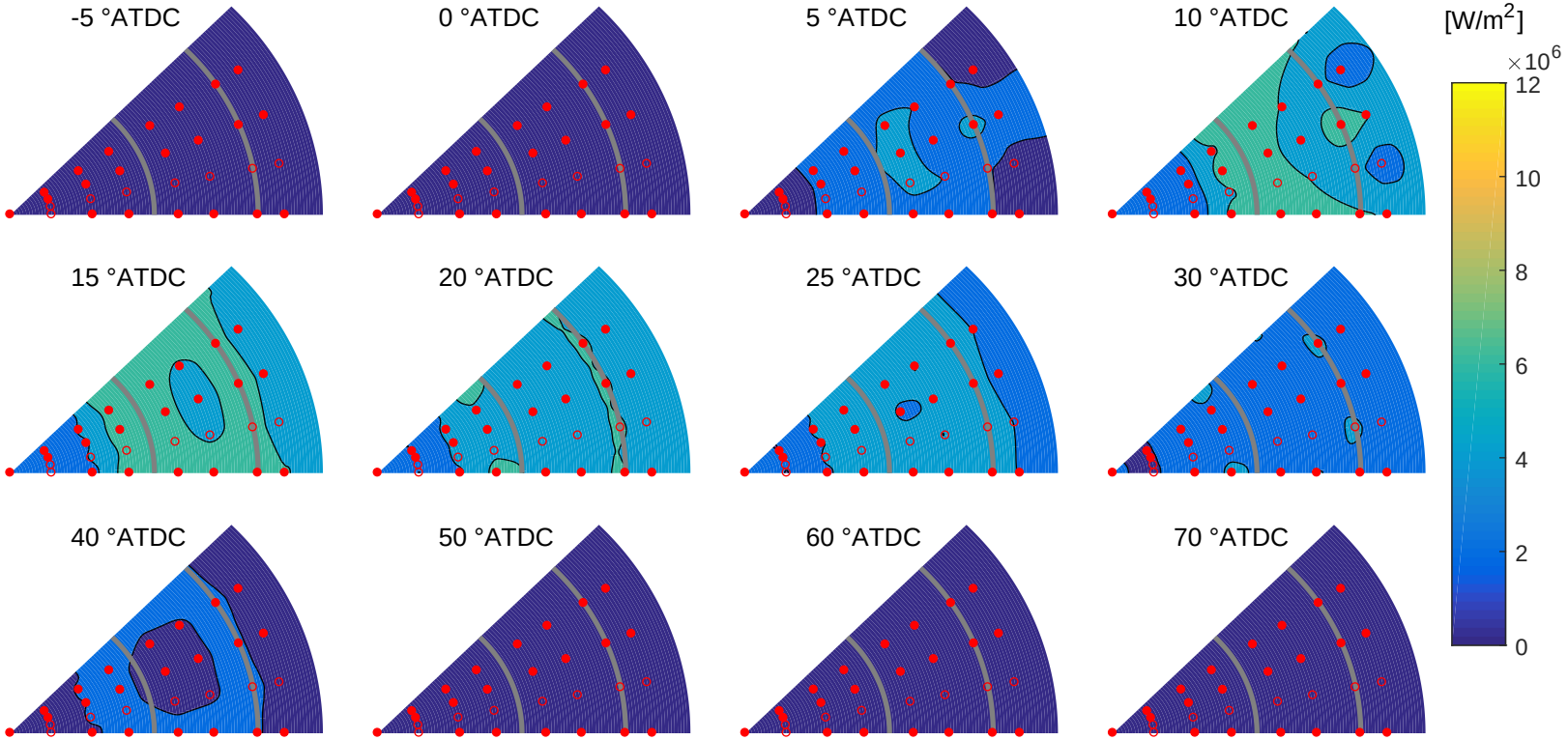


Figure A.16: Operating condition 1 (1700 rpm, 12.3 bar IMEPg) SOI timing of -16 °ATDC

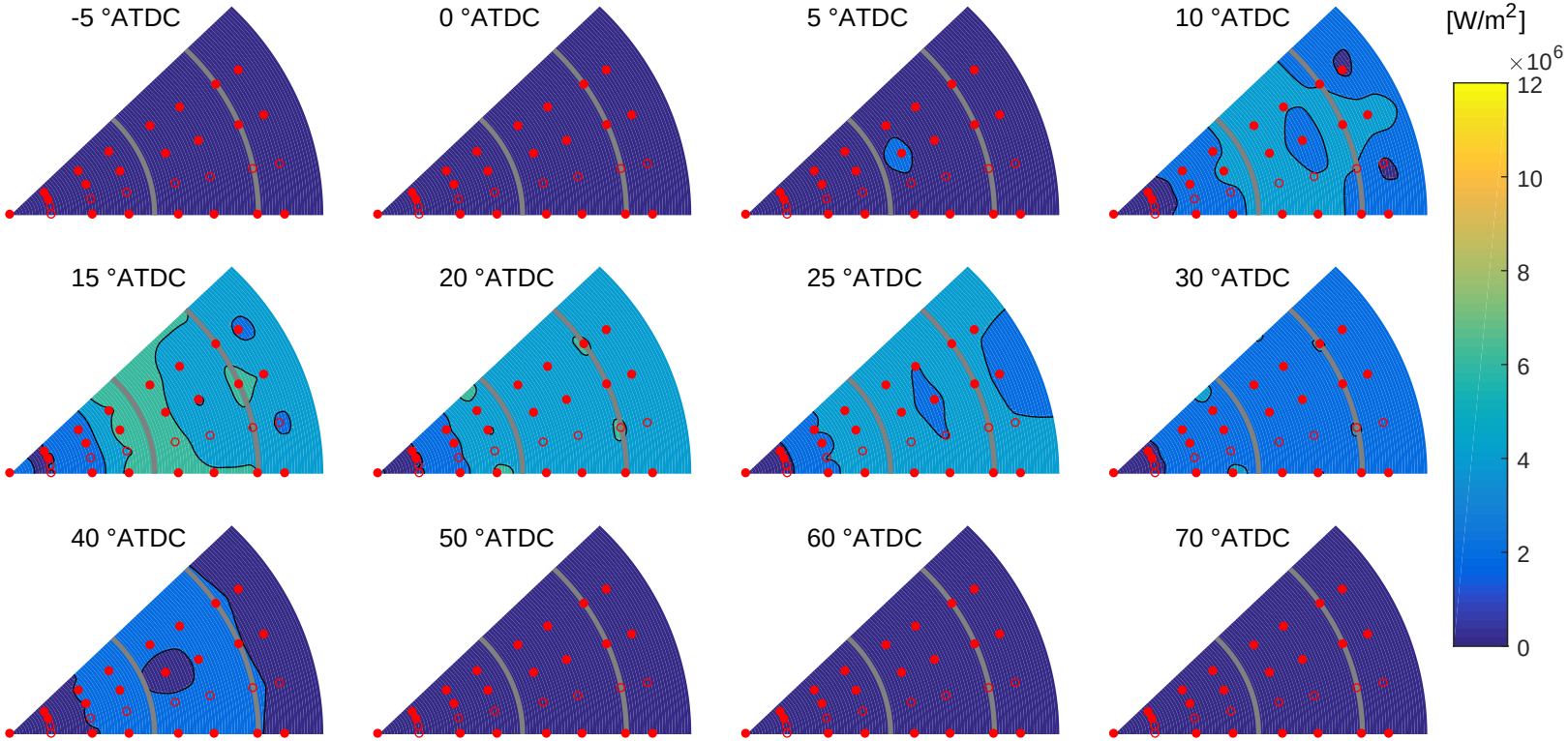


Figure A.17: Operating condition 1 (1700 rpm, 12.3 bar IMEPg) SOI timing of -13 °ATDC

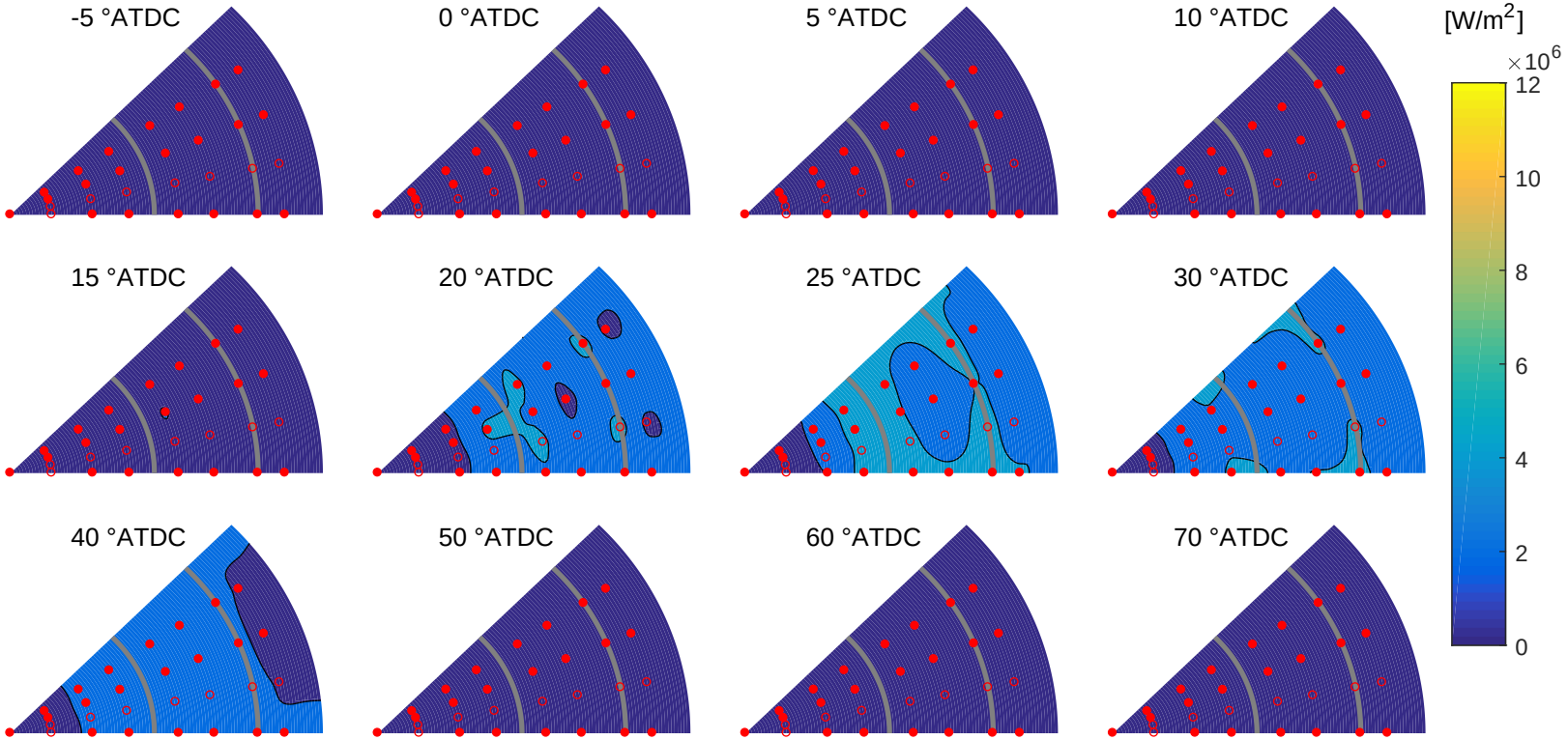


Figure A.18: Operating condition 1 (1700 rpm, 12.3 bar IMEPg) SOI timing of -5 °ATDC

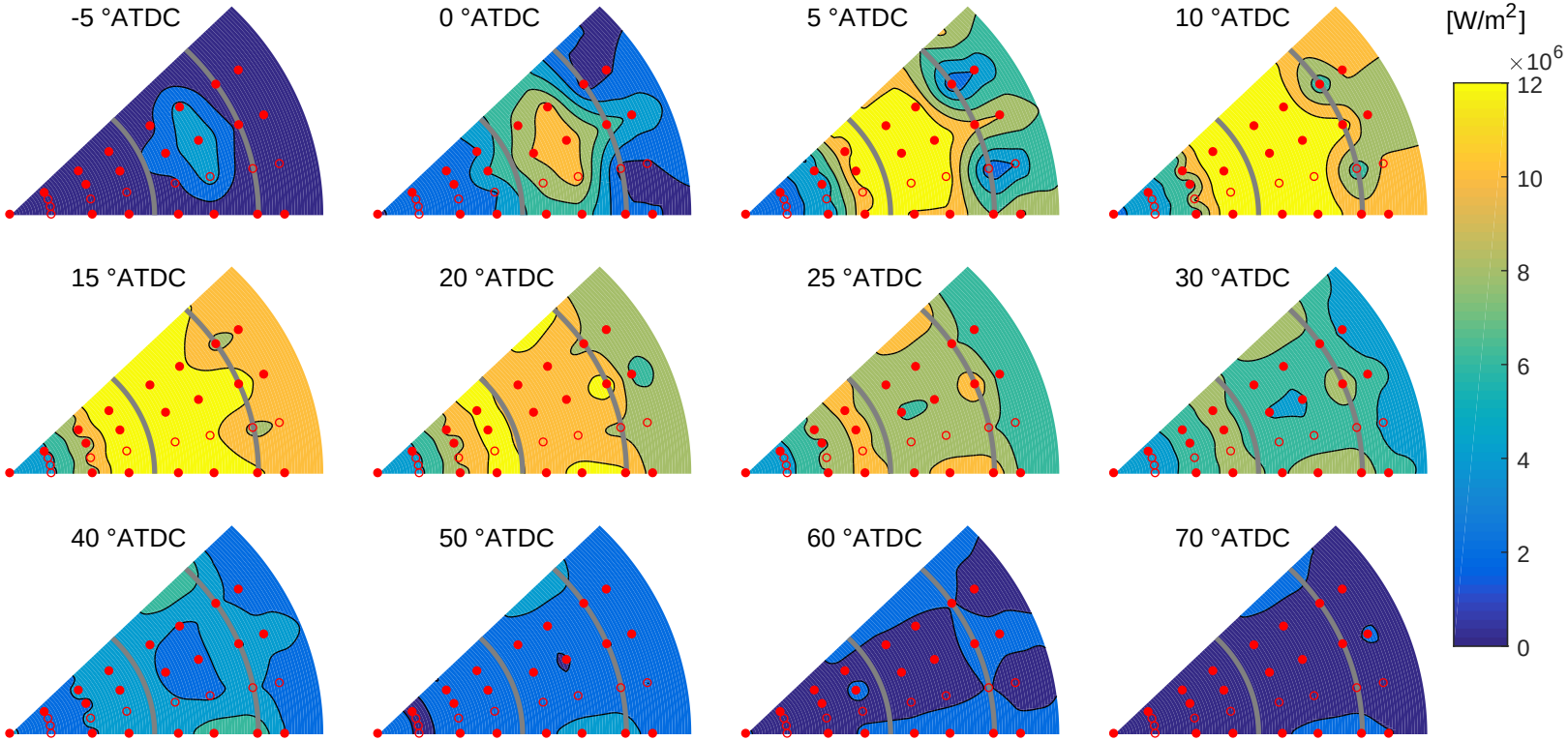


Figure A.19: Operating condition 2 (1500 rpm, 23.8 bar IMEPg) SOI timing of -19 °ATDC

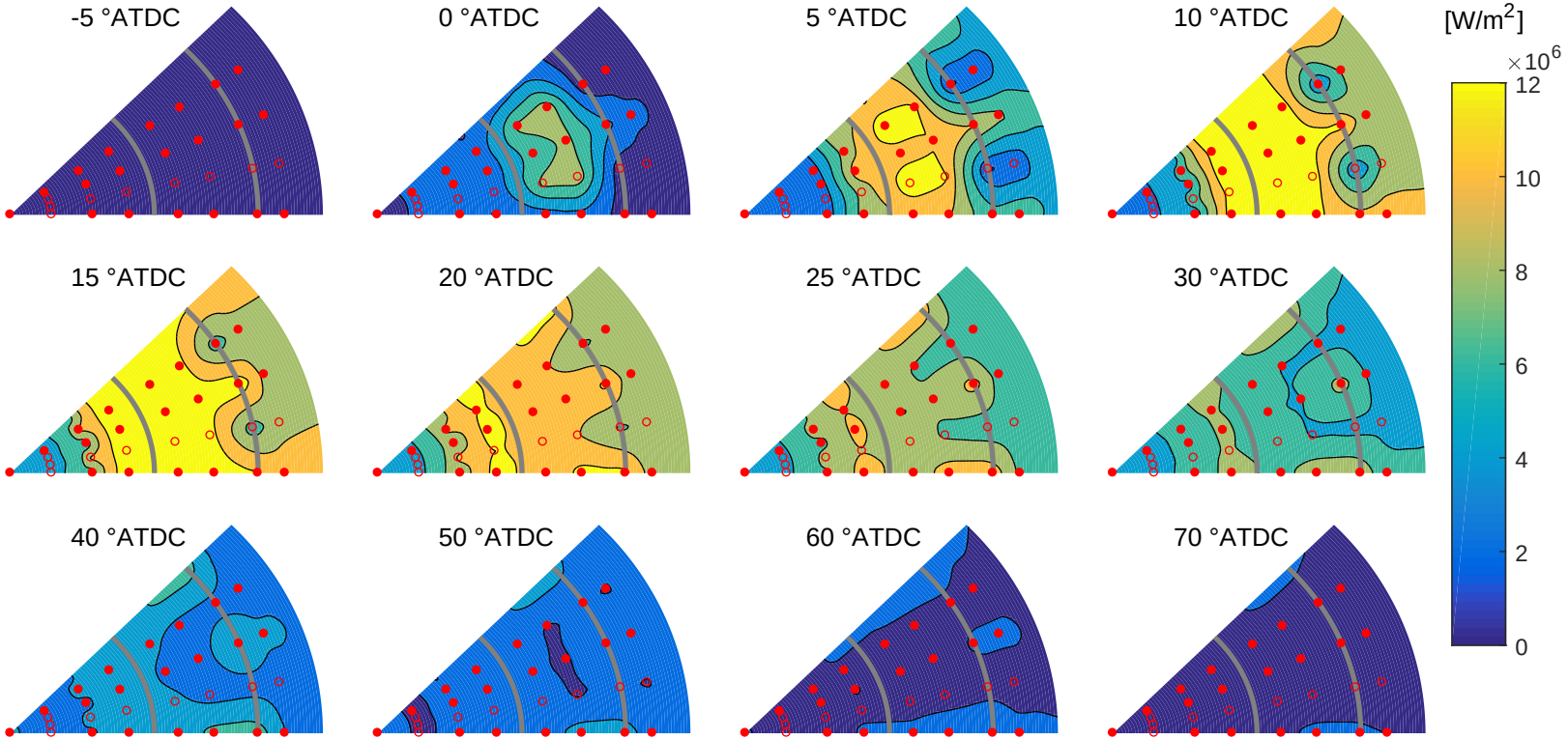


Figure A.20: Operating condition 2 (1500 rpm, 23.8 bar IMEPg) SOI timing of -17 °ATDC

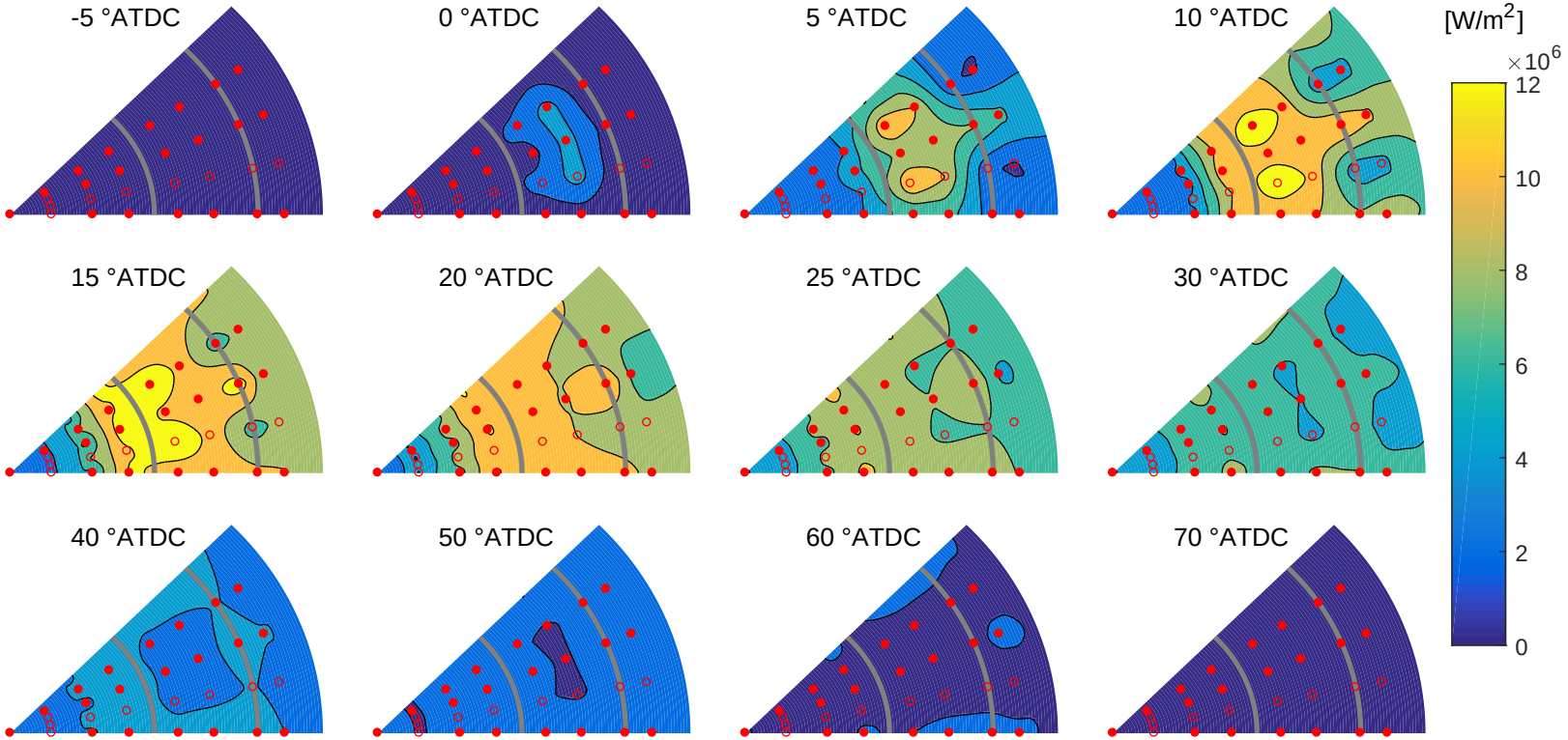


Figure A.21: Operating condition 2 (1500 rpm, 23.8 bar IMEPg) SOI timing of -14 °ATDC

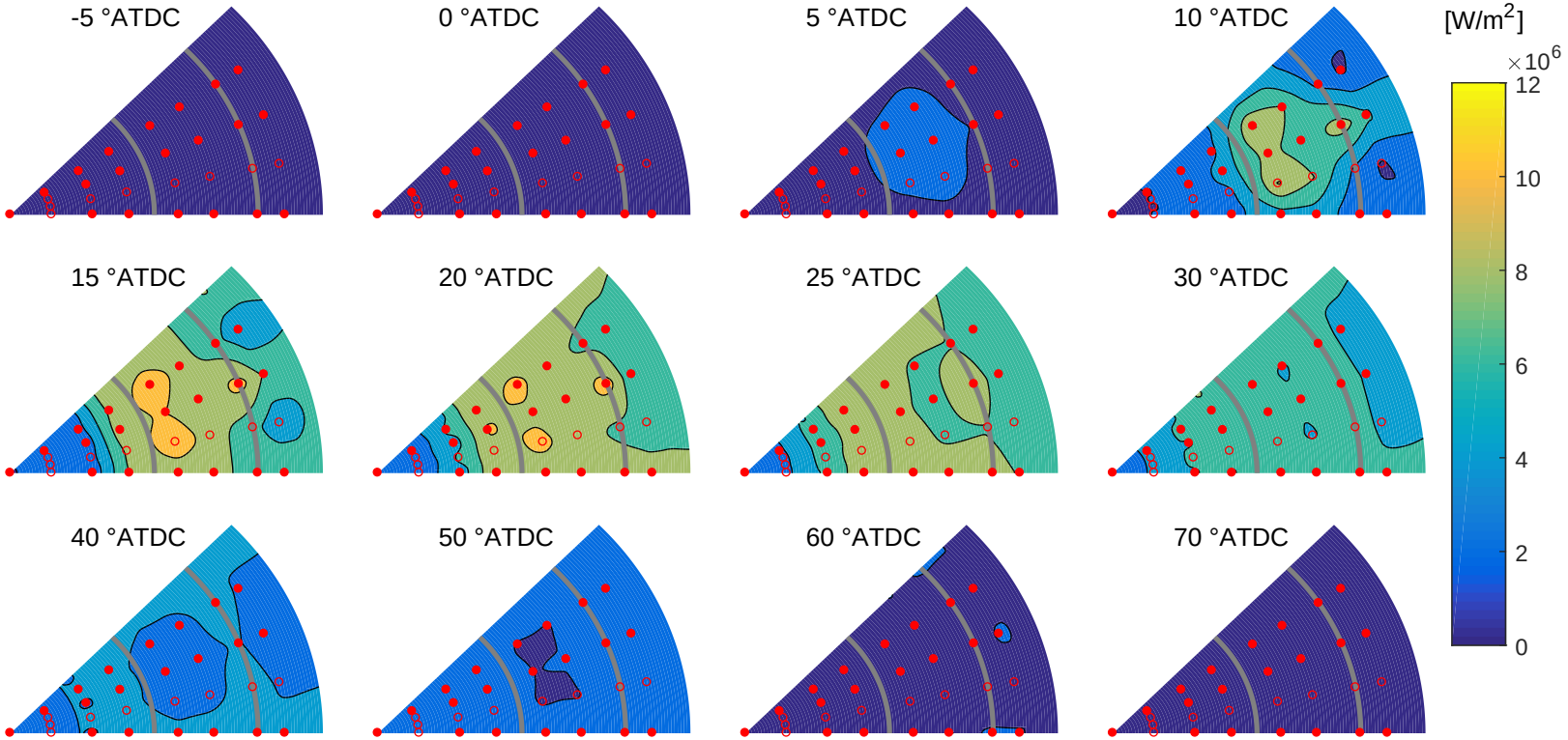


Figure A.22: Operating condition 2 (1500 rpm, 23.8 bar IMEPg) SOI timing of -9 °ATDC

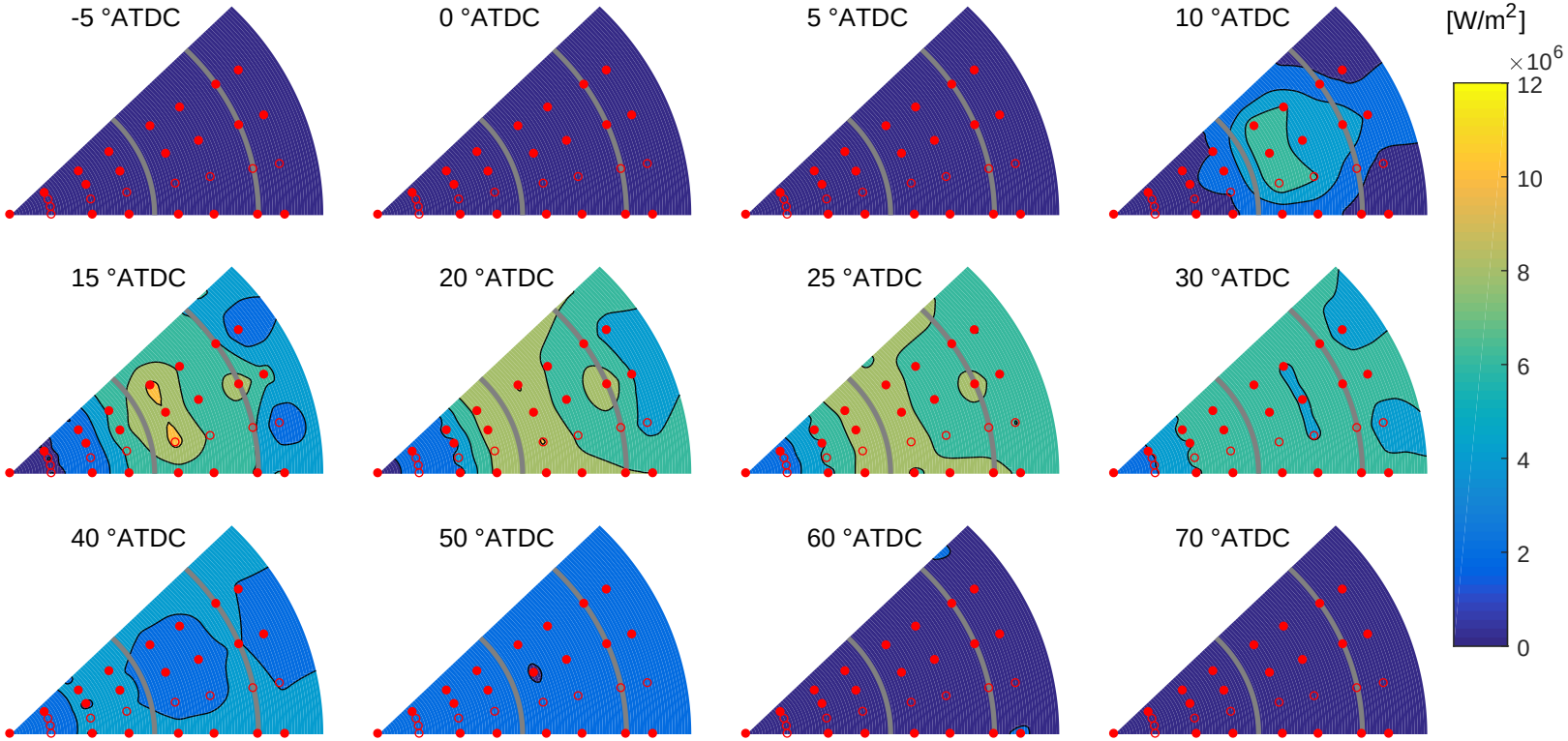


Figure A.23: Operating condition 2 (1500 rpm, 23.8 bar IMEPg) SOI timing of -7 °ATDC

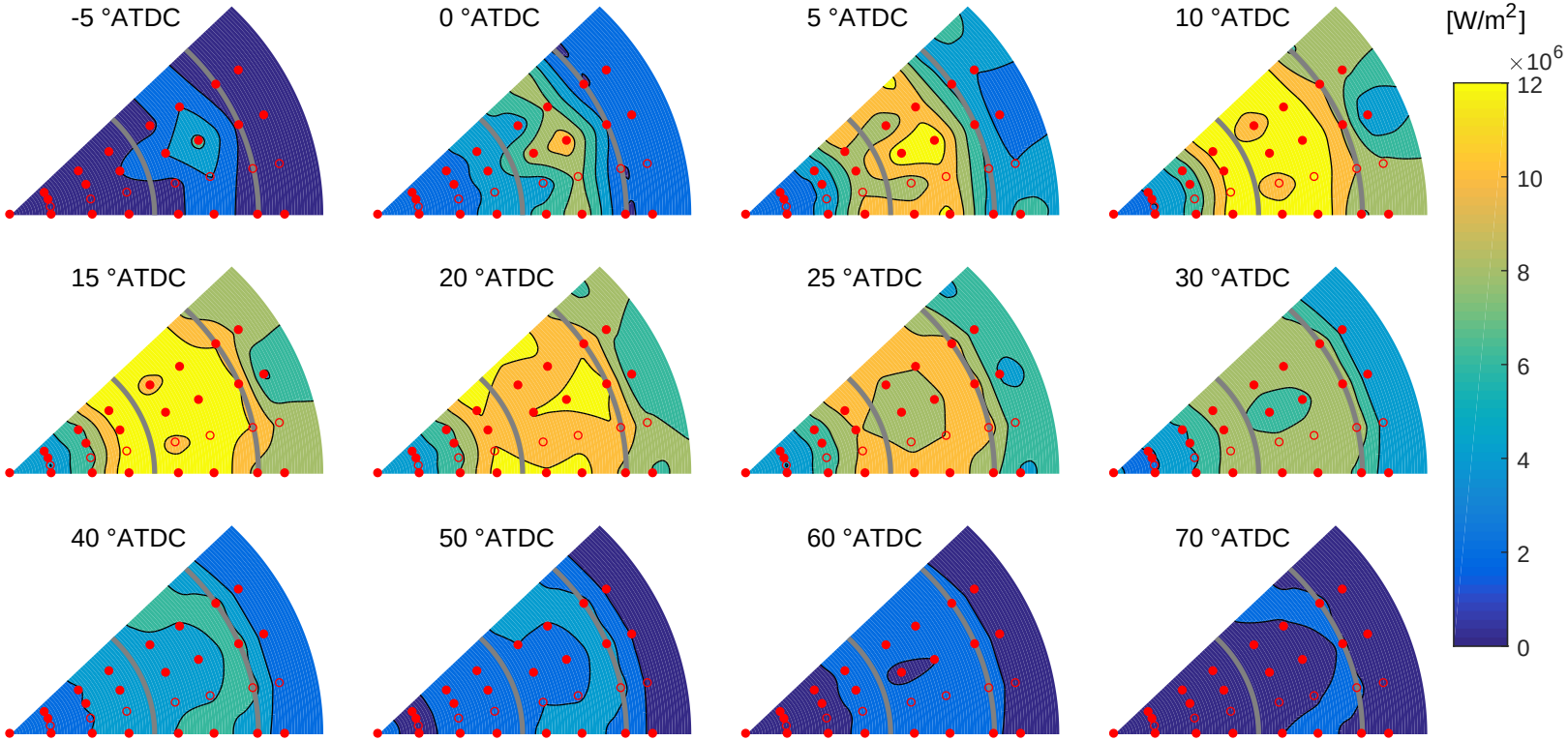


Figure A.24: Operating condition 3 (2500 rpm, 20.3 bar IMEPg) SOI timing of -29 °ATDC

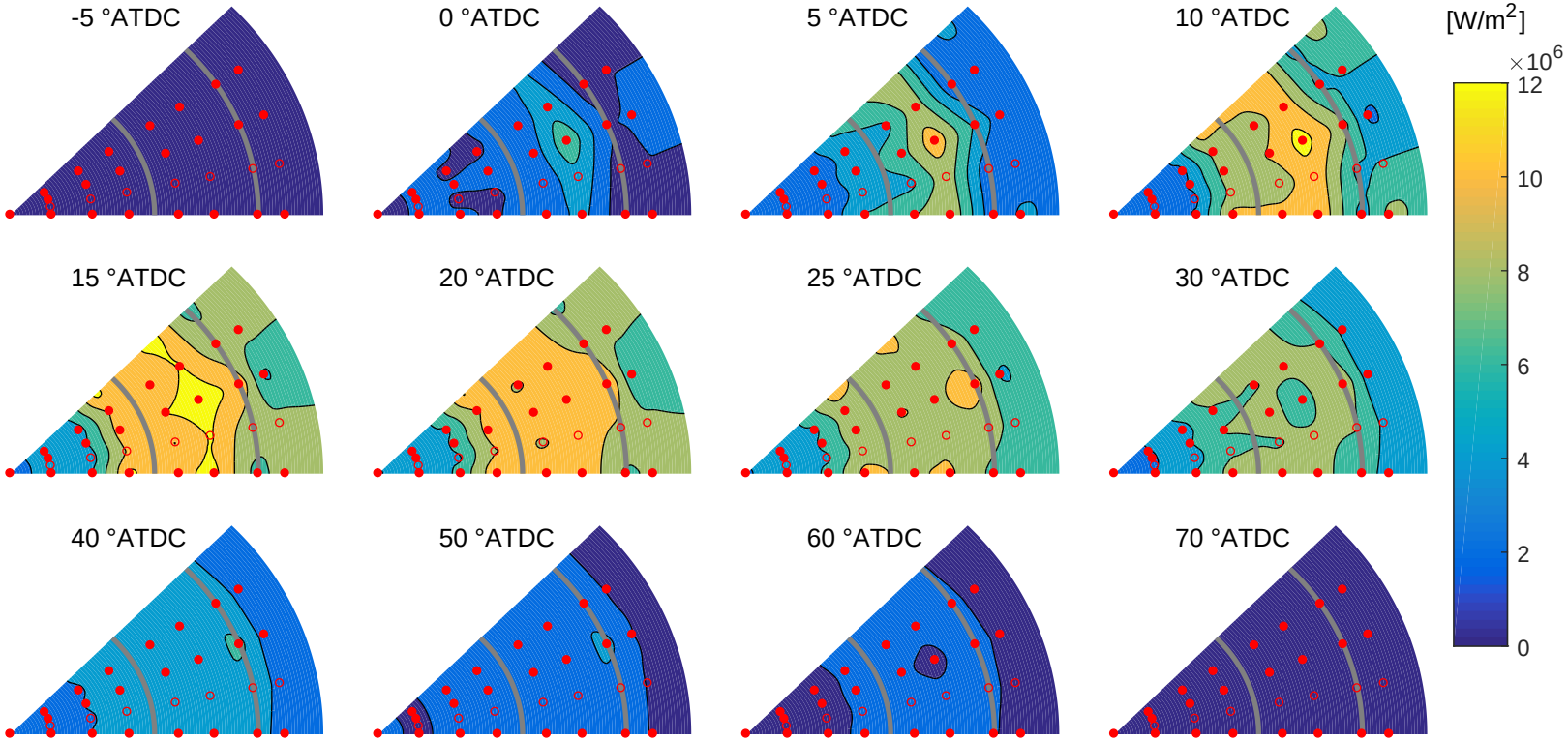


Figure A.25: Operating condition 3 (2500 rpm, 20.3 bar IMEPg) SOI timing of -25 °ATDC

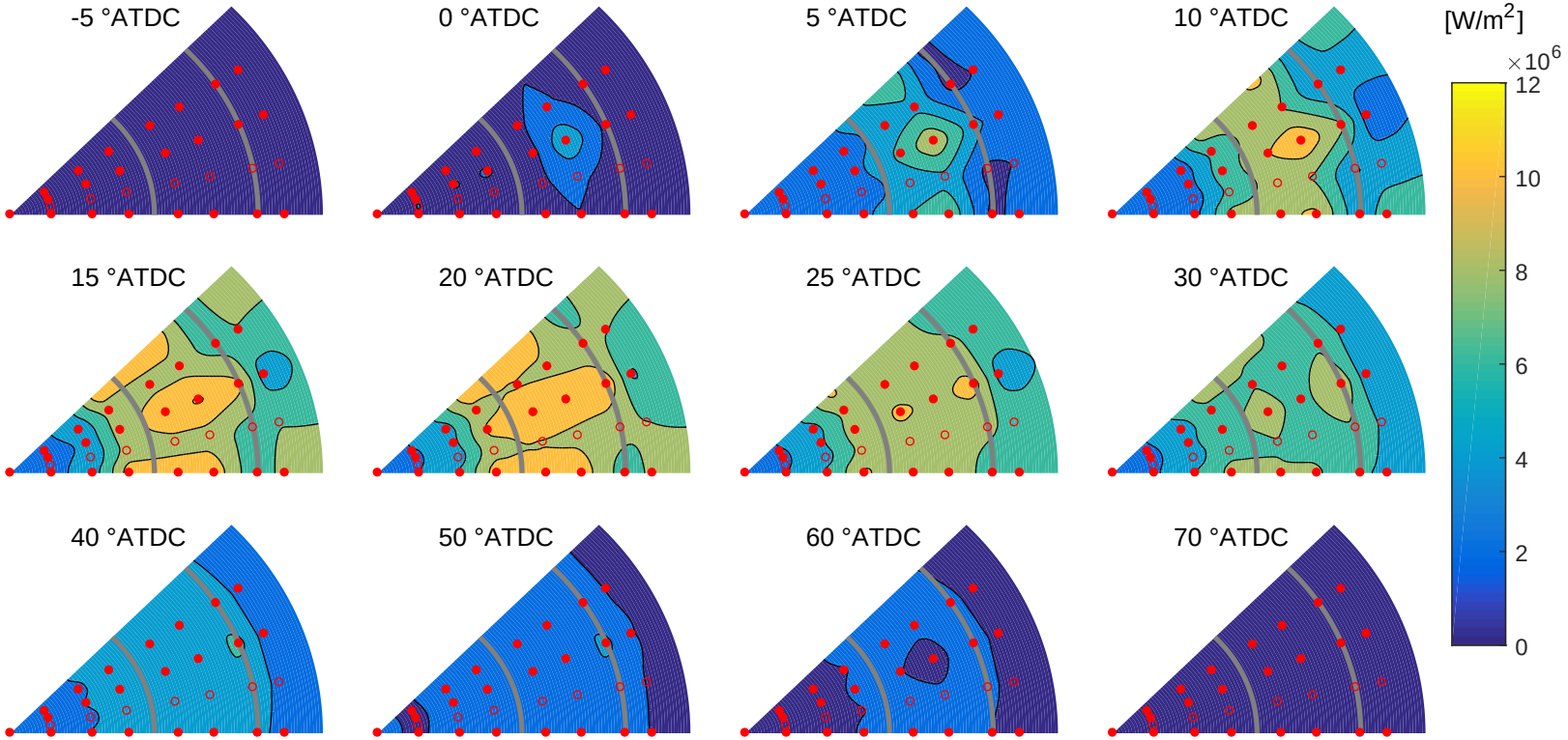


Figure A.26: Operating condition 3 (2500 rpm, 20.3 bar IMEPg) SOI timing of -23 °ATDC

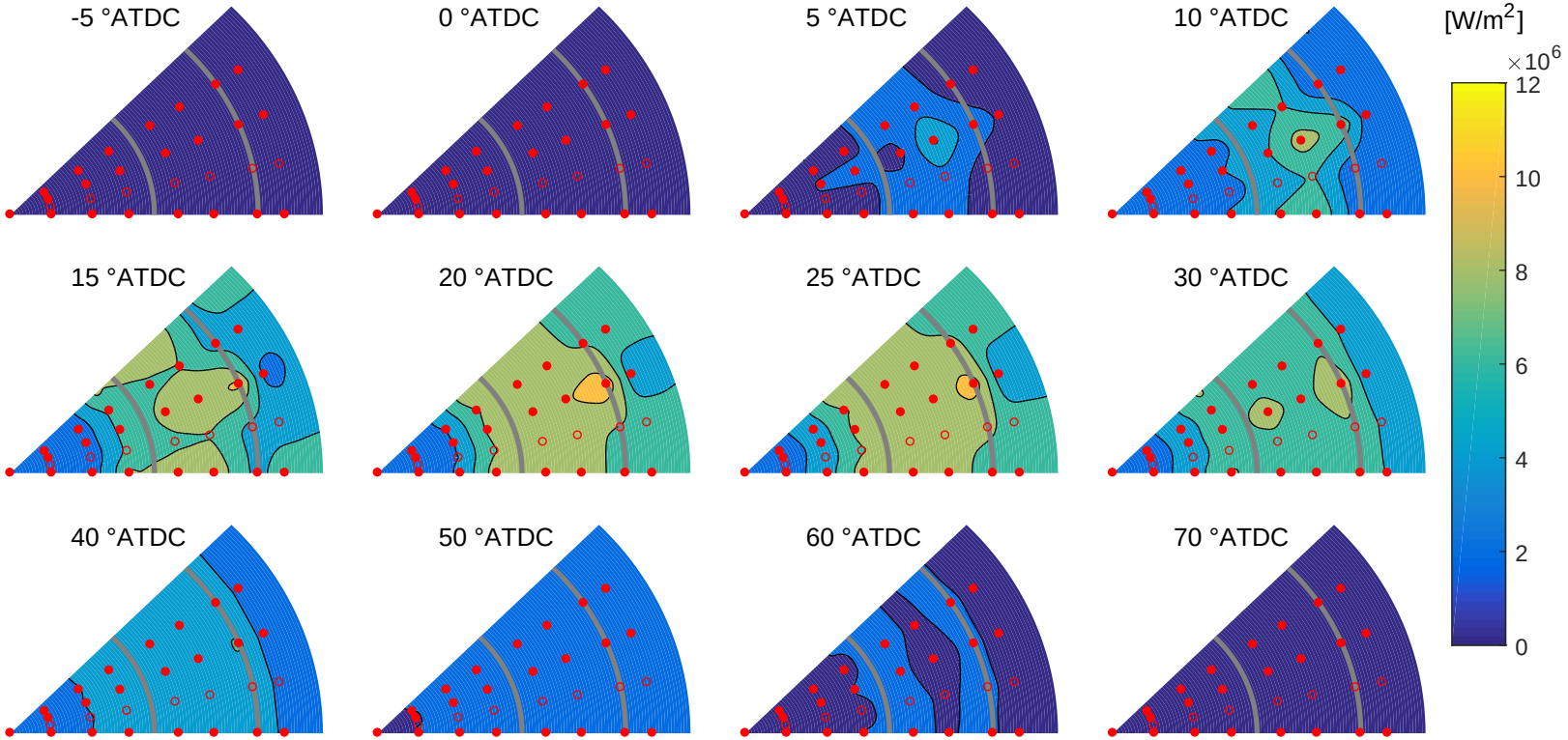


Figure A.27: Operating condition 3 (2500 rpm, 20.3 bar IMEPg) SOI timing of -19 °ATDC

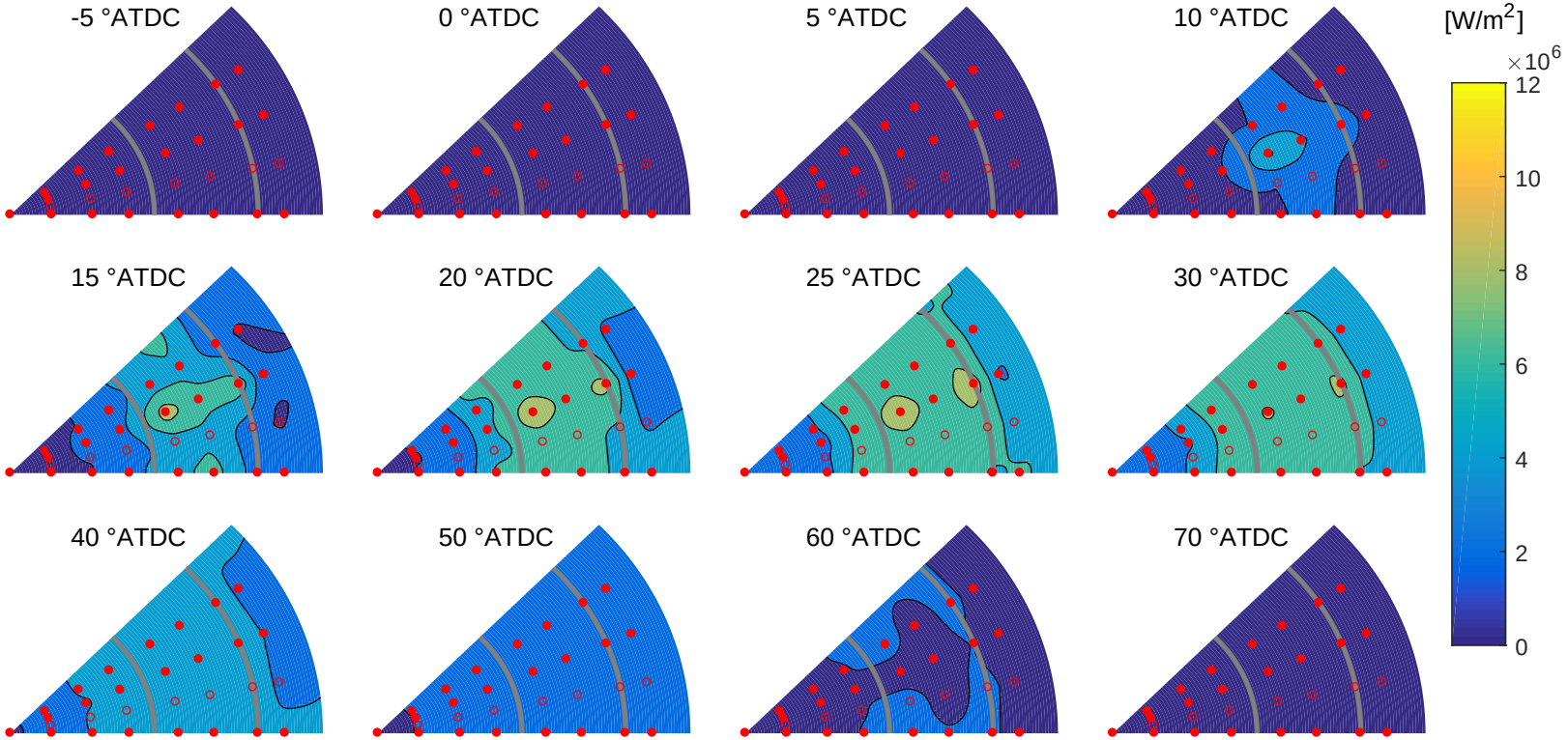


Figure A.28: Operating condition 3 (2500 rpm, 20.3 bar IMEPg) SOI timing of -14 °ATDC

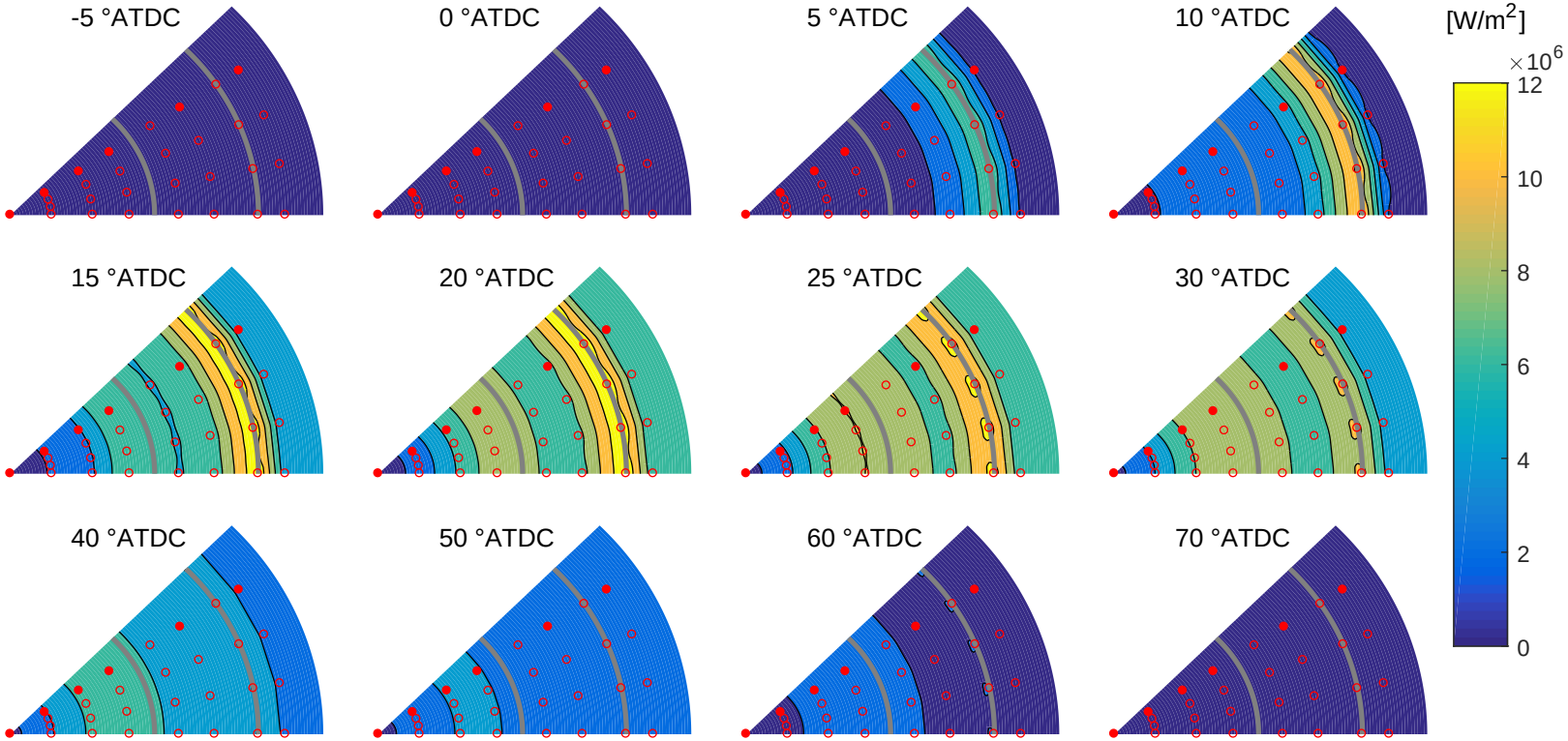


Figure A.29: Operating condition 4 (1700 rpm, 30.3 bar IMEPg) SOI timing of -12 °ATDC

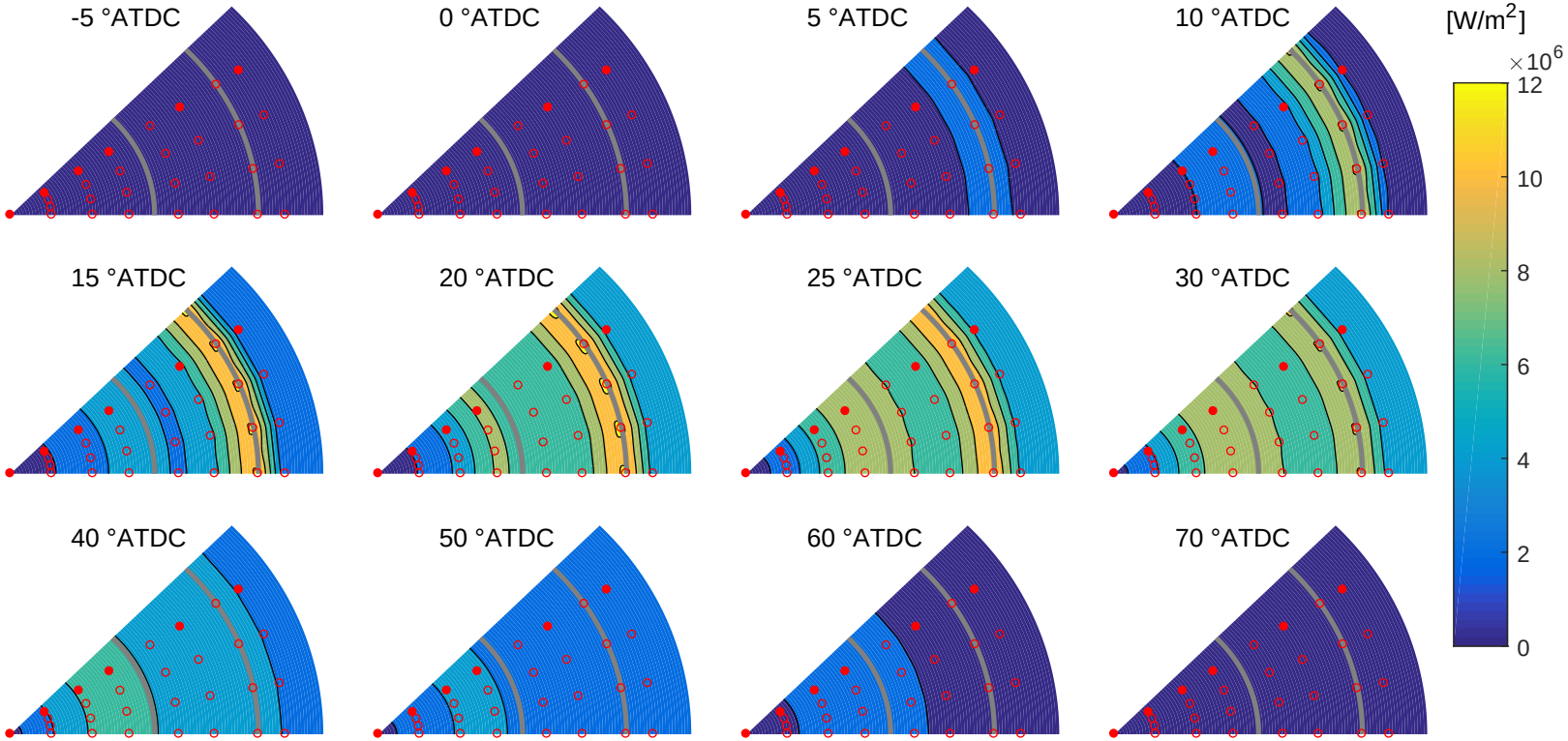


Figure A.30: Operating condition 4 (1700 rpm, 30.3 bar IMEPg) SOI timing of -10 °ATDC

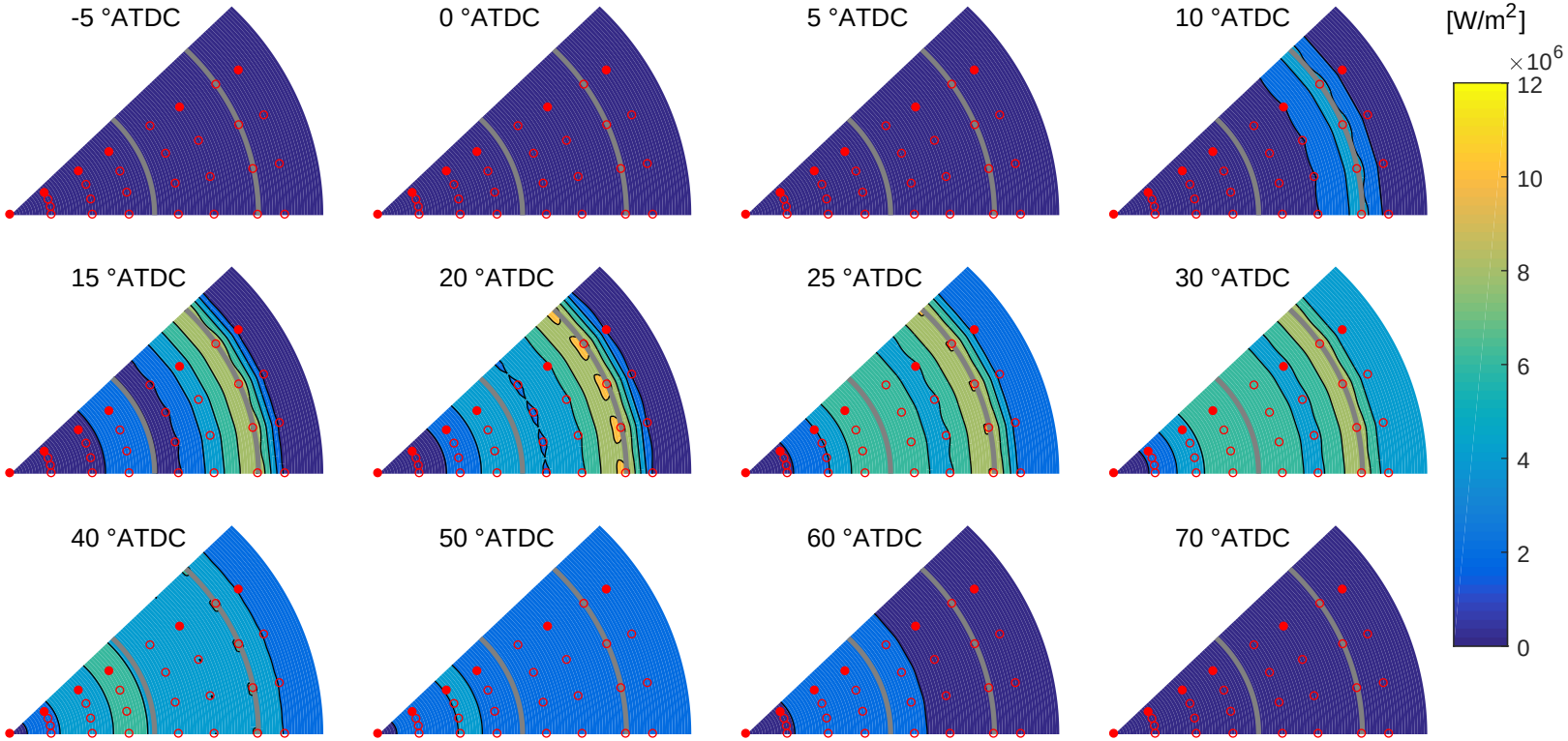


Figure A.31: Operating condition 4 (1700 rpm, 30.3 bar IMEPg) SOI timing of -6 °ATDC

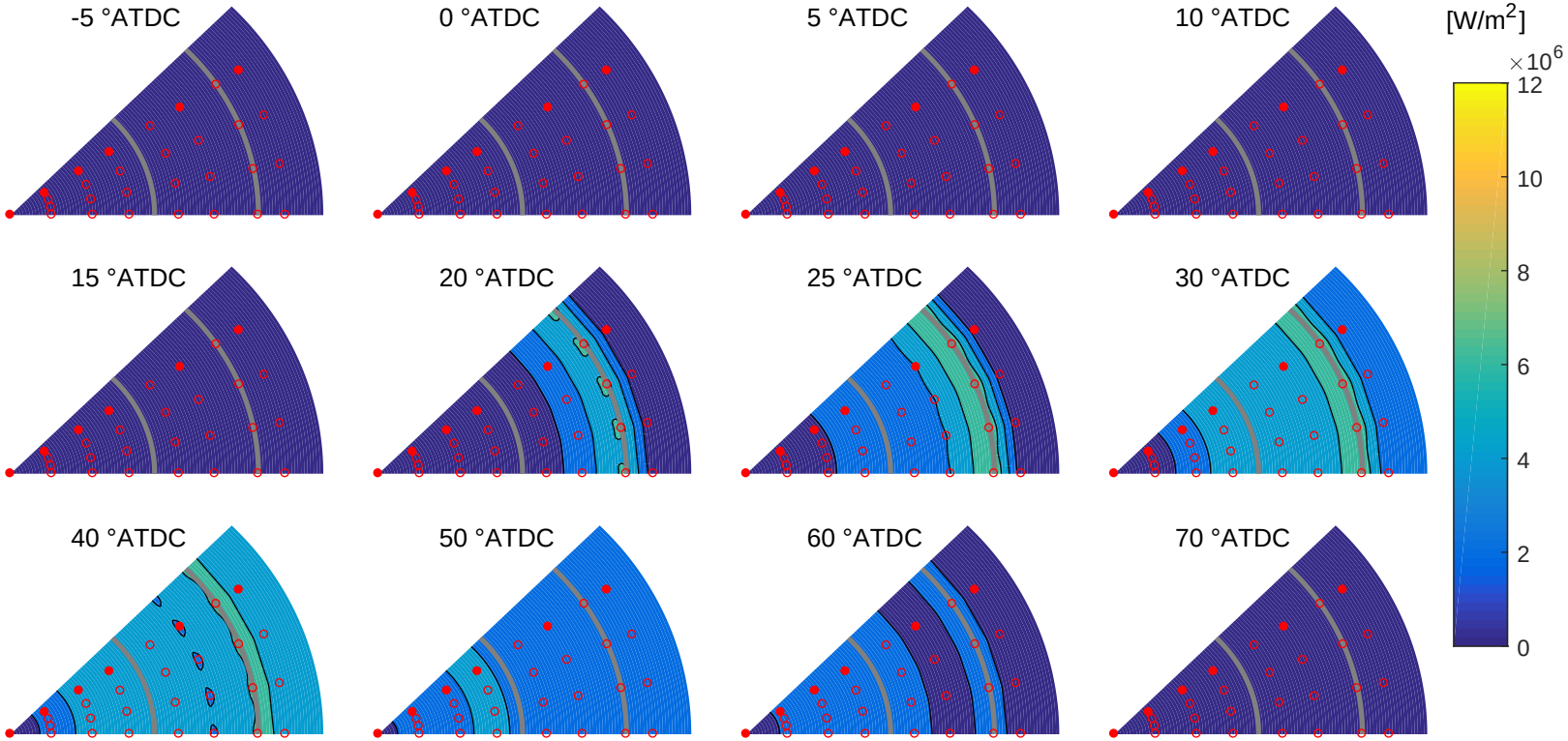


Figure A.32: Operating condition 4 (1700 rpm, 30.3 bar IMEPg) SOI timing of 0 °ATDC

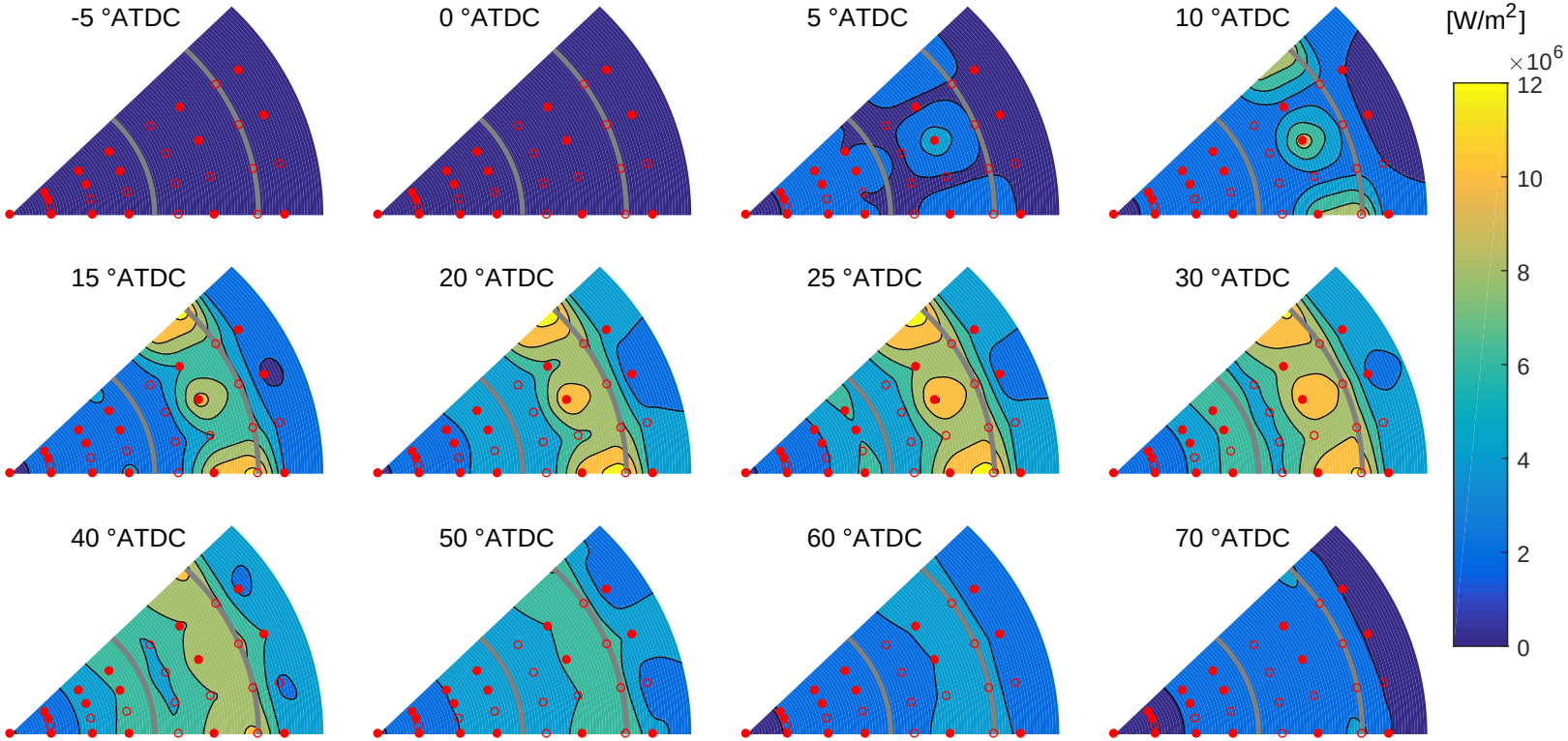


Figure A.33: Operating condition 5 (2750 rpm, 29.7 bar IMEPg) SOI timing of -21 °ATDC

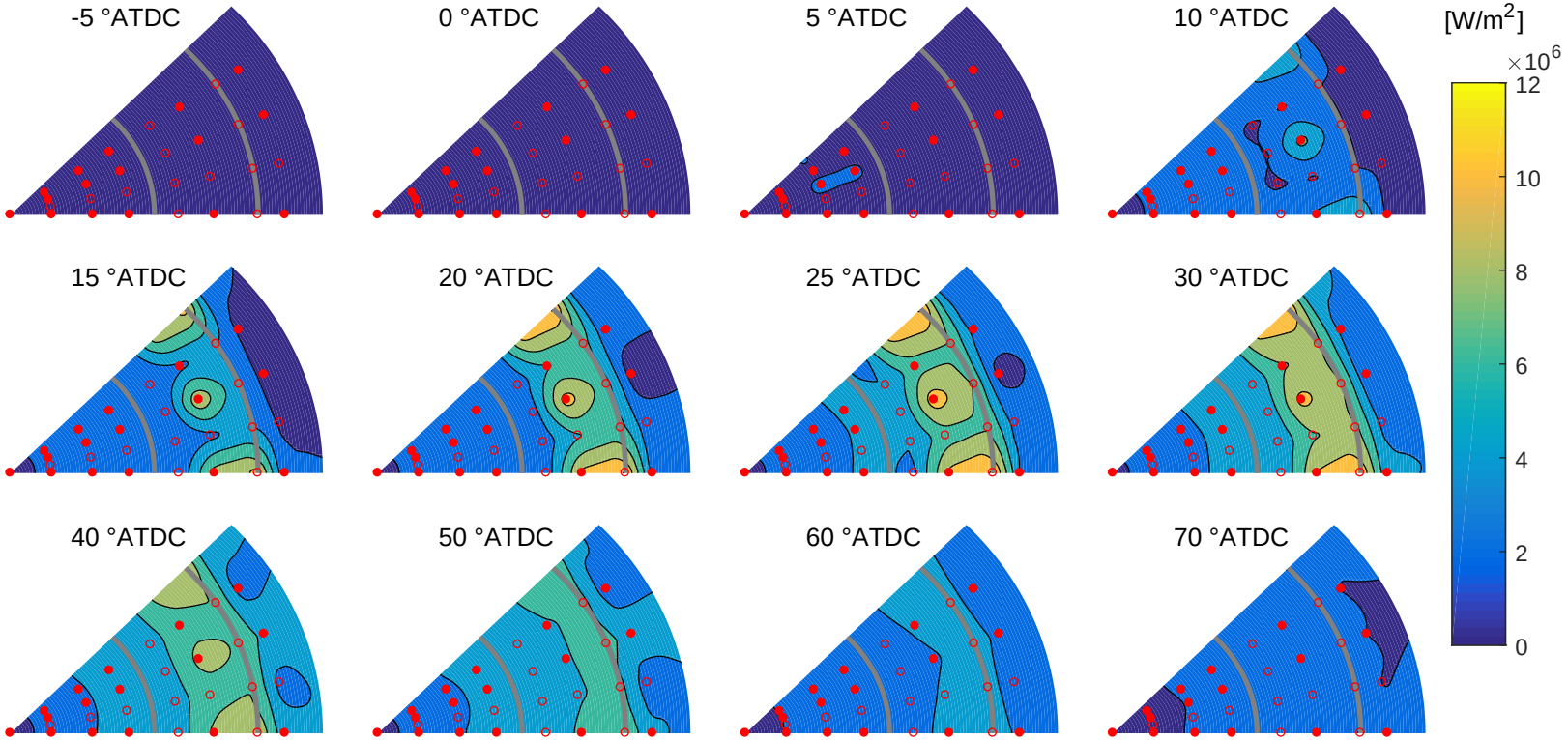


Figure A.34: Operating condition 5 (2750 rpm, 29.7 bar IMEPg) SOI timing of -17 °ATDC

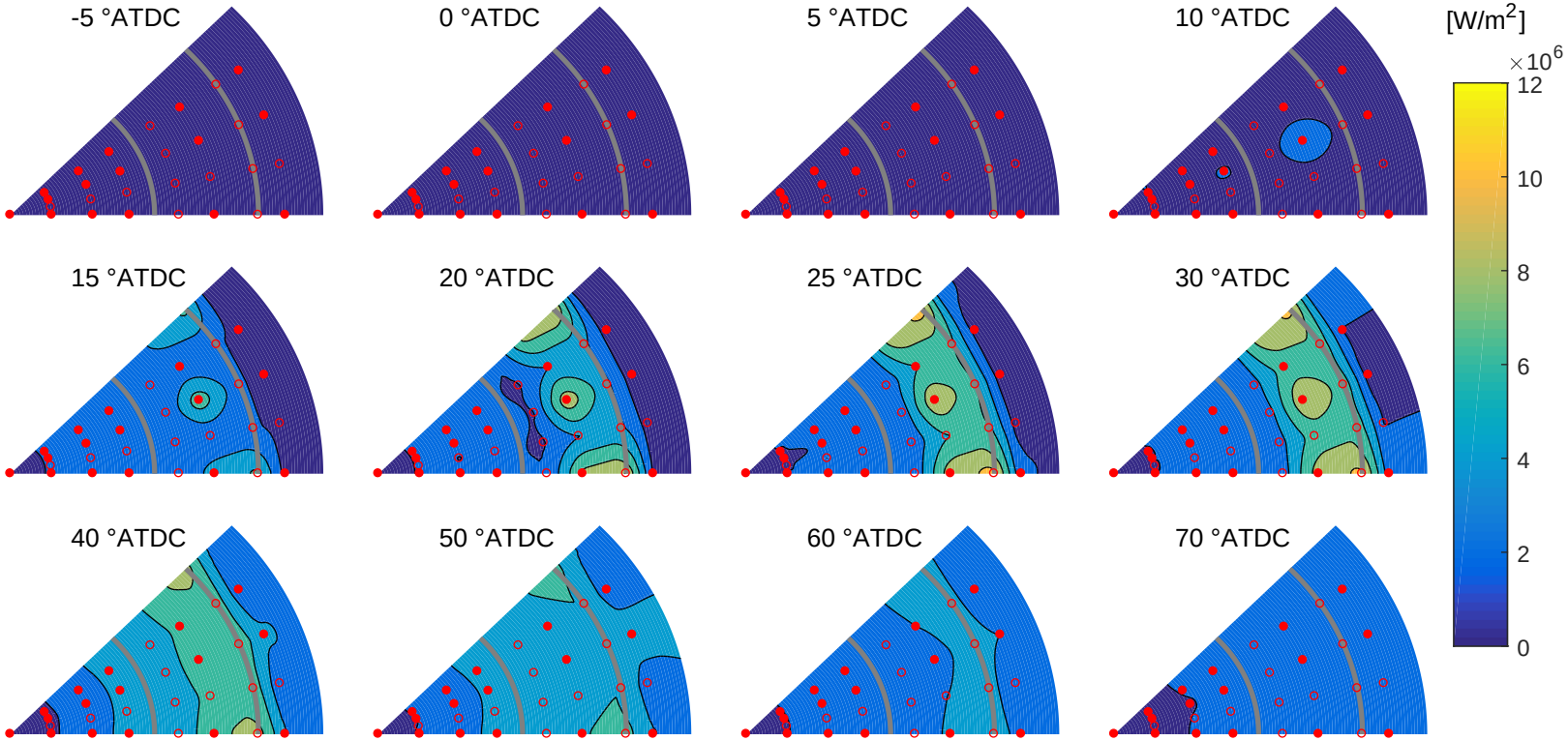


Figure A.35: Operating condition 5 (2750 rpm, 29.7 bar IMEPg) SOI timing of -13 °ATDC

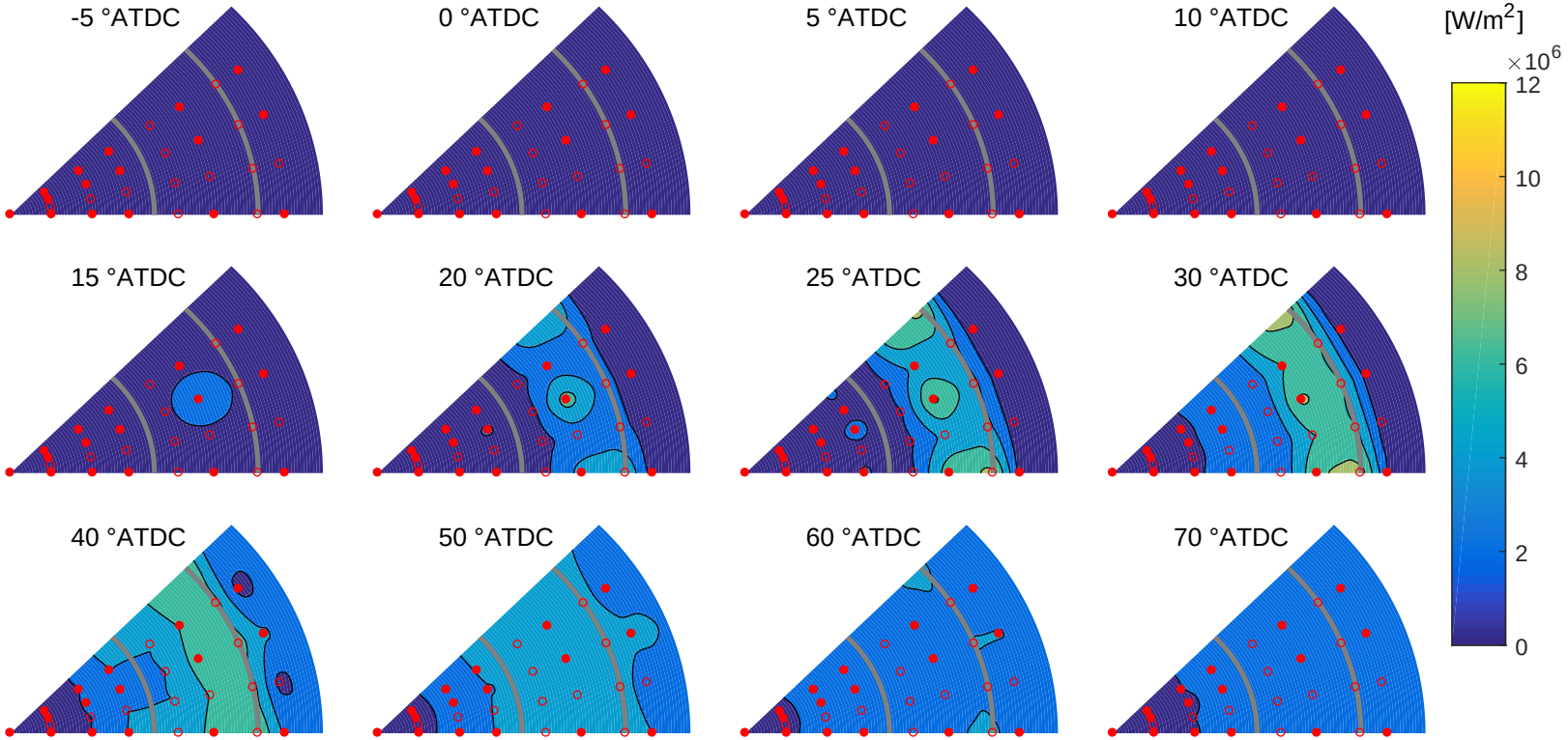


Figure A.36: Operating condition 5 (2750 rpm, 29.7 bar IMEPg) SOI timing of -9 °ATDC

A.13 Final Heat Transfer Correlation 2

The following figures are for final heat transfer correlation 2. A similar set of plots was provided in section 6.5 for final heat transfer correlation 1.

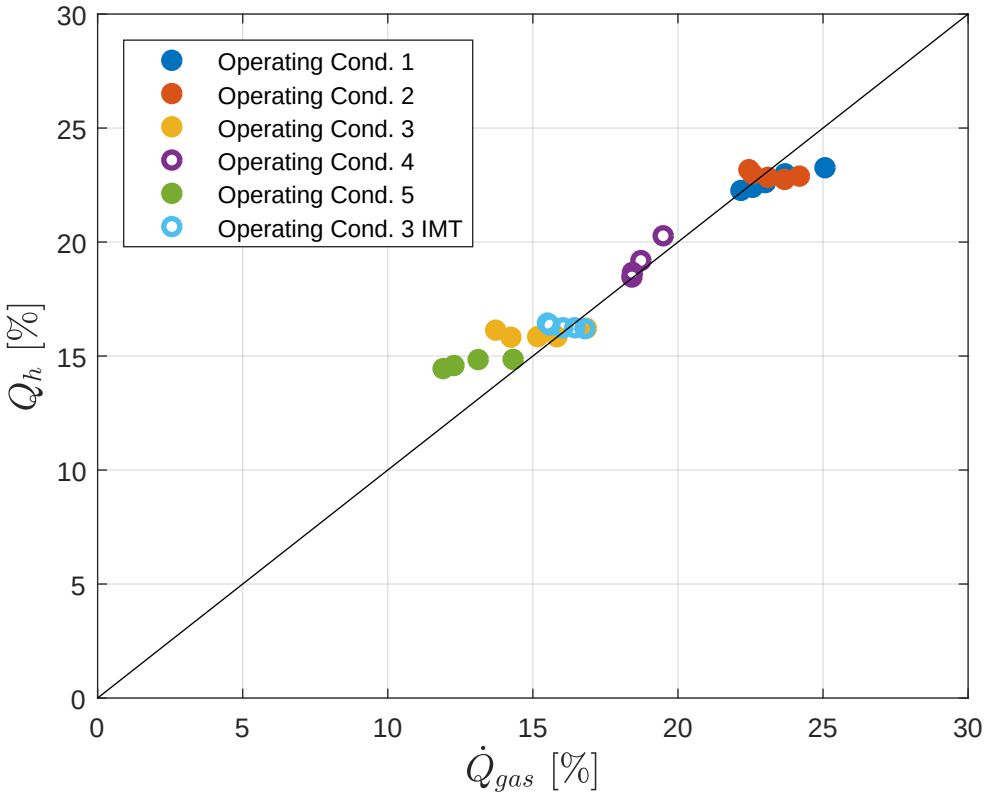


Figure A.37: Comparison of Q_h and Q_{gas} for final correlation 2

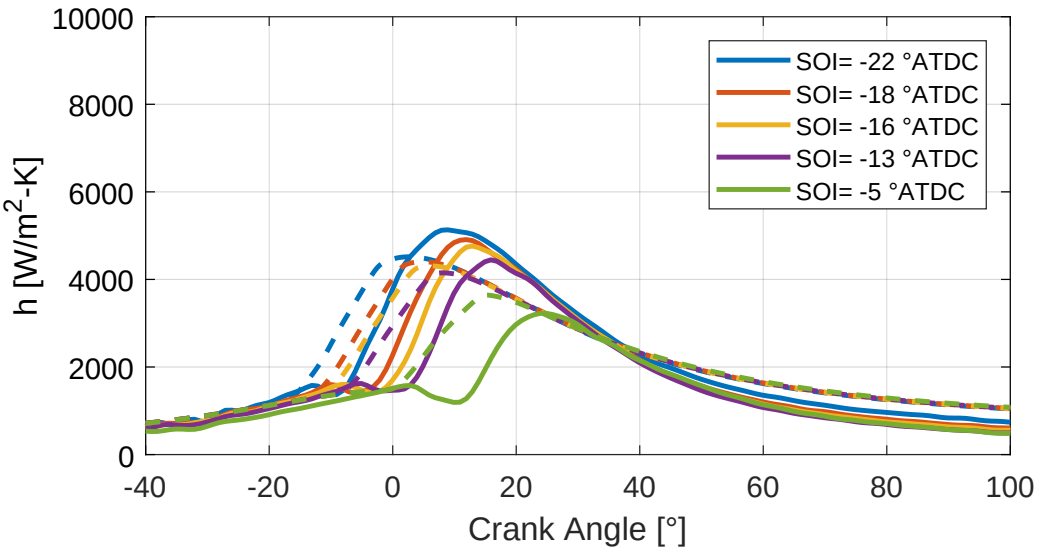


Figure A.38: Operating condition 1 (1700 rpm, 12.3 bar IMEPg), SOI sweep, comparing experimental data $\langle h \rangle$ (solid lines) and final correlation 2 (dashed lines)

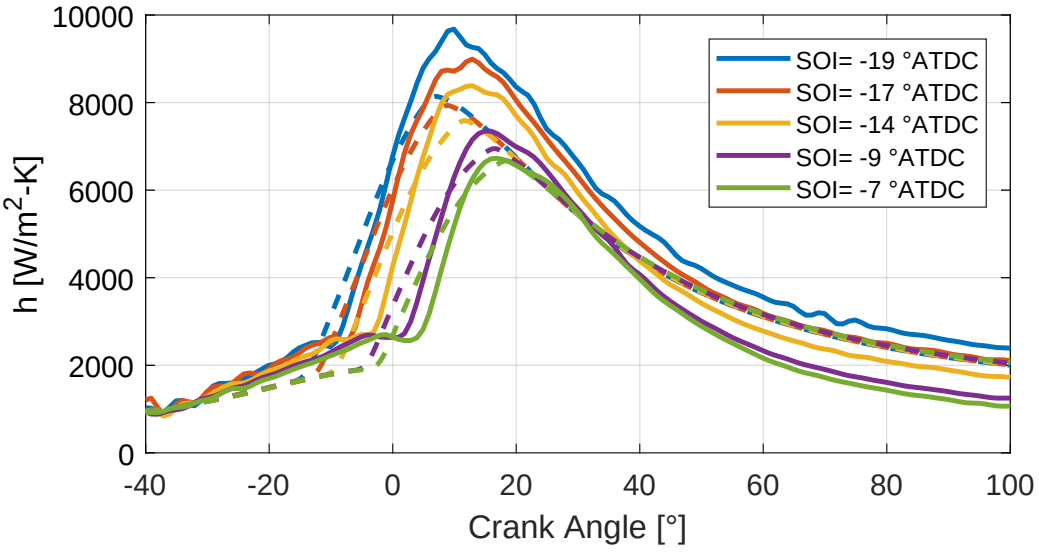


Figure A.39: Operating condition 2 (1500 rpm, 23.8 bar IMEPg), comparing experimental data $\langle h \rangle$ (solid lines) and final correlation 2 (dashed lines)

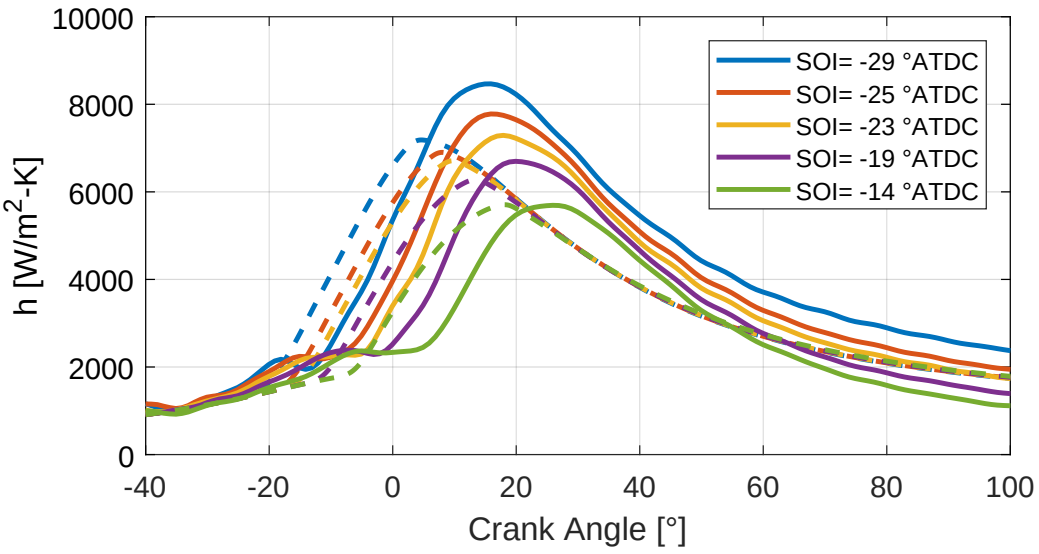


Figure A.40: Operating condition 3 (2500 rpm, 20.3 bar IMEPg), comparing experimental data $\langle h \rangle$ (solid lines) and final correlation 2 (dashed lines)

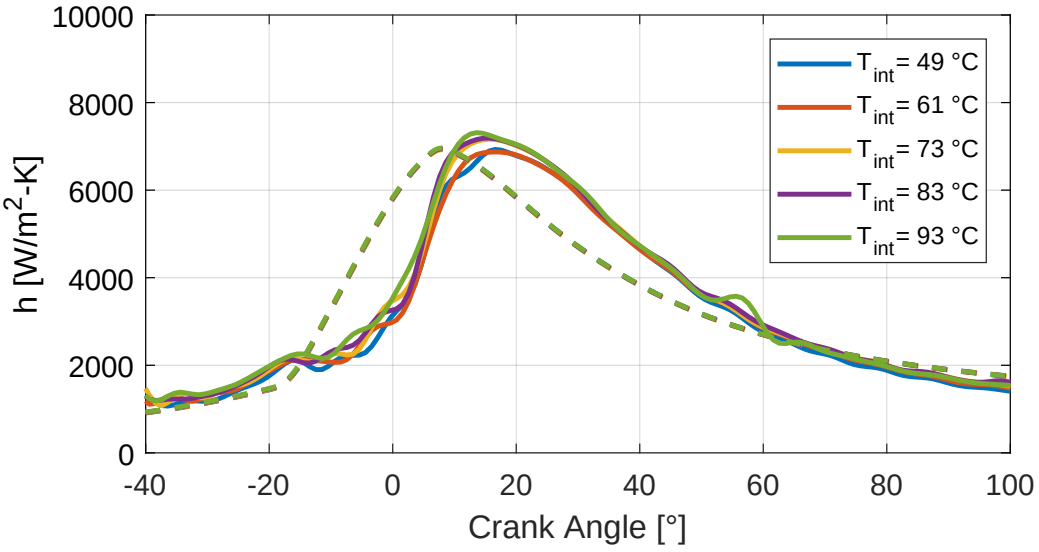


Figure A.41: Operating condition 3 IMT (2500 rpm, 20.3 bar IMEPg), comparing experimental data $\langle h \rangle$ (solid lines) and final correlation 2 (dashed lines)

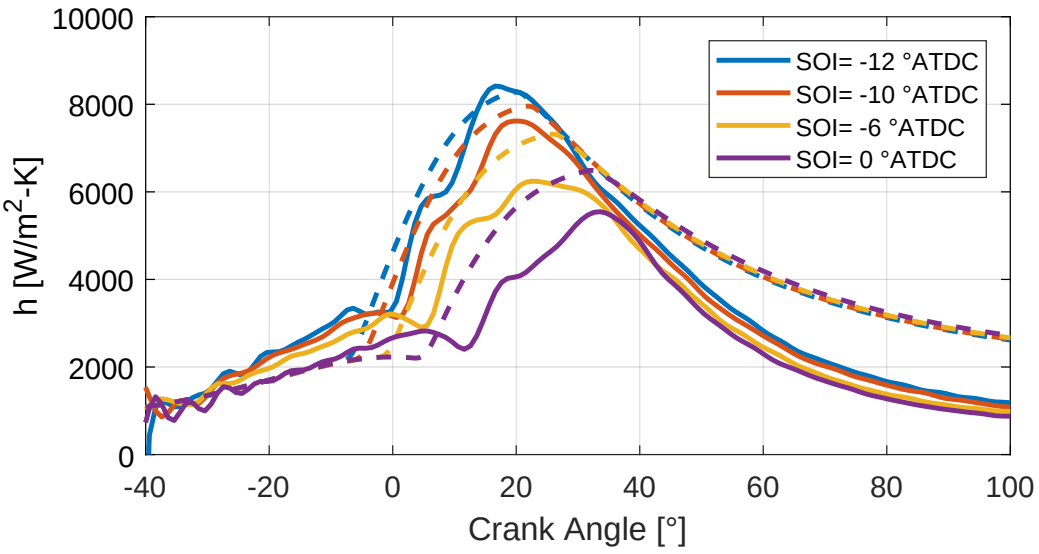


Figure A.42: Operating condition 4 (1700 rpm, 30.3 bar IMEPg), comparing experimental data $\langle h \rangle$ (solid lines) and final correlation 2 (dashed lines)

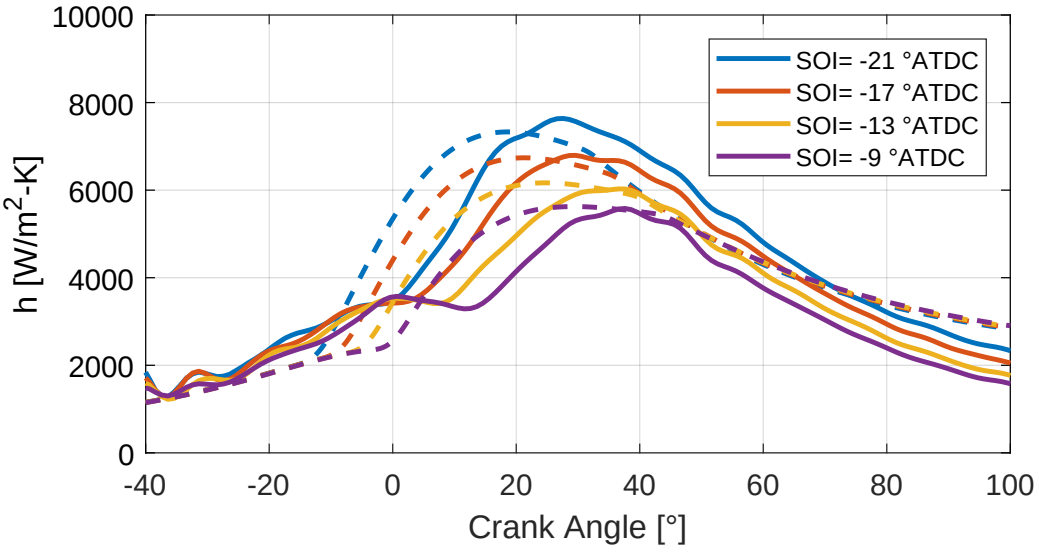


Figure A.43: Operating condition 5 (2750 rpm, 29.7 bar IMEPg), comparing experimental data $\langle h \rangle$ (solid lines) and final correlation 2 (dashed lines)

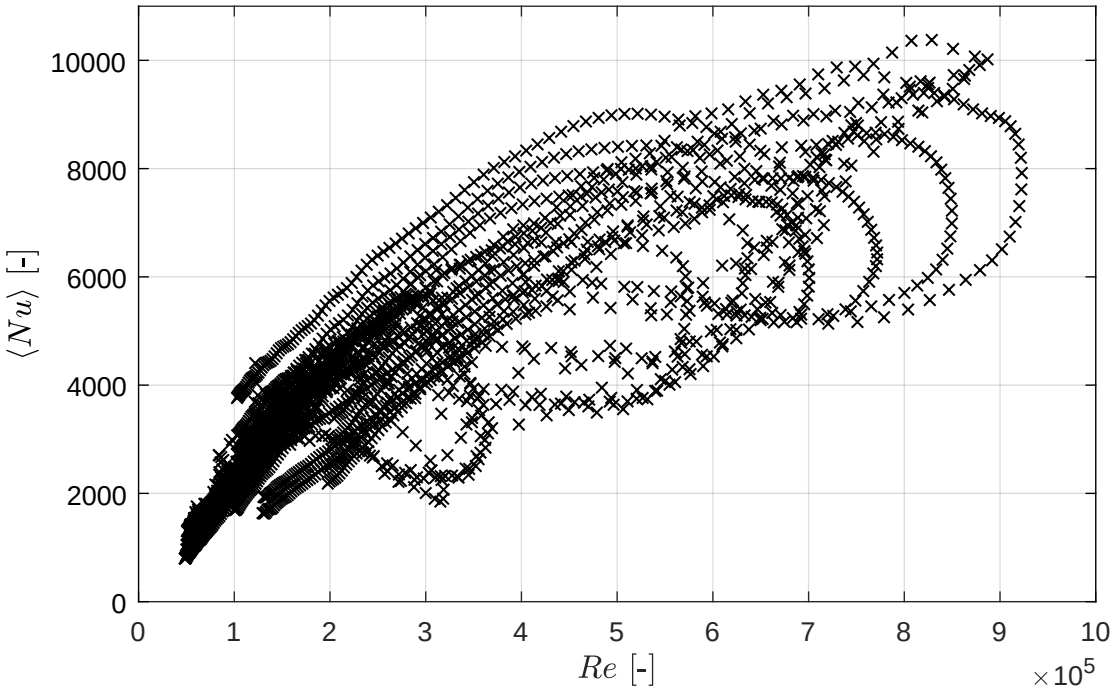


Figure A.44: Operating conditions 1, 2, 3 and 5 $\langle Nu \rangle$ as a function of Re using velocity from final correlation 2 all on same axes

A.14 MATLAB Functions

The MATLAB functions for AHRR, bulk in-cylinder temperature and the new heat transfer correlation are attached. Comments at the beginning of each function describe the inputs and outputs.

Two functions are attached:

1. *AHRR_BulkGas.m* - calculates AHRR and bulk temperature in a single function
2. *gingrich_PhD_correlation.m* - calculates heat transfer correlation using final correlation 1 and 2

```
function [AHRR,cumAHR,T,gamma,Phi_CA,x_CO2,x_H2O,x_N2,x_O2,MW,TotAHR,CA10,CA50,CA90,CA1090] =
AHRR_BulkGas(CA,P,V,m_dot_fuel_CA,CAstart,CAend,trapped_mass,fresh_mass,y,z,T_Intake_Manifold,T_E
xh_Manifold,IVC,EVO)
%
% Function to calculate in-cylinder bulk gas temperature and apparent heat
% release rate.
%
% A fuel injection rate shape, m_dot_fuel_CA, is used to calculate
% crank-angle resolved in-cylinder mass. Mole fractions are calculated
% assuming an instantaneous and ideal conversion of reactants  to products.
% Thermodynamic properties are calculated based on mixture mole fractions.
% The in-cylinder charge is assumed to be N2 and O2. No internal or
% external EGR is allowed. Specific heats are calculated using NASA ideal
% gas properties.
%
% For ideal combustion on a per carbon fuel basis where the reactants and products are:
% CH_yO_z + a_coeff*(O2 + 3.72N2) --> b_coeff*CO2 + c_coeff*H2O + d_coeff*N2 + e_coeff*O2
%
%
% Inputs:
    % CA -                  vector of crank angle [deg]
    % P -                   vector of cylinder pressure (averaged and filtered) [Pa]
    % V -                   vector of cylinder volume [m3]
    % m_dot_fuel_CA -       vector of fuel injection rate (sum to total mass/cyl) [kg/deg]
    % CAstart -             crank angle to start HR calculation [deg]
    % CAend -               crank angle to end HR calculation [deg]
    % trapped_mass          in-cylinder trapped mass including residuals [kg]
    % fresh_mass            fresh mass of air delivered to engine per cycle [kg]
    % y -                   H/C ratio of the fuel [molH/molC]
    % z -                   O/C ratio of the fuel [molO/molC]
    % T_Intake_Manifold -   intake manifold temperature [K]
    % T_Exh_Manifold -      exhaust manifold temperature [K]
    % IVC -                 intake valve close [deg]
    % EVO -                 exhaust valve open [deg]
%
% Outputs:
    % AHRR -                vector of AHRR [J/deg]
    % cumAHR -              vector of accumulated HR [J]
    % T -                   vector of in-cylinder bulk temperature [K]
    % gamma -               vector of ratio of specific heats
    % Phi_CA -              vector of equivalence ratio [-]
    % x_CO2 -               vector of mole fraction CO2 [-]
    % x_H2O -               vector of mole fraction H2O [-]
    % x_N2 -                vector of mole fraction N2 [-]
    % x_O2 -                vector of mole fraction O2 [-]
    % MW -                  vector of mixture molecular weight
    % TotAHR -              integrated accumulated AHR [J]
    % CA10 -                crank-angle of 10% AHRR
    % CA50 -                crank-angle of 50% AHRR
    % CA90 -                crank-angle of 90% AHRR
    % CA1090 -              crank-angle between 10% and 90% AHRR
%
% Written by:
% Eric M. Gingrich
% January 2019
%
%The MIT License (MIT)
%Copyright (c) 2020 Eric Gingrich
%Permission is hereby granted, free of charge, to any person obtaining a
%copy of this software and associated documentation files (the "Software"),
%to deal in the Software without restriction, including without limitation
%the rights to use, copy, modify, merge, publish, distribute, sublicense,
%and/or sell copies of the Software, and to permit persons to whom the
%Software is furnished to do so, subject to the following conditions:
%The above copyright notice and this permission notice shall be included in
%all copies or substantial portions of the Software.
%THE SOFTWARE IS PROVIDED "AS IS", WITHOUT WARRANTY OF ANY KIND, EXPRESS OR
%IMPLIED, INCLUDING BUT NOT LIMITED TO THE WARRANTIES OF MERCHANTABILITY,
%FITNESS FOR A PARTICULAR PURPOSE AND NONINFRINGEMENT. IN NO EVENT SHALL
%THE AUTHORS OR COPYRIGHT HOLDERS BE LIABLE FOR ANY CLAIM, DAMAGES OR OTHER
%LIABILITY, WHETHER IN AN ACTION OF CONTRACT, TORT OR OTHERWISE, ARISING
```

```
%FROM, OUT OF OR IN CONNECTION WITH THE SOFTWARE OR THE USE OR OTHER
%DEALINGS IN THE SOFTWARE.
%

%% Generate injection rate shape from SOI to EOI (copy into higher level script)
% m_dot_fuel_CA=zeros(CA_length,1);
% if ALPHA_d~=0;m_dot_fuel_CA(iid_SOI_EA:iid_EOI_EA)= m_fuel_cyc/(iid_EOI_EA-iid_SOI_EA+1); end
%% Constants
Rbar =8.314510;                                                 % [J/mol-K] universal gas consant
MW_C = 12.0107;                                                 % [kg/kmol]
MW_H = 1.0079;                                                  % [kg/kmol]
MW_O = 15.9994;                                                 % [kg/kmol]
MW_N = 14.0067;                                                 % [kg/kmol]

MW_CO2=MW_C+2*MW_O;                                             % [kg/kmol]
MW_H2O=2*MW_H+MW_O;                                             % [kg/kmol]
MW_N2=2*MW_N;                                                   % [kg/kmol]
MW_O2=2*MW_O;                                                   % [kg/kmol]

%% Generate crank-angle based varriables
a_stoic= 1 + y/4 - z/2;
AFR_stoic =(a_stoic*MW_O2+3.76*a_stoic*MW_N2)/(MW_C+y*MW_H+z*MW_O);
m_fuel_CA=cumsum(m_dot_fuel_CA); % Cumulative fuel mass function of CA
m_CA=m_fuel_CA+trapped_mass; % In-cylinder fuel and air mass function of CA
AFR_CA=fresh_mass./m_fuel_CA; % Air-fuel ratio as a function of CA, only us fresh air delivered
to engine, no internal or external EGR

Phi_CA=AFR_stoic./AFR_CA; %equivalence ratio

%% Calculate Mole-fraction of ideal combustion products
for i=1:length(CA)
    if Phi_CA(i)~=0 % For CA when Phi is not infinity
        % For ideal combustion on a per carbon fuel basis where the reactants and products are:
        % CH_yO_z + a_coeff*(O2 + 3.76N2) --> b_coeff*CO2 + c_coeff*H2O + d_coeff*N2 + e_coeff*O2
        a_coeff = (2+y/2-z)/(2*Phi_CA(i));        % from stoichiometric case
        b_coeff = 1;
        c_coeff = y/2;
        e_coeff = z/2 + a_coeff -1 - 1/y;
        d_coeff=3.76*a_coeff;

        Total_moles = b_coeff + c_coeff + d_coeff + e_coeff;

        % Mole fraction of mixture species
        x_CO2(i,1) = b_coeff/Total_moles;
        x_H2O(i,1) = c_coeff/Total_moles;
        x_N2(i,1) = d_coeff/Total_moles;
        x_O2(i,1) = e_coeff/Total_moles;

        MW(i,1) = MW_CO2*x_CO2(i,1) + MW_H2O*x_H2O(i,1)...
            + MW_N2*x_N2(i,1) + MW_O2*x_O2(i,1); % molecular weight of mixture (kg/kmol)

    else % Assume N2 and O2 (air)
        % Mole fraction of mixture species
        x_CO2(i,1) = 0;
        x_H2O(i,1) = 0;
        x_N2(i,1) = 3.76/4.76;
        x_O2(i,1) = 1/4.76;

        MW(i,1) = MW_CO2*x_CO2(i,1) + MW_H2O*x_H2O(i,1)...
            + MW_N2*x_N2(i,1) + MW_O2*x_O2(i,1); % molecular weight of mixture (kg/kmol)
    end
end

%% Bulk average temperature [K]
T = zeros(size(CA));
for i = 1 : length(CA)
    T(i,1) = P(i,1)*V(i,1)/(m_CA(i,1)*(Rbar*1000)/MW(i,1));
    if CA(i,1) < IVC
        T(i,1) = max(T(i,1),T_Intake_Manifold);
    elseif CA(i,1) > EVO
        T(i,1) = max(T(i,1),T_Exh_Manifold);
```

```
    end
end
%% Mixture specific heats, (see sub-functions for details)
for i=1:length(CA)
c_p(i,1) = c_p_CO2(T(i,1))*x_CO2(i,1) + c_p_H2O(T(i,1))*x_H2O(i,1)...
    + c_p_N2(T(i,1))*x_N2(i,1) + c_p_O2(T(i,1))*x_O2(i,1); % molar heat capacity at constant
pressure (kJ/kmol-K)
c_v(i,1) = c_p(i,1) - Rbar;
gamma(i,1) = c_p(i,1)/c_v(i,1); % ratio of specific heats
end
%% AHRR
iidHR = find(CA > CAstart & CA < CAend);
dPdCA = gradient(P,CA);
dVdCA = gradient(V,CA);
AHRR = zeros(size(CA));
AHRR(iidHR) = (dPdCA(iidHR) + gamma(iidHR).*P(iidHR)./V(iidHR).*dVdCA(iidHR))./(gamma(iidHR)-
1).*V(iidHR);
TotAHR = trapz(CA,AHRR);
cumAHR = cumtrapz(CA,AHRR);
iid_CA10=find(cumAHR>=0.1*TotAHR, 1 );
CA10 = CA(iid_CA10);
iid_CA50=find(cumAHR>=0.5*TotAHR, 1 );
CA50 = CA(iid_CA50);
iid_CA90=find(cumAHR>=0.9*TotAHR, 1 );
CA90 = CA(iid_CA90);
CA1090 = CA90-CA10;

end
%% Sub-functions to calculate enthalpy for each species using ideal gas properties

% Temperature range for each species is 200-1000K and 1000-6000K (unless specified below)
% Reference state is 298.15K for NASA tables (set to enthalpy of formation)
% Coefficients and equations taken from:
% McBride, B. J., Zehe, M. J., & Gordon, S. (2002). NASA Glenn coefficients for calculating
thermodynamic properties of individual species.

% Inputs:
% T - Temperature (K)

% Outputs:
% c_p - molar heat capacity at constant pressure (kJ/kmol-K)


    function [c_p] = c_p_CO(T)

        R=8.314510; % universal gas constant, J/(mol-K)

            if (T>=200) && (T<=1000.0007)
                a=[1.489045326D+04 -2.922285939D+02 5.724527170D+00 -8.176235030D-03
1.456903469D-05 -1.087746302D-08 3.027941827D-12];
                b=[-1.303131878D+04 -7.859241350D+00];
            elseif (T>1000) && (T<=6000.007)
                a=[4.619197250D+05 -1.944704863D+03 5.916714180D+00 -5.664282830D-04
1.398814540D-07 -1.787680361D-11 9.620935570D-16];
                b=[-2.466261084D+03 -1.387413108D+01];
            else error('Outside Temperature Range of NASA Polynomials')
            end
            c_p=R*(a(1)*T^-2 + a(2)*T^-1 + a(3) + a(4)*T + a(5)*(T^2) + a(6)*(T^3) + a(7)*(T^4));
        end


    function [c_p] = c_p_CO2(T)
        R=8.314510; % universal gas constant, J/(mol-K)

            if (T>=200) && (T<=1000.0007)
                a=[4.943650540D+04 -6.264116010D+02 5.301725240D+00 2.503813816D-03 -
2.127308728D-07 -7.689988780D-10 2.849677801D-13];
                b=[-4.528198460D+04 -7.048279440D+00];
            elseif (T>1000) && (T<=6000.007)
                a=[1.176962419D+05 -1.788791477D+03 8.291523190D+00 -9.223156780D-05
4.863676880D-09 -1.891053312D-12 6.330036590D-16];
```

```
            b=[-3.908350590D+04 -2.652669281D+01];
        else error('Outside Temperature Range of NASA Polynomials')
        end
        c_p=R*(a(1)*T^-2 + a(2)*T^-1 + a(3) + a(4)*T + a(5)*(T^2) + a(6)*(T^3) + a(7)*(T^4));
    end


function [c_p] = c_p_O2(T)
    R=8.314510; % universal gas constant, J/(mol-K)

        if (T>=200) && (T<=1000.0007)
            a=[-3.425563420D+04 4.847000970D+02 1.119010961D+00 4.293889240D-03 -
6.836300520D-07 -2.023372700D-09 1.039040018D-12];
            b=[-3.391454870D+03 1.849699470D+01];
        elseif (T>1000) && (T<=6000.007)
            a=[-1.037939022D+06 2.344830282D+03 1.819732036D+00 1.267847582D-03 -
2.188067988D-07 2.053719572D-11 -8.193467050D-16];
            b=[-1.689010929D+04 1.738716506D+01];
        else error('Outside Temperature Range of NASA Polynomials')
        end
        c_p=R*(a(1)*T^-2 + a(2)*T^-1 + a(3) + a(4)*T + a(5)*(T^2) + a(6)*(T^3) + a(7)*(T^4));
    end


function [c_p] = c_p_H2O(T)
    R=8.314510; % universal gas constant, J/(mol-K)

        if (T>=200) && (T<=1000.0007)
            a=[-3.947960830D+04 5.755731020D+02 9.317826530D-01 7.222712860D-03 -
7.342557370D-06 4.955043490D-09 -1.336933246D-12];
            b=[-3.303974310D+04 1.724205775D+01];
        elseif (T>1000) && (T<=6000.007)
            a=[1.034972096D+06 -2.412698562D+03 4.646110780D+00 2.291998307D-03 -
6.836830480D-07 9.426468930D-11 -4.822380530D-15];
            b=[-1.384286509D+04-7.978148510D+00];
        else error('Outside Temperature Range of NASA Polynomials')
        end
        c_p=R*(a(1)*T^-2 + a(2)*T^-1 + a(3) + a(4)*T + a(5)*(T^2) + a(6)*(T^3) + a(7)*(T^4));
    end


function [c_p] = c_p_N2(T)
    R=8.314510; % universal gas constant, J/(mol-K)

        if (T>=200) && (T<=1000.0007)
            a=[2.210371497D+04 -3.818461820D+02 6.082738360D+00 -8.530914410D-03
1.384646189D-05 -9.625793620D-09 2.519705809D-12];
            b=[7.108460860D+02 -1.076003744D+01];
        elseif (T>1000) && (T<=6000.007)
            a=[5.877124060D+05 -2.239249073D+03 6.066949220D+00 -6.139685500D-04
1.491806679D-07 -1.923105485D-11 1.061954386D-15];
            b=[1.283210415D+04 -1.586640027D+01];
        else error('Outside Temperature Range of NASA Polynomials')
        end
        c_p=R*(a(1)*T^-2 + a(2)*T^-1 + a(3) + a(4)*T + a(5)*(T^2) + a(6)*(T^3) + a(7)*(T^4));
    end


function [c_p] = c_p_NO(T)
    R=8.314510; % universal gas constant, J/(mol-K)

        if (T>=200) && (T<=1000.0007)
            a=[-1.143916503D+04 1.536467592D+02 3.431468730D+00 -2.668592368D-03
8.481399120D-06 -7.685111050D-09 2.386797655D-12];
            b=[9.098214410D+03 6.728725490D+00];
        elseif (T>1000) && (T<=6000.007)
            a=[2.239018716D+05 -1.289651623D+03 5.433936030D+00 -3.656034900D-04
9.880966450D-08 -1.416076856D-11 9.380184620D-16];
            b=[1.750317656D+04 -8.501669090D+00];
        else error('Outside Temperature Range of NASA Polynomials')
        end
```

```
            c_p=R*(a(1)*T^-2 + a(2)*T^-1 + a(3) + a(4)*T + a(5)*(T^2) + a(6)*(T^3) + a(7)*(T^4));
        end


    function [c_p] = c_p_NO2(T)
        R=8.314510; % universal gas constant, J/(mol-K)

            if (T>=200) && (T<=1000.0007)
                a=[-5.642038780D+04 9.633085720D+02 -2.434510974D+00 1.927760886D-02 -
1.874559328D-05 9.145497730D-09 -1.777647635D-12];
                b=[-1.547925037D+03 4.067851210D+01];
            elseif (T>1000) && (T<=6000.007)
                a=[7.213001570D+05 -3.832615200D+03 1.113963285D+01 -2.238062246D-03
6.547723430D-07 -7.611335900D-11 3.328361050D-15];
                b=[2.502497403D+04 -4.305130040D+01];
            else error('Outside Temperature Range of NASA Polynomials')
            end
            c_p=R*(a(1)*T^-2 + a(2)*T^-1 + a(3) + a(4)*T + a(5)*(T^2) + a(6)*(T^3) + a(7)*(T^4));
        end


    function [c_p] = c_p_H2(T)
        R=8.314510; % universal gas constant, J/(mol-K)

            if (T>=200) && (T<=1000.0007)
                a=[4.078323210D+04 -8.009186040D+02 8.214702010D+00 -1.269714457D-02
1.753605076D-05 -1.202860270D-08 3.368093490D-12];
                b=[2.682484665D+03 -3.043788844D+01];
            elseif (T>1000) && (T<=6000.007)
                a=[5.608128010D+05 -8.371504740D+02 2.975364532D+00 1.252249124D-03 -
3.740716190D-07 5.936625200D-11 -3.606994100D-15];
                b=[5.339824410D+03 -2.202774769D+00];
            else error('Outside Temperature Range of NASA Polynomials')
            end
            c_p=R*(a(1)*T^-2 + a(2)*T^-1 + a(3) + a(4)*T + a(5)*(T^2) + a(6)*(T^3) + a(7)*(T^4));
        end


    function [c_p] = c_p_CH4(T)
        R=8.314510; % universal gas constant, J/(mol-K)

            if (T>=200) && (T<=1000.0007)
                a=[-1.766850998D+05 2.786181020D+03 -1.202577850D+01 3.917619290D-02 -
3.619054430D-05 2.026853043D-08 -4.976705490D-12];
                b=[-2.331314360D+04 8.904322750D+01];
            elseif (T>1000) && (T<=6000.007)
                a=[3.730042760D+06 -1.383501485D+04 2.049107091D+01 -1.961974759D-03
4.727313040D-07 -3.728814690D-11 1.623737207D-15];
                b=[7.532066910D+04 -1.219124889D+02];
            else error('Outside Temperature Range of NASA Polynomials')
            end
            c_p=R*(a(1)*T^-2 + a(2)*T^-1 + a(3) + a(4)*T + a(5)*(T^2) + a(6)*(T^3) + a(7)*(T^4));
        end
```

```
function [h]=gingrich_PhD_correlation(P,T,V,m_dot_fuel_CA,AHRR,m_fuel_cyc,correlation)
%
% Function to calculate the instantaneous spatially averaged heat transfer
% coefficient using "final correlation 1" and "final correlation 2" as
% presented in:
% E. Gingrich, High-output Diesel Engine Heat Transfer, PhD Thesis 2020,
%    University of Wisconsin-Madison
%
%Inputs:
%   P - vector of in-cylinder pressure [Pa]
%   T - vector of temperature [K]
%   V - vector of volume [m^3]
%   m_dot_fuel_CA - vector of fuel rate of injection [kg/deg]
%   AHRR - *optional* vector of apparent heat release rate [J/deg]
%   m_fuel_cyc - total fuel mass injected per cycle [kg]
%   correlation - switch to select correlation 1 or correlation 2
%       correlation=1: Final Correlation 1
%       correlation=2: Final Correlation 2
%
%Output:
%   h - vector of heat transfer coefficients [W/m^2-K]
%
%Comments:
%   - AHRR must be provided when correlation 2 is selected unless fueling is
%     zero (m_fuel_cyc=0)
%   - The integral of m_dot_fuel_CA is scaled to m_fuel_cyc therefore  only
%     the "shape" of m_dot_fuel_CA is important
%   - All vectors must be the same length and correspond to a given crank
%    angle
%
% Written by:
% Eric M. Gingrich
% June 2020
%
%The MIT License (MIT)
%Copyright (c) 2020 Eric Gingrich
%Permission is hereby granted, free of charge, to any person obtaining a
%copy of this software and associated documentation files (the "Software"),
%to deal in the Software without restriction, including without limitation
%the rights to use, copy, modify, merge, publish, distribute, sublicense,
%and/or sell copies of the Software, and to permit persons to whom the
%Software is furnished to do so, subject to the following conditions:
%The above copyright notice and this permission notice shall be included in
%all copies or substantial portions of the Software.
%THE SOFTWARE IS PROVIDED "AS IS", WITHOUT WARRANTY OF ANY KIND, EXPRESS OR
%IMPLIED, INCLUDING BUT NOT LIMITED TO THE WARRANTIES OF MERCHANTABILITY,
%FITNESS FOR A PARTICULAR PURPOSE AND NONINFRINGEMENT. IN NO EVENT SHALL
%THE AUTHORS OR COPYRIGHT HOLDERS BE LIABLE FOR ANY CLAIM, DAMAGES OR OTHER
%LIABILITY, WHETHER IN AN ACTION OF CONTRACT, TORT OR OTHERWISE, ARISING
%FROM, OUT OF OR IN CONNECTION WITH THE SOFTWARE OR THE USE OR OTHER
%DEALINGS IN THE SOFTWARE.
%

if correlation==1&&m_fuel_cyc==0 % motoring case using correlation 1
    AHRR=0*P; % clear any values of AHRR if provided
end

if correlation==1 % final correlation 1
    a=[0.00340,0.278,6.57,1.97,58300]; % correlation constants
    m=0.805; % Reynolds number exponent
    c_p = specific_heat(T); % specific heat of air [kJ/kg-K]
    f_q_ch_tilde= combustion_multiplier(AHRR,P,V,c_p,a); % combustion multiplier, f(q_ch_tilde)
[-]

elseif correlation==2 % final correlation 2
    a=[0.337,0,1,1.97,86700]; % correlation constants
    m=0.564; % Reynolds number exponent
    f_q_ch_tilde=1; % combustion multiplier, f(q_ch_tilde) [-]

end
```

```
v = velocity(m_dot_fuel_CA,m_fuel_cyc,a); % velocity [m/s]
k = conductivity(T); % conductivity of air [W/m-K]
mu = viscosity(T); % viscosity of air [kg/m-s]

% heat transfer coefficient [W/m^2-K]
h= a(1).*(v.^m).*(P.^m).*T.^(-m).*k.*(mu.^-m).*f_q_ch_tilde;

end

function [v] = velocity(m_dot_fuel_CA,m_fuel_cyc,a)
% Sub-function to calculate velocity.
%
%Inputs:
%   m_dot_fuel_CA - vector of fuel rate of injection [kg/deg]
%   m_fuel_cyc - total fuel mass injected per cycle [kg]
%   a - vector of correlation constants
%
%Output:
%   v - vector of velocity [m/s]

if m_fuel_cyc~=0 % non-zero fuel cases (avoid divide by zero)
    % find cumulative fuel injected for each crank angle and scale to
    % amount of fuel injected per cycle
    m_fuel_CA=cumsum(m_dot_fuel_CA).*m_fuel_cyc./max(cumsum(m_dot_fuel_CA));
else % zero fuel case, i.e., motoring
    m_fuel_CA=0;
end

v = a(4) + a(5).*m_fuel_CA; % velocity [m/s]

end

function [f_q_ch_tilde] = combustion_multiplier(AHRR,P,V,c_p,a)
% Sub-function to calculate combustion multiplier, f(q_ch_tilde).
%
%Inputs:
%   AHRR - vector of apparent heat release rate [J/deg]
%   P - vector of in-cylinder pressure [Pa]
%   V - vector of volume  [m^3]
%   c_p - vector of specific heat [kJ/kg-K]
%   a - vector of correlation constants
%
%Output:
%   f_q_ch_tilde - combustion multiplier, f(q_ch_tilde) [-]

R_bar=0.2871;% gas constant of air [kJ/kg-K]
q_ch_tilde=360*R_bar*AHRR./(P.*V.*c_p); % dimensionless chemical energy release rate [-]
q_ch_tilde(q_ch_tilde<0)=0; % set negative values to zero
f_q_ch_tilde=(a(2).*q_ch_tilde+a(3))./(q_ch_tilde+a(3));

end

function [k] = conductivity(T)
% Conductivity of air at 130 bar found by fitting a power-law to
% data in the range of 300 to 2000 K.  Curve fit was generated using
% Engineering Equation Solver which sourced data from Lemmon and Jacobsen.
%
% References:
% E. W. Lemmon and R. T. Jacobsen. Viscosity and thermal conductivity
% equations for nitrogen, oxygen, argon, and air. International journal of
% thermophysics, 25(1):21-69, 2004.
%
% S. Klein. Engineering Equation Solver (Version 10.644-3D).
%  URL http://www.chartsoftware.com/ees/
%
%Input:
%   T - vector of temperature [K]
%
%Output:
%   k - vector of conductivity [W/m-K]
```

```
k = 0.000604295*T.^0.687791;

end

function [mu] = viscosity(T)
% Viscosity of air at 130 bar found by fitting a power-law to
% data in the range of 300 to 2000 K.  Curve fit was generated using
% Engineering Equation Solver which sourced data from Lemmon and Jacobsen.
%
% References:
% E. W. Lemmon and R. T. Jacobsen. Viscosity and thermal conductivity
% equations for nitrogen, oxygen, argon, and air. International journal of
% thermophysics, 25(1):21-69, 2004.
%
% S. Klein. Engineering Equation Solver (Version 10.644-3D).
%  URL http://www.chartsoftware.com/ees/
%
%Input:
%   T - vector of temperature [K]
%
%Output:
%   mu - vector of viscosity [kg/m-s]

mu= 6.00579E-07*T.^0.622048;

end

function [c_p] = specific_heat(T)
% Ideal gas specific heat found by fitting a fourth-order polynomial to
% data in the range of 300 to 2500 K. NASA ideal gas properties were used
% assuming a mixture of 21 percent O2 and 79 percent N2. Curve fit was
% generated using Engineering Equation Solver.
%
% References:
% B. J. McBride, M. J. Zehe, and S. Gordon. NASA Glenn coefficients for
%  calculating thermodynamic properties of individual species, 2002
%
% S. Klein. Engineering Equation Solver (Version 10.644-3D).
%  URL http://www.chartsoftware.com/ees/
%
%Input:
%   T - vector of temperature [K]
%
%Output:
%   c_p - vector of specific heat [kJ/kg-K]

c_p= 0.965761 + 0.000084381*T + 2.02410E-07*T.^2- ...
    1.29021E-10*T.^3 + 2.21140E-14*T.^4;

end
```